SPMS 2020/21
Stochastic and Physical Monitoring Systems

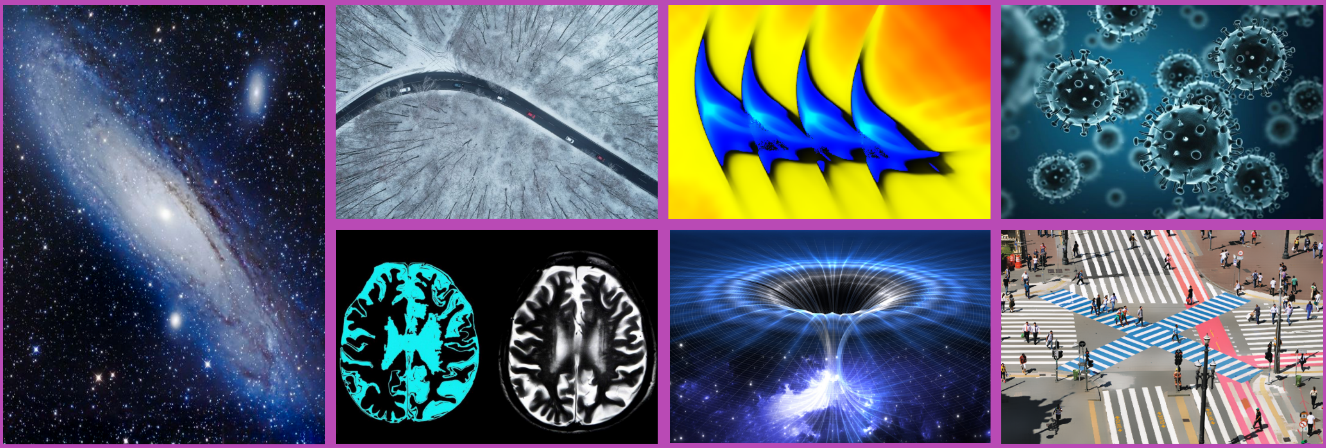

Proceedings

Group of Applied Mathematics and Stochastics
Faculty of Nuclear Sciences and Physical Engineering
Czech Technical University in Prague

CTU
CZECH TECHNICAL
UNIVERSITY
IN PRAGUE

SPMS 2020/21

Stochastic and Physical Monitoring Systems

Proceedings of the international conferences

September 17 - 21, 2020, Chlum u Třeboně

June 24 - 28, 2021, Malá Skála

Editors: Tomáš Hobza & Jiří Franc

Organized by: Group of Applied Mathematics and Stochastics (GAMS),
Faculty of Nuclear Sciences and Physical Engineering,
Czech Technical University in Prague

Sponsored by: SGS grants SVK 26/20/F4 and SVK 29/21/F4
and MŠMT grant LM2018113

SPMS 2020/21 - Stochastic and Physical Monitoring Systems
Proceedings of the international conferences

Editors: Tomáš Hobza & Jiří Franc
Contact: tomas.hobza@fjfi.cvut.cz | +420 224 358 547 | gams.fjfi.cvut.cz

Published by: Czech Technical University in Prague
Processed by: Faculty of Nuclear Sciences and Physical Engineering
Address: Trojanova 13, 120 00 Praha 2, Czech Republic
Printed by: QT studio s.r.o., Hornokrčská 60, 140 00 Praha 4, Czech Republic

Number of pages 188 | Number of copies 35 | First edition

ISBN 978-80-01-06922-6

Foreword

This issue contains contributed papers accepted for presentation at the Stochastic and Physical Monitoring Systems (SPMS2020) conference held in Chlum u Třeboně, Czech Republic, September 17 - 21, 2020 and SPMS2021 conference held in Malá Skála, Czech Republic, June 24 - 28, 2021.

The SPMS2020 and SPMS2021 conferences were held for the ninth and tenth time with the aim to bring together students and researchers with areas of interest related to the following topics:

- Analysis of microscopical structure of vehicular traffic streams and traffic modeling,
- Monitoring and classification of acoustic signals in material defectoscopy,
- Small area estimation of geographical characteristics gained from data sets,
- Data processing in high energy particle physics,

which are all together briefly called Stochastic and Physical Monitoring Systems.

The meetings were organized by the Group of Applied Mathematics and Stochastics (GAMS), Department of Mathematics, FNSPE, Czech Technical University in Prague.

Local Organizing Committee:

Václav Kůs (Chair)
Jiří Franc
Jana Vacková
Petr Bouř

Scientific and Program Committee / Reviewers:

Tomáš Hobza, CTU in Prague, Czech Republic
Jiří Grim, UTIA, Academy of Science, Prague, Czech Republic
Václav Kůs, CTU in Prague, Czech Republic
Domingo Morales, UMH de Elche, Spain
Zdeněk Převorovský, IT, Academy of Science, Prague, Czech Republic

Invited Speakers:

Milan Chlada, IT CAS, Prague, Czech Republic
Jarosław Was, AGH UST, Krakow, Poland
Antolino Gallego, University of Granada, Spain
Milan Krbálek, FNSPE, CTU in Prague, Czech Republic
Serge Dos Santos - INSA CVL, Blois, France

We gratefully acknowledge the institutional support provided by the funds of specific research, namely by the SGS grants SVK 26/20/F4 and SVK 29/21/F4. But our largest debt is to all authors who submitted their work, thus making the SPMS2020 and SPMS2021 such lively meetings.

The Organizers

Contents

SPMS2020

SPMS2021

Stochastic and Physical Monitoring Systems
SPMS 2020
September 17 - 21, 2020
Chlum u Třeboně, Czech Republic

Variational Bayes for Blind Image Deconvolution

Antonie Brožová[1], Václav Šmídl[2]

[1] Department of Mathematics, FNSPE, Czech Technical University in Prague, Czech Republic
[2] ÚTIA, Academy of Sciences of the Czech Republic, Prague, Czech Republic

Email: `brozoant@fjfi.cvut.cz`

Abstract. The aim of the blind image deconvolution is to estimate a latent sharp image from an observed blurry image when the blur is unknown. This problem is highly ill-posed. One of the approaches used for blind image deconvolution is variational Bayes, which allows to easily incorporate prior information. Priors have to be carefully chosen not only to regularize the problem well, but also to make it tractable. In this paper we compare two iterative algorithms for variational Bayes inference, one that was used previously and a new one that is not as strict when it comes to the choice of priors.

Key words: Blind image deconvolution; Variational Bayes; Stochastic gradient descent; Reparametrization trick.

1 Introduction

Images play an important role in many areas of life. In medicine they help with diagnosis, astronomers take images to discover distant stars and almost everyone takes a photo on their smartphone from time to time. Because of various reasons, like a relative motion of camera and scene, the images are often blurred and deblurring them is not straightforward. Assuming spatially invariant blur, the blurred image can be represented as a convolution of blur kernel $\boldsymbol{k}$ and the underlying sharp image $\boldsymbol{x}$

$$\boldsymbol{d} = \boldsymbol{k} \circledast \boldsymbol{x} + \boldsymbol{n}, \tag{1}$$

where $\boldsymbol{n}$ is noise. Deconvolution is basically an inverse operation to convolution with the aim to obtain the sharp image. The deconvolution is called blind when not only the sharp image, but also the blur is unknown. The task is then to minimize $||\boldsymbol{d} - \boldsymbol{k} \circledast \boldsymbol{x}||$ with respect to both $\boldsymbol{x}$ and $\boldsymbol{k}$. The problem is highly ill-posed so further regularization is necessary. The Bayesian approach is based on prior information which makes it a suitable tool for this task.

In the first section, variational Bayes (VB) will be introduced, together with the proposed model for blind image deconvolution. After that, two algorithms will be presented, followed by an experimental section where their performance will be compared on synthetic data.

2 Method

The problem of blind image deconvolution is highly ill-posed and prior information is needed to successfully recover the underlying sharp image. Two most common Bayesian approaches used for blind image deconvolution are MAP (maximum a posteriori) approach and variational Bayes method. The first mentioned was deeply studied by Levin et al. in, for example, [1]. Although it is often used, it usually requires some ad hoc steps to find the right solution.

Variational Bayes inference uses an approximation of posterior which makes the problem tractable for common distributions. Fergus et al. suggested to use this approach for blind image deconvolution in [2] in the same year with Molina et al. [3]. A brief explanation of this method follows.

The variational Bayes method is based on the Bayes theorem

$$p(\boldsymbol{x},\boldsymbol{k}|\boldsymbol{d}) = \frac{p(\boldsymbol{d}|\boldsymbol{x},\boldsymbol{k})p(\boldsymbol{x},\boldsymbol{k})}{p(\boldsymbol{d})},$$

where $p(\boldsymbol{x},\boldsymbol{k}|\boldsymbol{d})$ is posterior distribution, $p(\boldsymbol{x},\boldsymbol{k}) = p(\boldsymbol{x})p(\boldsymbol{k})$ is prior distribution and $p(\boldsymbol{d}|\boldsymbol{x},\boldsymbol{k})$ is distribution of noise from (1). If we assign prior to each variable and get the joint posterior distribution, marginalization is needed in order to find the estimates of the sharp image and the blur kernel. Variational Bayes overcomes the marginalization by approximating the posterior by $q(\boldsymbol{x},\boldsymbol{k}|\boldsymbol{d})$ for which holds

$$q(\boldsymbol{x},\boldsymbol{k}|\boldsymbol{d}) = q(\boldsymbol{x}|\boldsymbol{d})q(\boldsymbol{k}|\boldsymbol{d}). \tag{2}$$

The model is usually hierarchical and it is assumed that each random variable has the property (2). Let denote $\boldsymbol{\theta}$ all random variables in the model. Kullback-Leibler (KL) divergence of q from p is defined as

$$KL\left(q(\boldsymbol{\theta}|\boldsymbol{d}) \parallel p(\boldsymbol{\theta}|\boldsymbol{d})\right) = \mathbb{E}_{q(\boldsymbol{\theta}|\boldsymbol{d})}\left[\ln\frac{q(\boldsymbol{\theta}|\boldsymbol{d})}{p(\boldsymbol{\theta}|\boldsymbol{d})}\right], \tag{3}$$

where $\mathbb{E}_{q(\boldsymbol{\theta}|\boldsymbol{d})}[.]$ denotes expected value with respect to $q(\boldsymbol{\theta}|\boldsymbol{d})$. Then approximations of the posteriors that minimize KL divergence from the real posteriors are of following form

$$q(\boldsymbol{\theta_i}|\boldsymbol{d}) \propto \exp\left[\mathbb{E}_{q(\boldsymbol{\theta}_{\setminus i}|\boldsymbol{d})}\left[\ln p(\boldsymbol{\theta},\boldsymbol{d})\right]\right],$$

where $\boldsymbol{\theta}_{\setminus i}$ means all variables in $\boldsymbol{\theta}$ except for i-th one.

2.1 Priors

The choice of priors is crucial, especially when it comes to an image prior. Wipf and Zhang in [4] argue that it is more important that the image prior discriminates the no-blur solution (i. e. sharp image is estimated as the blurred one and kernel as δ-function) than that it reflects the real image statistics. An image is usually assumed to be smooth, thus models promoting sparsity in its gradients ([5], [6]) are used.

It is favourable to rewrite (1) in the matrix form

$$\boldsymbol{k} \circledast \boldsymbol{x} + \boldsymbol{n} = \boldsymbol{K}\boldsymbol{x} + \boldsymbol{n} = \boldsymbol{X}\boldsymbol{k} + \boldsymbol{n},$$

where $\boldsymbol{x}$ is vectorized image of size $n \times p$, $\boldsymbol{k}$ is vectorized blurring kernel of size $2s+1 \times 2s+1$, $\boldsymbol{K}$ and $\boldsymbol{X}$ are convolution matrices in block Toeplitz form, where blocks are Toeplitz matrices, constructed from $\boldsymbol{k}$ and $\boldsymbol{x}$, respectively. The distribution of noise is assumed to be normal with zero mean and precision matrix $\omega\mathbb{I}$, where $\mathbb{I}$ is identity matrix and ω is a hyperparameter, therefore distribution of observation $\boldsymbol{d}$ is normal with mean $\boldsymbol{K}\boldsymbol{x}$ and each pixel has precision ω. The prior distribution of ω is gamma with shape γ_0 and rate η_0.

ARD (Automatic Relevance Determination) model [5] was chosen for image prior. The ARD model achieves sparsity by combination of normal and gamma distribution

$$\begin{aligned} \nabla\boldsymbol{x}|\boldsymbol{\tau}_x &\sim \prod_i \mathcal{N}\left(0, \tau_{xi}^{-1}\right), \\ \tau_{xi} &\sim \mathcal{G}\left(\alpha_{x0}, \beta_{x0}\right), \end{aligned}$$

where ∇ denotes derivative operator, i.e. $\nabla\boldsymbol{x}$ is a vector of horizontal and vertical differences, and τ_{xi} is precision of i-th difference on image. This model is also called scale mixture of gaussians which is considered to be super-gaussian prior [7].

The blur kernel's prior distribution was chosen as

$$\begin{aligned} \boldsymbol{k}|\tau_k &\sim \mathcal{N}\left(\boldsymbol{0}, \tau_k\mathbb{I}\right), \\ \tau_k &\sim \mathcal{G}\left(\alpha_{k0}, \beta_{k0}\right). \end{aligned}$$

2.2 Posteriors

The combination of gamma and normal distributions makes it extremely easy to infer the posterior distributions. As they are conjugate, posteriors of $\boldsymbol{x}$ and $\boldsymbol{k}$ are normal

$$\begin{aligned} q(\boldsymbol{x}|\boldsymbol{d}) &\sim \mathcal{N}\left(\boldsymbol{\mu}_x, \boldsymbol{\Sigma}_x\right), \\ q(\boldsymbol{k}|\boldsymbol{d}) &\sim \mathcal{N}\left(\boldsymbol{\mu}_k, \boldsymbol{\Sigma}_k\right). \end{aligned}$$

The posteriors of precisions were chosen to be Dirac δ-functions with nonzero values in $\boldsymbol{\tau}_x^*$, τ_k^* and ω^*. After some manipulations we get that

$$\begin{aligned} \boldsymbol{\Sigma}_x &= \left(\mathbb{E}_q\left[\omega\boldsymbol{K}^T\boldsymbol{K}\right] + \nabla^T\mathrm{diag}(\mathbb{E}_q\left[\boldsymbol{\tau}_x\right])\nabla\right)^{-1}, \\ \boldsymbol{\mu}_x &= \boldsymbol{\Sigma}_x\mathbb{E}_q\left[\omega\boldsymbol{K}^T\right]\boldsymbol{d}, \\ \boldsymbol{\Sigma}_k &= \left(\mathbb{E}_q\left[\omega\boldsymbol{X}^T\boldsymbol{X}\right] + \mathbb{E}_q\left[\tau_k\right]\mathbb{I}\right)^{-1}, \\ \boldsymbol{\mu}_k &= \boldsymbol{\Sigma}_k\mathbb{E}_q\left[\omega\boldsymbol{X}^T\right]\boldsymbol{d}, \\ \boldsymbol{\tau}_x^* &= \left(\frac{1}{2}\mathbb{E}_q\left[\boldsymbol{x}^T\nabla^T\nabla\boldsymbol{x}\right] + \beta_{x0}\right)^{-1}\left(\alpha_{x0} - \frac{1}{2}\right), \end{aligned}$$

$$
\begin{aligned}
\tau_k^* &= \left(\frac{1}{2}\mathbb{E}_q\left[\boldsymbol{k}^T\boldsymbol{k}\right] + \beta_{k0}\right)^{-1}\left(\frac{(2s-1)^2}{2} + \alpha_{k0} - 1\right),\\
\omega^* &= \left(\frac{1}{2}\mathbb{E}_q\left[\boldsymbol{d}^T\boldsymbol{d} - \boldsymbol{d}^T\boldsymbol{K}\boldsymbol{x} - \boldsymbol{x}^T\boldsymbol{K}^T\boldsymbol{d} + \boldsymbol{x}^T\boldsymbol{K}^T\boldsymbol{K}\boldsymbol{x}\right] + \eta_0\right)^{-1}\left(\frac{np}{2} + \gamma_0 - 1\right),
\end{aligned}
\tag{4}
$$

where $\mathbb{E}_q[.]$ denotes expected value w.r.t. $q(\boldsymbol{\theta}, \boldsymbol{d})$.

2.3 Iterative Variational Bayes algorithm

The first algorithm to be presented in this paper is the iterative variational Bayes (IVB) algorithm used in, for example, [9]. This algorithm utilizes the fact, that the forms of posterior distributions are known and we only need to find values of their parameters. The expressions for the parameters form a set of linear equations that need to be solved to minimize the KL divergence of approximation from real posterior.

The covariance matrix of the image posterior is ill-conditioned, therefore, it is assumed to be diagonal. The expression for the mean of the image posterior requires an inverse of the covariance of the image. For higher accuracy, the estimate of $\boldsymbol{\mu}_k$ is obtained with conjugate gradients instead of using the diagonal covariance. The pseudocode is written below as Algorithm 2. This algorithm is basically E-M algorithm, getting estimates of parameters of normal distributions corresponds to E-step and recomputing $\tau_k^*, \boldsymbol{\tau}_x^*$ and ω^* is M-step.

Algorithm 1: IVB

```
Initialize all variables
While not converged
    Update $\boldsymbol{\Sigma}_x$ as inverse of diagonal matrix from $\omega\boldsymbol{K}^T\boldsymbol{K} + \nabla^T\mathrm{diag}(\boldsymbol{\tau}_x^*)\nabla$
    Update $\boldsymbol{\mu}_x$ as a solution of $\left(\omega\boldsymbol{K}^T\boldsymbol{K} + \nabla^T\mathrm{diag}(\boldsymbol{\tau}_x^2)\right)\boldsymbol{\mu}_x = \omega^*\boldsymbol{K}^T\boldsymbol{d}$
    Construct $\mathbb{E}_q[\boldsymbol{X}]$, $\mathbb{E}_q\left[\boldsymbol{X}^T\boldsymbol{X}\right]$ and $\mathbb{E}_q\left[\boldsymbol{k}^T\boldsymbol{X}^T\boldsymbol{X}\boldsymbol{k}\right]$ from $\boldsymbol{\mu}_x$, $\boldsymbol{\Sigma}_x$, $\boldsymbol{\mu}_k$, $\boldsymbol{\Sigma}_k$
    Update $\omega^*$ according to (4)
    Update $\tau_k^*$ according to (4)
    Update $\tau_x^*$ according to (4)
    Update $\boldsymbol{\Sigma}_k$ according to (4)
    Update $\boldsymbol{\mu}_k$ according to (4)
Return image estimate $\boldsymbol{\mu}_x$ and kernel estimate $\boldsymbol{\mu}_k$.
```

2.4 ELBO optimization

IVB algorithm requires conjugate priors so that it can only recompute parameters of the distributions, which is very restrictive. Lets rewrite KL divergence into another form

$$KL(q(\boldsymbol{\theta}|\boldsymbol{d})||p(\boldsymbol{\theta}|\boldsymbol{d})) = \int q(\boldsymbol{\theta}|\boldsymbol{d}) \ln \left[\frac{q(\boldsymbol{\theta}|\boldsymbol{d})}{p(\boldsymbol{\theta}, \boldsymbol{d})}\right] \mathrm{d}\boldsymbol{\theta} + \ln p(\boldsymbol{d}) = -\mathcal{L} + \ln p(\boldsymbol{d}). \tag{5}$$

KL divergence is always non-negative, therefore, $\mathcal{L}$ in equation (5) is lower bound on $\ln p(\boldsymbol{d})$. It is called evidence lower bound (ELBO). The goal of VB is to minimize the KL divergence which is equivalent to maximizing ELBO. From (5) we can see that

$$\mathcal{L} = \mathbb{E}_{q(\boldsymbol{\theta}|\boldsymbol{d})} \left[\ln q(\boldsymbol{\theta}|\boldsymbol{d}) - \ln p(\boldsymbol{\theta}, \boldsymbol{d})\right]. \tag{6}$$

Negative value of (6) can be minimized, for example, via stochastic gradient descent, but it requires the expectations w.r.t. $q(\boldsymbol{\theta}|\boldsymbol{d})$ to be known in closed forms so that is possible to take their derivatives. When it is not the case, some expected values can be approximated with a reparametrization trick as was suggested for variational autoencoders [8]. Let's say, that it is hard to find an expected value of some function $f(\theta_i)$ w.r.t. $q(\theta_i|\boldsymbol{d})$ and that it is possible to reparametrize $\theta_i = g(\boldsymbol{m}, \epsilon)$, where $\boldsymbol{m}$ are parameters of $q(\theta_i|\boldsymbol{d})$ and ϵ is a random variable with distribution $p(\epsilon)$. Then

$$\nabla_{\boldsymbol{m}} \mathbb{E}_{q(\theta_i|\boldsymbol{d})} \left[f(\theta_i)\right] = \nabla_{\boldsymbol{m}} \mathbb{E}_{p(\epsilon)} \left[f(g(\boldsymbol{m}, \epsilon))\right] \approx \frac{1}{L} \sum_{l=1}^{L} \nabla_{\boldsymbol{m}} f(g(\boldsymbol{m}, \epsilon^l)),$$

where ∇_m is gradient operator with respect to $\boldsymbol{m}$ and ϵ^l is l-th sample of ϵ.

In order to test the approach from the previous paragraph, a second algorithm will be proposed. Parameters of the posterior distribution of $\boldsymbol{k}$ will be estimated via stochastic gradient descent and the reparametrization trick will be used. The function to be minimized w.r.t. $\boldsymbol{\Sigma}_k$ and $\boldsymbol{\mu}_k$ is

$$-p(\boldsymbol{d}|\boldsymbol{x}, \boldsymbol{k}, \omega) - p(\boldsymbol{k}|\tau_k) + q(\boldsymbol{k}|\boldsymbol{d}). \tag{7}$$

The first element of (7) contains the most complicated expected value in the whole model: $\mathbb{E}_q \left[\boldsymbol{x}^T \boldsymbol{K}^T \boldsymbol{K} \boldsymbol{x}\right]$. To approximate this expression, the reparametrization trick was used and $\boldsymbol{k}$ was repametrized as follows

$$\begin{aligned} \boldsymbol{k} &= \boldsymbol{\mu}_k + \boldsymbol{\Sigma}_k^{\frac{1}{2}} \boldsymbol{\epsilon}, \\ \boldsymbol{\epsilon} &\sim \mathcal{N}\left(\boldsymbol{0}, \mathbb{I}\right). \end{aligned}$$

Covariance matrix $\boldsymbol{\Sigma}_k$ is estimated as a product of two matrices $\boldsymbol{S}_k \boldsymbol{S}_k^T$, which means that the covariance matrix is symmetric and makes the reparametrization easier. The pseudocode of the IVB algorithm with two estimates obtained by ELBO maximization, named IVB+ELBO, is below as Algorithm 2.

```
Algorithm 2: IVB+ELBO
Initialize all variables
While not converged
    Update $\boldsymbol{\Sigma}_x$ as inverse of diagonal matrix from $\omega \boldsymbol{K}^T \boldsymbol{K} + \nabla^T \mathrm{diag}(\boldsymbol{\tau}_x^*) \nabla$
    Update $\boldsymbol{\mu}_x$ as a solution of $\left(\omega \boldsymbol{K}^T \boldsymbol{K} + \nabla^T \mathrm{diag}(\boldsymbol{\tau}_x^2)\right) \boldsymbol{\mu}_x = \omega^* \boldsymbol{K}^T \boldsymbol{d}$
    Construct $\mathbb{E}_q\left[\boldsymbol{X}\right]$, $\mathbb{E}_q\left[\boldsymbol{X}^T \boldsymbol{X}\right]$ and $\mathbb{E}_q\left[\boldsymbol{k}^T \boldsymbol{X}^T \boldsymbol{X} \boldsymbol{k}\right]$ from $\boldsymbol{\mu}_x$, $\boldsymbol{\Sigma}_x$, $\boldsymbol{\mu}_k$, $\boldsymbol{\Sigma}_k$
    Update $\omega^*$ according to (4)
    Update $\tau_k^*$ according to (4)
    Update $\tau_x^*$ according to (4)
    Set $\eta_{ADAM}$ of SGD with ADAM to 0.001
    For 1000 steps
        Generate new $\boldsymbol{\epsilon}$ and get gradients of (7)
        Update $\boldsymbol{\mu}_k$, $\boldsymbol{S}_k$
Return image estimate $\boldsymbol{\mu}_x$ and kernel estimate $\boldsymbol{\mu}_k$.
```

3 Experiments

The two algorithms were tested on synthetic data. A cut-out from Lena [10] was blurred with a gaussian kernel and white noise was added to the degraded image. Figure 1 shows the sharp image, blur kernel and degraded image. Figure 2 shows estimates of the sharp image and the blurring kernel returned by both algorithms. Nonblind deconvolution (matrix inversion with a small value added to its diagonal) with estimated kernel $\boldsymbol{\mu}_k$ is then used to find the sharp image. Signal to noise ratio was set to 50dB in this case. The kernel estimate found by Algorithm 2 is symmetric and very similar to the correct one and the image seem to be sharper than the degraded image in Figure 1. The blur kernel found by Algorithm 2 is not that accurate at all, although the reconstructed image seems to be quite sharp. To compare them reliably, PSNR (peak signal to nose ratio)

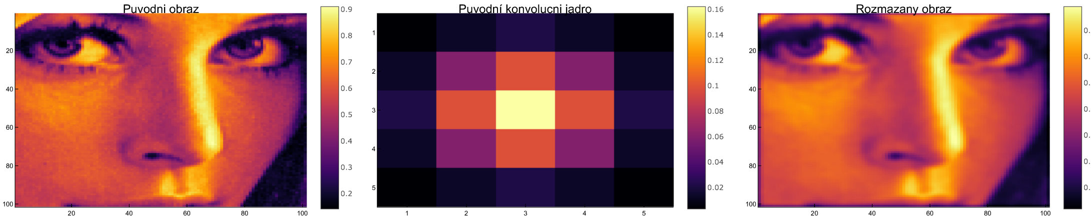

Figure 1: The left image is the sharp image, the blur kernel is in the middle and the degraded image is shown on the right side.

was computed for each estimate, the values can be found in Table 1. From the values of PSNR, it is obvious, that reconstruction performed by Algorithm 2 is better than the one by Algorithm 2. For noise level 50dB and full posterior covariance matrix of $\boldsymbol{k}$, which corresponds to the images in Figure 2, PSNR of the image obtained by Algorithm 2 is lower than 30, which is assumed to be a threshold for good reconstruction. Moreover, the PSNR of the estimate obtained by Algorithm 2 is approximately 36.5, which is a lot better result than the one obtained with ELBO optimization.

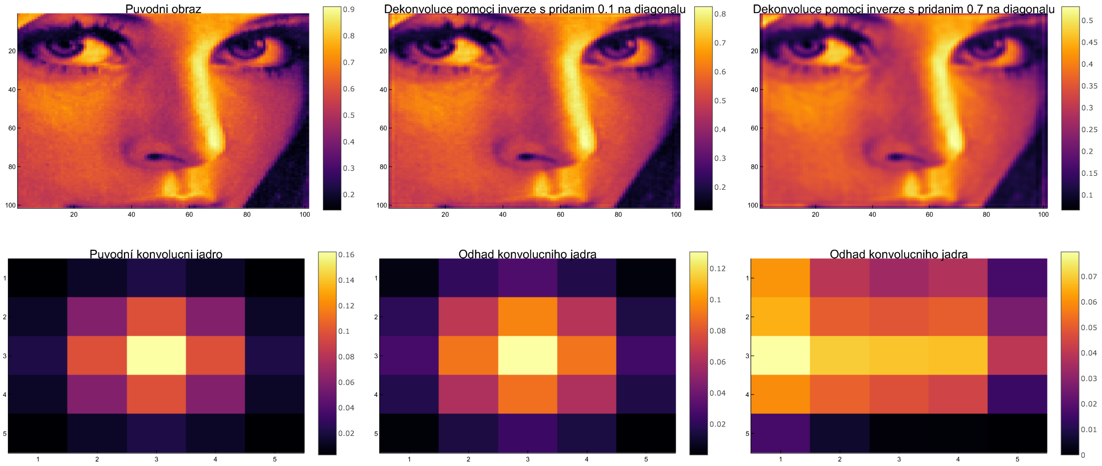

Figure 2: The first column shows the sharp image and the blur kernel, the second column shows estimates obtained with the IVB algorithm and the third column estimates obtained with the IVB+ELBO algorithm. The covariance of the blur is full, SNR is 50dB.

Inversion of a covariance matrix is usually costly and inaccurate, so the two algorithms were also tested for the case when the covariance matrix of blur is diagonal. The estimates for SNR 50dB are shown in Figure 3. In this case, the estimate of the blur kernel is very similar for both algorithms, it is not that accurate as the estimate found by Algorithm 2 with full covariance of blur, but still strongly reminds of the real one. The PSNR values (in Table 1) are comparable for both algorithms and for Algorithm 2, the results with diagonal covariance matrix are even better than the ones obtained with full covariance.

In order to reach higher accuracy, another form of covariance matrix was tested. $\boldsymbol{S}_k$ (square root of the covariance matrix) was assumed to be tridiagonal, so that the covariance matrix had 5 nonzero diagonals: the variance of elements of $\boldsymbol{k}$ was nonzero and also the covariance with directly neighbouring pixels. When tested with Algorithm 2, the PSNR of estimated sharp images was very similar to values obtained with diagonal covariance, as can be seen in Table 1. The algorithm was able to estimate the blur well, but the accuracy was not improved in comparison with the simpler diagonal case. This form of a covariance matrix cannot be easily used by the Algorithm 2, which show the higher flexibility of the Algorithm 2.

Algorithm 2 is faster as it does not perform 1000 steps of stochastic gradient descent with the reparametrization trick, so there is no need to use the Algorithm 2 unless some expected values need to be approximated.

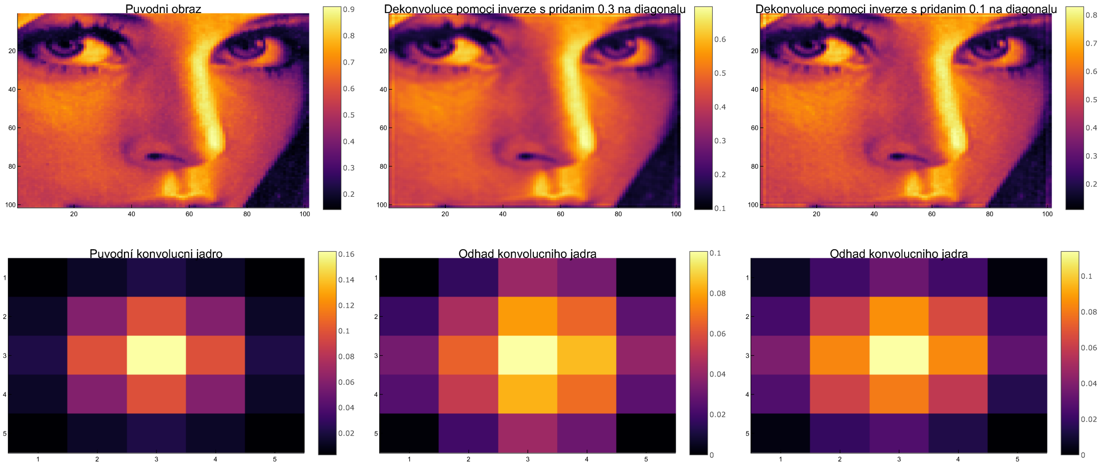
Puvodni obraz

Dekonvoluce pomoci inverze s pridanim 0.3 na diagonalu

Dekonvoluce pomoci inverze s pridanim 0.1 na diagonalu

Puvodní konvolucni jadro

Odhad konvolucniho jadra

Odhad konvolucniho jadra

Figure 3: The first column shows the sharp image and blur kernel, the second column shows estimates obtained with the IVB algorithm and the third column estimates obtained with the IVB+ELBO algorithm. The covariance of blur is diagonal and SNR is 50dB.

4 Conclusion

In this paper, the problem of blind image deconvolution was examined through variational Bayes framework. ARD model was chosen for image gradients because the image is assumed to be piecewise-constant. Two algorithms were compared. First of them is the iterative variational Bayes algorithm which utilizes the fact, that prior distributions were chosen to be from the conjugate system, thus only parameters of posteriors are unknown. It iteratively recomputes the parameters and minimizes Kullback-Leibler divergence of approximation of posterior from real posterior. The assumption of conjugate priors is very restrictive, hence another approach to minimization of Kullback-Leibler divergence was proposed. The second algorithm uses steps from the first one, but parameters of the posterior of blur are estimated via maximization of evidence lower bound by stochastic gradient descent. Moreover, the reparametrization trick was used to approximate complicated expected value, which could be necessary if the priors were not chosen so conveniently. Both algorithms were tested on a blurred cut-out from Lena. The posterior of the blur kernel was chosen to be normal and when the covariance matrix of the blur was assumed to be diagonal, the estimates of the sharp image were comparable for both algorithms. However, for full covariance, the algorithm with gradient descent did not find the correct estimate of the kernel. This may be caused by the reparametrization trick, which uses only one sample to estimate the gradient. To conclude, steps of the IVB algorithm can be replaced by stochastic gradient descent when needed, for example, if the blur was spatially variant and had different distributions for different areas of the image.

Acknowledgements

This work was supported by the grant GA20-27939S.

Covariance	Blur	SNR	PSNR IVB	PSNR IVB+ELBO
full	gauss	20	25.93823	25.12414
full	gauss	30	29.91891	28.29330
full	gauss	40	32.58748	29.25239
full	gauss	50	36.51204	29.01416
diag	gauss	20	25.67324	25.91173
diag	gauss	30	30.25197	29.96938
diag	gauss	40	33.04796	32.57338
diag	gauss	50	33.76192	34.88439
tdmat	gauss	20	–	25.86696
tdmat	gauss	30	–	29.84517
tdmat	gauss	40	–	32.47787
tdmat	gauss	50	–	32.82565

Table 1: PSNR of image reconstruction for different levels of noise (SNR) and forms of the covariance matrix of the blur - tdmat stands for the tridiagonal $\vec{S}_k$.

References

[1] A. Levin, W. Yair, D. Fredo. Understanding Blind Deconvolution Algorithms. *IEEE Trans Pattern Anal Mach Intell.*, 33(12), 2354–2367, 2011.

[2] R. Fergus et al. Removing camera shake from a single photograph. *SIGGRAPH '06: ACM SIGGRAPH 2006 Papers*, 787–794, 2006.

[3] R. Molina, J. Mateos, A. K. Katsaggelos. Blind Deconvolution Using a Variational Approach to Parameter, Image, and Blur Estimation. *IEEE Transactions on Image Processing.*, 15(12), 3715–3727, 2006.

[4] D. Wipf, H. Zhang. Revisiting Bayesian Blind Deconvolution. *Journal of Machine Learning Research*, 15, 3775–3814, 2014.

[5] F. Šroubek, V. Šmídl, J. Kotera. Understanding image priors in blind deconvolution. *In 2014 IEEE International Conference on Image Processing (ICIP)*, 4492–4496, 2014.

[6] S. D. Babacan, R. Molina, A. K. Katsaggelos. Bayesian Blind Deconvolution with General Sparse Image Priors. *In: Fitzgibbon, A. et al. Computer Vision – ECCV 2012. ECCV 2012. Lecture Notes in Computer Science, vol 7577, Springer, Berlin, Heidelberg.*, 341–355, 2012.

[7] J. A. Palmer, K. Kreutz-Delgado, S. Makeig. Strong Sub- and Super-Gaussianity. *In: V. Vigneron et al.:Latent Variable Analysis and Signal Separation. LVA/ICA 2010. Lecture Notes in Computer Science, vol 6365. Springer, Berlin, Heidelberg.*, 303–310, 2010.

[8] D. Kingma, M. Welling. Auto-encoding Variational Bayes. *arXiv preprint arXiv:1312.6114.*,2013.

[9] J. Kotera, V. Šmídl, F. Šroubek. Blind Deconvolution With Model Discrepancies. *IEEE Transactions on Image Processing*, 26(5), 2533-2544. 2017.

[10] Lena [online]. Available from: https://www.cosy.sbg.ac.at/ pmeerw/Watermarking/lena.html, cited 2020-10-12.

Stochastic and Physical Monitoring Systems
SPMS 2020
September 17 - 21, 2020
Chlum u Třeboně, Czech Republic

Cellular or Continuous?

Marek Bukáček, Jana Vacková

Faculty of Nuclear Sciences and Physical Engineering, Czech Technical University in Prague, Trojanova 13, Prague, 120 00, Czech Republic

Email: `mbukacek@fjfi.cvut.cz`

Abstract. The history of pedestrian modeling is close to 10 years anniversary. Within this period, two models have been developed aside of experimental research: cellular and continuous. Even the motivation was the same and both models use microscopic, rule base approach, there are many different features – benefits and drawbacks on both side. The aim of this article is to revisit the development process, discuss differences and show the most important results.

Key words: Pedestrian dynamics; Cellular automata; Rule based model.

1 Introduction

Modeling of crowd motion or, more general, any kind of traffic is an important part of urbanity planning process. From the engineering perspective, there are just few features that must a model fulfill: reliability, simple calibration, reasonable calculation demands and ability to return desired quantities. Different model types are more appropriate for different requested outputs, but usually there are multiple ways how to achieve them.

The spectrum of desired model outputs may be quite wide. On the macroscopic level, we are mostly interested in flow, i.e. how many people pass given checkpoint during given time interval. Such variable is affected by the pedestrian density (number of people in given area), geometry and pedestrian mindset (motivation, knowledge of given facility and cultural aspects). The total evacuation time is another crucial quantity from engineering perspective, it may be replaced by the evacuation time of desired sub-population (all clients, 98% of all people, ...).

In more detail, we may focus on trajectory level producing individual evacuation time, local densities, velocity distribution in space and many more fancy features. From scientific perspective such microscopic research brings additional information as macroscopic quantities may be always derived from microscopic measurements. Moreover, microscopic observation may explain why the system generates given macroscopic observation.

On the other hand, microscopic models always require more computational power, their validation is more demanding and they are quite hard to calibrate and to correctly set up initial and boundary conditions. That's why engineers prefers to use simple, well known models, even they are outdated. The transition to modern requires special motivation, thus the scientific state of the art is quite ahead on engineering .. as always.

Historically there are multiple research streams, each of them dominated some period in past, based on fashion and available PC performance:

- Hand calculations. Applying queuing theory or 'physical' mechanics, we can answer many elemental questions. E.g. from given inflow and bottleneck capacity (maximal flow), one can predict whether the evacuation will be smooth or whether a congestion would appear.
- Grid models. These models discrete in space and time are using simple movements rules. Reasonable discretization allows even microscopic approach, as will be shown later on implemented cellular automata model.
- Force based models. The interaction pedestrians and infrastructure may be defined as the set of social forces. Then, similarly to classic mechanics, we may introduce and solve large set of equations to get detail movement description. Quite expensive and not accurate for large simulations as pedestrian interaction is quite complex, yet successful in simple geometries.
- Agent based models. The most modern approach is based on intelligent agent moving in continuous space and time according predefined rules. This approach combines advantages of all above mentioned approaches yet it may be difficult to calibrate.
- Data driven models. Another quite new approach based on machine learning technology. With sufficiently large database, model could predict the next movements based on some smart mix of historical trajectories. But the ability to process situation that is not in database is questionable.

Further in this paper, we will focus on two models implemented by our research group – a cellular automata and agent based model. Both are implemented on microscopical level but they have quite different rules as they are facing different challenges given by different spatial limits.

2 Brief model definition

Briefly, cellular automata model is defined on rectangular matrix with cell size 0.5 m. A cell is either empty or occupied by one pedestrian, thus a movement is realized by "jump" to a cell in neighborhood. The timespan is therefore set to 0.3 s giving the free flow velocity up to 6 m/s. The pedestrian update is parallel, each pedestrian pick up desired cell based on calculated profitability and some random element. The profitability used to be composed of the distance to the exit, occupancy, conflict anticipation and other quantities that are either static or easy to update, see visualization on Figure 1. At the end, potential conflicts (more pedestrian choose the same cell) are resolved – maximally one pedestrian moves and the others stay. See [1], [2] and [3].

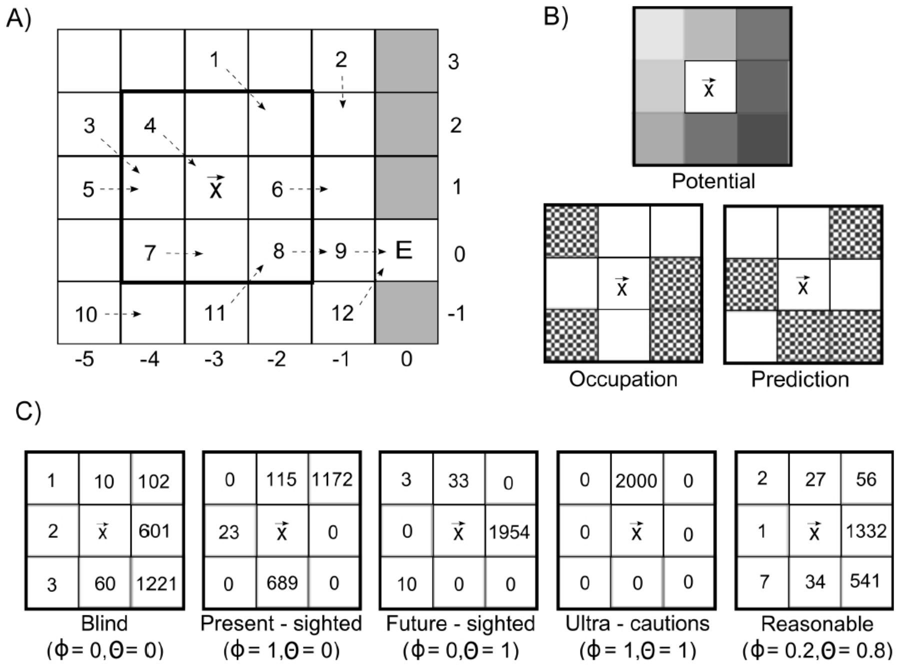

Figure 1: Profitability of cells in pedestrian neighborhood. ϕ refers to occupancy, θ to prediction. Potential is always reflected.

The rule based model is fully continuous in the way that timespan can be as small as desired and the velocity or course change can as smooth as numerically possible. Let's assume each pedestrian has set a checkpoint that he/she wants to reach (an exit, a counter, ...). A set of checkpoints may be used to model complex infrastructure, but in this paper we will focus only on simple geometry. The rules itself should hierarchically follow "natural" behavior, from smooth motion toward the checkpoint to some crowd behavior playbook, to more details check [8].

It may seem suspicious that so different models can bring comparable results but as mentioned in the introduction, it depends on scale and selected variables. Obviously cellular model generate discrete trajectories, but they can be interpolated, if needed. Moreover, time frames below 1 s are mostly too smooth even for microscopic analysis. Targeted variables as travel time distribution, individual velocity – density relation (e.i. fundamental diagram), local flow and others may be the same.

On the first sight it may seem easier to find a set of rules for continuous model than express profitability of a cell, but the reality is completely different. The rules are much easier to develop in a system with finite (actually very low) number of constellations. As will be shown further, continuous space and the fact that all logic is carried by the agents make some situations tricky to solve. On the other hand, even a cellular model need adjustments that would never be required in continuous space.

Moreover, randomness in boundary condition of continuous model may play the same role as decision randomness in ca model. Small differences in initial positions are multiplied in time to obtain various set of trajectories.

3 Environmental issues

Before we will consider "desired behavior", we have to avoid "undesired effects", meaning pedestrian can't overlap, motion have to be independent on the grid definition and model should not generate any artifacts.

Continuous rule base model does not bring any unnatural mechanisms, the only thing to solve is the size of pedestrian. The model itself approximates pedestrian by a point, let say the center of mass. To keep the rules simple, we were implementing hard core repulsion for spherical area defined by individualized radius. To prevent two agents to overlap, it is sufficient to check that they are more distant than the sum of their diameters.

The cellular model has completely different issues. As a cell may be occupied just by one pedestrian, any potential overlap is excluded. On the other hand, the grid makes any "skew" trajectory partially rectangular. To enrich limited number of directions from four to eight, we have allowed diagonal steps. This portfolio is sufficient to reasonably model the motion, but it brings new complication.

By diagonal step, agent moves $\sqrt{2}$ further than by orthogonal one. To conserve the pedestrian velocity, we have to compensate it by adjusting time consumption of these steps – they will take $\sqrt{2}$ times longer. But how to realize that in system discrete in time?

First, we used approximation $\sqrt{2} \approx 3/2$ which keeps all pedestrians in discrete (semi-integer) steps. Time unit was cut to half and an agent moves each second or third tick, with respect to the type of step he realized.

This approach opened the door to "dynamic time span" assuming that pedestrians may have different velocity i.e. they would need different amount of time to realize one step. Such behavior may be modeled by adaptive time steps, i.e. each pedestrian has its own clock where time of next step is calculated and then model clock moves always to the next individual event.

But completely asynchronous update would mitigate all conflicts, thus we defined different approach. Each pedestrian still has its own "time of next update" (ref. tnu), but the model clock are ticking by predefined frequency. All agents with their tnu within given tick are updated at once, but their next tnu is calculated from previous tnu, see schema on Figure 2. E.g. when two pedestrians have similar but not the same velocity, they would update simultaneously for a while and then the slower pedestrian would miss one update. The model clock frequency represents the parameter of synchronicity – long time steps keep the movement synchronous while short time steps emphasizes differences among pedestrian frequencies.

The diagonal steps deforms even the probability distribution of deviation from straight trajectory. When the straight direction to the goal follows diagonal steps, potential deviations would be orthogonal, i.e. shorter steps. Such steps would be much less beneficial thus the probability of these deviations would be low. In contrary when the straight direction to the goal follows orthogonal steps, potential diagonal deviation would move pedestrian further. Even the straight step would bring a pedestrian closer than diagonal deviations, the difference would not be significant, see illustration on Figure 3. To compensate this issue, we have to adjust profitability metric by diagonal penalization.

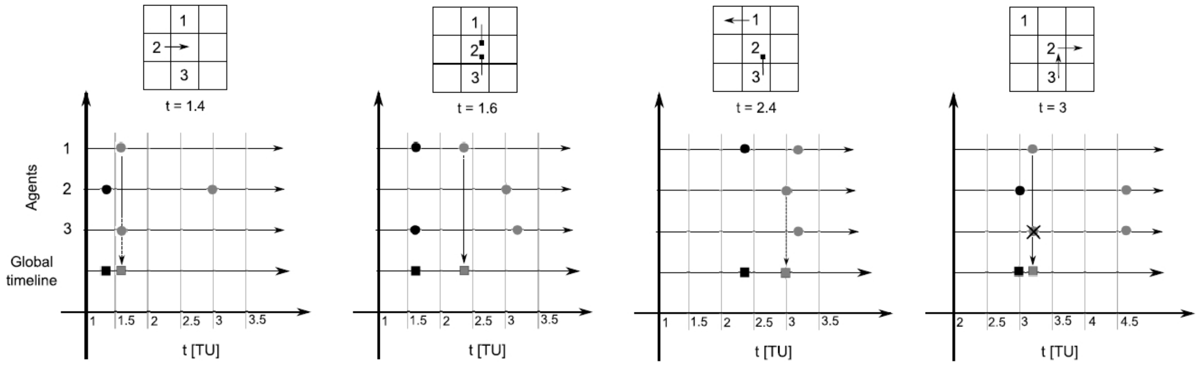

Figure 2: The visualization of timeline.

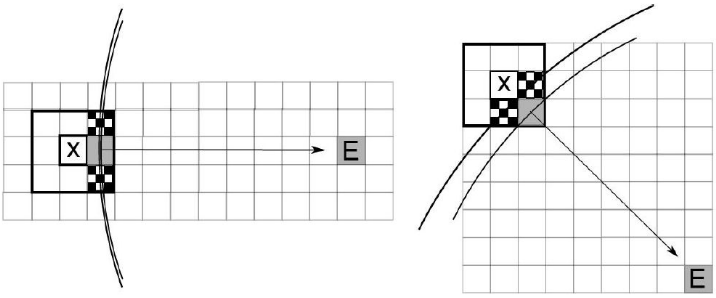

Figure 3: The illustration of diagonal movement issue.

4 Interaction issues

As mentioned above, different sets of rules have to describe free flow and congestion behavior. While free flow is quite simple to model and to calibrate, congestion introduces some challenges. First, the dense crowd slow down the motion, but id did not stop it. Moreover, there are secondary crowd motion phenomena ”nice to have” in the model as line formation, overtaking zones near walls, absence of holes and others.

In the rule based model, the interaction is realized mainly through the conflicts. When two pedestrians are close enough, their neighborhood profitability is deformed to reduce the change of the conflict. But they truly restrain each other only when they select the same cell. In such case, friction function is applied to test whether this conflict blocks the motion of all pedestrians. If it does not, one pedestrian is (randomly/based on priority parameters) picked to move.

Such design simply solves the only real issue that cellular model can have in crowd situations. A conflict is always localized in time and space and its resolution does not affect other pedestrians. Moreover, implemented system of conflicts is something desired within CA models – as observed, movement in crowd is much slower than in free flow and staying after a conflict is the most natural way how to slow down a cellular agent. Actually to bring the cellular model closer to the experimental / real pedestrian behavior, a friction had to be set quite high thus the probability that no one moves is high

In case of continuous agent based model, hierarchical rules were developed to manage crowd situation, mainly to avoid deadlocks, i.e. the situation when a set of agents forms a constellation preventing further movement. Such "arches" could live in some naive model for ever, but actually they survive even more sophisticated rules.

In our model, one level of rules is applied and the agent next-step position is evaluated and the availability is checked. If this position is not blocked by any other pedestrian, the movement is executed, if not, next rule is applied:

- naive: firstly, a pedestrian walks towards his/her checkpoint by his/her desired speed or he/she is accelerating to reach it
- maneuvers: if such "optimal" trajectory is blocked, a pedestrian tries to adjust direction or speed
- downsizing: if a velocity of pedestrian drops to zero, pedestrian reduce his/her velocity up to certain level
- jump: if a velocity is zero and size reached its minimum, pedestrian jumps to empty space toward the exit, if reachable

Here we should note that only jump rule defeats arches, previous rules tend to long lasting deadlock.

Another approach to fight with arches comes from engineers. When the have to store some granular material e.g. in a silo, they have to prevent any mechanical deadlocks. To achieve that, they are installing some vibrating equipment to destabilize any grain formation. Such approach could be implemented in models by increasing of randomness .. but it is not our path.

Our goal was to keep all movement logic in the head of the agent, without coordination or environmental support. From this perspective, rule based model is more individualistic than cellular one which uses agent cooperation to solve conflicts. Unfortunately such approach can't be used in continuous model because the arch is not standardized thus there is no way to prepare some template how to solve it, global rules may be quite hard to define and (mainly) they could be misleadingly interpreted that pedestrian cooperates even in competitive scenarios. Instead, we are proposing possible actions what to do when motion vanishes (for any reason).

Another cellular automata feature relates to the fact that we enable to pick occupied cell. In that case, a "bond" (between follower and leader) is created and whenever an leader moves, follower moves as well. Again, in case more agents are bonded to another, standard conflict procedure is applied when leader agent moves. This construct significantly improves movement in lines and increases the flow in the crowd.

It seems that such rule is not needed for continuous model. Continuous time line does not require to make links between events. Everything happens in given time, there in no "death time".

5 Results

As the cellular model was finished almost five years ago, plenty of different simulations has been generated and analyzed – [1],[4]or [5].

Here we would like to point out the heterogeneity analysis, where we studied the effect of velocity (controlled over the frequency of updates), the aggressiveness (controlled by the ability to win conflicts) and the overtaking (controlled by the willingness to select occupied cell). Our experimental study [6],[7] uncovered that pedestrians significantly differ in all three mentioned features, thus the goal was to simulate this behavior.

We have measured individual travel times, trying to find parametric sets generating corresponding distributions. The overtaking parameter itself does not affect travel time, thus it was excluded from simulation results illustrated on 4 and 5.

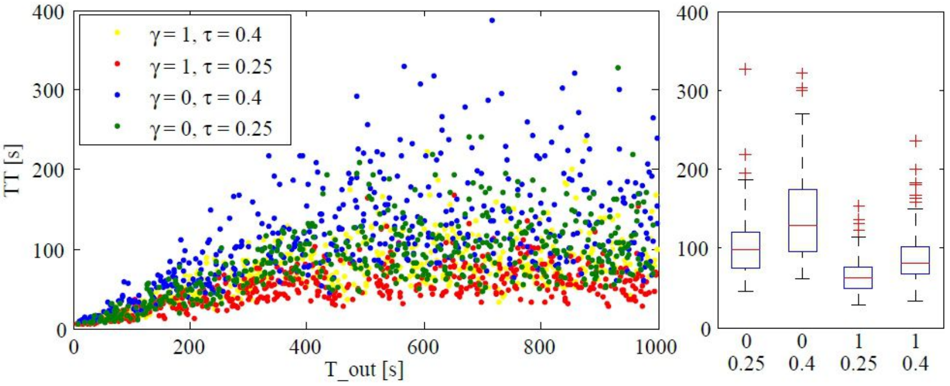

Figure 4: Individual travel time for heterogeneous population, development in time. $\gamma = 1$ refers to aggressive behavior, τ is the update period.

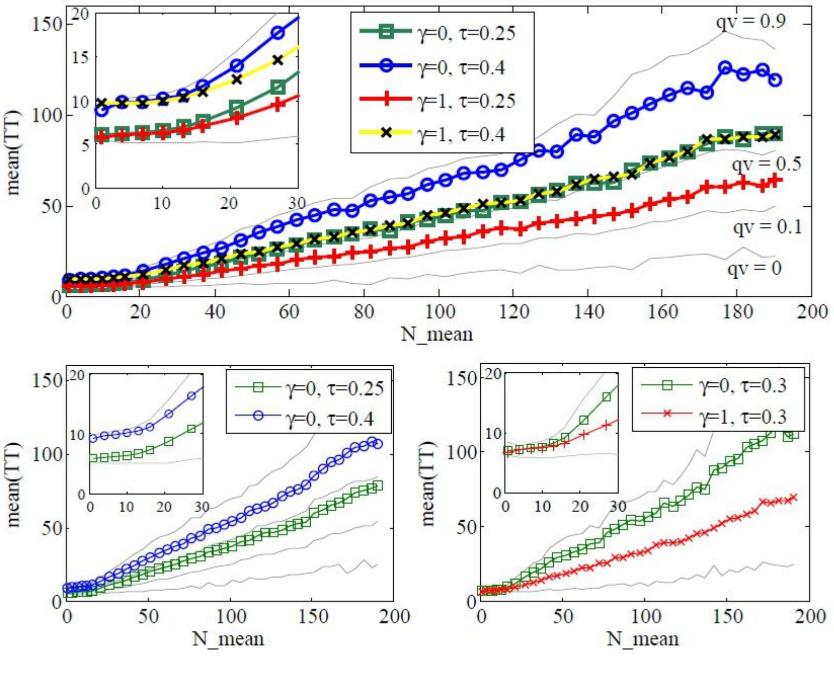

Figure 5: Individual travel time for heterogeneous population, trend with increasing occupancy.$\gamma = 1$ refers to aggressive behavior, τ is the update period.

When parameters were set, we tried to reproduce observed phase transition induced by inflow to the experimental room. As illustrated on Figure 6, the phase transition from free flow to congested state is rather smooth than jump-like, we can even observe metastable intermezzo.

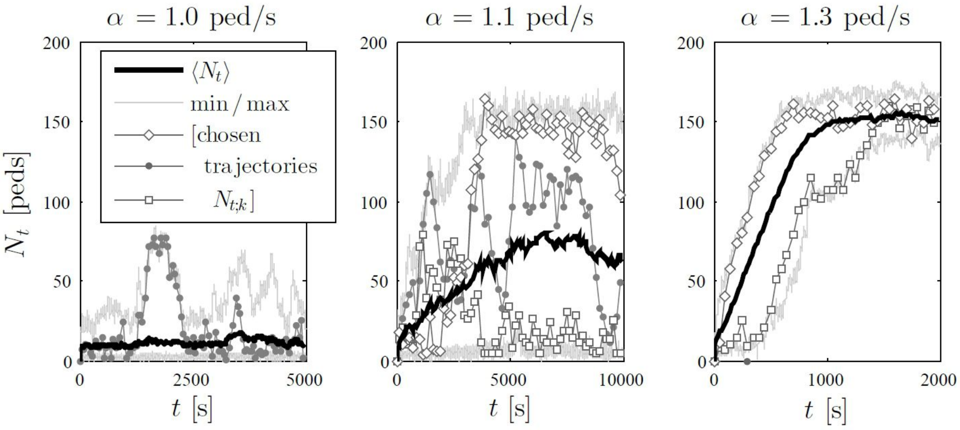

Figure 6: Trend of occupancy in time for different values of friction parameter.

The rule based model is still in calibration process [9], thus such simulations has not been executed. At least the calibration indicates that the model is able to reproduce demanded range of flow based on dynamic parameters, see Figure 7.

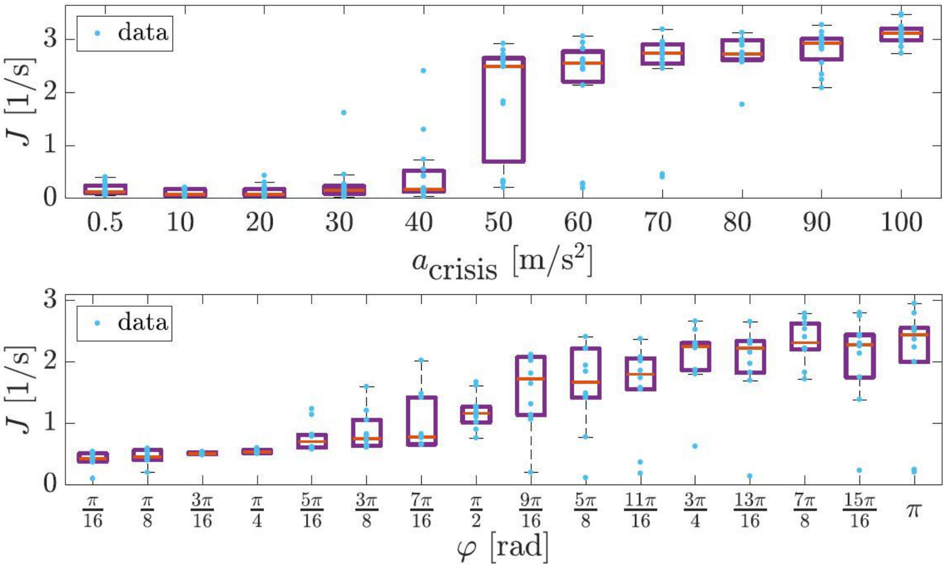

Figure 7: The outflow with respect to critical acceleration and course change range.

6 Conclusions

This paper compared cellular and continuous model of pedestrian behavior. As discussed, both approaches had to face several difficulties – fortunately all cellular issues had been solved using smart tweaks improving the rule base and the continuous model seems promising as well.

These improvements are beneficial not only for implemented models, but for the whole pedestrian modeling community because addressed problematic situations are common for wide range of models.

Next work will focus on finalizing of continuous model calibration. We are trying to standardize the calibration process using independent episodes focusing in different model features. After that, the model will be verified on complex simulations and hopefully used for next projects.

Acknowledgements

This work was supported by the grant SGS18/188/OHK4/3T/14.

References

[1] P. Hrabák, M. Bukáček and M. Krbálek. Cellular Model of Room Evacuation Based on Occupancy and Movement Prediction, Comparison with Experimental Study. *JCA*, **8**, 383–395, 2013.

[2] M. Bukáček, P. Hrabák and M. Krbálek. Cellular Model of Pedestrian Dynamics with Adaptive Time Span. *In: PPAM 2013, LNCS*, **8385**, 669–678, 2014.

[3] M. Bukáček and P. Hrabák. Conflict Solution According to Aggressiveness of Agents in Floor-Field-Based Model. *In: PPAM 2015, LNCS* **9574**, 507–516, 2016.

[4] M. Bukáček and P. Hrabák. Boundary Induced Phase Transition in Cellular Automata Models of Pedestrian Flow. *JCA* **11/4**, 327–338, 2016.

[5] P. Hrabák and M. Bukáček. Influence of Agents Heterogeneity in Cellular Model of Evacuation. *JCS* **21/7**, 486–493, 2017.

[6] M. Bukáček, P. Hrabák and M. Krbálek, Experimental Study of Phase Transition in Pedestrian Flow, *Transportation Research Procedia* **2**, 105–113, 2014.

[7] M. Bukáček, P. Hrabák and M. Krbálek. Microscopic Travel Time Analysis of Bottleneck Experiments. *Transportmetrica A* **5–6**, 375–391, 2018.

[8] J. Vacková and M. Bukáček. Ruling Principles for Decision-Based Pedestrian Model. *In SPMS 2019*, 141–154, 2019.

[9] J. Vacková and M. Bukáček. Social and Physical Pedestrian Sizes and their impact on the decision-based modeling. *In FEMTC 2020*, Accepted.

Stochastic and Physical Monitoring Systems
SPMS 2020
September 17 - 21, 2020
Chlum u Třeboně, Czech Republic

Le Cam Index of Elasticity Evaluated for Earthquake Dampers through Preisach formalism

Erik Dolejš and Václav Kůs

Department of Mathematics, FNSPE, Czech Technical University in Prague, Trojanova 13, 12000 Praha 2, Czech Republic

Email: `dolejeri@fjfi.cvut.cz, vaclav.kus@fjfi.cvut.cz`

Abstract. We apply Preisach-Mayergoyz (PM) model to the hysteretic material. In PM space of hysterons the kernel density estimators are used for the construction of index of elasticity through Le Cam divergence. We work with one-dimensional PM space projection and two-dimensional pyramid kernel. This elasticity index is then used for earthquake steal dampers and the degree of its damage is evaluated.

Key words: Defectoscopy; PM space; Hysteresis; Elasticity; Kernel density estimates; Divergences; Damage index.

1 PM space model characterization

In this paper, the Preisach-Mayergoyz (PM) model [1] of hysteresis is introduced as a tool for describing hysteretic material and its elastic structure. This approach is mainly associated with the nondestructive testing (NDT) defectoscopy technologies [2]. The PM space model is based on the idea that a given material is composed of a large number of small elastic units (particles, ferromagnetic elements, cracks, etc.) called here hysterons, Figure 1a). The Preisach's operator $\widehat{\gamma}_{\alpha,\beta}$ of hysteron is mathematically expressed as

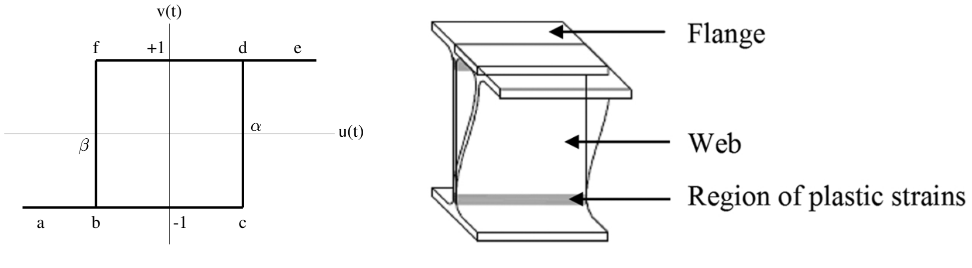

Figure 1: (a) Hysterons can be found either in closed state assigned to +1 or open state assigned to -1 (b) Profile of earthquake damper I-section [3].

$$\widehat{\gamma}_{\alpha,\beta}(u(t)) = \begin{cases} -1, & u(t) \leq \beta, \\ 1, & u(t) \geq \alpha, \\ k, & u(t) \in (\beta, \alpha), \end{cases}$$

whith $\beta \leq \alpha$ and $u(t) \in (\beta, \alpha)$ as an input signal, where

$$k = \begin{cases} 1, & \text{if } \exists t^* : u(t^*) > \alpha \text{ and } \forall \tau \in (t^*, t), \\ -1, & \text{if } \exists t^* : u(t^*) < \beta \text{ and } \forall \tau \in (t^*, t). \end{cases}$$

Our goal is the evaluation of elasticity of dissipative dampers, which are used for building protection against earthquakes. The principle instrument of this passive protection can be seen in Figure 1b) and the series of these energy dissipating devices (EDDs) are used as the web plastifying damper (WPD). The PM based method of fatigue evaluation of these dampers is the crucial point in health monitoring of nowadays architecture objects in endangered countries. In case of the dampers, α and β represent closing (P_c) and opening (P_o) values of damper's plastifying cells with respect to the form of loading (e.g. tensile force/presure). Applying the input signal $u(t)$, the output of hysteretic system, denoted by $v(t)$, can be described in the continuous case as a double integral over the PM space

$$v(t) = \iint_{\beta \leq \alpha} \mu(\alpha, \beta)\, \widehat{\gamma}_{\alpha,\beta}(u(t))\, \mathrm{d}\alpha\, \mathrm{d}\beta,$$

where $\mu(\alpha, \beta)$ is a probability density on the Preisach triangle $\beta \leq \alpha$, see Fig. 2.

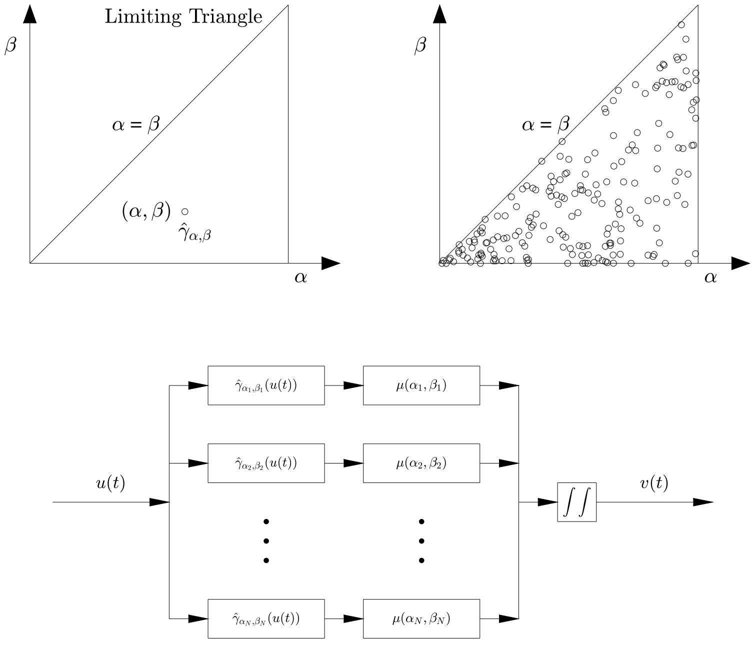

Figure 2: Schema of Preisach-Mayergoyz model [1].

2 PM space density identification

The main objective of PM space modelling is the identification of corresponding probability density function of hysterons $\mu(P_c, P_o)$ in PM space only from the knowledge of the input load and the corresponding hysteresis curve of the damper under testing load. We applied the standard statistical distributions as Gaussian, Exponential, Weibull, Uniform, but also Guyer's distributions [4, 5]. As an example, we present here only the third distributions of Guyer and Koen. PM distribution **Guyer 3** is defined by

$$P_c = \max \cdot r_c^{\alpha}, \quad P_o = P_c \cdot (\gamma \times r_o)^{\beta}, \qquad \alpha, \beta \in \mathbb{R}_0^+, \quad \gamma \in (0,1),$$

where 'max' is the maximum of input load, P_c and P_o are closing and opening values, r_c and r_o are random numbers uniformly distributed in interval (0,1), while α, β, γ represent free parameters of the distribution. Further, PM distribution **Koen** can be expressed as

$$P_c = \max \cdot r_c, \qquad P_o = (P_c/\alpha)^{\beta} \cdot r_o, \qquad \alpha, \beta \in \mathbb{R}_0^+,$$

where α, β represent free distributional parameters again. Notice that the Koen distribution uses quite different parametrization compared to Guyer 3. To identify potentially complex structure of PM spaces of a given material/damper, we apply statistical theory of distribution mixtures [6]. It means, we seek for the best convex combination of M density components p_i in the form

$$p(x|\,\Theta) = \sum_{i=1}^{M} \lambda_i \, p_i(x|\,\theta_i), \qquad \sum_{i=1}^{M} \lambda_i = 1,$$

where $p_i(x|\,\theta_i)$ are probability density functions with parameters θ_i and the component weights $\lambda_i > 0$ for all $i \in \{1, ..., M\}$.

3 Jaya numerical optimization technique

The optimization problem consists of minimizing distance measure between the calculated hysteresis curve and the observed hysteresis curve in each iteration step. We applied classical L_2-distance or Hellinger and Le Cam ϕ-divergences, which are more robust against measurement errors. We focus here on the Le Cam divergence

$$LC^2(p,q) = \int \frac{(p-q)^2}{p+q} \, \mathrm{d}\mu,$$

Hellinger distance

$$H^2(P,Q) = \int (\sqrt{p} - \sqrt{q})^2 \, \mathrm{d}\mu,$$

where p and q are probability densities with respect to a σ-finite measure μ on $\mathbb{R}$. LC is a special case of the general information-theoretic measure called *ϕ-divergence between p and q*,

$$D_\phi(p,q) = \int q \, \phi(p/q) \, \mathrm{d}\mu,$$

for convex function $\phi(t) \in [0, \infty)$, $\phi(1) = 0$, strictly convex at $t = 1$ (details in [7, 8]). The identification process of PM density is carried out by choosing a novel numerical minimization meta-heuristic algorithm called Jaya presented by Rao [9] in 2016. It is based on Jaya operator applied in each iteration to the argument $\boldsymbol{x} = (x_1, x_2, ..., x_D)$ of the minimized functional $f(\boldsymbol{x})$ in the form

$$u_{i,j,k} = x_{i,j,k} + rand_{1,i,j} \cdot (x_{best,j,k} - |x_{i,j,k}|) - rand_{2,i,j} \cdot (x_{worst,j,k} - |x_{i,j,k}|)\,,$$

where the index i is population index, j is the component index of $\boldsymbol{x}$, and k denotes iteration number, $rand_{1,i,j}$, $rand_{2,i,j}$ are uniformly distributed pseudorandom numbers from interval $[0, 1]$. We present the pseudo-code of this Jaya algorithm below. Performance of the Jaya algorithm was tested many times and it surpassed the well-known Simulated Annealing algorithm in most cases of our PM density identification task.

Algorithm 3: Pseudo-code for Jaya numerical minimization algorithm

```
Generate initial population, evaluate $f(\boldsymbol{x})$
Choose the best ($\boldsymbol{x_{best}}$) and the worst ($\boldsymbol{x_{worst}}$) solution in the population
while Stoping rule do
    for $i = 1$ to $NP$ do // $NP$ number of populations
        for $j = 1$ to $D$ do // $D$ dimension of vector $\boldsymbol{x}$
            $u_{i,j} = x_{i,j} + rand_{1,j} \cdot (x_{best,j} - |x_{i,j}|) - rand_{2,j} \cdot (x_{worst,j} - |x_{i,j}|)$
              // Jaya op.
        end
        Evaluate $f(\boldsymbol{x})$ in $\boldsymbol{u_i}$
        if $f(\boldsymbol{u_i}) \leq f(\boldsymbol{x_i})$ then
            $\boldsymbol{x_i} = \boldsymbol{u_i}$
        else
            $\boldsymbol{x_i} = \boldsymbol{x_i}$
        end
    end
    Actualize $\boldsymbol{x_{best}}$ and $\boldsymbol{x_{worst}}$
end
```

4 Elasticity index of hysteretic dampers

We have at disposal the signals obtained from 6 vibration tests of the web plastifying dampers measured at the University of Granada by prof. A.Gallego research group, an example for the third damper cycle see in Figure 3.

The goal is to propose and evaluate a new index of damage/elasticity [3]. Our new procedure is the following. First, the numerical PM space density automatic identification for all 6 damper cycles is proceed, then the PM points are generated. Second, these points from PM triangle are projected onto the right leg of PM space, followed by the one-dimensional nonparametric kernel estimator evaluated for optimally chosen bandwidth under Gaussian kernel [10]. The scheme of this evaluation process is shown in Figure 4.

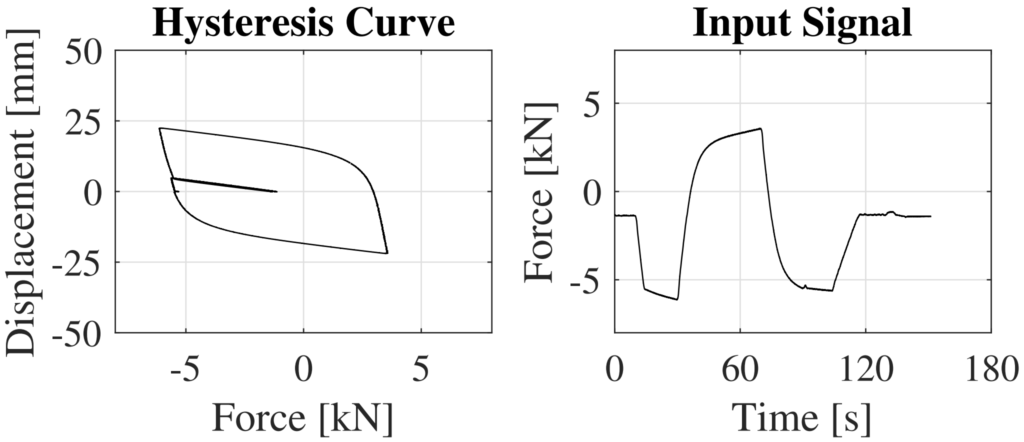

Figure 3: Hysteresis loops and input loads measured for earthquake damper (data from A.Gallego's research group/UG).

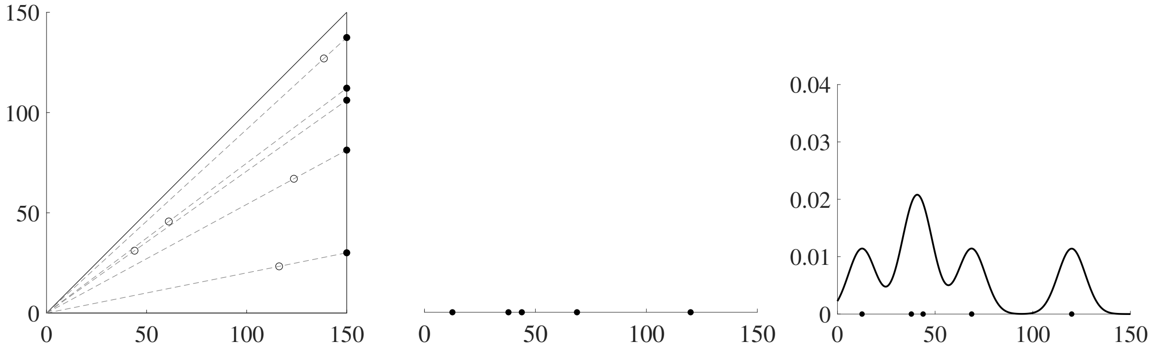

Figure 4: Scheme of 1D-kernel estimator after right leg projection of all PM points, i.e. projection to right leg → 1D representation of PM space → Gaussian kernel estimate.

Alternatively, we have used fully two-dimensional kernel estimator on Preisach triangle for the specific triangle binning leading to pyramid kernel (Figure 5)

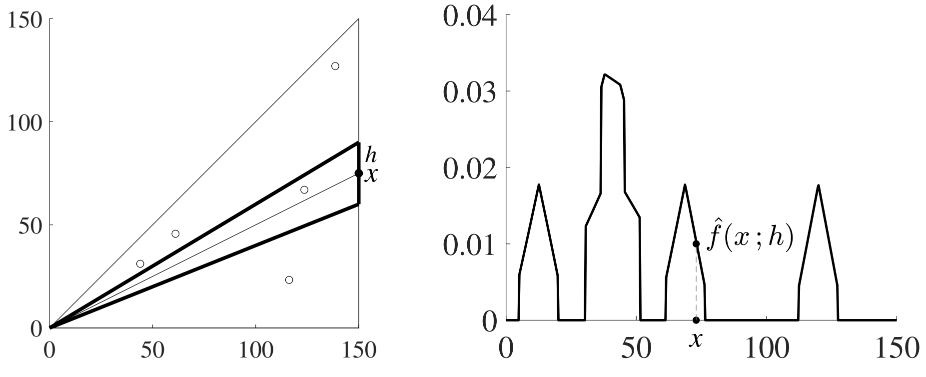

Figure 5: 2D-pyramid kernel estimate in PM space with smoothing parameter h.

$$\hat{f}\left(x\,;h\right)=\frac{1}{nS}\sum_{i=1}^{n}s\left(x\,;h\right)\left(1-\frac{d_i\left(x\right)}{h}\right)\mathbb{I}_{s(x\,;\,h)}\left(X_i\right),$$

where n is number of PM points, S denotes area of Preisach triangle, $s\,(x\,;h)$ is the area of pyramid kernel support with smoothing parameter h, $d_i\,(x)$ measures distance of i-th hysteron X_i from the point x, and $\mathbb{I}_{s(x\,;h)}$ represents characteristic function of $s\,(x\,;h)$. These designs of 1D-projection and 2D-triangle binning is based on the knowledge of PM space of ideally elastic non-hysteretic material when all the PM points are located at the diagonal of PM space and these hysterons are moving to the bottom leg of the PM triangle as damage level increases.

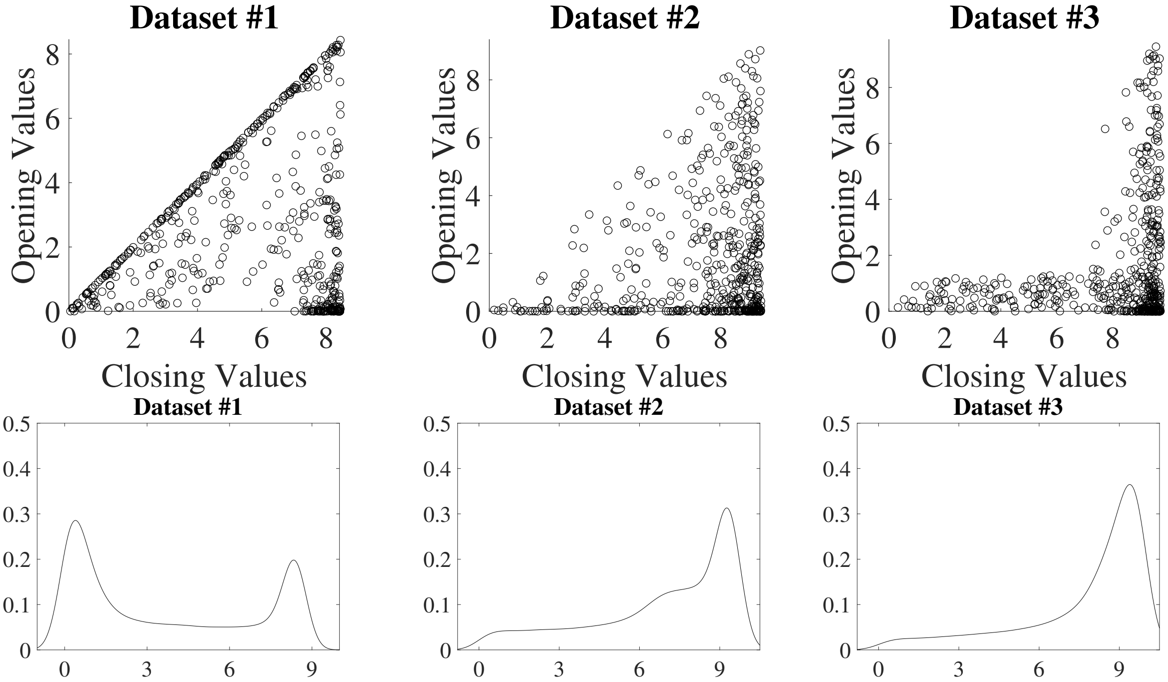

Figure 6: Identified PM spaces and corresponding 1D-Gaussian kernel estimates for the 3 first cycles of earthquake damper.

The final PM space Jaya-Le Cam identifications for the 6 cycles of earthquake EDD damper under increasing damage are shown in Figures 6 and 7 for 1000 hysterons (plastifying cells). Consequently, for all 6 damper loading cycles, the indexes of elasticity/damage IE were computed as appropriately scaled and normalized Le Cam divergence between the identified PM density kernel estimate against referential ideally elastic PM density, i.e.

$$IE = \frac{(LC \cdot 100)^{1+LC\cdot 100}}{IE_{max}} \in [0,1],$$

where IE_{max} is the maximal value of IE for absolutely nonelastic PM space. These relative IE indexes for successive 6 testing cycles of earthquake damper are presented in Table 1.

The greatest increase of the proposed PM elasticity/damage index occurred during the first cyclic loading, afterwards growing gradually up to 0.915 referring to significant damage of this earthquake damper and developing disruption of its elasticity (plasticity).

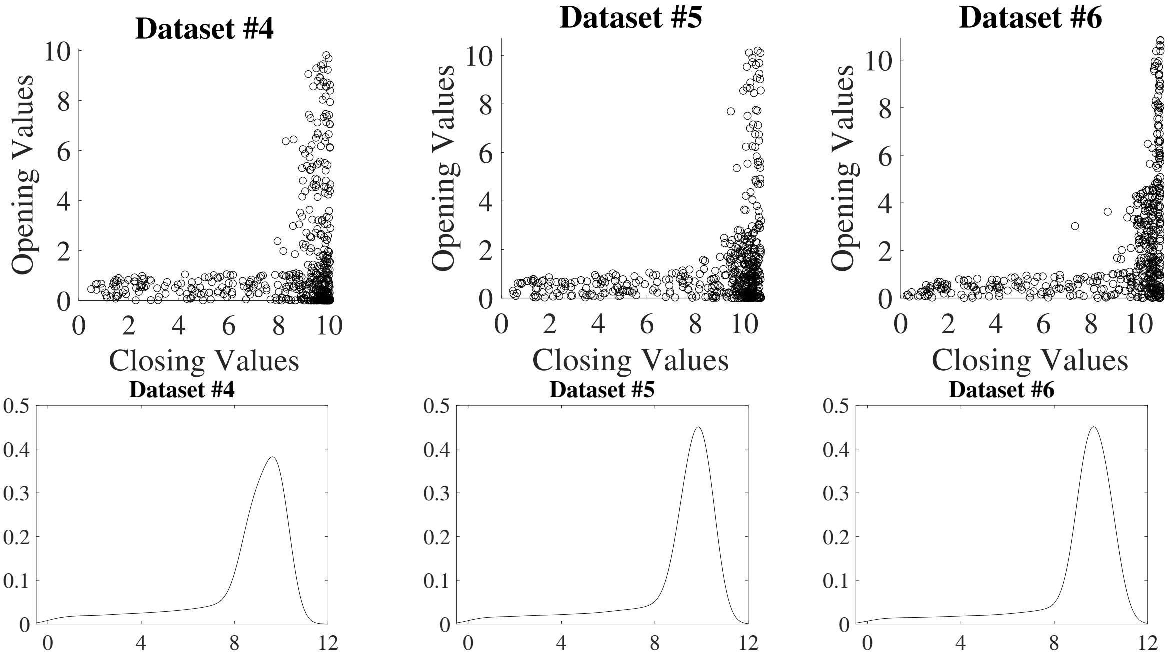

Figure 7: Identified PM spaces and corresponding 1D-Gaussian kernel estimates for the cycles 4-6 of earthquake damper.

Test	#1	#2	#3	#4	#5	#6
IE	0.538	0.872	0.899	0.908	0.91	0.915

Table 1: Indexes of elasticity for 6 damper cycles under successive loading resulting from our new identification 1D-kernel PM procedure.

Acknowledgements

These results were supported by the research grants LTT180001 (MEYS), LM2015068, and SGS18/188/OHK4/3T/14 (MEYS).

References

[1] I.D. Mayergoyz. *Mathematical Models of Hysteresis and Their Applications.* AcademicPress-Elsevier, London, 2003.

[2] C. Kožená, V. Kůs, S. Dos Santos. Hysteresis and memory effects in skin aging using PM space density identification. *In: BEC 2016, 15th Biennial Baltic Electronics Conference*, Tallinn 179-182, 2016.

[3] A. Benavent-Climent, A. Gallego, L. Romo-Melo, L. Morillas. Health monitoring of web plastifying dampers subjected to cyclic loading through vibration tests. *Structural Health Monitoring* **13**(1), 33-49, 2014.

[4] R.A. Guyer, K.R. McCall. Equation of state and wave propagation in hysteretic nonlinear elastic materials. *Journal of Geophysical Research* **99**(B12), 1994.

[5] R.A. Guyer, K.R. McCall, G. Boitnott. Hysteresis, Discrete Memory, and Nonlinear Wave Propagation in Rock: A New Paradigm. *Physical Review Letters* **74**(17), 1995.

[6] G.J. McLachlan, D. Peel. *Finite Mixture Models.* Wiley Inter-Science, 2000.

[7] V. Kůs V, D. Morales, I. Vajda. Extensions of the parametric families of divergences used in statistical inference. *Kybernetika* **44**, 95-112, 2008.

[8] J. Hrabáková, V. Kůs. Notes on consistency of some minimum distance estimators with simulation results. *Metrika* **80** (2), 243-257, 2017.

[9] R.V. Rao. Jaya: A simple and new optimization algorithm for solving constrained and unconstrained optimization problems. *International Journal of Industrial Engineering Computations* **7**(1), 19-34, 2016.

[10] B. W. Silverman. *Density estimation for statistics and data analysis.* Boca Raton: Chapman & Hall/CRC, 1998.

Stochastic and Physical Monitoring Systems
SPMS 2020
September 17 - 21, 2020
Chlum u Třeboně, Czech Republic

Estimating Size of the Support Space of Learnt Distribution

Kristina Jarůšková

Department of Mathematics, FNSPE, Czech Technical University in Prague, Czech Republic

Email: `jaruskri@fjfi.cvut.cz`

Abstract. Deep generative algorithms such as variational autoencoder (VAE) and generative adversarial networks (GANs) became very important in the field of image generation. Many works suggest that the GANs are able to learn the underlying distribution sufficiently closely given enough data and time. However, different methods of evaluation of the generative models focus on different issues. This article examines the test presented in [1] which focuses on measuring the support size of the generated distribution.

Key words: Birthday paradox; Generative models; Image simulations, Support size.

1 Introduction

Deep learning models are nowadays widely used for discriminative purposes, they very often represent the state-of-the-art methods for mapping a high-dimensional input to a class label. Recently, the deep models turned out to be efficient for simulation purposes as well. The deep generative models represent a probability distribution over the given space which they learn from the training dataset. Such model can then be used to generate new samples from the learnt distribution. Several approaches were taken to tackle this task, among them the most successful are the variational autoencoder (VAE) [2] and the generative adversarial netowrks (GANs) [3]. The latter one were first tested for image generation using the MNIST dataset [4] and CIFAR-10 dataset [5, 3] but they experienced a recent spread to many other areas such as face images generation, video generation or simulations of particle detectors in high energy physics (HEP) [6].

In many applications, the quality of the images or videos generated by GANs can be inspected visually by human eye. However, this is not applicable to all types of data and it does not provide an information about the variance or the support space of the generated distribution. Specifically, the GANs do not provide an estimate of some measure of distributional fit which makes it uneasy to determine if the GAN actually learnt the original distribution. The question of evaluating the generative models still remains open.

2 Generative Adversarial Networks

Generative adversarial networks (GANs) consist of two neural network models, the generator and the discriminator. The former maps a latent noise vectors (e.g. sampled from the Gaussian distribution) to synthetic examples that are similar to real samples. The latter is a discriminative network that has been trained to distinguish between the real and synthetic (fake) samples. These two networks are trained concurrently. The goal of the generator is to fool the discriminator in distinguishing between the real and fake samples - these two networks act as "adversaries". The output from the discriminator gives feedback to the generator - if the discriminator is able to recognize the fake samples, the weights of the generator are changed. By the end, the generator net produces realistic samples that the discriminator is unable to recognize.

Let $\{G_u, u \in \mathcal{U}\}$, $\mathcal{U} \subset \mathbb{R}^p$, denote the class of generators, where G_u is a function from $\mathbb{R}^l \to \mathbb{R}^d$ representing a generator with parameters u that produces samples from a distribution $\mathcal{D}_{G_u}$. The generator G_u takes a latent vector z from the l-dimensional spherical Gaussian distribution as its input. Similarly, let $\{D_v, u \in \mathcal{V}\}$, $\mathcal{V} \subset \mathbb{R}^p$ denote the set of discriminators, where D_v is a function from $\mathbb{R}^d$ to $[0,1]$ with parameters v. The distribution of the real samples is denoted $\mathcal{D}_{real}$.

A well trained discriminator should output a high value (equal or close to 1) when the given sample x is sampled from a distribution $\mathcal{D}_{real}$ of the real samples and a low value (equal or close to 0) when the sample x comes from the generated distribution $\mathcal{D}_{G_u}$. Therefore, the discriminator tries to maximize its objective function J_D, i.e.

$$\max_{v \in \mathcal{V}} J_{D_v} = \max_{v \in \mathcal{V}} \left[\mathbb{E}_{x \sim \mathcal{D}_{real}} [\log D_v(x)] + \mathbb{E}_{x \sim \mathcal{D}_{G_u}} [\log (1 - D_v(x))] \right].$$

On the other hand, the generator attempts to fool the discriminator, i.e. it tries to minimize the objective function J_{G_u}

$$\min_{u \in \mathcal{U}} J_{G_u} = \min_{u \in \mathcal{U}} \mathbb{E}_{x \sim \mathcal{D}_{G_u}} [\log (1 - D_v(x))].$$

These definitions correspond to the standard GAN training presented in [3]. The overall optimization problem can be formulated as a minimax game over J_{D_v}, i.e.

$$\min_{u \in \mathcal{U}} \max_{v \in \mathcal{V}} \left[\mathbb{E}_{x \sim \mathcal{D}_{real}} [\log D_v(x)] + \mathbb{E}_{x \sim \mathcal{D}_{G_u}} [\log (1 - D_v(x))] \right].$$

In other words, the generator tries to fool the best discriminator as much as possible. From the point of view of the game theory, solving this minimax game is equivalent to inding the *Nash equilibrium*, i.e. a pair (G_{u*}, D_{v*}) such that no network can improve its objective function by an unilateral change in parameters [7].

3 Estimating Support Size

The previous section ended with the remark that the GAN training is equivalent to searching for the Nash equilibrium of the minimax game. However, it might not be possible to find the exact equilibrium and even when the equilibrium is found, it does not mean that the generated distribution is the same as the real distribution. In fact, the quality of the generated samples depends on the quality of the discriminator.

In [1], the authors proposed a method for estimating the support size of the generated distribution based upon the *birthday paradox*. The birthday paradox concerns the probability that, in a set of n randomly chosen people, there will be at least one pair of them with the same birthday. The probability of having two people with the same birthday is 0.5 for only 23 people in the room. In other words, assume N possible different samples. According to the birthday paradox, a set of $\sqrt{N}$ samples will contain a duplicate with the probability of 0.5. This idea can be used to estimate the support size of the distribution learnt by the GAN. The test is as follows.

1. Take a set of s samples generated from the GAN.
2. Identify duplicates.
3. Repeat.

If the test reveals that the set of size s has duplicates with the probability ≥ 0.5, then the support size of the distribution is less than s^2.

4 Experimental Results

Assume, that the real data are three-dimensional images of energy deposition of a particle in a particle detector. The 3DGAN algorithm [6] was trained on this data to produce synthetic images of events in a detector. To identify the duplicates and measure the support space, it is first necessary to select a feature that will be compared and a suitable metric on that feature. Here, we select energy distributions along axes x, y and z as our features and the Jensen-Shannon divergence for the unnormalized distributions

$$JSD\left(p,q\right) = \frac{1}{2}D\left(p, \frac{p+q}{2}\right) + \frac{1}{2}D\left(q, \frac{p+q}{2}\right),$$

where $D(p,q) = p \cdot \log\left(\frac{p}{q}\right) - p + q$ is the unnormalized Kullback-Leibler divergence. Other divergences suitable for unnormalized distribution, such as those proposed in [8, 9] or the Rényi divergence used in [10, 11], could be used as well.

First, the real data (denoted as G4 in this paper) were used to determine the threshold values of the Jensen-Shannon divergence for which a pair of samples will be considered as duplicates in the given direction. A set of 5 000 samples of the real data was taken and the JSD was computed for all possible pairs. Then the 0.05-quantile was taken as the threshold determining the duplicates. The quantile values for energy distributions in each direction are in the table 1.

Then, these quantiles are used to detect duplicates in both real data and the generated data for sets of different sizes, the numbers of duplicates are in the table 2. We can immediately see, that the dataset of generated samples contains more pairs for which the JSD is below the threshold in comparison with the G4 dataset. The histograms 1 depicts the distribution of the values of the JSD for the three directions of the energy

Axis	0.05-quantile
x	0.0114
y	0.0200
z	0.0071

Table 1: 0.05-quantiles of the Jensen-Shannon divergence for all axes computed using the G4 (real) data.

distributions for datasets of 500 samples. We observe that the histograms of the distances computed on energy distributions along the y axis are alike for the G4 and the GAN data. On the other hand, the histograms for the z axis distributions are significantly different, the GAN dataset has obviously lower values of the JSD between the samples indicating that the GAN produces more duplicates than are present in the real data. To impose more restrictions, we now mark as duplicates only those pairs of samples for which the Jensen-Shannon divergence is below the thresholds for energy distributions along all three axes. The table 3 contains the numbers of duplicates that are found by this combination of three restrictions.

	G4 (real data)			GAN (generated data)		
Dataset size	x	y	z	x	y	z
100	204	225	300	489	248	834
200	978	1 081	1 074	1 860	1 152	3 459
500	6 255	6 267	6 496	11 189	6 889	20 962

Table 2: Number of duplicates in datasets of different number of samples for both the G4 and the GAN data.

Dataset size	G4 (real data)	GAN (generated data)
100	2	25
200	8	93
500	31	491

Table 3: Numbers of pairs of samples that are below the 0.05-quantile threshold for distributions in all three directions.

Finally, these observations were used to perform the evaluation based on the birthday paradox. The 0.05-quantiles of the Jensen-Shannon divergences were computed separately for the energy distribution along each axis using 5 000 samples of the real data. Then a subsample of size s was taken from both real data and generated data and the duplicates were detected using the combined condition on all three directions. This step was repeated 500 times. It was observed that for as little as $s = 20$ samples, the GAN subsample contained at least one duplicate in 272 cases out of 500 which means that the probability of encountering a duplicate in a set of size 20 is ≥ 0.5 and by the birthday paradox,

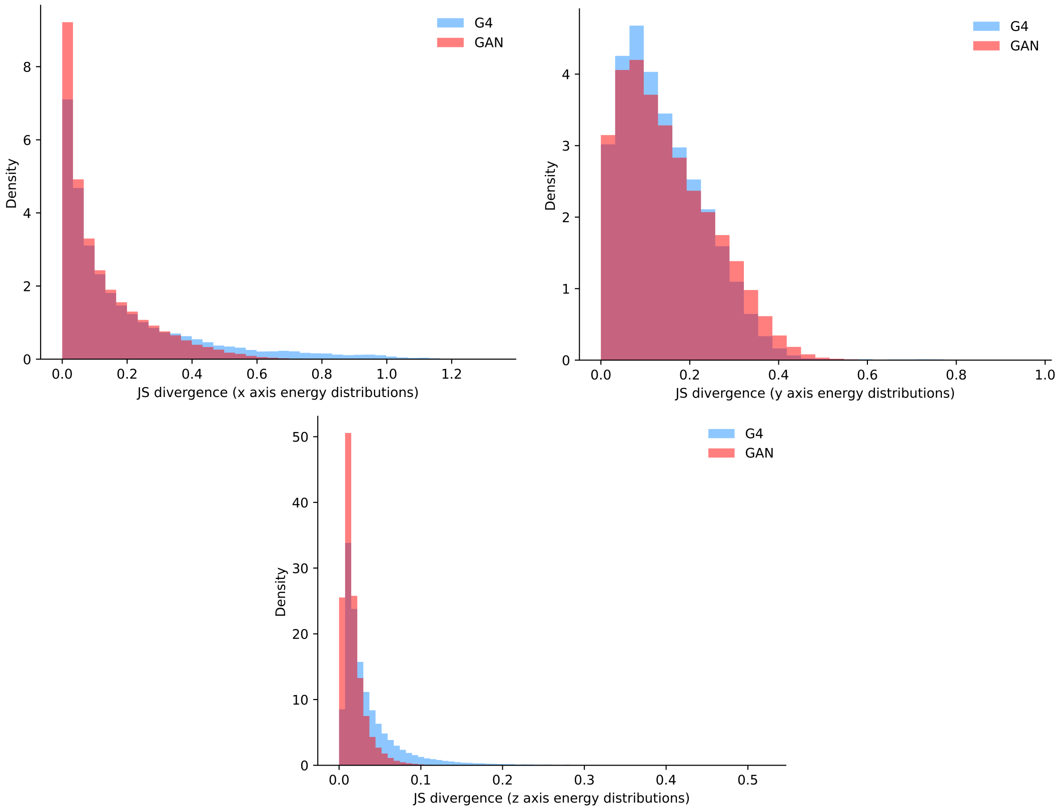

Figure 1: Histograms of the Jensen-Shannon divergences for datasets of 500 samples.

the support size of the GAN distribution is approximately 400. The G4 subsets contained duplicates in only 27 cases out of 500. This only confirms the surmise that the distribution learnt by the GAN does not cover the whole support space of the original distribution.

Closer examination of the duplicates revealed that the 0.05-quantile might be too large, lower quantiles are currently tested. If the 0.05-quantile is truly too large, it means that our previous estimate of the support space is a lower bound of the actual size of the support space of the generated distribution.

Summary

In the first two sections, this article introduced the basic concept of the generative adversarial networks (GANs). In the third section, the newly proposed method of estimating support size of the generated distribution based on the birthday paradox was briefly described. The last section focused on implementing this method for estimating the support size for data from particle detector simulations. At first, the energy distributions along axes x, y and z were selected as the features of interest. Then the unnormalized Jensen-Shannon divergence was used as a measure of distance between these energy distributions. Using the real samples (G4 data), the threshold value was determined as the 0.05-quantile of the divergences between the real samples. Finally, the birthday paradox test was performed.

It was observed that the distances between the generated samples are smaller than for the real samples. This is particularly significant for the energy distributions along the z axis. In addition to that, it was determined that the lower bound for the support size of the generated distribution is 400. Because the 0.05-quantile might be too large, lower quantiles are currently being tested.

Acknowledgements

These results were supported by the research grants LTT180001, LM2015068, as well as by SGS18/188/OHK4/3T/14 (MEYS), and CAAS EF16 019/0000778 (MEYS/EU).

References

[1] S. Arora and Y. Zhang. *Do GANs actually learn the distribution? An empirical study.* ArXiv e-prints, 2017.

[2] D. P Kingma and M. Welling. *Auto-Encoding Variational Bayes.* ArXiv e-prints, 2013.

[3] I. J. Goodfellow et al. *Generative Adversarial Networks.* ArXiv e-prints, 2014.

[4] Y. LeCun et al. *Gradient-based learning applied to document recognition.* Proceedings of the IEEE, **86**(11), 2278–2324, 1998.

[5] A. Krizhevsky and G. Hinton. *Learning multiple layers of features from tiny images.* Technical report, University of Toronto, 2009.

[6] G. R. Khattak, S. Vallecorsa, F. Carminati, and G. M. Khan. *Particle detector simulation using generative adversarial networks with domain related constraints. 18th IEEE International Conference On Machine Learning And Applications (ICMLA)*, 28-33, 2019.

[7] P. Grnarova et al. *A Domain Agnostic Measure for Monitoring and Evaluating GANs. 33rd Conference on Neural Information Processing Systems (NeurIPS)*, 12092 - 12102, 2019.

[8] I. Frydlova, I. Vajda, V. Kus. *Modified power divergence estimators in normal model - simulation and comparative study. Kybernetika* **48**, 795-808, 2012.

[9] J. Hrabakova, V. Kus. *Notes on consistency of some minimum distance estimators with simulation results. Metrika* **80** (2), 243-257, 2017.

[10] P. Bour, V. Kus, J. Franc. *Kernel and divergence techniques in high energy physics separations. Journal of Physics: Conference Series* **898** (072004), 2017.

[11] P. Bour, V. Kus, J. Franc. *Statistical classification techniques in high energy physics (SDDT algorithm). Journal of Physics: Conference Series* **738** (012034), 2016.

Stochastic and Physical Monitoring Systems
SPMS 2020
September 17 - 21, 2020
Chlum u Třeboně, Czech Republic

Blind Source Extraction of Moving Source from Linear Mixtures

Václav Kautský[1,2] and Zbyněk Koldovský[2]

[1]Department of Mathematics, FNSPE, Czech Technical University in Prague, Czech Republic
[2] Faculty of Mechatronics, Informatics, and Interdisciplinary Studies, Technical University of Liberec

Email: `kautsvac@fjfi.cvut.cz`

Abstract. This paper focuses on extraction of a moving source of interest (SOI) form a linear mixture. The rest of the mixture is called the background. The mixture is designed according to a famous independent component analysis (ICA) model, however, ICA deals only with static mixtures. Thus, the extension to dynamic sources is completely novel. The model dynamics is described in two ways: moving SOI with static background, and static SOI with moving background. In the experimental part, novel approaches are applied to real speech sources, and compared to state-of-the-art algorithms. The asymptotic performance, expressed in terms of Cramér-Rao Lower Bound on separation accuracy, shows huge potential of proposed methods.

Key words: Blind source extraction; Cramér-Rao lower bound; Independent component extraction; Speech sources.

1 Introduction

Blind source separation (BSS) aims at recovering a set of unobservable signals from a set of observed mixtures [1]. When the sources are statistically independent, BSS can be solved through the statistical tool of independent component analysis (ICA). Blind source extraction (BSE) aims at recovering a single signal of interest (SOI) from a set of observed mixtures of sources [1], and can be solved through independent component extraction (ICE).

Since different ICA/ICE methods provides different performance, lower bound on separation accuracy help to compare them. The Cramér-Rao lower bound (CRLB) plays the role of the limit on achievable accuracy. This paper deals with the BSE problem where the SOI is assumed to be independent from the background. The focus is on the *piecewise* determined mixing model designed for dynamic mixtures, i.e., the moving source in a static background.

In the assumed model, the observed sources are partitioned into multiple blocks where each block obey the standard determined model, see [2].

The paper is organized as follows. The proposed model is described in Section 2. Section 3 provides lower bounds on separation accuracy, and Section 5 introduces the real speech separation example. Section 6 concludes the paper.

2 Proposed Model

The ICE model is based on a re-parameterization of ICA model, see [3]. Let $\mathbf{u} \in \mathcal{C}^d$ be a vector of original sources, and $\mathbf{A} \in \mathcal{C}^{d\times d}$ be a random mixing matrix. ICE assumes, without loss of generality, that the SOI is the first source u_1. Partitioning of the data into M blocks can be represented by the following mixing model

$$\mathbf{x}^m = \mathbf{A}^m\mathbf{u}^m = \mathbf{a}^m s^m + \mathbf{y}^m, \tag{1}$$

where $m = 1, \dots, M$, the mixing matrix can be partitioned as $\mathbf{A}^m = [\mathbf{a}^m, \mathbf{A}_2^m]$ and $s^m = u_1^m$, $\mathbf{y}^m = \mathbf{A}_2^m\mathbf{u}_2^m$ and $\mathbf{u}_2^m = [u_2^m, \dots, u_d^m]^T$. Since neither $\mathbf{u}_2^m$ nor $\mathbf{A}_2^m$ is needed to be estimated to extract s^m, we can consider any auxiliary background signals $\mathbf{z}^m$ such that $\mathbf{y}^m = \mathbf{A}_2^m\mathbf{u}_2^m = \mathbf{Q}^m\mathbf{z}^m$. Compared to $\mathbf{u}_2^m$, the elements of $\mathbf{z}^m$ need not be independent, thus, $\mathbf{Q}^m$ can be arbitrary.

Without any further assumption, (1) corresponds to a sequential application of the standard mixing model, which is straightforward for on-line signal processing but does not bring any advantage. Therefore, we propose special parameterizations useful for the BSE problem that assumes the SOI is active in all blocks and some mixing parameters related to the SOI are fixed on all the blocks. Specifically, the mixing matrices $\mathbf{A}^1, \dots, \mathbf{A}^M$ are parameterized according to the following two scenarios:

$$\mathbf{A}_{\mathrm{CMV}}^m = \begin{pmatrix} \gamma & (\mathbf{h}^m)^H \\ \mathbf{g} & \frac{1}{\gamma}\left(\mathbf{g}(\mathbf{h}^m)^H - \mathbf{I}_{d-1}\right) \end{pmatrix} \tag{2}$$

$$\mathbf{A}_{\mathrm{CSV}}^m = \begin{pmatrix} \gamma^m & \mathbf{h}^H \\ \mathbf{g}^m & \frac{1}{\gamma}\left(\mathbf{g}^m\mathbf{h}^H - \mathbf{I}_{d-1}\right). \end{pmatrix}. \tag{3}$$

The models will be referred to as constant mixing vector (CMV) and constant separating vector (CSV), respectively, because in CMV the mixing vectors $\mathbf{a}^1, \dots, \mathbf{a}^M$ are constant over blocks and are equal to $\mathbf{a}$ while in CSV the separating vectors $\mathbf{w}^1, \dots, \mathbf{w}^M$ are all equal to $\mathbf{w}$. CMV is useful for situations where the SOI is a static source while the background is varying. CSV involves a moving SOI (varying mixing vector) under the assumption that a constant separating vector such that extracts the signal from all blocks exists. These models have been considered for the first time in [4], where they were applied to blind audio source extraction. Their theoretical analysis were provided in [2] through the CRLB theory.

3 Lower Bounds on Accuracy

Let N_b be the length of the block, and let N_b be constant over all blocks. The accuracy of BSS/BSE methods is usually measured in terms of Interference-to-Signal Ration (ISR).

The ISR for blockwise determined ICE model is defined as

$$\mathrm{ISR} = \frac{\sum_{m=1}^{M} \mathrm{E}[|(\widehat{\mathbf{w}}^m)^H \mathbf{y}^m|^2]}{\sum_{m=1}^{M} \mathrm{E}[|(\widehat{\mathbf{w}}^m)^H \mathbf{a}^m s^m|^2]}, \tag{4}$$

where $\widehat{\mathbf{w}}^m$ is an estimated separating vector for the mth block, $m = 1, \ldots, M$. The CRLB for ISR, called Induced-CRLB, plays here the role of the lower bound on a separation accuracy. The bound for block ICE model without any constraints on constant separating/mixing vector (derived in [2]) is

$$\mathrm{E}[\mathrm{ISR}] \geq \frac{1}{N_b} \frac{d-1}{\sum_{m=1}^{M} \sigma^2_{s^m}} \sum_{m=1}^{M} \frac{\sigma^2_{s^m}}{\kappa_{s_m} \sigma^2_{s^m} - 1}, \tag{5}$$

where N_b is the number of samples on a block, $\sigma^2_{s^m}$ is variance of s^m, $\kappa_s = \mathrm{E}\left[\left|\frac{\partial \ln p_s(s,s^*)}{\partial s^*}\right|^2\right]$ for the pdf of the SOI $p_s(s, s^*)$. The comparison of this bound with corresponding bounds of CSV and CMV mixing models show the performance potential of both novel approaches. The bound for CMV is given by

$$\mathrm{E}\left[\mathrm{ISR}\right] \geq \frac{1}{N_b \sum_{m=1}^{M} \sigma^2_{s^m}} \sum_{m=1}^{M} \frac{1}{\kappa_{s^m}} \mathrm{tr}\left(\mathbf{I}_{d-1} + \left(\sum_{i=1}^{M} \frac{\kappa_{s^i} - 1}{\kappa_{s^i}} \mathbf{C}^{-1}_{\mathbf{z}^i}\right)^{-1} \frac{1}{\kappa_{s^m}} \mathbf{C}^{-1}_{\mathbf{z}^m}\right), \tag{6}$$

and the bound for CSV is

$$\mathrm{E}\left[\mathrm{ISR}\right] \geq \frac{1}{N_b \sum_{m=1}^{M} \sigma^2_{s^m}} \mathrm{tr}\left(\left(\sum_{m=1}^{M} \frac{\kappa_{s^m} - 1}{\sigma^2_{s^m}} \mathbf{C}_{\mathbf{z}^m}\right)^{-1} \sum_{m=1}^{M} \mathbf{C}_{\mathbf{z}^m}\right). \tag{7}$$

where $\mathbf{C}_{\mathbf{z}}$ is a covariance matrix of $\mathbf{z}$.

4 Numerical simulations

To validate the bounds for CMV and CSV, both are compared with empirical results achieved by block-wise versions of OGICE introduced in [4]. The methods will be jointly referred to as BOGICE (in [4], $\mathrm{BOGICE}_{\mathbf{a}}$ is the variant for CMV while $\mathrm{BOGICE}_{\mathbf{w}}$ is for CSV).

In the presented simulation we assume the SOI is i.i.d. non-Gaussian over all blocks. The background is assumed circular Gaussian i.i.d. with unit variance in all blocks.

In trials, $d = 5$ independent complex-valued signals are generated. The SOI is drawn from a circular complex Generalized Gaussian Distribution (GGD) with zero mean, unit variance, $\alpha = 2$. The nonlinearity is given by the true score function. M blocks of the same length are considered. Each block is mixed by a random mixing matrix. The mixing matrices obey the mixing models CMV or CSV, respectively.

The empirical ISRs achieved by BOGICE and BICE are compared with the corresponding I-CRLB. For completeness, we also show the hypothetical I-CRLB of the alternative piecewise mixing model. Nevertheless, it should be kept in mind that CMV and

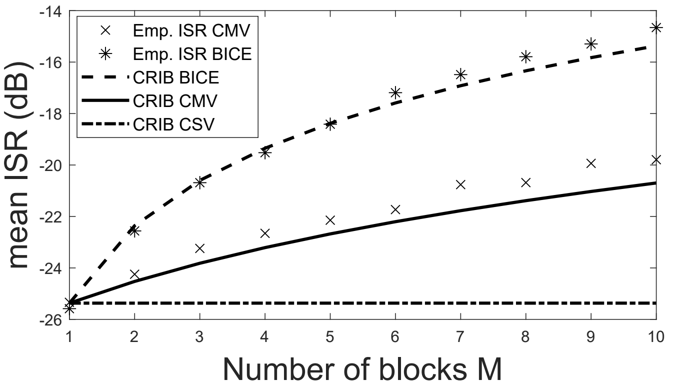

Figure 1: Average ISR for CMV mixing model when $d = 5$, $N = N_b M = 5040$, and varying number of blocks M.

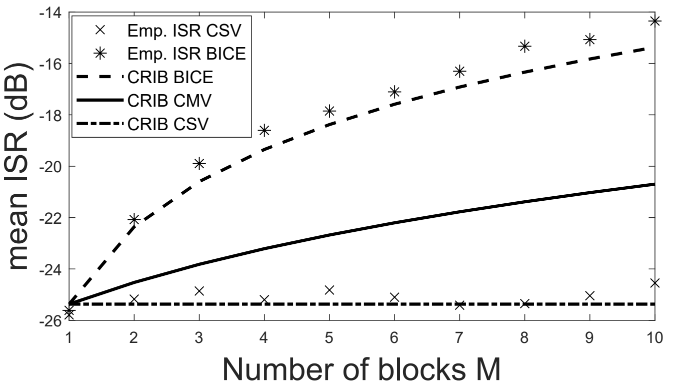

Figure 2: Average ISR for CSV mixing model when $d = 5$, $N = N_b M = 5040$, and varying number of blocks M.

CSV are incompatible unless all the mixing parameters related to the SOI are constant over the blocks (which is not the case of the experiments here).

Fig. 1 corresponds to the simulation considering the CMV model for varying number of blocks, that is, $M = 1, 2, 5, 10$. It shows the mean ISR achieved by BOGICE averaged over 500 trials and the I-CRLB given by (6) (CMV) and, for comparison, also the I-CRLBs (5) (BICE) and (7) (CSV). Similar simulation was done with the CSV model; the results are shown in Fig. 2. As can be seen bounds for BICE and CMV depend on the number of blocks, but the I-CRLB for CSV does not.

Figs. 1 and 2 show the coincidence between the empirical results by the variants of BOGICE and the I-CRLB corresponding to the mixing model of the given simulation. The performances of the methods follow the same dependence on the number of blocks M as these I-CRLBs. The results also show that BOGICE takes the advantage of the special mixing model CMV/CSV compared to BICE, as its mean ISR is lower, unless $M = 1$ where all mixing models coincide.

5 Speech sources separation

A real speech experiment was designed to test the benefits that piecewise determined approach brings to BSE. Since in practice the more interesting situation is a moving SOI with static background, the following setup was proposed. The SOI was a women reader that was moving around sensors while the background was a male voice and a noise of the office. The background sources were static. The sampling frequency of the signal was $F_s = 16$kHz. The data was transformed to the frequency domain by the Fast Fouriere Transform (FFT) with a frame length $f_{len} = 1024$. For detailed description of the experiment see [5].

As expected, BICE-based and CSV-based methods succeeded to converge to the desired SOI. CMV-based method extracted the background and suppressed the SOI, since it is designed for static sources and varying background. Thus, the important goal was to compare BICE to CSV. Despite both methods converged to the right SOI, BICE was not able to capture the dynamic character of the mixture. The amplitude of the extracted SOI is varying, so the listener is disturbed by the changing volume of the sound. CSV model proved its strength also on real-world data.

6 Conclusions

The computed CRLBs for piecewise determined models uncovered a great potential in terms of separation accuracy when dealing with moving sources. The CSV model does not suffer from the increasing number of blocks or decreasing number of samples on a block. Simulations coincide with the theoretical results and confirm derived bounds. The BOGICE methods applied to a separation of a moving speaker from a static background achieved better results than standard ICA methods.

Acknowledgements

This work was supported by The Czech Science Foundation through Project No. 17-00902S, by the United States Department of the Navy, Office of Naval Research Global, through Projects No. N62909-18-1-2040 and N62909-19-1-2105, and by the grant SGS18/188/OHK4/3T/14.

References

[1] P. Comon and C. Jutten, *Handbook of Blind Source Separation: Independent Component Analysis and Applications*, ser. Independent Component Analysis and Applications Series, Elsevier Science, 2010.

[2] V. Kautský, Z. Koldovský, P. Tichavský, V. Zarzoso, *Cramér-Rao Bounds for Complex-Valued Independent Component Extraction: Determined and Piecewise Determined Mixing Models*, in IEEE Transactions on Signal Processing (accepted for publication).

[3] Z. Koldovský and P. Tichavský, *Gradient algorithms for complex non-gaussian independent component/vector extraction, question of convergence*, IEEE Transactions on Signal Processing, vol. 67, no. 4, pp.1050–1064, Feb 2019.

[4] Z. Koldovský, J. Málek, and J. Janský Extraction of independent vector component from underdetermined mixtures through block-wise determined modeling, in ICASSP 2019 - 2019 IEEE International Conference on Acoustics, Speech and Signal Processing (ICASSP), May2019, pp. 7903–7907.

[5] , J. Janský and Z. Koldovský and J. Málek and T. Kounovský and J. Čmejla, Fast Algorithm for Blind Independence-Based Extraction of a Moving Speaker, 2020, eprint 2002.12619, arXiv.

Stochastic and Physical Monitoring Systems
SPMS 2020
September 17 - 21, 2020
Chlum u Třeboně, Czech Republic

On Rivalry between Attractive and Repulsive Stimuli in Vehicular Traffic

Milan Krbálek[1], František Šeba[2], and Michaela Krbálková[2,3]

[1] Department of Mathematics, Faculty of Nuclear Science and Physical Engineering, Czech Technical University in Prague, Prague, Czech Republic
[2] Department of Physics, Faculty of Science, University of Hradec Králové, Hradec Králové, Czech Republic
[3] Department of Transport Technology and Control, Jan Perner Transport Faculty, University of Pardubice, Pardubice, Czech Republic

Email: `milan.krbalek@fjfi.cvut.cz`

Abstract. Studying original empirical traffic data, we show surprising statistical anomalies in the traffic microstructure that can not be explained by current scientific approaches used in physics of traffic. We quantify these anomalies mathematically and explain their cause. By means of particle gas, which represents a specific version of the traffic model described by the general Langevin equation, we show that all these anomalies can be explained by an occurrence of attractive force components in the model. This approach (in addition to the explanation of the statistical properties in vehicular microstructure) also makes it possible to detect conditions in real traffic flows, under which the attractive stimuli are considerable. The detected area, where the presence of strong inter-vehicle attraction stimuli is fully manifested, perfectly matches the reality of traffic.

Key words: Traffic Data, Vehicular Headway Modelling, Traffic Models, Statistical Rigidity.

1 Introduction, Motivation, Goals

Probabilistic modeling of inter-vehicular gaps (headways/clearances; spatial/temporal) has very rich and interesting history [1, 2]. Consistently during last four decades, experts in the field have been offering various headway models tailored to specific traffic situations and, generally speaking, the efforts to describe a vehicular microstructure by a relevant probabilistic description can be considered as successful. On the other hand, generally accepted and generally applicable statistical model still does not exist. However, a proper decryption of statistical patterns in vehicular microstructure plays a key role for most tasks dealing with traffic capacities, travel times, traffic optimization, or autonomous driving of vehicles. This highlights the importance of Vehicular Headway Modeling (VHM) in an extensive portfolio of Transportation Science disciplines.

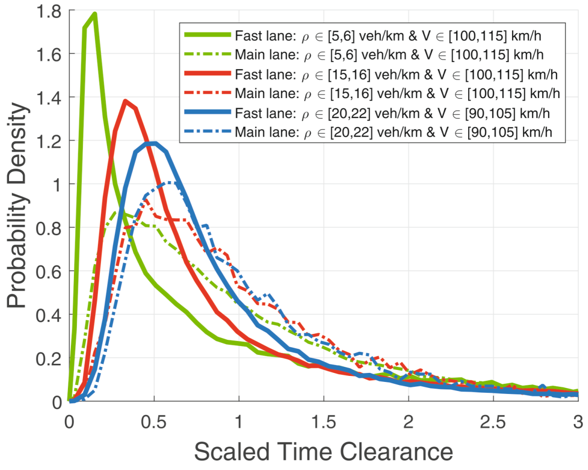

Figure 1: Empirical time headway distributions detected in the same subsegments of the ID plane for both lanes. We demonstrate how HDs measured for fast and main lanes can be significantly dissimilar, even if the associate macroscopic quantities (see legend) are the same.

This paper focuses on advanced methods of VHM linking a proposed probabilistic model with corresponding traffic force-based model. From such a link, it is possible to decipher interaction rules representing, in fact, a basic control procedure, by which the driver changes his/her movement in a stream of other vehicles. This close relationship between a traffic model and statistical description of vehicular microstructure allows us to answer several questions and open problems in physics of traffic. For unidirectional two-lane (or multi-lane) traffic flow (with a main lane and a lane for overtaking cars) these open problems can be formulated as follows.

- Is any one-component and low-parametric distribution model able to describe headway distributions (HDs) in all traffic regimes, lanes, and phase segments (two-dimensional subregions of the phase plane)?
- *Anomaly 1:* Why HDs measured in a fast lane differ so significantly from HDs detected in a main (slow) lane, even if the values of the macroscopic quantities (density ϱ, mean speed V, intensity/flow I) are the same in both lanes (see Fig. 1)?
- *Anomaly 2:* Why distributions detected in a region of intermediate densities for fast-lane vehicles usually lies outside the typical distribution families?
- *Anomaly 3:* Why a variance of empirical scaled clearances (for some traffic data samples) exceeds theoretically calculated limit values (see Fig. 2)?
- *Anomaly 4:* Why empirical statistical rigidity of traffic data [3] occasionally exhibits unexpected anomalies from analytical predictions (see Fig. 3)?
- Is, as presumed by many reputable traffic models (see [4]), a repulsive stimulus between succeeding cars really one and only substantial interactive impulse (together

with a standard driving term) influencing a driver's reaction? Or, to the contrary, is there present any perspicuous attraction between cars as well? Are these attractive force components detectable, in principle?

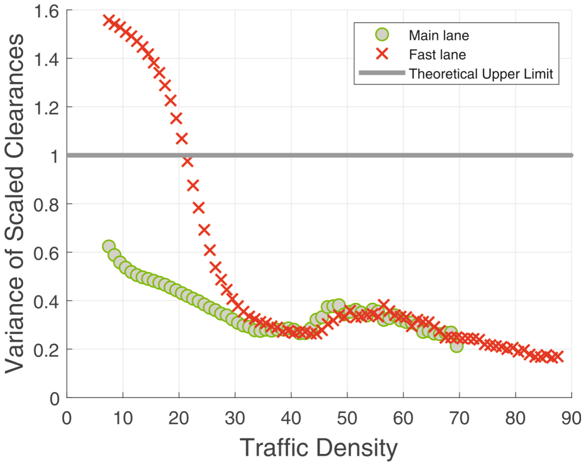

Figure 2: Empirical variance of temporal clearances (after scaling procedure) as a function of traffic density. Note that variance determined for small-density fast-lane samples exceeds the upper limit calculated theoretically for all one-dimensional stochastic systems of repelling particles.

In this article we aim to introduce a robust, theoretically/empirically arguable, and statistically verified headway model (interconnected with corresponding dynamics description), which leads to satisfactory answers to the questions raised above.

2 Stochastic dynamics of vehicular stream

2.1 Fokker-Planck equation approach

In this article, one-lane traffic flow is modelled by means of a one-dimensional stochastic gas of n point-like particles playing the role of vehicles. Actual state of the gas is naturally described by positions $\xi_1(t) > \xi_2(t) > \ldots > \xi_n(t)$ and instantaneous velocities $v_1(t), v_2(t), \ldots, v_n(t)$ of all particles at time t. Time evolution is driven by the Langevin acceleration equation

$$\frac{\mathtt{d}v_k(t)}{\mathtt{d}t} = \frac{v_0 - v_k(t)}{\tau} + F(\xi_{k-1}(t) - \xi_k(t)) - \gamma F(\xi_k(t) - \xi_{k+1}(t)) + \Xi_k(t) \tag{1}$$

inspired by optimal velocity models [6]. Herein, v_0 stands for the desired velocity, τ for the relaxation time, and $(v_0 - v_k(t))/\tau$ then represents the so-called driven term. $F(x)$ is the interaction force (repulsive, usually) depending on the front headway $x_k = \xi_{k-1} - \xi_k$. Stochastic background is generated by the Gaussian components $\Xi_k(t)$ fulfilling the white-noise relationships $\langle \Xi_k(t) \rangle = 0$ and $\langle \Xi_k(t)\, \Xi_\ell(t') \rangle = D\delta_{k\ell}\delta(t - t')$, where $\delta_{k\ell}$, $\delta(t)$ are the

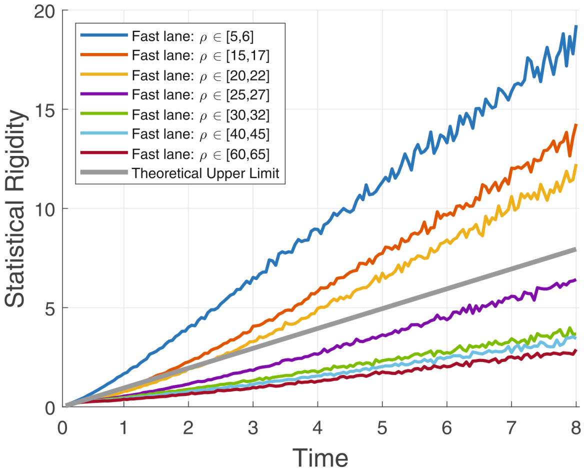

Figure 3: Statistical rigidity in empirical traffic samples. Figure shows that, provided that traffic density is low, the rigidity analyzed for fast lane data lies outside the theoretically substantiated region.

Kronecker delta and Dirac function, respectively, and the constant D is the diffusion coefficient determining the intensity of fluctuations. Symmetrizing parameter $\gamma \in [0,1]$ regulates how much a given particle is influenced by an immediately following particle. Whereas a value $\gamma = 1$ corresponds to the case of symmetrical interactions fulfilling Newton's Third Law, value $\gamma = 0$ corresponds to forwardly directed potentials.

The acceleration equations (1) define a stochastic process whose stationary solution is mathematically described by a joint probability density $P(x_1, x_2, \ldots, x_n, v_1, v_2, \ldots, v_n)$. To find it, the afore-mentioned stochastic process have to be reformulated (see [5]) in terms of a Fokker-Planck equation. It reads

$$\frac{\partial P}{\partial t} = \sum_{k=1}^{n} \left\{ -\frac{\partial[(v_{k+1}-v_k)P]}{\partial x_k} - \frac{\partial}{\partial v_k}\left[\frac{W(x_k, x_{k-1}) - v_k}{\tau} P\right] + \frac{D}{2}\frac{\partial^2 P}{\partial v_k^2} \right\}, \tag{2}$$

where the periodic boundary conditions $v_k(t) = v_{k+n}(t)$ and $\xi_k(t) = \xi_{k+n}(t)$ are assumed for a freeway of length L. The function $W(x_k, x_{k-1}) = v_0 + \tau[F(x_k) - \gamma F(x_{k-1})]$ is introduced for brevity. Provided that headways and velocities are understood as statistically independent variables, which means that $\langle x_k(t)\, v_\ell(t)\rangle = 0$ for any k, ℓ, authors of [5] proved that joint p.d.f. can be factorized

$$P(x_1, x_2, \ldots, x_n, v_1, v_2, \ldots, v_n) = \prod_{k=1}^{n} g(x_k) q(v_k) \tag{3}$$

via velocity distributions

$$q(v_k) = \frac{1}{\sqrt{\pi D \tau}} \mathrm{e}^{-\frac{(v_k - v_0)^2}{D\tau}}, \tag{4}$$

and headway distributions

$$g(x_k) = A \mathrm{e}^{-\beta \varphi(x_k) - \lambda x_k}, \tag{5}$$

where

$$F(x) = \frac{2}{1+\gamma}\frac{\mathtt{d}\varphi(x)}{\mathtt{d}x}. \tag{6}$$

In this notation, the function $\varphi(x)$ corresponds to the distance-dependent potential, $\beta = D\tau/2$, A is a normalization constant, and $\lambda > 0$ is a scaling constant calibrated by means of the particle density ϱ as

$$\int_0^\infty x_k g(x_k)\mathtt{d}x_k = \frac{1}{\varrho}. \tag{7}$$

2.2 Thermodynamic gas approach

Working with the afore-mentioned particle concept, we can introduce a thermodynamic alternative of the system. Defining the Hamiltonian

$$H(x_1, x_2, \ldots, x_n, v_1, v_2, \ldots, v_n) = \sum_{k=1}^{n} \frac{(v_k - v_0)^2}{\tau} + \sum_{k=1}^{n} \varphi(x_k) \tag{8}$$

acting on a freeway of length L with periodic boundary conditions and being exposed to the heat bath with the temperature T, one can prove (similarly to approaches published in [7]) that an associated steady state is described by formulas analogical to (3),(4),(5), where $D = 2k_BT$, k_B is the Boltzmann factor, and $\beta = 1/k_BT$ is the stochastic resistivity. Furthermore, one can show (see [8]) that p.d.f.

$$g(x) = A\mathtt{e}^{-\hat{\beta}\varphi(x)-\lambda x}, \tag{9}$$

with $\hat{\beta}$ understood as an estimated value (usually significantly different from β), is a very good approximation for headway distribution analyzed far from equilibrium. It means that vehicular flows, as typical systems driven far from equilibrium, can be inspected by probabilistic instruments applied usually in classical many-particle systems with symmetrical interactions. This property is confirmed also in the article [9].

The presented similarity between non-equilibrium and equilibrium systems opens interesting perspectives for detection of interaction forces among elements in one-dimensional driven dissipative many-particle systems such as vehicular flows.

3 Statistical description and analysis of vehicular microstructure

There are two natural ways for analysing statistical properties of one-dimensional particle ensembles. Except continuous random variables, like gaps or multi-gaps between particles, there exists an alternative description working with discrete random variables. Typical representatives of such variables are the interval frequencies $\mathcal{N}_L$ representing a number of particles occurring in the interval $(\xi_0, \xi_0 + L)$, where ξ_0 is a position of a chosen reference particle. Alternatively, $\mathcal{N}_T$ means a number of particles passing a given point (detector) during the time interval $(t_0, t_0 + T)$, where t_0 denotes the time when reference particle has been passing the detector. For one-dimensional systems of point-like particles or for related systems, e.g. spectra of random matrices [10] the very effective statistical tool is the stochastic rigidity $\Delta(L)$ defined as the variance of $\mathcal{N}_L$ (or $\mathcal{N}_T$). Indeed, stochastic rigidity of traffic samples has been studied in previous investigations [3, 11, 12, 13] and has helped to confirm/reject several intuitive hypotheses on traffic flow (e.g. rejection of the hypothesis on short-ranged nature of inter-vehicular interactions [12]) and to reveal many new and surprising properties of vehicular microstructure.

The both descriptions are strongly interconnected by mathematical linkages. To briefly summarize such a relationship we remind [13] the following assertion.

Let $g(x)$ be the p.d.f. of inter-particle gaps in an arbitrary one-dimensional many particle system. Let us denote $\mu_k = \int_0^\infty x^k g(x)\mathtt{d}x$ the kth statistical moment. Provided that succeeding gaps are i.i.d., $\mu_0 = \mu_1 = 1$, and $\mu_2, \mu_3 < +\infty$, the associated statistical rigidity of the ensemble reads

$$\Delta(L) = (\mu_2 - 1)L + \frac{3\mu_2^2 - 2\mu_3}{6} + o(1), \quad L \to +\infty. \tag{10}$$

It means that in systems, whose headway sequences are independent and identically distributed, the slope (referred usually to as statistical compressibility and denoted by χ) of linear asymptote of the statistical rigidity is equal to the variance of headways.

3.1 Theoretical limits for vehicular random variables

In the following text we assume, without any loss of generality, that all headway variables are re-scaled so that average value is equal to one. Such an unification view brings many advantages when interpreting data or searching for theoretical relations among statistical quantities, which is the objective of the immediately following advisements.

Suppose that a non-negative (and scaled) random variable $\mathcal{X}$ is distributed via one-parametric p.d.f.

$$g(x|\beta) = A\mathtt{e}^{-\beta\varphi(x)-\lambda x} \quad (x > 0,\ A = A(\beta),\ \lambda = \lambda(\beta)), \tag{11}$$

where $\varphi(x) \geq 0$ is differentiable on $(0, +\infty)$, $\varphi(0_+) = +\infty$, and $\lim_{x\to\infty} \varphi(x) = 0$, where $\varphi(x)$ and $\varphi'(x)$ play roles of interaction potential and force, respectively. If, additionally, $\varphi'(x) < 0$, then for the second non-central moment it holds $\mu_2 \leq 2$, which means that variance of $\mathcal{X}$ is in all the circumstances less or equal to one. As far as vehicular systems are concerned, this fact can be interpreted as follows. If the dynamics of the particle systems is driven by a strictly repulsive force (6) then variance of scaled headways must not exceed the upper limit $\mathtt{VAR}(\mathcal{X}) = 1$, which implies directly that statistical rigidity $\Delta(L) = L$ of Poissonian ensembles of non-interacting elements represents, in fact, the unreachable limit for all systems with interacting elements.

This theoretical knowledge is crucial for deeper understanding statistical features of vehicular observables, as presented below.

3.2 Empirical analysis of statistical rigidity in phase segments and consequences

One of the well-known properties of vehicular traffic is the very strong sensitivity of HDs to values of macroscopical traffic quantities (density ϱ, intensity I, or mean speed

V). Such a sensitivity will not disappear even after the scaling procedure is applied [15, 7, 3, 12]. For this reason it is necessary to perform all estimation procedures by means of a segmentation [14], i.e. analyze data respective to a fixed phase segment (a small sub-region of phase plane), where estimation procedure is significantly stable. Typical choices for the phase segments are e.g. $(\varrho_0, \varrho_0 + \delta_\varrho) \times (I_0, I_0 + \delta_I)$ in ID plane or $(\varrho_0, \varrho_0 + \delta_\varrho) \times (V_0, V_0 + \delta_V)$ in VD plane.

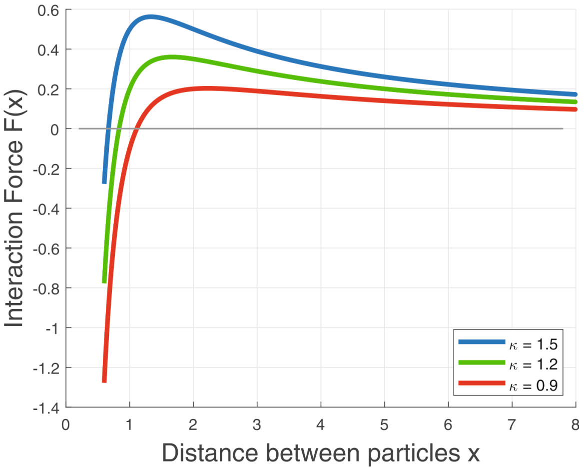

Figure 4: Graphical visualization of composite inter-vehicular forces used for headway modelling.

Fig. 3 we show how significantly the rigidities (analyzed in the same phase segment) differ for different lanes. Whereas the rigidity of main-lane data samples lies below the line $\Delta(L) = L$, in some segments extracted from fast-lane samples the rigidity exceeds this theoretically calculated limit. This implies, according to the above considerations, that vehicular dynamics is not induced by inter-vehicle repulsions only. Quite the contrary, as confirmed by accompanying investigations of the clearance variances (see Fig. 2), vehicles moving in a fast lane are attracted to a predecessor. Moreover, this attractive force component is very intense since it causes substantial deviations from behaviour of systems driven by strictly repulsive forces.

Therefore, being inspired by outputs of the rigidity test we suggest (for purposes of headway modelling) the dynamic description combining the both, attractive and repulsive components. To be specific, a 2-component force/potential proposed may be written as

$$F(x) = -\frac{\kappa}{x} + \frac{1}{x^2}, \quad \varphi(x) = \kappa \ln(x) + \frac{1}{x}, \quad x > 0, \tag{12}$$

respectively, where $\kappa \geq 0$ is the constant expressing a ration between repulsive and attractive components (see Fig. 4). Thus, the potentials used commonly in the transportation literature [7, 15, 3, 16, 17, 18] represent, in fact, special (purely repulsive) variants of (12), where $\kappa = 0$.

3.3 Headway distributions in phase segments

The above-suggested force description implies the HD, which is described mathematically via two-parametric family

$$g_{\alpha,\beta}(x) = Ax^{-\alpha}\mathrm{e}^{-\frac{\beta}{x}}\mathrm{e}^{-\lambda x} \quad (x>0), \tag{13}$$

where $\alpha \geq 0$, $\beta \geq 0$ represent distribution parameters. Positive constants $A = A(\alpha,\beta)$, $\lambda = \lambda(\alpha,\beta)$ ensure the proper normalization and scaling, i.e. $\mu_0(g) = \mu_1(g) = 1$. Parametr α is connected to a force constant $\varkappa$ via $\alpha = \varkappa{\cdot}\beta$. Therefore, for purely repulsive potentials it holds $\alpha = 0$, whereas for potentials with a significant attractive component it holds $\alpha > 0$.

A procedure estimating values α, β from empirical traffic samples is based on standard Minimum Distance Estimation method. It means that we minimize the L_2-distance

$$\sigma(g_{\alpha,\beta},h) = \|g_{\alpha,\beta}-h\| = \left(\int_0^\infty (g_{\alpha,\beta}(x)-h(x))^2\,\mathtt{d}x\right)^{1/2}$$

between the empirical histogram-function $h(x)$ and p.d.f. (13), i.e. we solve a optimization problem

$$(\hat{\alpha},\hat{\beta}) = \mathrm{argmin}_{\alpha\geq 0,\beta\geq 0}\sigma(g_{\alpha,\beta},h).$$

For comparison, an analogy using distribution functions instead of probability densities has been applied, as well. Estimated values obtained are, however, independent on a method used.

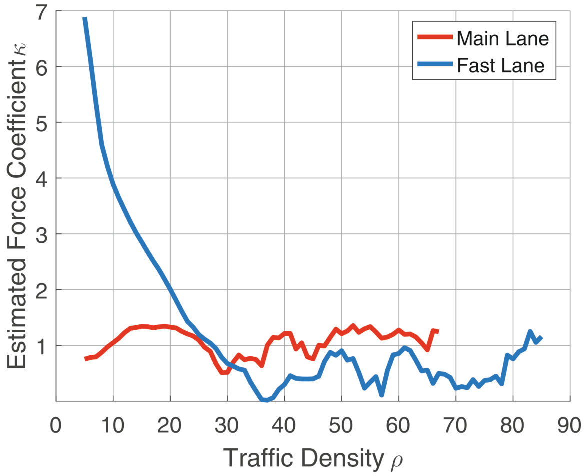

Figure 5: Estimated value of the force coefficient κ extracted from empirical traffic samples by means of Minimum Distance Estimation method.

To be specific, we have analyzed vehicle-by-vehicle data samples provided by The Road and Motorway Directorate of the Czech Republic and measured during 90 days at several segments of highway circuit R1 Prague, Czech Republic by technology of induction double-loop detection. Extensive data record has been divided into small rectangular subsegments $\Omega(\varrho) = (\varrho, \varrho+5) \times (50\varrho, 100\varrho)$ (in units veh/km vs. veh/h) of the intensity-density map (see a phase diagram in [19], page 1272). Time clearance extracted from the phase segments is then subjected to the estimation procedure above (see Fig. 7). Estimated values $\hat{\beta}$ and $\hat{\varkappa}$ are visualized in (Fig. 5 and 6). As apparent, statistical resistivity of segmented samples shows almost linear increase with traffic density, which means that statistical self-organization of vehicular systems grows from slightly correlated states (being close to non-correlated events in Poissonian systems) to strongly organized states, which (at the theoretical level) converge (for resistivity approaching to infinity) to equidistantly organized ensembles (deterministic systems). The behavior of the second parameter show considerably more interesting features. For congested (synchronized or wide-moving-jam flows with traffic density above $30\,veh/km$) the force coefficient $\varkappa$ gains very low values, which means that a leading interaction term is a repulsion between succeeding cars, which holds similarly for both lanes. However, for free-flow and transition regimes there is a significant difference between fast and slow lanes. Whereas main-lane vehicles are attracted to their forerunners quite weakly, for fast-lane drivers the influence of a attractive force component prevails over a repulsive component. Such a difference between both lanes clearly distinguishes a competitive way of driving in fast lanes from tranquil maneuvering of cars in a main lane. It is also very clear from Fig. 6 that the aggressive nature of fast lane maneuvering is suppressed in the condensed phase due to the increased traffic density, in which an aggressive driving style may be dangerous. The increase in traffic density then visibly causes synchronization not only in driving style (where the ratio between attractive and repulsive force component is practically the same in both lanes) but also in the stochastic synchronization in vehicular microstructure (as the respective HDs are very similar in both lanes).

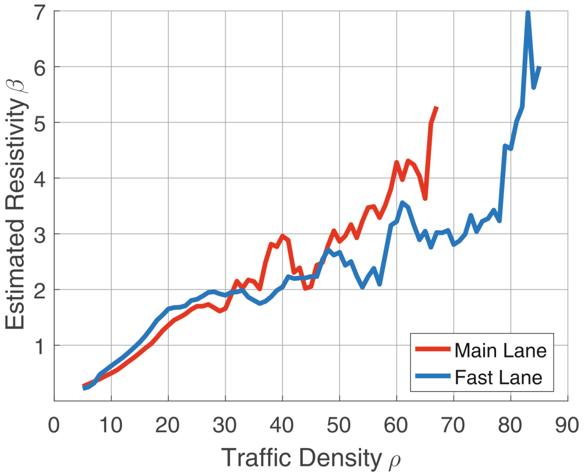

Figure 6: Estimated value of statistical resistivity β extracted from empirical traffic samples by means of Minimum Distance Estimation method.

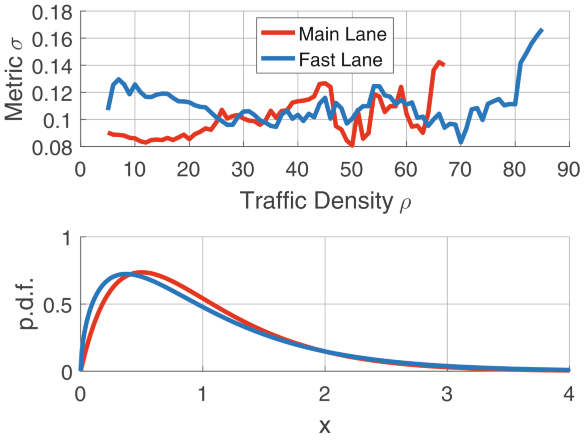

Figure 7: Statistical metric σ between empirical headway and estimated (GIG) distributions. For comparative purposes, the bottom subfigure shows two functions with mutual distance equal exactly to 1/10.

4 Conclusions

Based on analytically calculated statistical distributions of microscopic quantities in thermodynamic particle gas and with the help of statistical analysis of empirical traffic data, we show that standard traffic micromodeling is able to explain the dynamics of statistical properties in traffic systems only under certain specific conditions (e.g. traffic flow in the condensed phase). For fast lane vehicles moving in the free traffic phase, this approach fails. By standard traffic modeling we mean models, which are based on the assumption that interaction forces (i.e. forces induced by changing inter-vehicle distances) between vehicles are of a purely repulsive nature. Indeed, segmentation analysis of data samples reveals that HDs extracted from a fast lane show significant deviations from the particle systems controlled by repulsive force components only. These samples show unexpected statistical anomalies, which can be explained by the presence of attractive forces in the system.

Thus, if the particle gas is reformulated into a variant that imposes both repulsive and attractive forces between the particles in a logical manner (see below), then the respective equilibrium (and even non-equilibrium) states of the gas exhibit statistical anomalies similar to those detected in empirical traffic data. By means of the above-introduced description, it is then possible to determine under what conditions these attractive force components are active in a given traffic system. The outlined procedure has revealed that the attractive forces are well-founded in the case of vehicles moving in a fast lane in the free flow phase, or in transition states between the two traffic phases. The presence of these forces can logically be explained by a competitiveness of the drivers (often forced by overtaking maneuver), which is suppressed when traffic goes from free to condensed phase and which vanishes with increasing density.

In addition, the established force description strongly corresponds to the traffic reality. This is because the attractive component decreases with the first power of the distance, while the repulsive component decreases with the square of the distance. This means that for small distances the repulsive force always outweighs the attractive force. And conversely, for long distances, the repulsive component is suppressed so that the attraction is the main motion impulse (see Fig. 4).

Thus, it has been shown that the open problems of the area VHM (associated with statistical anomalies in the transport microstructure) can be explained very compactly and elegantly with the help of an idealized particle gas which is controlled by composite force potentials. The theoretical solution of such a gas fully corresponds to the statistics of empirical data in all segments of the phase space.

Acknowledgements

Research presented in this work has been supported by the Grant SGS18/188/OHK4/-3T/14 provided by the Ministry of Education, Youth, and Sports of the Czech Republic (MŠMT ČR). The authors would also like to thank The Road and Motorway Directorate of the Czech Republic (Ředitelství silnic a dálnic ČR) for providing traffic data analyzed in this paper.

References

[1] Li, L., Chen, X.M., 2017. *Vehicle headway modeling and its inferences in macroscopic/microscopic traffic flow theory: A survey,* Transportation Research Part C 76, 170.

[2] Ha, D., Aron, M., Cohen, S., 2012. *Time headway variable and probabilistic modeling,* Transportation Research Part C 25, 181.

[3] Krbálek, M., Šeba, P., 2009. *Spectral rigidity of vehicular streams (Random Matrix Theory approach),* J. Phys. A: Math. Theor. 42, 345001.

[4] Helbing, D., 2001. *Traffic and related self-driven many-particle systems,* Rev. Mod. Phys. 73, 1067.

[5] Helbing, D., Treiber, M., Kesting, A., 2006. *Understanding interarrival and interdeparture time statistics from interactions in queuing systems,* Physica A 363, 62.

[6] Bando, M., Hasebe, K., Nakayama, A., Shibata, A., Sugiyama, Y., 1995. *Dynamical Model of Traffic Congestion and Numerical Simulation,* Phys. Rev. E 51, 1035.

[7] Krbálek, M., 2007. *Equilibrium distributions in a thermodynamical traffic gas,* J. Phys. A: Math. Theor. 40, 5813.

[8] Groverová, N., Krbálek, M., 2018. *Statistic resistivity of non-equilibrium states in transport gases,* Proceedings of Stochastic and Physical Monitoring Systems Conference 2018, 25.

[9] Treiber, M., Helbing, D., 2009. *Hamilton-like statistics in onedimensional driven dissipative many-particle systems,* Eur. Phys. J. B 68, 607.

[10] Mehta, M.L., 2004. *Random matrices (Third Edition),* New York: Academic Press

[11] Helbing, D., Treiber, M., 2003. *Interpreting the wide scattering of synchronized traffic data by time gap statistics,* Phys. Rev. E 68, 067101.

[12] Krbálek, M., Apeltauer, J., Apeltauer, T., Szabová, Z., 2018. *Three methods for estimating a range of vehicular interactions,* Physica A 491, 112.

[13] Krbálek, M., Kollert, O., Hobza, T., Krbálková, M., 2019. *Statistical rigidity of vehicular streams – theory vs. reality,* Journal of Physics Communications 3, 035020.

[14] Krbálek, M., Krbálková, M., 2018. *3s-Unification for Vehicular Headway Modeling,* Proceedings of Stochastic and Physical Monitoring Systems Conference 2018, 69. (arXiv: https://arxiv.org/abs/1811.05325)

[15] Krbálek, M., Helbing, D., 2004. *Determination of interaction potentials in freeway traffic from steady-state statistics,* Physica A 333, 370.

[16] Treiber, M., Hennecke, A., Helbing, D., 2000. *Congested traffic states in empirical observations and microscopic simulations,* Physical Review E, 62 (2), 1805.

[17] Gazis, D.C., Herman, R., Rothery, R.W., 1961. *Nonlinear follow-the-leader models of traffic flow,* Operations Research 9, 545.

[18] Mahnke, R., Kaupuzs, J., Hinkel, J., Weber, H., 2007. *Application of thermodynamics to driven systems,* The European Physical Journal B 57 (4), 463.

[19] Krbálek, M., 2017. *Quantitative analysis of interaction range in vehicular flows,* Transportation Research Procedia 25, 1268.

Stochastic and Physical Monitoring Systems
SPMS 2020
September 17 - 21, 2020
Chlum u Třeboně, Czech Republic

Machine Learning Estimators for Jet Shapes Background Correction

Miroslav Kubů

Department of Mathematics, FNSPE, Czech Technical University in Prague, Czech Republic

Email: `kubumiro@fjfi.cvut.cz`

Abstract. Jet shapes and structure observables are the key point of interest in heavy-ion physics. As the dominant background of soft processes complicates the measurement of jet properties, it is necessary to perform the correction of the jet properties. Machine learning (ML) methods such as artificial neural networks (ANN), decision trees and random forests are commonly used for the regression tasks. Thus, the observed uncorrected jet properties can be used as the input variables for the ML models estimating the real corrected jet properties. In this paper, we explore the potential of ML algorithms for different combinations of input jet properties. Furthermore, we use a convolutional neural network (CNN) model to test whether the deep learning approaches can improve the estimation performance. Today, deep learning models are typically used for the neutrino experiments, such as the NOvA experiment [1, 2]. We aim to improve the background correction of the jet properties in comparison to the established area-based method.

Key words: Machine learning; Neural Networks; Decision Trees; Heavy-ion physics .

1 Introduction

Due to the overwhelmingly large background of particles not originated from hard interactions, the reconstruction of particle jets in heavy ion collisions is a crucial, but also a non-trivial task. The area-based background estimator is the standard established method for this task [3]. The area-based method estimates the reconstructed p_T^{rec} from the raw p_T^{raw} value of the jet with area $A \in \mathbb{R}^+$ as

$$p_T^{rec} = p_T^{raw} - \rho A, \tag{1}$$

where $\rho \in \mathbb{R}$ is the jet density coefficient.

In this paper, we estimate the mapping between uncorrected and true jet properties using ML techniques. The goal is a measurement of the jet transverse momenta, mass, radial moment and jet $p_T D$ in Pb-Pb collisions with the ML background correction and a detailed comparison to existing correction method. In contrast to the area-based approach, ML techniques can learn the mapping of jet properties on a training dataset. For this purpose, a toy model that embeds jets with known true transverse momenta and true jet shape observables in a simulated thermal heavy-ion background is used for training the ML estimators. If needed, such data can be pre-processed by various statistical methods before the regression procedure is carried out (e.g. [4, 5, 6]). Finally, we compare the resolution of the shallow ML estimators to the performance of deep CNN model [7].

2 Dataset

As ML techniques learn the target pattern from the training samples, the quality of the training dataset is essential for the final performance. To create events with particle jets, PYTHIA-generated events are embedded in a thermal background. Then, the true jet properties correspond to the properties of the jets generated by PYTHIA [8] only, while the background consists of all the particles from the thermal model. The toy dataset of 3.17M samples was used, 10% of the dataset was used as the training set, while the remaining 90% was used for the model performance evaluation. In total, 28 features including uncorrected transverse momentum, number of tracks, area-based corrected jet properties, transverse momentum with a relative position for a chosen number of leading tracks, and several jet shape observables were used as the input parameters. Total uncorrected transverse momentum, number of tracks and jet radial moment were observed as the most influential parameters by feature importance method for decision trees and random forests.

3 Estimators

Several ML algorithms have been used for the regression task. Decision trees, random forests and shallow ANN were used as the shallow regression models [9]. For the decision tree and random forest algorithms, the grid search method was used for the hyperparameter optimization. The shallow ANN consists of three hidden layers with 100, 100 and 50 neurons with $\mathrm{ReLU} : \mathbb{R} \to \mathbb{R}^0_+$ activation functions defined for $x \in \mathbb{R}$ as

$$\mathrm{ReLU}(x) = \begin{cases} x & x \geq 0, \\ 0 & \text{otherwise.} \end{cases} \tag{2}$$

The ADAM algorithm was used for network training [10]. Furthermore, a CNN was used for comparison. A custom deep model with 15 1D convolution layers and batch normalization layers [11] was implemented. Similarly to the shallow ANN, the ADAM optimization algorithm and ReLU activation functions were used for the CNN model. We tested additional DL models including recurrent neural networks (RNN) as well, but the CNN estimator showed the most promising performance.

In [3], it has been already shown that it is possible to estimate the true jet transverse momentum with higher performance than with the established methods. In this paper, we extended the one parameter regression and performed a two-parameter regression task with another jet properties, namely jet mass, radial moment and $p_T D$.

4 Comparison of the estimators

In this section, we compare the results for the different estimators on three 2D regression tasks. In addition to the transverse momentum correction, we performed the jet shape correction for jet mass, angularity and $p_T D$. Only samples with $p_T^{true} > 3$ GeV/c were used for the training. This cut-off reduced the number of training samples from 317K to 207K.

4.1 2D regression for p_T and jet mass

Firstly, we present the comparison of the estimators for p_T and jet mass 2-dimensional correction. We plot the residual distribution as a direct measure for the resolution and the overall bias of an estimator. In Figure 1, we compare the residual plots for area-based approach, decision tree, neural network and CNN estimators.

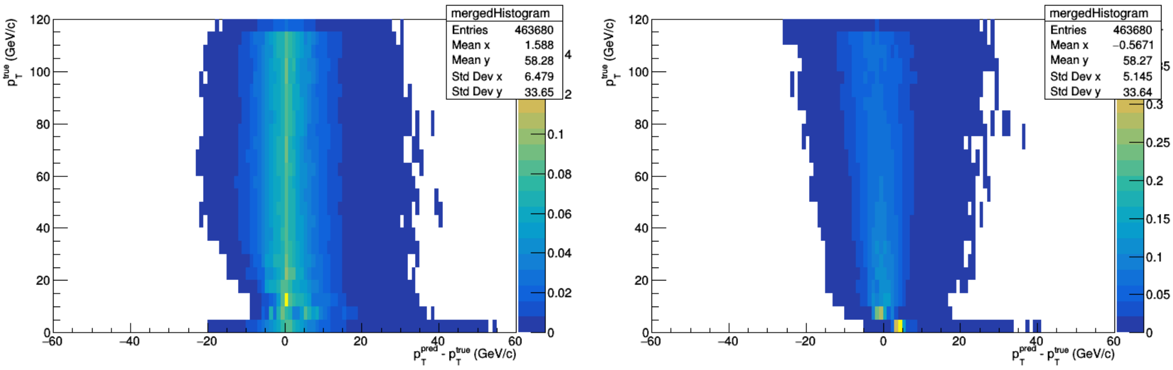

(a) Area-based (b) Decision Tree

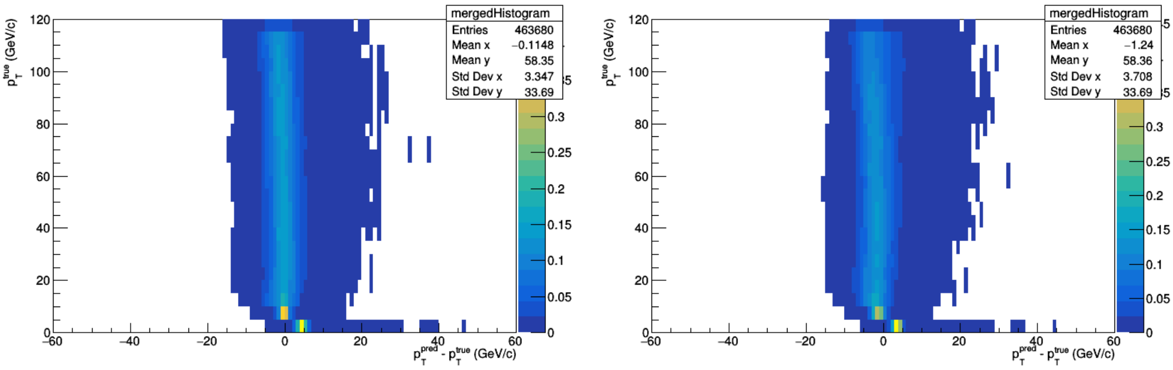

(c) Neural Network (d) CNN

Figure 1: p_T residual plots

It can be seen that the new ANN and CNN background estimators work similarly for different p_T^{true} values. Furthermore, neural network and CNN estimators clearly provide better resolution for p_T estimation compared to the other estimators. However, it is hard to directly compare the resolution between neural network and CNN estimator. Thus, we plot p_T^{true} projections for $60 < p_T^{true} < 80$ GeV/c in Figure 2. The estimated standard deviation for neural network is slightly lower, so the DL model has not improved the performance for p_T correction.

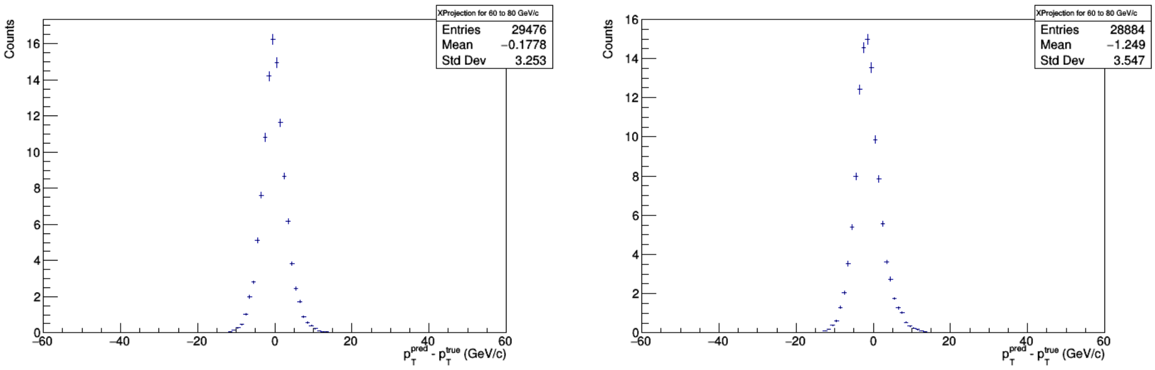

(a) Neural Network (b) CNN

Figure 2: p_T residual plot projections for $60 < p_T^{true} < 80$ GeV/c

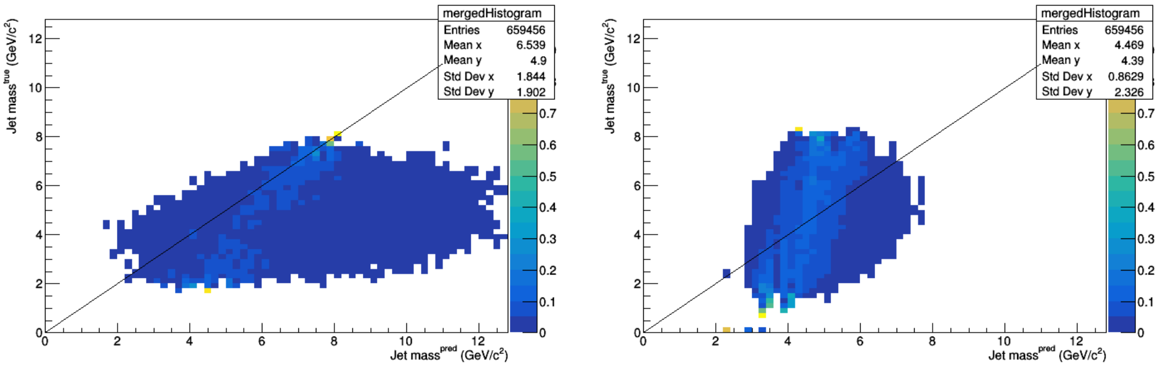

(a) Area-based (b) Decision Tree

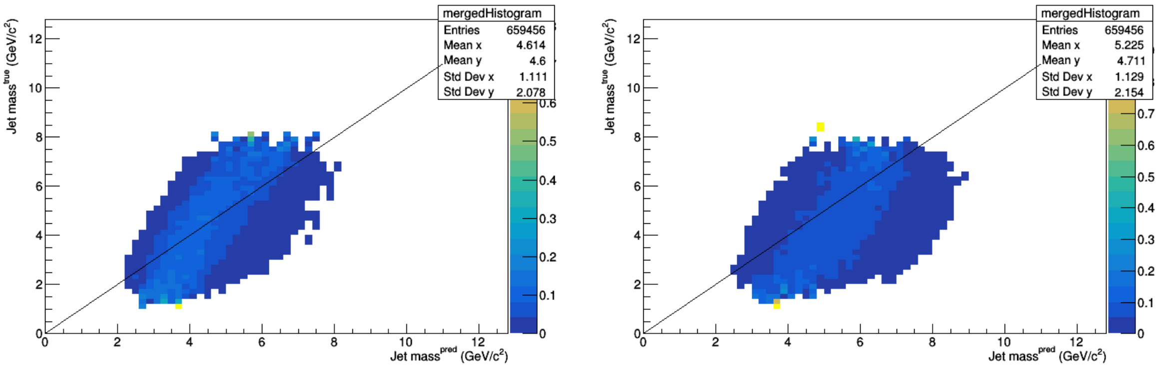

(c) Neural Network (d) CNN

Figure 3: Jet mass true versus predicted plot

In Figure 3, we plot the predicted jet mass versus true jet mass values. It is clearly seen that all the ML estimators exhibit a better performance compared to the area-based correction method. However, the CNN model does not perform observably better than the ANN estimator.

4.2 2D regression for p_T and p_TD

The next step of the project is testing the estimators for 2-dimensional p_T and p_TD correction. In this case, the CNN has turned to be unusable as it did not converge at feasible time. Figure 4 present the performance of the other models depicted in the true versus predicted p_TD plots. The shallow models perform superior compared to the area-based method. We observe promising performance especially for the random forest estimator. The residual plots for depicted correction methods are presented in Figure 5. It is immediately seen that the p_TD residuals are condensed around zero with no significant dependence on p_TD^{true} values for the random forest estimator. This indicates promising potential of ML techniques for p_TD correction.

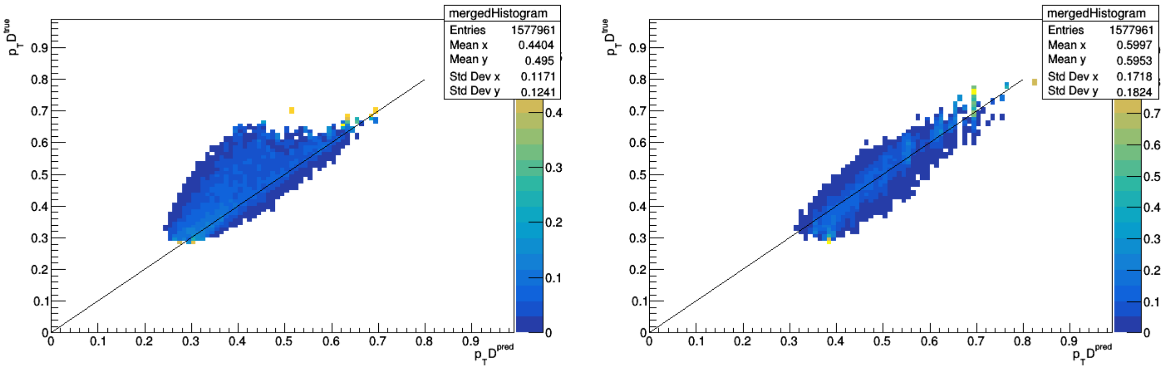

(a) Area-based (b) Decision Tree

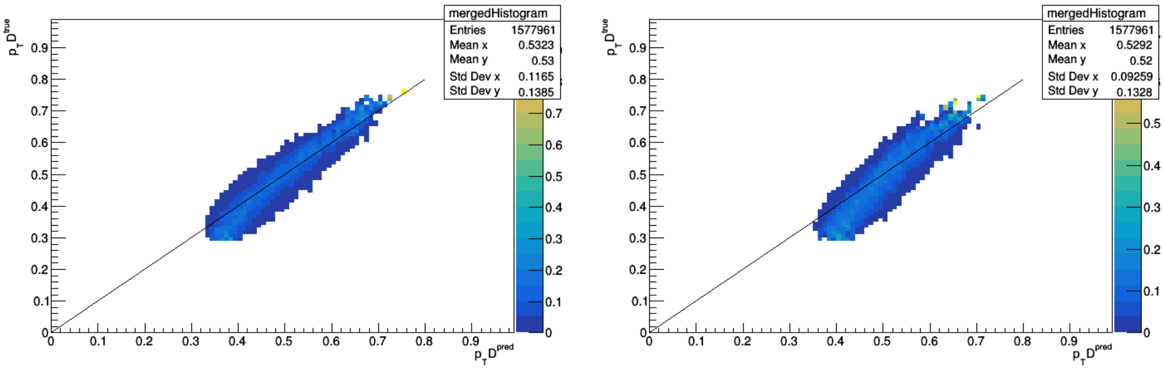

(c) Random Forest (d) Neural Network

Figure 4: p_TD true versus predicted plot

4.3 2D regression for p_T and jet angularity

Finally, we observe the performance of our models on 2-dimensional p_T and jet angularity correction. Similarly to the p_TD correction, the CNN model did not converge and ANN

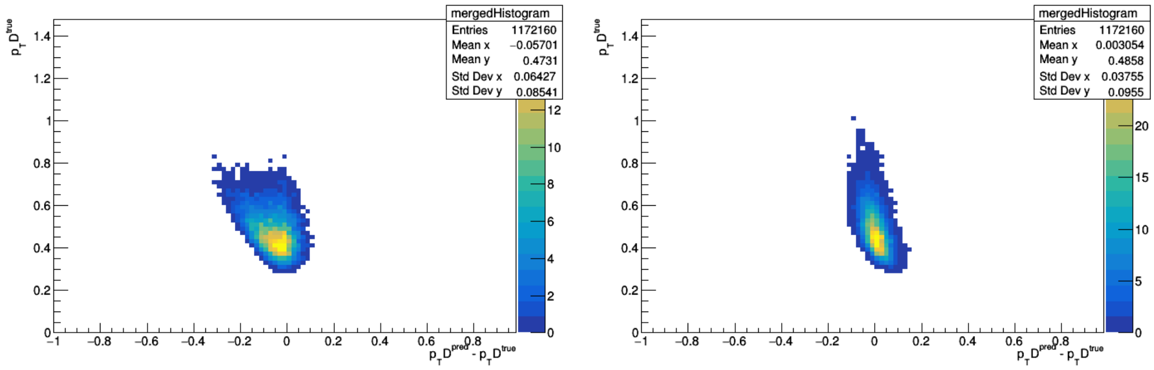

(a) Area-based (b) Random Forest

Figure 5: $p_T D$ residual plot

model performed rather poorly. In Figure 6, we observe that the resolution of the random forest estimator is significantly better compared to the resolution of the ANN model. However, the performance of the ML methods is not as superior as for the previous $p_T D$ correction.

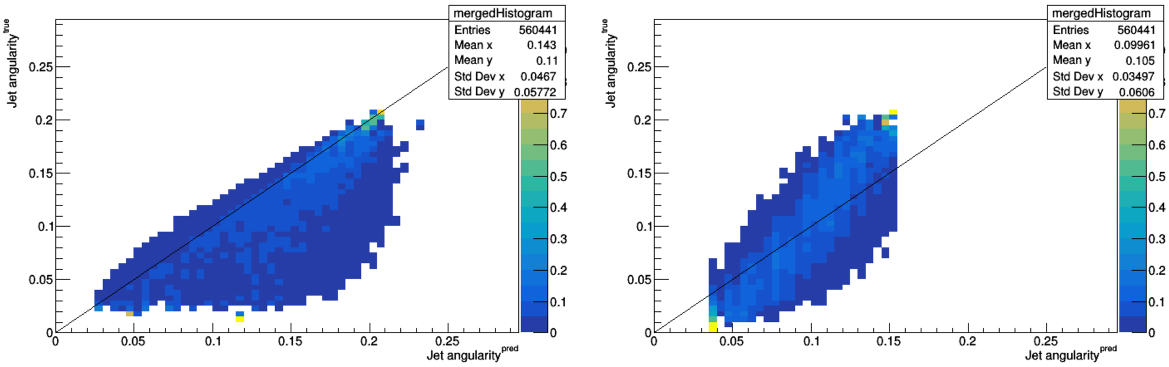

(a) Area-based (b) Decision Tree

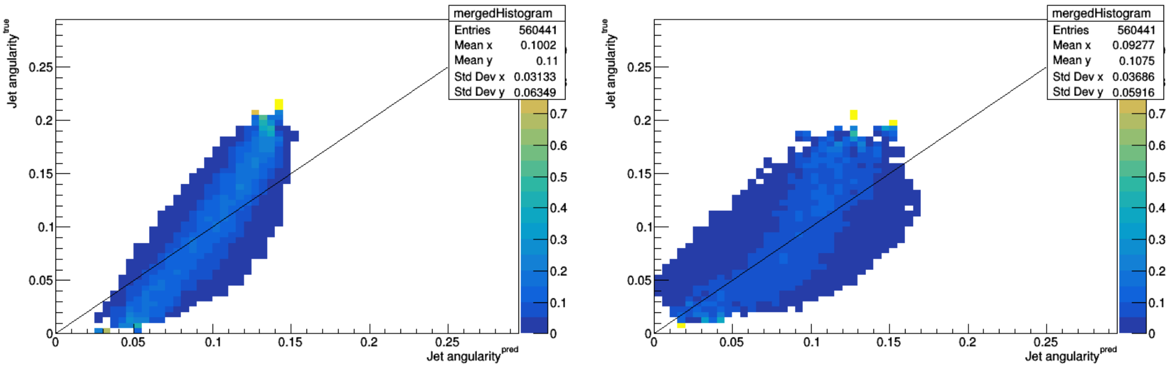

(c) Random Forest (d) Neural Network

Figure 6: Jet angularity true versus predicted plots

5 Summary and conclusion

In this paper, we explored the potential of several ML methods for correction of several jet properties. We defined several ML estimators and compared their performance to the performance of the established area-based approach. Furthermore, we built deep CNN model to explore the possible use of DL models for jet shape correction. For p_T, jet mass, p_TD and angularity, the use of ML techniques has lead to superior performance compared to the established area-based approach. We have observed promising performance when using random forest and neural network estimators. Especially for p_T & p_TD correction, shallow ML techniques lead to huge improvement of resolution and overall bias.

Furthermore, we have not seen any signs of improvement when using DL models. For p_T & jet mass 2D correction, the tested deep CNN model has not outperformed shallow neural network. In addition, it could not be used for p_T & p_TD and p_T & jet angularity correction, as it failed to converge. Thus, the shallow models outperformed the tested DL model for all the correction tasks.

Acknowledgements

These results were supported by the research grants LTT180001, LM2015068, SGS18/188/OHK4/3T/14 (MEYS), and CAAS EF16 019/0000778 (MEYS/EU).

References

[1] M. A. Acero et al. 2018 New constraints on oscillation parameters from ν_e appearance and ν_μ disappearance in the NOvA experiment *PHYSICAL REVIEW D* **98** (3), 2018.

[2] M. A. Acero et al. First measurement of neutrino oscillation parameters using neutrinos and antineutrinos by NOvA *Physical Review Letters* **123** (15), 2019.

[3] R. Haake, C. Loizides. *Machine Learning based jet momentum reconstruction in heavy-ion collisions*. Phys.Rev. C 99, 064904, 2019.

[4] V. Kůs, R. Finger Unifying approach to score based statistical inference in physical sciences *Journal of Physics Conference Series* **1391** (1), 012124, 2019.

[5] M. Stěpánek, J. Franc, V. Kůs. Model based clustering method as a new multivariate technique in high energy physics *Journal of Physics: Conference Series* **490** (012225), 2014.

[6] P. Bouř, V. Kůs, J. Franc. Statistical classification techniques in high energy physics (SDDT algorithm) *J. Phys.: Conf. Series* **738** (012034), 2016.

[7] Z. Qin et al. How Convolutional Neural Networks See the World - A Survey of Convolutional Neural Network Visualisation Methods. *Journal of CoRR*, Vol. 1804.11191, 2018. `http://arxiv.org/abs/1804.11191`.

[8] T. Sjostrand, S. Mrenna, P. Skands *PYTHIA 6.4 Physics and Manual,* JHEP 0605 (2006) 026, `arXiv:hep-ph/0603175[hep-ph]`.

[9] C. M. Bishop. *Neural networks for pattern recognition.* Oxford University Press, 1995.

[10] D. Kingma, J. Ba. *Adam: A method for stochastic optimization,* CoRR (2014). `arXiv:1412.6980`.

[11] S. Ioffe, C. Szegedy. Batch Normalization: Accelerating Deep Network Training by Reducing Internal Covariate Shift. *Proceedings of 2nd International Conference on International Conference on Machine Learning* - Vol. 37, 2015, str. 448-456.

Stochastic and Physical Monitoring Systems
SPMS 2020
September 17 - 21, 2020
Chlum u Třeboně, Czech Republic

Field Crops Classification Using Sentinel-2 Satellite Image Data

Adam Novotný

Department of Mathematics, Faculty of Nuclear Sciences and Physical Engineering, Czech Technical University, Prague, Czech Republic

Email: `novotad2@fjfi.cvut.cz`

Abstract. Sentinel-2 mission, developed and operated by European Space Agency (ESA), is designed to provide high-resolution image data over land and coastal waters, which are further used for a multitude of applications, such as agricultural monitoring. Acquired data by the Sentinel-2 satellite are publicly available under the Copernicus Programme and can be accessed straightforwardly. In addition, we are provided with annotated maps of agricultural fields, which can be used as ground truth data. These maps include the location and additional specification of fields and crops grown on the field. In this paper, we are interested in field crop classification within the specified region. Aforementioned Sentinel-2 satellite image data and field labels are therefore combined to provide a dataset. This dataset can be then utilized by the classifier. For this cause, convolutional neural networks are used, as they have shown outstanding results of image classification over the past years.

Key words: convolutional neural networks; Sentinel-2; field crop classification.

1 Introduction

Machine learning methods, and deep learning methods as their subset, are nowadays used in various fields of study. Moreover, utilization of deep learning techniques is day by day on its rise. With multitude of deep learning algorithms and techniques, it is more than fitting for them to be applied on various types of data. Convolutional neural networks (CNNs), as a deep learning algorithm, have successfully been used for analyzing visual image data over the past years. In our case, satellite imagery can be utilized as a great visual data source. As some fields struggle with a lack of data, satellite imagery does not.

Sentinel-2 satellite, a space mission from the Copernicus Programme developed and operated by European Space Agency (ESA), provide wide-swath, high-resolution, multi-spectral visual image data. In addition to the satellite images, agricultural maps provided by State Agricultural Intervention Fund (SAIF) offer various information about fields and crops grown on the field. Mentioned maps cover the area of the Czech Republic within the year 2018. This can be utilized as a ground truth data for supervised learning.

In this paper, we present a proof of concept of field crop classification based on Sentinel-2 satellite image data and agricultural maps. The procedure combines multi-temporal multi-spectral Sentinel-2 data and geographical location and crop grown on the field.

2 Data Description

The dataset, which is later used to feed into CNN, is created from publicly available Sentinel-2 data and agricultural maps provided by SAIF.

2.1 Sentinel-2

Sentinel-2 mission is composed of two satellites (Sentinel-2A and Sentinel-2B) orbiting Earth in the same orbit and phased by 180°. Single satellite revisits the Equator every ten days so both satellites give a high revisit frequency of 5 days at the Equator. This frequency is even shortened for higher latitudes. The mission land surfaces from latitude 56° south to 84° north, coastal waters, and all of the Mediterranean Sea.

Optical sensor gives 13 bands ranging from visible spectrum to near infrared (NIR) and short wave infrared (SWIR). Four of the bands have the resolution of 10 meters, six bands of 20 meters and three bands of 60 meters [1]. The full specification of spectral bands can be seen in the figure 1. In addition to the 13 bands, another indices, which use the bands, can be derived, such as normalized difference water index (NDWI) or normalized difference vegetation index (NDVI) etc. to obtain additional information.

Figure 1: Thirteen spectral bands of Sentinel-2 satellite [1].

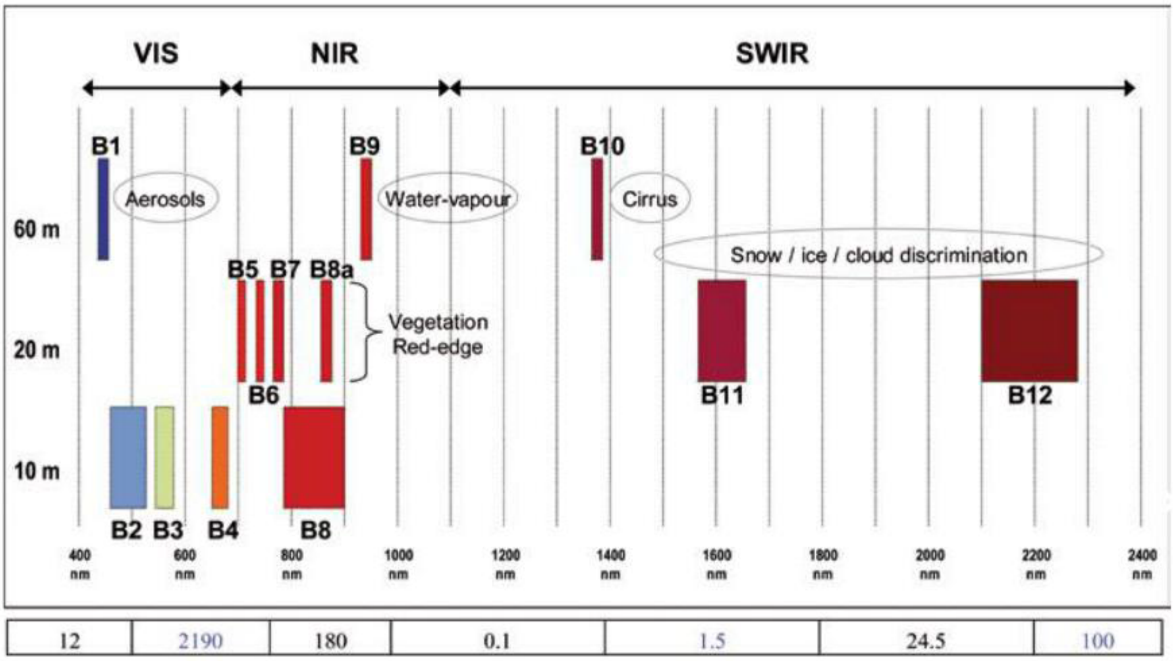

The Sentinel-2 satellite images come in three different levels of pre-processing. Level 2-A offers data in form of *tiles* with atmospheric corrections in form of bottom-of-atmosphere reflectance in cartographic projection. Each tile covers the area of 100 × 100 km^2 and is octorectified into UTM/WGS84 projection [1]. The Level 2-A also contains cloud masks. The area of Czech Republic is covered by more than ten tiles.

The Sentinel data can be accessed and downloaded via the Copernicus APIs. The OpenSearch API gives information about each tile, including dates. This is later utilized to download tiles by OData API. In addition to the Sentinel-2 images, the framework can be easily extended to include both Sentinel-1 and Sentinel-3 images.

2.2 Agricultural data

We are provided with almost 600 thousand samples of fields in Esri shapefile format. These fields cover the area of the Czech Republic and were obtained in 2018. Each field is annotated with its own metadata which includes unique ID, geographical polygon, bounding box and area in UTM/WGS84 projection and crop grown on the field.

The overall number of crops grown over the area is 14, namely annual forage crops, annual fruit and vegetable, flax and hemp, hopyards, maize, other crops, permanent fruit, permanent grassland, rapeseed, sugar beat, summer cereals, vineyards, winter cereals and not classified. The counts of each crop can be seen in the figure 2.

Figure 2: Counts of crops grown in the Czech Republic in 2018.

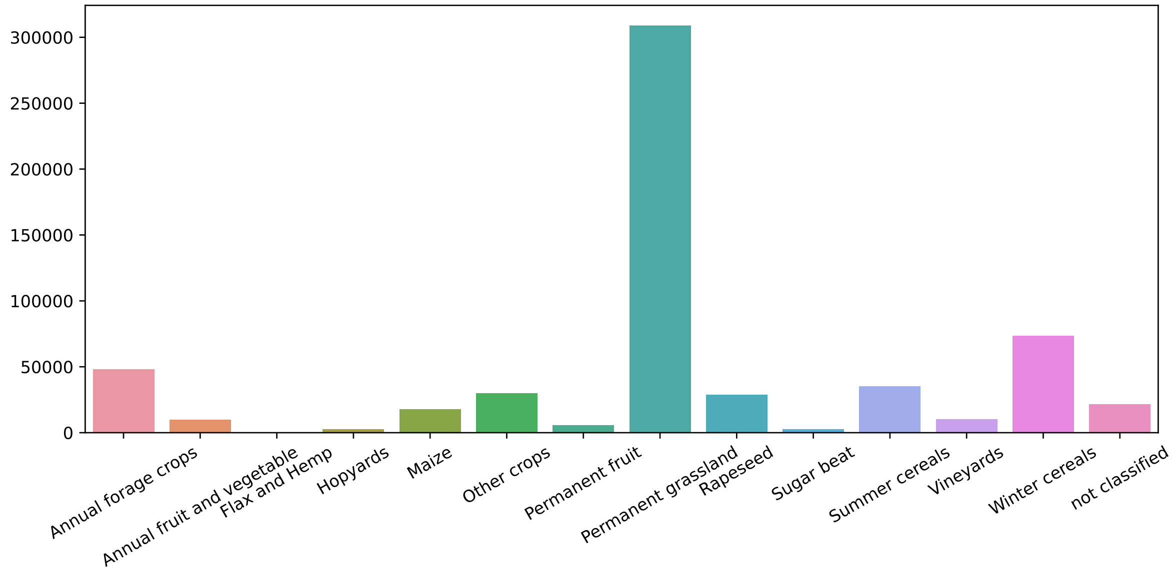

2.3 Dataset

Combined dataset constists of 593,787 multi-temporal (up to 36 timestamps per year) multi-spectral (13 + additional indices) images with different size, as each field has different height and width. If needed, such data can be pre-processed by various statistical methods (e.g. [2])

3 Convolutional Neural Network

The created dataset can be utilized by CNNs. The goal is multi-class classification into 14 classes. For the training of the CNN, categorical cross-entropy loss function is used. As the dataset is quite unbalanced, this problem needs to be addressed. This can be achieved either primarily by weighing the loss function (based on counts) or secondarily by even excluding some classes (e.g. flax and hops class has only hundreds samples). As the dataset is quite large, on-the-fly generator during the training is incorporated into training. This is accompanied by data augmentation.

In order to prevent overtraining, the dataset is further divided into training, validation and test set. Metrics observed both during validation and testing phase are accuracy, confusion matrix, receiver operating curve (ROC) and area under ROC (AUC).

For all of the mentioned, Python 3.6.8 within the Tensorflow 2.3.0 framework deployed on GPUs are used.

Early results of classification are quite promising. The initial classification was performed on only one timestamp (in August 2018) and on narrowed dataset consisting of only 40 thousand images. The used architecture is ResNet18. The test accuracy was over 60 % and test AUC 80 %.

4 Conclusion

In this paper, we presented a proof of study of field crop classification based on two data sources, namely multi-temporal multi-spectral Sentinel-2 satellite image data and annotated maps of Czech agricultural fields in 2018 by SAIF. The initial results, which are expected to be improved by far, were measured by test accuracy and AUC, yielding over 60 % and 80 % respectively.

Acknowledgements

This work was supported by the grant SGS18/188/OHK4/3T/14 (MEYS) and CAAS EF16 019/0000778 (MEYS/EU).

References

[1] A. Gatti, A. Bertolini, Sentinel-2 products specification document, available online (accessed September 2, 2020) `https://sentinel.esa.int/documents/247904/349490/S2_MSI_Product_Specification.pdf`, (2015).

[2] V. Kůs, R. Finger, Unifying approach to score based statistical inference in physical sciences, *Journal of Physics Conference Series* **1391** (1), 012124, 2019.

Stochastic and Physical Monitoring Systems
SPMS 2020
September 17 - 21, 2020
Chlum u Třeboně, Czech Republic

Real Options Valuation: A Dynamic Programming Approach

Filip Rolenec

Department of Mathematics, FNSPE, Czech Technical University in Prague, Czech Republic

Email: `rolenfil@fjfi.cvut.cz`

Abstract. Investment opportunities are currently valuated via metrics and algorithms formed by the economical theory. The majority of investors still values projects with the net present value (NPV) method, which takes into account the time value of money and gives solid results for simple projects with minimal requirements on mathematical skills. More complicated projects, which are in this contribution thought of as projects with a substantial degree of inner uncertainty and with an existence of further managerial decisions, can be valuated by the real options analysis (ROA). This method comes from an imperfect analogy to financial option valuation and it recognizes the value of the ability to change the course of a given project.

My contribution presents a new valuation framework for projects, which are understood as stochastic decision problems. This framework incorporates the NPV and ROA methods, relaxes their assumptions and allows for decades of research in the field of stochastic decision theory (SDT) to be used. The main contributions of the new framework are: ability to incorporate multiple sources of uncertainty, usage of any distribution for uncertainty modeling, ability to conveniently incorporate Bayesian learning, ability to model user's approach to risk and ability to model any type and number of managerial actions.

The new framework significantly expands the class of projects that can be reasonably valuated and can be understood as a unification of project valuation in business management.

Key words: Real Option Analysis, Stochastic Decision Theory, Time Value of Money, Risk Aversion, Black-Scholes Model, Power Industry, Approximate Dynamic Programming.

1 Introduction

Derivative market as an idea of hedging and taking risk for a fee can be traced back thousands of years back into the human history [3]. Financial options as a part of the derivative market allow the holder to buy (or sell) given asset in the future for a predetermined price. The holder of the option can decide to use his option (exercise it) or not to, based on the circumstances (predominantly if the price evolved in a favorable way or not).

The ideas of option trading appear as early as the 17th century in Netherlands [4]. However, first publications about the logic of their valuation appear with the beginning of the early 20th century with Bachelier [5] and Bronzin [6]. Later, in the 1970's a new wave of option valuation research emerged, culminating in the Nobel-prize-winning Black-Scholes valuation algorithm [7] (BSM), which is a standard option valuation tool today.

The researcher's focus on the ideas about option valuation resonated within the community and lead to the concept of Real Option Analysis (ROA) for project valuation, term coined by Stewart Myers in 1977. The ability of buying and selling an asset in the future has value, thus as analogy, having an option to invest in a project now or later (timing option) has also some value.

The basic logic of simple options in project management was improved through the decades and many articles and books were published on the topic of ROA since.

When studying the current state of ROA, one realizes that there exist three classes of authors that interpret the logic of ROA in various level of analogy with the BSM model. First group, which I call *Economical textbook authors* (i.e. [10]) presents ROA as a clean analogy with the financial options. Second group, where I consider Guthrie [8] to be the most influential, focuses on introduction of new possible options within the project while keeping the core of BSM model, namely the assumption of non-existence of arbitrage. The third class, to which also the father of the name ROA (Myers) belongs to, understands ROA as a purely philosophical idea about the project management. Third class recognizes that options have value, but does not elaborate on how to compute it.

In this contribution, I will be focusing on the second class of authors, where my main inspiration is Graeme Guthrie [8].

When a person that is educated in the theory of decision making under uncertainty reads the ideas of ROA, it is hard to not realize the potential applicability of the stochastic decision theory (SDT) on the outlined problems in ROA publications.

In this contribution I want to argue that problems and ideas outlined in books of ROA can be interpreted in terms of SDT. This interpretation relaxes some ROA assumptions and allows for solving more complex problems while preserving the economical truths of a given project.

The newly developed project valuation technique is demonstrated on the problem of gas power plant valuation. The actual computation is due to its complexity computed by the value iteration algorithm, coming from the Approximate Dynamic Programming (ADP) theory.

2 ROA in SDT

The core of ROA is the idea that options (possible future action) have value. The uncertainty that encompasses all ventures will result in some realizations, determining its realized profitability. The ability to counter negative realizations increases the expected realized profitability by lowering the losses, while the ability to exploit the positive realizations increases the profit when "good times" are realized.

When a scholar that is educated in the theory of decision making under uncertainty reads the publications about ROA, it is hard to not see the similarities. The authors of stochastic decision theory like to point out, that basically every human interaction with the environment can be understood as decision making under uncertainty, however, I argue, that SDT as a framework fits for ROA problems neatly.

Two publications that this contribution is inspired by are Graeme Gutrhie - Real Option Analysis [8] and Alexander Vollert - A Stochastic Control Framework for Real Options in Strategic Evaluation [11]. Guthrie presents a well structured list of different options project might have and offers a reasoning behind probability modeling by binomial trees, which is coming from the law of one price from economical theory. Vollert then goes deep into stochastic differential equations and presents new structures for thinking about real options.

Mr. Guthrie and his approach is well explained and build on a firm ground, however it is not build for a complex problems, which he himself acknowledges. I also believe that the findings of Vollert are presented in much more complex mathematical language than the majority of practitioners is able to understand.

These two statements prepare the ground for the reason behind this contribution of mine. I strive to bring a valuation algorithm that allows for solving a rather complex problems, with unified structure, but with simple steps, that can be understood by the managers, not necessarily educated in deep mathematics.

I also want to accent the importance of respecting the economical truths important for project valuation, namely the time value of money and the risk aversion of investors.

2.1 ROA in terms of SDT

The Real Option Analysis focuses on valuation of projects with high uncertainty and possible management interventions. I argue that the structure of Markov decision processes (MDPs) is ideal for such modeling.

Definition 1 (Markov Decision Process) *Markov decision process is a framework that can be represented by 3 sets and two functions:*

- *Set of time epochs -* $\mathbf{T}$*;*
- *Set of states -* $\mathbf{S}$*;*[1]
- *Set of actions -* $\mathbf{A}$*;*[2]
- *Reward function of transition from one state to another -* $r(s_t|a_t, s_{t-1})$*;*
- *Transition probabilities governing the transitions from one state to another -* $p(s_t|a_t, s_{t-1})$.

Options are in this structure represented by the action set $\mathbf{A}$, and as a result there is no need for distinction like "time option" or "scale option".

---

[1] Possibly conditioned on the time epoch.

[2] Possibly conditioned on the state.

The value of a project is then determined by the value function in the current (zero) state of the project. This value can be in theory computed by the iterative process starting at the problem horizon with the Bellman equation:

$$V(s_{t-1}) = \max_{a_t \in \mathbf{A}} \sum_{s_t \in \mathbf{S}} p(s_t|a_t, s_{t-1})[r(s_t|a_t, s_{t-1}) + V(s_t)]. \tag{1}$$

The problem with Bellman equation is the computation complexity, where we require $|\mathbf{T}| * |\mathbf{S}| * |\mathbf{A}| * |\mathbf{S}|$ computations, where the cardinality of state set $|\mathbf{S}|$ is usually large. Another related problem is that this approach needs to assume discrete state spaces. Continuous spaces can be made discrete but that brings us back to the problem with computational complexity.

The problem of complexity of dynamic programming is known as a "Curse of dimensionality" [9] and it is approached with the theory of ADP.

2.2 Approximate dynamic programming

The theory of ADP copes with the complexity problem of classical dynamic programming by accepting that the value functions, or evaluation of policies cannot be computed exactly, but can be only approximated.

ADP can be divided into two classes, policy and value iterations. We will be focusing on value iteration, since I believe it fits more the project valuation problems.

The idea of value iteration starts with having some value function estimate which is updated based on the samples of possible future states.

In this contribution we focus on the ADP algorithm, where we model the value function in each time epoch v_t as a linear model with basis functions $\phi_{i,t}$ and parameters $\theta_{i,t}$:

$$v_t(s) = \sum_i \theta_{i,t} \cdot \phi_{i,t}(s), \tag{2}$$

where the basis functions reflect some heuristically important value of each state. For example the difference between price of power and sum of gas and CO2 price, or indicator function of being and not being in debt.

The update of v_t then unfolds as follows:

- Sample of states in time t is generated;
- In each of these states the optimal action is chosen (based also on the approximation of the following value function v_{t+1});
- The action is actually taken, reward is obtained and the pair s_t - $r(s_{t+1})$ is saved.
- Based on all state-reward pairs a fit of linear model is made, resulting in the new parameters $\theta_{i,t}$.

By updating the value functions in different time epochs (this contribution uses updating from the horizon) we get more and more precise values to the actual value function representing the expected reward, in our case the cash equivalent in time epoch 0.

2.3 Preserving economical truths

While creating the algorithm for project valuation one cannot forget the objective economical truths that need to hold if this algorithm has the ambition to be ever used by practitioners. In other words the concepts of time value of money and risk aversion of investors needs to be respected. Luckily, the SDT theory is prepared for the interpretation of both of them.

The time value of money can be easily approached by the introduction of a discount factor (in SDT denoted as γ) if we discount the future cash flow with the same interest rate for money that we borrow as for those we earn in surplus.

This contribution goes a step further and discounts the cash flow with the rate given by the current state of debt or cash surplus of the company.

The second economical truth is the risk aversion of investors. Investors are usually not driven by the clear expected values as defined in mathematics as was shown multiple times in studies like [12]. The SDT is again a step ahead an offers an alternation of the search for the maximal reward in Bellman equation. It is called utility theory and instead of maximizing the expected reward, we are maximizing the expected utility with each optimal action choice.

The problem of obtaining the transformation function that pairs rewards with utility is out of the scope of this contribution and it is discussed in [9].

3 Valuation of gas power plant

In the last section of this contribution I would like to illustrate the application of the introduced framework on a real project valuation problem. Inspired by Graeme Guthrie and with the gained knowledge from the power industry, I would like to value a gas power plant.

The current price of gas, CO2 allowances and electric power in EUR are: 23, 9 and 40, after unit normalization and assumption of some reasonable power plant efficiency. For each MW of installed capacity there is a 3 EUR maintenance cost (lowered to 1 EUR when the plant is mothballed). There is a possibility to build up to two 200MW blocks of the power plant, where each costs 65M EUR. The cost of mothballing is 1M EUR.

One time epoch is set to be one month and the lifespan of the power plant is assumed to be 25 years.

There are 6 different actions in total, some of which are restricted:

- *Do nothing* - available in all times and states. Does not change the power plant state.
- *Run* - Run the installed capacity. Available when some capacity has already been built.
- *Run and build* - Run what is installed and build a new stage. Available only when the capacity is 200MW.
- *Do not run and build* - Do not run and build new stage. Unexpected behavior from a heuristic perspective. Not allowed with 400MW installed capacity.

- *Mothball* - Mothball the plant. Not available when already mothballed or when there is nothing to mothball.
- *Sell* - Sell the power plant. Allowed only when there is some installed capacity to sell.

These actions represent the following option types as described by Guthrie:

- *Timing option* - ability to postpone the investment.
- *Switching option* - I can run the plant or not. I can mothball the plant.
- *Scaling option* - I can build more than one block.
- *Abandonment option* - I can sell the plant.

The prices of power, CO2 and gas are understood as continuous variables and they are assumed to follow a lognormal random process with volatilities chosen as educated guess from looking at the actual market prices.

Furthermore, to show how is the new model able to incorporate multiple sources of uncertainty, we are adding a variable representing **government policy** that is supposed to reflect the subsidies for the renewable energy. With higher support of renewable energy the volatility on the power market rises.

This government policy variable has 5 levels, ranging from no support to maximal support and each new stage increases the volatility of power prices by 20%.

By using the ADP, one does not obtain an optimal strategy, only the parameters of the individual value functions.

In the end of this contribution, I would like to present the results of a Monte Carlo simulation where in both cases the strategy follows the approximation of optimal decision making based on the value function representation. All actions listed above are allowed in the first case, whereas the second simulation does not allow the plant to stay idle, whet it has some installed capacity.

Acknowledgements

I would like to express a great appreciation for the work of my supervisor Ing. Rudolf Kulhavý, DrSc. and his guidance through this research.

References

[1] F. Mittelbach et al. *The LaTeX Companion, 2nd ed.* Addison-Wesley, 2004.

[2] B. V. Gnedenko. Sur la distribution limite du terme maximum d'une série aléatoire. *Ann. Math.*, **44**, 423–453, 1943.

[3] Ernst Juerg Weber. *A Short History of Derivative Security Markets*, pages 431–466. Springer Berlin Heidelberg, Berlin, Heidelberg, 2009.

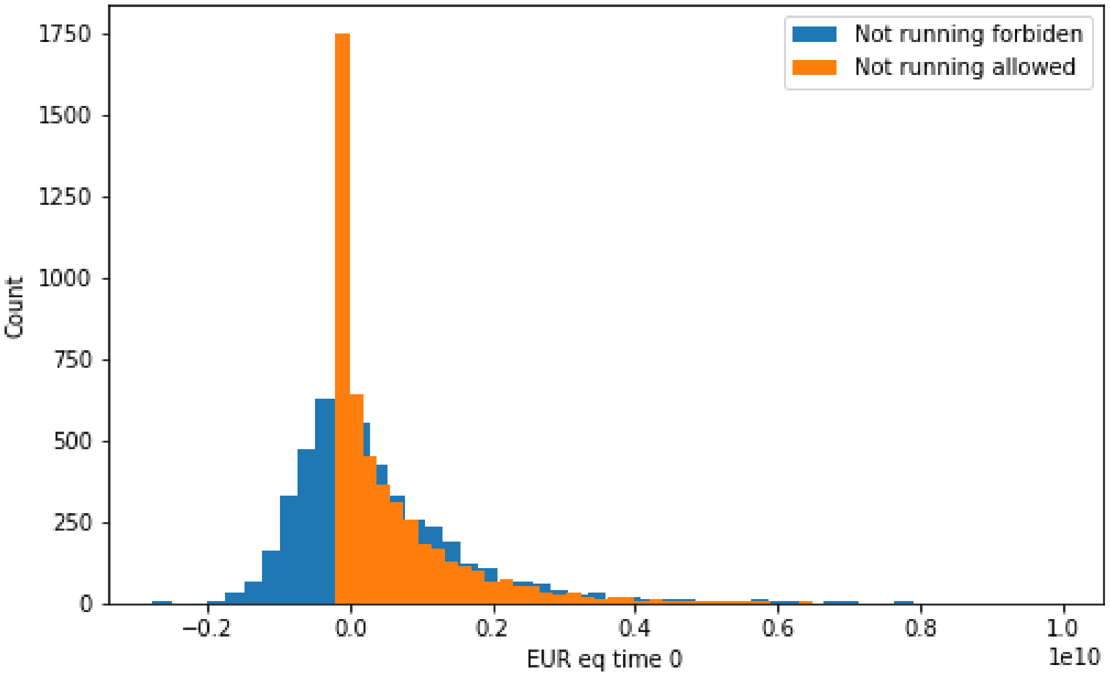

Figure 1: Distribution of realized profits when the ability of not running the plant exists and not.

[4] J. De La Vega and H. Kellenbenz. *Confusion de Confusiones [1688]: Portions Descriptive of the Amsterdam Stock Exchange.* Martino Publishing, 1688.

[5] Louis Bachelier. Théorie de la spéculation. *Annales Scientifiques de L'Ecole Normale Supérieure*, 17:21–88, 1900. Reprinted in P. H. Cootner (ed), 1964, The Random Character of Stock Market Prices, Cambridge, Mass. MIT Press.

[6] V. Bronzin. *Theorie der Prämiengeschäfte.* Verlag Franz Deticke, 1908.

[7] Fischer Black and Myron Scholes. The pricing of options and corporate liabilities. *Journal of Political Economy*, 81(3):637–654, 1973.

[8] G. Guthrie. *Real Options in Theory and Practice.* Financial Management Association Survey and Synthesis. Oxford University Press, 2009.

[9] S. Bacci and B. Chiandotto. *Introduction to Statistical Decision Theory: Utility Theory and Causal Analysis.* CRC Press, 2019.

[10] J. Berk and P. DeMarzo. *Corporate Finance.* Pearson, 2014.

[11] A. Vollert. *A Stochastic Control Framework for Real Options in Strategic Evaluation.* Birkhäuser Boston, 2012.

[12] Charles A Holt and Susan K Laury. Risk aversion and incentive effects: New data without order effects. *American Economic Review*, 95(3):902–912, 2005.

Stochastic and Physical Monitoring Systems
SPMS 2021
June 24 - 28, 2021
Malá Skála, Czech Republic

Blind Image Deconvolution Using Stochastic Variational Inference

Antonie Brožová[1], Václav Šmídl[2]

[1] Department of Mathematics, FNSPE, Czech Technical University in Prague, Czech Republic
[2] ÚTIA, Academy of Sciences of the Czech Republic, Prague, Czech Republic

Email: `brozoant@fjfi.cvut.cz`

Abstract. Blind image deconvolution aims at recovering sharp image from a blurred one while the blur is unknown. It is a highly ill-posed problem requiring proper regularization, and variational Bayesian inference is often used to tackle it. Hierarchical Bayesian models can represent well both sharp image and blur, and variational Bayes can be used to approximate posterior distributions. While Variational Bayes offers easy optimization, it is very restrictive when it comes to the choice of prior distributions. For example, if the blur is spatially variant, finding a solution under this framework would be very complicated. Higher flexibility could be achieved via direct numerical optimization of evidence lower bound, which does not require the distributions to be from the conjugate system. These two methods - Variational Bayes and ELBO optimization - will be compared in this paper.

Key words: blind image deconvolution, variational Bayes, ELBO, Vadam, variational inference.

1 Introduction

Images can be degraded in many ways, for example by blurring, noise or low resolution. In this paper we focus on blurring which may be caused by relative motion of a camera and a scene, turbulence in the atmosphere or wrong focus. Assuming spatially invariant blur, the blurred image can be represented as a convolution of a blur kernel $\boldsymbol{k}$ and an underlying sharp image $\boldsymbol{x}$

$$\boldsymbol{d} = \boldsymbol{k} \circledast \boldsymbol{x} + \boldsymbol{n}, \tag{1}$$

where $\boldsymbol{n}$ is noise. The deconvolution is basically an inverse operation to convolution with the aim to obtain the sharp image. The deconvolution is called blind when not only the sharp image but also the blur is unknown. The task is then to minimize $||\boldsymbol{d} - \boldsymbol{k} \circledast \boldsymbol{x}||$ with respect to both $\boldsymbol{x}$ and $\boldsymbol{k}$. The problem is highly ill-posed, so further regularization is necessary. The Bayesian approach is based on prior information which makes it a suitable tool for this task.

In the first section, variational Bayes (VB) will be introduced, together with the evidence lower bound and its optimization. Consequently, a hierarchical model representing the blurred image will be constructed and three algorithms for blind deconvolution will be presented, where one of them uses Vadam optimiser. Lastly, these three algorithms will be compared on a test image with gaussian blur.

2 Method

The problem of blind image deconvolution is highly ill-posed and prior information is needed to successfully recover the underlying sharp image. The two most common Bayesian approaches used for blind image deconvolution are MAP (maximum a posteriori) approach and variational Bayes method. The first mentioned was deeply studied by Levin et al. in, for example, [1]. Although it is often used, it usually requires some ad hoc steps to find the right solution.

Variational Bayes inference uses an approximation of posterior which makes the problem tractable for common distributions. Fergus et al. suggested to use this approach for blind image deconvolution in [2] in the same year with Molina et al. [3]. A brief explanation of this method follows.

The variational Bayes method is based on the Bayes theorem

$$p(\boldsymbol{x},\boldsymbol{k}|\boldsymbol{d}) = \frac{p(\boldsymbol{d}|\boldsymbol{x},\boldsymbol{k})p(\boldsymbol{x},\boldsymbol{k})}{p(\boldsymbol{d})},$$

where $p(\boldsymbol{x},\boldsymbol{k}|\boldsymbol{d})$ is a posterior distribution, $p(\boldsymbol{x},\boldsymbol{k}) = p(\boldsymbol{x})p(\boldsymbol{k})$ is a prior distribution and $p(\boldsymbol{d}|\boldsymbol{x},\boldsymbol{k})$ is a distribution of the original image, therefore has the same form as the distribution of the noise from (1). If we assign prior to each variable and get the joint posterior distribution, marginalization is needed in order to find the estimates of the sharp image and the blur kernel. Variational Bayes overcomes the marginalization by approximating the posterior by $q(\boldsymbol{x},\boldsymbol{k}|\boldsymbol{d})$ for which holds

$$q(\boldsymbol{x},\boldsymbol{k}|\boldsymbol{d}) = q(\boldsymbol{x}|\boldsymbol{d})q(\boldsymbol{k}|\boldsymbol{d}). \tag{2}$$

The model is usually hierarchical, and it is assumed that each random variable has the property (2). Let denote $\boldsymbol{\theta}$ all random variables in the model. Kullback-Leibler (KL) divergence of q from p is defined as

$$KL\left(q(\boldsymbol{\theta}|\boldsymbol{d}) \parallel p(\boldsymbol{\theta}|\boldsymbol{d})\right) = \mathbb{E}_{q(\boldsymbol{\theta}|\boldsymbol{d})}\left[\ln \frac{q(\boldsymbol{\theta}|\boldsymbol{d})}{p(\boldsymbol{\theta}|\boldsymbol{d})}\right], \tag{3}$$

where $\mathbb{E}_{q(\boldsymbol{\theta}|\boldsymbol{d})}\left[.\right]$ denotes expected value with respect to $q(\boldsymbol{\theta}|\boldsymbol{d})$. Then, approximations of the posteriors that minimize KL divergence from the real posteriors are of following form

$$q(\boldsymbol{\theta_i}|\boldsymbol{d}) \propto \exp\left[\mathbb{E}_{q(\boldsymbol{\theta}_{\setminus i}|\boldsymbol{d})}\left[\ln p(\boldsymbol{\theta},\boldsymbol{d})\right]\right],$$

where $\boldsymbol{\theta}_{\setminus i}$ means all variables in $\boldsymbol{\theta}$ except for i-th one. When the priors are chosen to be conjugate, forms of the approximations of posteriors are known and the only task left is to find values of parameters of the distributions. When it is not the case, another approach is usually required.

Lets rewrite KL divergence into another form

$$KL(q(\boldsymbol{\theta}|\boldsymbol{d})||p(\boldsymbol{\theta}|\boldsymbol{d})) = \int q(\boldsymbol{\theta}|\boldsymbol{d}) \ln \left[\frac{q(\boldsymbol{\theta}|\boldsymbol{d})}{p(\boldsymbol{\theta}, \boldsymbol{d})}\right] \mathrm{d}\boldsymbol{\theta} + \ln p(\boldsymbol{d}) = -\mathcal{L} + \ln p(\boldsymbol{d}). \tag{4}$$

KL divergence is always non-negative, therefore, $\mathcal{L}$ in equation (4) is lower bound on $\ln p(\boldsymbol{d})$. It is called evidence lower bound (ELBO). The goal of VB is to minimize the KL divergence which is equivalent to maximizing ELBO. From (4) we can see that

$$\mathcal{L} = \mathbb{E}_{q(\boldsymbol{\theta}|\boldsymbol{d})} \left[\ln q(\boldsymbol{\theta}|\boldsymbol{d}) - \ln p(\boldsymbol{\theta}, \boldsymbol{d})\right]. \tag{5}$$

Negative value of (5) can be minimized, for example, via stochastic gradient descent, but it requires the expectations w.r.t. $q(\boldsymbol{\theta}|\boldsymbol{d})$ to be known in closed forms so that it is possible to take their derivatives. When it is not the case, some expected values can be approximated with a reparametrization trick as was suggested for variational autoencoders in [9]. Let's say, that it is hard to find an expected value of some function $f(\theta_i)$ w.r.t. $q(\theta_i|\boldsymbol{d})$ and that it is possible to reparametrize $\theta_i = g(\boldsymbol{m}, \epsilon)$, where $\boldsymbol{m}$ are parameters of $q(\theta_i|\boldsymbol{d})$ and ϵ is a random variable with distribution $p(\epsilon)$, which is easy to draw samples from. Then

$$\nabla_{\boldsymbol{m}} \mathbb{E}_{q(\theta_i|\boldsymbol{d})} \left[f(\theta_i)\right] = \nabla_{\boldsymbol{m}} \mathbb{E}_{p(\epsilon)} \left[f(g(\boldsymbol{m}, \epsilon))\right] \approx \frac{1}{L} \sum_{l=1}^{L} \nabla_{\boldsymbol{m}} f(g(\boldsymbol{m}, \epsilon^l)),$$

where ∇_m is gradient operator with respect to $\boldsymbol{m}$ and ϵ^l is l-th sample of ϵ.

The strength of ELBO optimization lies the fact that it can be used for any choice of approximation of posterior and, therefore, it could be more flexible than VB approximation.

2.1 Priors

The choice of priors for blind image deconvolution is crucial, especially when it comes to an image prior. Wipf and Zhang in [4] argue that it is more important for the image prior to discriminate the no-blur solution (i.e. sharp image is estimated as the blurred one and kernel as δ-function) than to reflect the real image statistics. An image is usually assumed to be smooth, therefore, models promoting sparsity in its gradients ([5], [6]) are used.

It is favourable to rewrite (1) in the matrix form

$$\boldsymbol{k} \circledast \boldsymbol{x} + \boldsymbol{n} = \boldsymbol{K}\boldsymbol{x} + \boldsymbol{n} = \boldsymbol{X}\boldsymbol{k} + \boldsymbol{n},$$

where $\boldsymbol{x}$ is vectorized image of size $n \times p$, $\boldsymbol{k}$ is vectorized blurring kernel of size $2s+1 \times 2s+1$, $\boldsymbol{K}$ and $\boldsymbol{X}$ are convolution matrices in block Toeplitz form, where blocks are Toeplitz matrices, constructed from $\boldsymbol{k}$ and $\boldsymbol{x}$, respectively. The distribution of noise is assumed to be normal with zero mean and precision matrix $\omega\mathbb{I}$, where $\mathbb{I}$ is an identity matrix and ω is a hyperparameter, therefore, distribution of observation $\boldsymbol{d}$ is normal with mean $\boldsymbol{K}\boldsymbol{x}$ and each pixel has precision ω. The prior distribution of ω was chosen to be gamma with shape γ_0 and rate η_0.

ARD (Automatic Relevance Determination) model [5] was chosen for the image prior. The image is assumed to be piecewise-constant, which is represented by assumption of sparse gradients in the image. The ARD model achieves sparsity by combination of normal and gamma distribution

$$\begin{aligned} \nabla \boldsymbol{x} | \boldsymbol{\tau}_x &\sim \prod_i \mathcal{N}\left(0, \tau_{xi}^{-1}\right), \\ \tau_{xi} &\sim \mathcal{G}\left(\alpha_{x0}, \beta_{x0}\right), \end{aligned}$$

where ∇ denotes derivative operator, i.e. $\nabla \boldsymbol{x}$ is a vector of horizontal and vertical differences, and τ_{xi} is precision of i-th difference in image. This model is also called scale mixture of gaussians which is considered to be super-gaussian prior [7].

The blur kernel's prior distribution was chosen to be normal with common precision for all its pixels

$$\begin{aligned} \boldsymbol{k} | \tau_k &\sim \mathcal{N}\left(\boldsymbol{0}, \tau_k^{-1} \mathbb{I}\right), \\ \tau_k &\sim \mathcal{G}\left(\alpha_{k0}, \beta_{k0}\right). \end{aligned}$$

2.2 Posteriors

The combination of gamma and normal distributions makes it extremely easy to infer the posterior distributions. As they are conjugate, the posteriors of $\boldsymbol{x}$ and $\boldsymbol{k}$ are normal

$$\begin{aligned} q(\boldsymbol{x}|\boldsymbol{d}) &\sim \mathcal{N}\left(\boldsymbol{\mu}_x, \boldsymbol{\Sigma}_x\right), \\ q(\boldsymbol{k}|\boldsymbol{d}) &\sim \mathcal{N}\left(\boldsymbol{\mu}_k, \boldsymbol{\Sigma}_k\right). \end{aligned}$$

The posteriors of the precisions were chosen to be Dirac δ-functions with non-zero values in $\boldsymbol{\tau}_x^*$, τ_k^* and ω^*. After some manipulations we get that

$$\begin{aligned} \boldsymbol{\Sigma}_x &= \left(\mathbb{E}_q\left[\omega \boldsymbol{K}^T \boldsymbol{K}\right] + \nabla^T \mathrm{diag}(\mathbb{E}_q\left[\boldsymbol{\tau}_x\right]) \nabla\right)^{-1}, \\ \boldsymbol{\mu}_x &= \boldsymbol{\Sigma}_x \mathbb{E}_q\left[\omega \boldsymbol{K}^T\right] \boldsymbol{d}, \\ \boldsymbol{\Sigma}_k &= \left(\mathbb{E}_q\left[\omega \boldsymbol{X}^T \boldsymbol{X}\right] + \mathbb{E}_q\left[\tau_k\right] \mathbb{I}\right)^{-1}, \\ \boldsymbol{\mu}_k &= \boldsymbol{\Sigma}_k \mathbb{E}_q\left[\omega \boldsymbol{X}^T\right] \boldsymbol{d}, \\ \boldsymbol{\tau}_x^* &= \left(\frac{1}{2} \mathbb{E}_q\left[\boldsymbol{x}^T \nabla^T \nabla \boldsymbol{x}\right] + \beta_{x0}\right)^{-1} \left(\alpha_{x0} - \frac{1}{2}\right), \\ \tau_k^* &= \left(\frac{1}{2} \mathbb{E}_q\left[\boldsymbol{k}^T \boldsymbol{k}\right] + \beta_{k0}\right)^{-1} \left(\frac{(2s-1)^2}{2} + \alpha_{k0} - 1\right), \\ \omega^* &= \left(\frac{1}{2} \mathbb{E}_q\left[\boldsymbol{d}^T \boldsymbol{d} - \boldsymbol{d}^T \boldsymbol{K} \boldsymbol{x} - \boldsymbol{x}^T \boldsymbol{K}^T \boldsymbol{d} + \boldsymbol{x}^T \boldsymbol{K}^T \boldsymbol{K} \boldsymbol{x}\right] + \eta_0\right)^{-1} \left(\frac{np}{2} + \gamma_0 - 1\right), \qquad (6) \end{aligned}$$

where $\mathbb{E}_q[.]$ denotes expected value w.r.t. $q(\boldsymbol{\theta}, \boldsymbol{d})$.

2.3 Iterative Variational Bayes algorithm

The first algorithm to be presented in this paper is the iterative variational Bayes (IVB) algorithm used in, for example, [10]. This algorithm utilizes the fact, that the forms of the posterior distributions are in the case of conjugate priors known, and we only need to find the values of their parameters. The expressions for the parameters form a set of linear equations that need to be solved to minimize the KL divergence of the approximation from the real posterior.

The covariance matrix of the image posterior is usually ill-conditioned, therefore, it is assumed to be diagonal. The expression for the mean of the image posterior requires an inverse of the covariance of the image. For higher accuracy, the estimate of $\boldsymbol{\mu}_k$ is obtained with conjugate gradients instead of using the diagonal covariance. The pseudocode is written below as Algorithm 2. This algorithm is basically E-M algorithm, getting estimates of parameters of normal distributions corresponds to E-step and recomputing $\tau_k^*, \boldsymbol{\tau}_x^*$ and ω^* is M-step.

```
Algorithm 4: IVB
Initialize all variables
While not converged
    Update $\boldsymbol{\Sigma}_x$ as an inverse of diagonal matrix from $\omega \boldsymbol{K}^T \boldsymbol{K} + \nabla^T \mathrm{diag}(\boldsymbol{\tau}_x^*) \nabla$
    Update $\boldsymbol{\mu}_x$ as a solution of $\left(\omega \boldsymbol{K}^T \boldsymbol{K} + \nabla^T \mathrm{diag}(\boldsymbol{\tau}_x^*)\right) \boldsymbol{\mu}_x = \omega^* \boldsymbol{K}^T \boldsymbol{d}$
    Construct $\mathbb{E}_q[\boldsymbol{X}]$, $\mathbb{E}_q\left[\boldsymbol{X}^T \boldsymbol{X}\right]$ and $\mathbb{E}_q\left[\boldsymbol{k}^T \boldsymbol{X}^T \boldsymbol{X} \boldsymbol{k}\right]$ from $\boldsymbol{\mu}_x$, $\boldsymbol{\Sigma}_x$, $\boldsymbol{\mu}_k$, $\boldsymbol{\Sigma}_k$
    Update $\boldsymbol{\Sigma}_k$ and then $\boldsymbol{\mu}_k$ according to (6)
    Update $\boldsymbol{\tau}_x^*$, then $\tau_k^*$ and then $\omega^*$ according to (6)
Return image estimate $\boldsymbol{\mu}_x$ and blur kernel estimate $\boldsymbol{\mu}_k$.
```

2.4 ELBO optimization

In order to compare ELBO optimization and VB, a second algorithm will be proposed. Parameters of the posterior distribution of $\boldsymbol{k}$ will be estimated via stochastic gradient descent and the reparametrization trick will be used. The function to be minimized w.r.t. $\boldsymbol{\Sigma}_k$ and $\boldsymbol{\mu}_k$ is

$$\mathbb{E}_q\left[-p(\boldsymbol{d}|\boldsymbol{x}, \boldsymbol{k}, \omega) - p(\boldsymbol{k}|\tau_k) + q(\boldsymbol{k}|\boldsymbol{d})\right]. \tag{7}$$

The first element of (7) contains the most complicated expected value in the whole model: $\mathbb{E}_q\left[\boldsymbol{x}^T \boldsymbol{K}^T \boldsymbol{K} \boldsymbol{x}\right]$. To approximate this expression, the reparametrization trick was used and $\boldsymbol{k}$ was repametrized as follows

$$\begin{aligned} \boldsymbol{k} &= \boldsymbol{\mu}_k + \boldsymbol{\Sigma}_k^{\frac{1}{2}} \boldsymbol{\epsilon}, \\ \boldsymbol{\epsilon} &\sim \mathcal{N}(\boldsymbol{0}, \mathbb{I}). \end{aligned}$$

Covariance matrix $\boldsymbol{\Sigma}_k$ is estimated as a product of two matrices $\boldsymbol{S}_k \boldsymbol{S}_k^T$, which means that the covariance matrix is symmetric and makes the reparametrization easier. The pseudocode of the IVB algorithm with the two estimates obtained by ELBO maximization, named ELBO algorithm, is below as Algorithm 2.

Algorithm 5: ELBO

```
Initialize all variables
While not converged
    Update $\boldsymbol{\Sigma}_x$ as an inverse of diagonal matrix from $\omega \boldsymbol{K}^T \boldsymbol{K} + \nabla^T \mathrm{diag}(\boldsymbol{\tau}_x^*) \nabla$
    Update $\boldsymbol{\mu}_x$ as a solution of $\left(\omega \boldsymbol{K}^T \boldsymbol{K} + \nabla^T \mathrm{diag}(\boldsymbol{\tau}_x^*)\right) \boldsymbol{\mu}_x = \omega^* \boldsymbol{K}^T \boldsymbol{d}$
    Construct $\mathbb{E}_q[\boldsymbol{X}]$, $\mathbb{E}_q\left[\boldsymbol{X}^T \boldsymbol{X}\right]$ and $\mathbb{E}_q\left[\boldsymbol{k}^T \boldsymbol{X}^T \boldsymbol{X} \boldsymbol{k}\right]$ from $\boldsymbol{\mu}_x$, $\boldsymbol{\Sigma}_x$, $\boldsymbol{\mu}_k$, $\boldsymbol{\Sigma}_k$
    For 1000 steps
        Generate new $\boldsymbol{\epsilon} \sim \mathcal{N}(\boldsymbol{0}, \mathbb{I})$ and get gradients of (7) w.r.t. $\boldsymbol{\mu}_k$ and $\boldsymbol{S}_k$
        Update $\boldsymbol{\mu}_k$, $\boldsymbol{S}_k$ using Adam optimiser
    Update $\boldsymbol{\tau}_x^*$, then $\tau_k^*$ and then $\omega^*$ according to (6)
Return image estimate $\boldsymbol{\mu}_x$ and blur kernel estimate $\boldsymbol{\mu}_k$.
```

2.5 Vadam

Vadam (Variational Adam) is an optimizer proposed by Khan et al. in [8] for distributions from exponential family. It was inferred to maximize ELBO using natural gradient and samples from posterior distribution are used to approximate the value of the gradient. In the case when the posterior distribution is normal it is possible to get the estimate of the variance right from the update of the mean, so it is not necessary to construct another gradient to find its value. Assuming the prior distribution of parameter $\boldsymbol{\theta}$ to be normal with zero mean and precision τ and posterior to be normal with mean $\boldsymbol{\mu}$ and variance $\boldsymbol{\sigma}$, its $(t+1)$-th update is given as follows

$$
\begin{aligned}
\boldsymbol{u}_{t+1} &= \gamma_1 \boldsymbol{u}_t + (1-\gamma_1)\left(\boldsymbol{g}\left(\boldsymbol{\theta}^{(t)}\right) + \tilde{\tau}\boldsymbol{\mu}_t\right), \\
\boldsymbol{s}_{t+1} &= \gamma_2 \boldsymbol{s}_t + (1-\gamma_2)\hat{\boldsymbol{g}}\left(\boldsymbol{\theta}^{(t)}\right)^2, \\
\hat{\boldsymbol{u}}_{t+1} &= \boldsymbol{u}_{t+1}\left(1-\gamma_1^t\right)^{-1}, \\
\hat{\boldsymbol{s}}_{t+1} &= \boldsymbol{s}_{t+1}\left(1-\gamma_2^t\right)^{-1}, \\
\boldsymbol{\theta}_{t+1} &= \boldsymbol{\theta}_t - \alpha \hat{\boldsymbol{u}}_{t+1}\left(\sqrt{\hat{\boldsymbol{s}}_{t+1}} + \tilde{\tau}\right)^{-1},
\end{aligned}
$$

where $\boldsymbol{\theta}^{(t)}$ is a sample taken from the estimate of the posterior $\mathcal{N}(\boldsymbol{\mu}_t, \mathrm{diag}(\boldsymbol{\sigma}_t))$, the variance $\boldsymbol{\sigma}_t$ is given as $(N\boldsymbol{s}_t + \tau\boldsymbol{1})^{-1}$ and $\tilde{\tau} = \tau/N$, where N is a number of measurements (pixels). Vadam optimiser will be used similarly as Adam optimizer in Algorithm 2. This algorithm will be called ELBO-Vadam and is presented here as Algorithm 2.

3 Experiments

The three algorithms were tested on synthetic data. A cut-out from Lena image [11] was blurred with a gaussian kernel, and white noise was added to the degraded image. Signal

Algorithm 6: ELBO-Vadam

```
Initialize all variables
While not converged
    Update $\boldsymbol{\Sigma}_x$ as an inverse of diagonal matrix from $\omega \boldsymbol{K}^T \boldsymbol{K} + \nabla^T \mathrm{diag}(\boldsymbol{\tau}_x^*) \nabla$
    Update $\boldsymbol{\mu}_x$ as a solution of $\left(\omega \boldsymbol{K}^T \boldsymbol{K} + \nabla^T \mathrm{diag}(\boldsymbol{\tau}_x^*)\right) \boldsymbol{\mu}_x = \omega^* \boldsymbol{K}^T \boldsymbol{d}$
    Construct $\mathbb{E}_q\left[\boldsymbol{X}\right]$, $\mathbb{E}_q\left[\boldsymbol{X}^T \boldsymbol{X}\right]$ and $\mathbb{E}_q\left[\boldsymbol{k}^T \boldsymbol{X}^T \boldsymbol{X} \boldsymbol{k}\right]$ from $\boldsymbol{\mu}_x$, $\boldsymbol{\Sigma}_x$, $\boldsymbol{\mu}_k$, $\boldsymbol{\Sigma}_k$
    For 1000 steps
        Generate new $\boldsymbol{\epsilon} \sim \mathcal{N}\left(\boldsymbol{0}, \mathbb{I}\right)$ and get gradients of (7) w.r.t. $\boldsymbol{\mu}_k$
        Update $\boldsymbol{\mu}_k$ using Vadam optimiser and $\boldsymbol{S}_k$ as $(N \boldsymbol{s}_t + \tau_k^* \boldsymbol{1})^{-1/2}$
    Update $\boldsymbol{\tau}_x^*$, then $\tau_k^*$ and then $\omega^*$ according to (6)
Return image estimate $\boldsymbol{\mu}_x$ and blur kernel estimate $\boldsymbol{\mu}_k$.
```

to noise ratio (SNR) was set to 40dB in this case. Together with blind deconvolution, non-blind was performed on the blurred image with the estimate of blurring kernel as it often returns more accurate results. The image was reconstructed using matrix inversion of $\boldsymbol{K}$ with a small value added to its diagonal.

The first two rows of Figure 1 show estimates of the blurring kernel, sharp image and the results of non-blind deconvolution returned by Algorithm 2 and Algorithm 2, respectively. In both cases, it is assumed that a covariance matrix of $\boldsymbol{k}$ is diagonal. The kernel estimate found by Algorithm 2 is symmetric and similar to the correct one, and the estimate of sharp image seems to be sharper than the degraded image. The blurring kernel found by Algorithm 2 looks almost the same as the one found by Algorithm 2, but the image estimate does not seem to be as smooth as the one of Algorithm 2, although it is still sharper than the blurred one. In both cases, there are apparent constant areas in the image estimates caused by the ARD prior on the differences. Both images found by non-blind deconvolution show improvement in comparison with the blurred image.

The next two rows of images of Figure 1 (the third and fourth) show results found by Algorithms 2 and 2 assuming that the covariance matrix of $\boldsymbol{k}$ is full. In this case, the estimates should be closer to the original values because there is one less approximation than in the case of diagonal matrix, but it is not the truth for the Algorithm 2. The algorithm was not able to reconstruct the image well and the estimate of blurring kernel is far from reality. This behaviour happens because only one sample from the posterior is taken in the reparametrization trick and that is not enough to approximate full covariance matrix. The solution to this problem is to draw more samples and estimate the gradient as an average, but it is computationally too expensive.

The last tested version was the Algorithm 2 with Vadam optimiser. The results are shown in the last row of Figure 1. They appear to be comparable with the estimates found by Algorithm 2 with full covariance (ELBO-Vadam assumes it is diagonal). The estimated image is sharp, there are almost no visible constant areas, and the blur estimate

Figure 1: The first row shows results of IVB algorithm with diagonal covariance, second results of ELBO with diagonal covariance, third results of IVB algorithm and full covariance, fourth results of ELBO algorithm with full covariance, and fifth results of ELBO-Vadam algorithm. The upper image on the left side of a row shows the original blur, the lower its estimate. The first image of Lena in the row is the original one, the second one is the blurred one, the third is the direct estimate from the algorithm, and the last one shows the result of non-blind deconvolution.

is close to the real one.

Figure 2 shows PSNR (peak signal-to-noise ratio) of the reconstructed images. The first graph shows PSNR of the direct estimate of sharp image $\boldsymbol{\mu_x}$. The best result were achieved by Algorithm 2 with full covariance and Algorithm 2, for the weakest noise they reach PSNR of 30 dB. Results of Algorithm 2 are even worse than PSNR of the blurred image, although it looks sharper in Figure 1, which is probably caused by the piecewise-constant character of the estimate. As can be seen from the second graph, the non-blind deconvolution performs better PSNR-wise, yet the images seem less sharp than direct estimates in Figure 1. All the algorithms reach similar values on the SRN levels of 20, 30 and 40 dB, but for SNR 50 dB Algorithm 2 with full covariance and Algorithm 2 outperform the rest.

Overall, Algorithm 2 is the best alternative to the analytical solution of Algorithm 2, as it reaches the same accuracy, even though it assumes that the covariance of the blur is diagonal. The reason why it outperforms Algorithm 2 may lie in the fact that Vadam draws samples from the posterior and, therefore, it is able to find better local minima. Algorithm 2 evaluates gradient in randomly drawn samples as well, but its estimate of covariance may not be that good as it does not depend directly on the changes of $\boldsymbol{k}$.

4 Conclusion

In this paper, the problem of blind image deconvolution was examined through the variational Bayes framework. ARD model was chosen for image gradients because the image is assumed to be piecewise-constant. Three algorithms were compared. First of them is the iterative variational Bayes algorithm, which utilizes the fact that prior distributions were chosen to be from the conjugate system, thus only parameters of posteriors are unknown. It iteratively recomputes the parameters and minimizes Kullback-Leibler divergence of approximation of posterior from real posterior. The assumption of conjugate priors is very restrictive, hence another approach to minimization of Kullback-Leibler divergence was proposed. The second algorithm uses steps from the first one, but parameters of the posterior of the blur are estimated via maximization of evidence lower bound by stochastic gradient descent, where the reparametrization trick was used to approximate a complicated expected value, which could be necessary if the priors were not chosen so conveniently. Moreover, stochastic gradient descent with Vadam optimizer was introduced as the third algorithm. All algorithms were tested on a blurred cut-out from Lena. It was shown that optimization of ELBO with Vadam optimiser achieves as good results as the iterative variational Bayes algorithm with full covariance matrix. This suggests that the direct numerical optimisation could be used instead of VB when a more flexible model is required, possibly without any loss of precision.

Acknowledgements

This work was supported by the grant GA20-27939S.

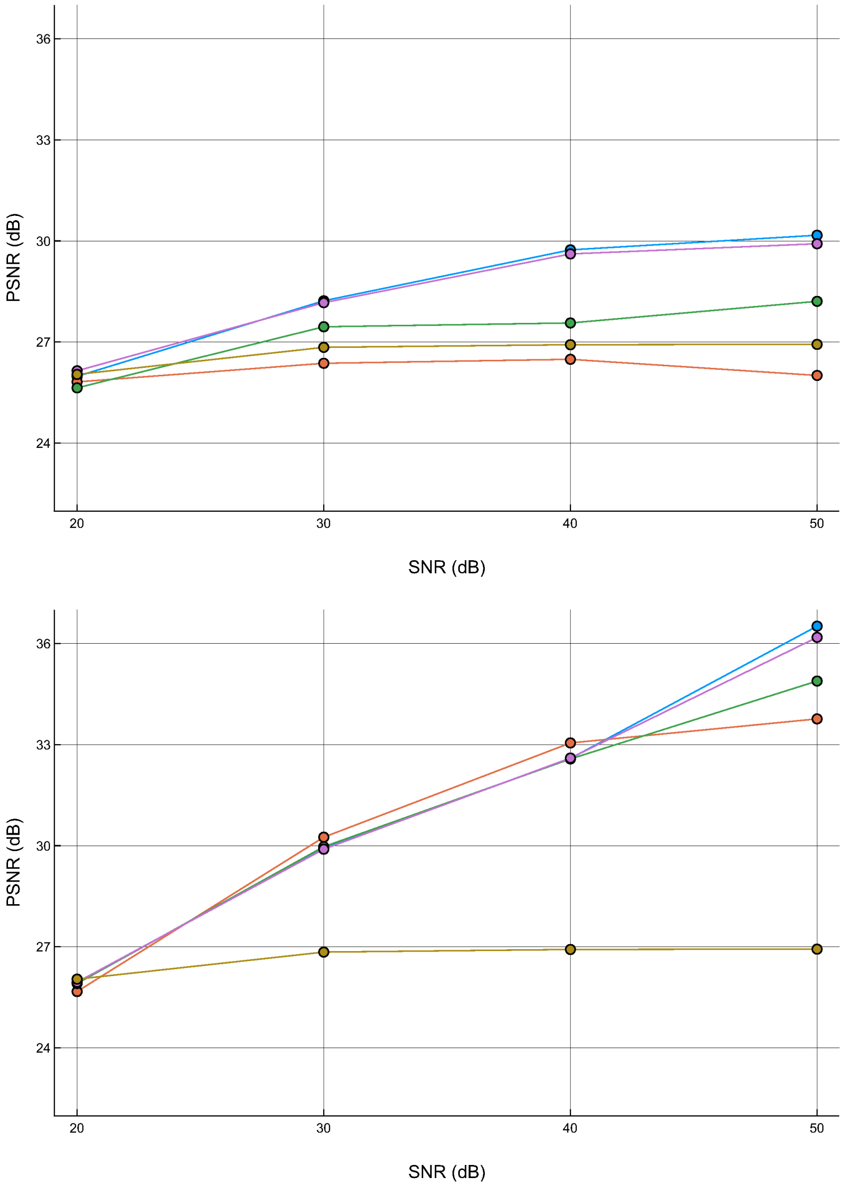

Figure 2: The graphs show values of PSNR of sharp image estimate for four levels of SNR. The upper one shows values for the direct estimate of the image, the lower one for the non-blind deconvolution. The blue line is of IVB algorithm with full covariance and the red one with diagonal covariance, green line is of ELBO algorithm with diagonal covariance, purple of ELBO-Vadam algorithm and brown shows PSNR of the blurred image.

References

[1] A. Levin, W. Yair, D. Fredo. Understanding Blind Deconvolution Algorithms. *IEEE Trans Pattern Anal Mach Intell.*, 33(12), 2354–2367, 2011.

[2] R. Fergus et al. Removing camera shake from a single photograph. *SIGGRAPH '06: ACM SIGGRAPH 2006 Papers*, 787–794, 2006.

[3] R. Molina, J. Mateos, A. K. Katsaggelos. Blind Deconvolution Using a Variational Approach to Parameter, Image, and Blur Estimation. *IEEE Transactions on Image Processing.*, 15(12), 3715–3727, 2006.

[4] D. Wipf, H. Zhang. Revisiting Bayesian Blind Deconvolution. *Journal of Machine Learning Research*, 15, 3775–3814, 2014.

[5] F. Šroubek, V. Šmídl, J. Kotera. Understanding image priors in blind deconvolution. *In 2014 IEEE International Conference on Image Processing (ICIP)*, 4492–4496, 2014.

[6] S. D. Babacan, R. Molina, A. K. Katsaggelos. Bayesian Blind Deconvolution with General Sparse Image Priors. *In: Fitzgibbon, A. et al. Computer Vision – ECCV 2012. ECCV 2012. Lecture Notes in Computer Science, vol 7577, Springer, Berlin, Heidelberg.*, 341–355, 2012.

[7] J. A. Palmer, K. Kreutz-Delgado, S. Makeig. Strong Sub- and Super-Gaussianity. *In: V. Vigneron et al.:Latent Variable Analysis and Signal Separation. LVA/ICA 2010. Lecture Notes in Computer Science, vol 6365. Springer, Berlin, Heidelberg.*, 303–310, 2010.

[8] M. E. Khan, W. Lin. Fast and Scalable Bayesian Deep Learning by Weight-Perturbation in Adam. *Im: 35th International Conference on Machine Learning, ICML 2018*, 4088-4113, 2018.

[9] D. Kingma, M. Welling. Auto-encoding Variational Bayes. *arXiv preprint arXiv:1312.6114.*,2013.

[10] J. Kotera, V. Šmídl, F. Šroubek. Blind Deconvolution With Model Discrepancies. *IEEE Transactions on Image Processing*, 26(5), 2533-2544. 2017.

[11] Lena [online]. Available from: https://www.cosy.sbg.ac.at/ pmeerw/Watermarking/ lena.html, cited 2020-10-12.

Stochastic and Physical Monitoring Systems
SPMS 2021
June 24 - 28, 2021
Malá Skála, Czech Republic

PM Elasticity Evaluation Based on Statistical Kernel Density Estimators

Erik Dolejš and Václav Kůs

Department of Mathematics, FNSPE, Czech Technical University in Prague, Trojanova 13, 12000 Praha 2, Czech Republic

Email: `dolejeri@fjfi.cvut.cz, vaclav.kus@fjfi.cvut.cz`

Abstract. The main objectives of this paper is to evaluate the hysteretic properties of materials using the Preisach-Mayergoyz (PM) model. A new kernel density estimation methods are proposed to describe the distribution in PM space. These kernel descriptions are based either on the projections of hysterons or on two-dimensional kernel estimator on specific support. These estimates are used to construct elasticity indexes, which are evaluated on the steal earthquake dampers.

Key words: Binary classification; Divergences measure; Kernel density estimates; Preisach-Mayergoyz model.

1 Preisach-Mayergoyz hysteresis model

Hysteresis phenomenon refers to the evolution of a dynamical system that depends not only on the input independent variable, but also on the previous evolution of the system state. Thus, in a system with hysteretic behavior, we are unable to describe the relationship between the input variable and the outcome without knowing the history of previous states. In this paper, we use hysteresis to evaluate the elastic properties of a material, specifically to determine the degree of damage of dissipative dampers that are installed in building structures for earthquake protection.

To describe the hysteresis, we used the so-called Preisach-Mayergoyz (PM) model. The basic building block of this model is the so-called hysteresis operator $\hat{\gamma}_{\alpha,\beta}$, also referred to as the hysteron. This operator can be represented by the rectangular curve in Fig. 1(a), where the numbers α and β, $\beta < \alpha$, denote the closing and opening values. For our case with dampers, the fact that the hysteron is open means that when this pressure is reached, the hysteron loses its ability to absorb additional load and no longer helps damping. If the input signal $u(t)$ increases monotonically, the curve '$abcde$' corresponds to this in the graph in Fig. 1(a). Conversely, a monotonic decrease in the signal will result in a curve '$edfba$'. Mathematically, we write the output of the hysteresis operator

$$\hat{\gamma}_{\alpha,\beta} = \begin{cases} -1, & u(t) \leq \beta, \\ 1, & u(t) \geq \alpha, \\ k, & u(t) \in (\,\beta, \alpha)\,, \end{cases} \tag{1}$$

where

$$k = \begin{cases} 1, & \text{pokud}\, \exists\, t^* : u(t^*) > \alpha, \quad \forall \tau \in (t^*, t)\,,\, u(\tau) \in (\,\beta, \alpha)\,, \\ -1, & \text{pokud}\, \exists\, t^* : u(t^*) < \beta, \quad \forall \tau \in (t^*, t)\,,\, u(\tau) \in (\,\beta, \alpha)\,. \end{cases}$$

The opening and closing values of the hysterons appear in the right triangle as points (α, β), which uniquely correspond to the hysteresis operator $\hat{\gamma}_{\alpha,\beta}$ (Fig. 1(b)). The hypotenuse of this triangle is the limit line $\alpha = \beta$ of ideal elasticity. If we now consider an infinite set of hysteresis operators $\hat{\gamma}_{\alpha,\beta}$ and the so-called Preisach function $\mu\,(\alpha, \beta)$, which is a non-degenerate probability density on $\alpha \leq \beta$ and which therefore gives the density of hysterons in PM space, we can write the PM model of hysteresis as a superposition of such operators

$$v(t) = \hat{\Gamma}\,[u(t)] = \iint\limits_{\beta \leq \alpha} \mu\,(\alpha, \beta)\,\hat{\gamma}_{\alpha,\beta}\,(u\,(t))\,\mathrm{d}\alpha\,\mathrm{d}\beta. \tag{2}$$

The symbol $\hat{\Gamma}$ is used here to express properly the output of PM hysteresis model. This definition of PM space is shown in Fig. 1(c).

2 Identification of PM space

One of the fundamental problems is to find efficiently the PM space that corresponds to the appropriate hysteretic behaviour of the material. We first introduce suitable probability distributions that describe well the distribution of hysterons in the material. Next, we introduce divergence measures that will be used to evaluate the difference between the measured and optimization-derived hysteresis curves.

The first two distributions are proposed specifically for heterogeneous materials by Guyer and McCall ([4]), followed by Koen distribution. For the purpose of our work, the value of the input load $u\,(t)$ will be represented by the pressure P interacting in the material, which is described by the following distributions. Thus, the first Guyer distribution (Guyer1)

$$P_c = max \cdot r_c^{\,\alpha}, \quad P_o = P_c \cdot r_o^{\,\beta}, \tag{3}$$

the second Guyer distribution (Guyer2)

$$P_c = max \cdot r_c^{\,\alpha}, \quad P_o = P_c \cdot r_o^{\,0.25+0.75\mu}, \tag{4}$$

and Koen's PM distribution (Koen)

$$P_c = max \cdot r_c, \quad P_o = \left(\frac{P_c}{\alpha}\right)^{\beta} \cdot r_o, \tag{5}$$

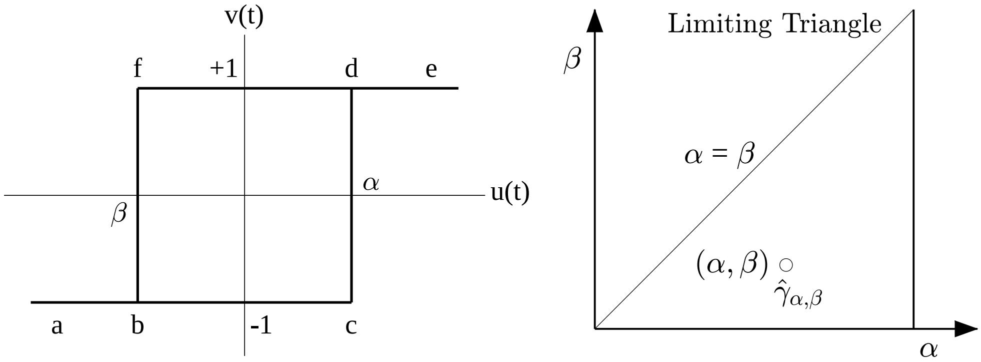

(a) Hysteresis operator (b) PM triangle

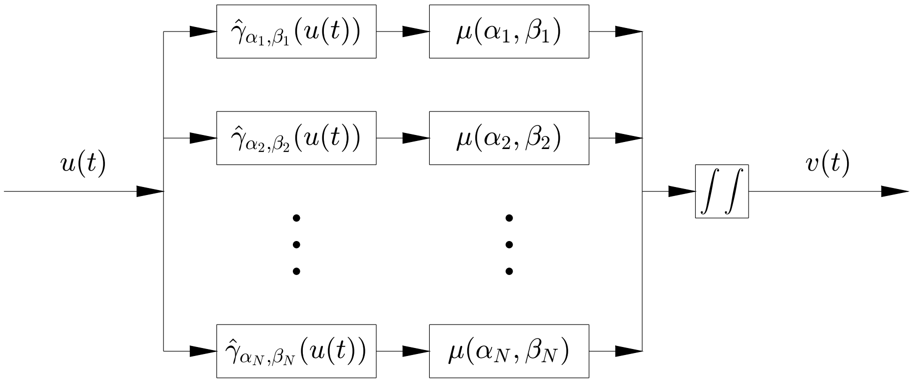

(c) Superposition of hysteresis operators

Figure 1:

where $\alpha, \beta, \mu \in \mathbb{R}_0^+$ are the parameters of the distribution, P_c and P_o denote values of the closing and opening pressure, max is the maximum value of input pressure, and r_c, r_o are random numbers uniformly generated from interval $(0, 1)$. Further, bivariate normal distribution, truncated into a PM triangle, is also used due to its potential to describe elliptic clusters of hysterons

$$f\left(x, \mu, \mathbb{C}\right) = \frac{1}{2\pi\sqrt{|\mathbb{C}|}} \exp\left(-\frac{1}{2}\left(x-\mu\right)^T \mathbb{C}^{-1}\left(x-\mu\right)\right), \tag{6}$$

where the parameters are the vector of means $\mu = (\mu_1, \mu_2)$ and the positively definite, symmetric correlation matrix $\mathbb{C}$, where $x = (x_1, x_2)$, $x_1, x_2 \in [0, max]$ and $x_1 \geq x_2 \geq 0$.

To determine the divergence between the found and measured hysteresis curves, which is the value that must be minimized, we use, in addition to the classical L2-metric, the ϕ-divergences, particularly the Hellinger distance

$$H^2\left(P, Q\right) = \frac{1}{2}\int\left(\sqrt{f} - \sqrt{g}\right)^2 \mathrm{d}\,\mu, \tag{7}$$

and also the LeCam distance

$$LC^2\left(P, Q\right) = \int \frac{\left(f-g\right)^2}{f+g} \mathrm{d}\,\mu, \tag{8}$$

which we also use to describe the difference between the probability density estimates of PM spaces. The optimization algorithms themselves have been the main focus of previous work and will not be discussed here.

3 Kernel estimates on PM space

In this paper, we discuss the techniques of kernel probability density estimation to the distribution of hysterons in PM space. This knowledge is then used to design an elasticity index or damage index.

Definition 1 *(Kernel probability density estimation). Let $X_1, ..., X_n$ be a random sample of size n from a continuous random variable X with probability density $f(x)$. Let the symmetric function $K(x) \geq 0$, which will be called the kernel, satisfies the conditions*

$$\int K(x)\,\mathrm{d}x = 1, \qquad \int x\,K(x)\,\mathrm{d}x = 0, \qquad \int x^2\,K(x)\,\mathrm{d}x > 0. \tag{9}$$

Then for all $x \in \mathbb{R}$ we define the kernel density estimate by

$$\hat{f}(x\,;h) = \frac{1}{nh}\sum_{i=1}^{n} K\left(\frac{x - X_i}{h}\right) = \frac{1}{n}\sum_{i=1}^{n} K_h(x - X_i), \tag{10}$$

where $K_h(x) = \frac{1}{h}K\left(\frac{x}{h}\right)$ is the scaled kernel and $h \in \mathbb{R}^+$ is the smoothing parameter.

The first method proposed for kernel estimation of the PM space consists of projecting the hysterons from the PM space onto the vertical side of Preisach triangle via its lower left vertex and then applying standard one-dimensional kernel estimators. For illustration, the principle of this estimation is shown in Fig. 2. Each hysteron, together with its lower left vertex, forms a line, and its intersection with the vertical right leg is a projected point (Fig. 2). We then apply a kernel estimator to this data lying on the vertical right-hand line (Fig. 2(b)), and this estimator proceeds in the top-to-bottom direction chosen to ensure that perfectly elastic hysterons are represented at the beginning of the estimation region and elastically damaged hysterons at the end (Fig. 2(c)).

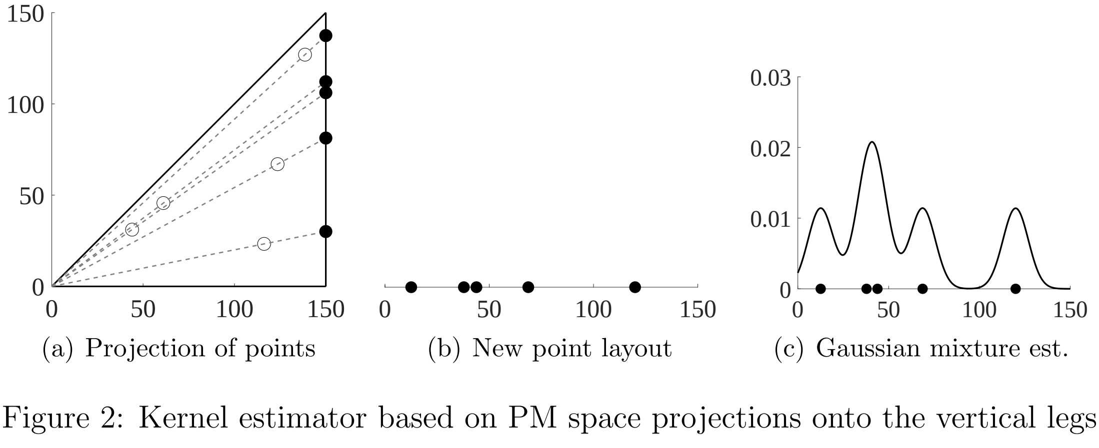

(a) Projection of points (b) New point layout (c) Gaussian mixture est.

Figure 2: Kernel estimator based on PM space projections onto the vertical legs

In addition, a symmetrically inverted estimator is used in this paper, where the individual hysterons are projected from the upper right corner of the triangle onto the horizontal side. In the same way, we apply the kernel estimator to the newly distributed points, with the estimation proceeding from left to right to capture the direction from the elastic diagonal. Next, the information from the projections in both directions is combined by projecting the points onto the horizontal perpendicular, and again performing the classical one-dimensional kernel estimation on these newly distributed points, this time in the top-to-bottom direction, which proceeds smoothly from right to left.

Another method is based on direct kernel estimation of the PM space using a kernel with a special shape of its support. This support traverses the Preisach triangle in the given way and the resulting kernel estimate is given by the following expression

$$\hat{f}\left(x\,;h\right) = \frac{1}{const}\sum_{i=1}^{n}\frac{1}{s\left(x\,;h\right)}\mathbb{I}_{s(x\,;h)}\left(X_i\right), \tag{11}$$

where n denotes the size of data sample, $s\left(x\,;h\right)$ is the area of kernel support depending on variable x and smoothing parameter h, $const$ is the normalization constant to make $\hat{f}\left(x\,;h\right)$ be the probability density, and $\mathbb{I}_{s(x\,;h)}$ is the characteristic function for the support $s\left(x\,;h\right)$.

The first such 2D-kernel estimate of PM space is using a kernel with a triangle-shaped support. This always has a lower left vertex identical to the Preisach triangle, and the opposite to it lies on a line, again given by the vertical branch of the Preisach triangle. This opposite side of the kernel support K has length h, where h is the smoothing parameter (Fig. 3(a)). An inverted estimator was also used, where the carrier has a peak in the upper right corner and the opposite side moves along the horizontal axis. As with the kernel estimator with PM space projection, a combination of these two directions connected in sequence to form a double-length estimator was also used.

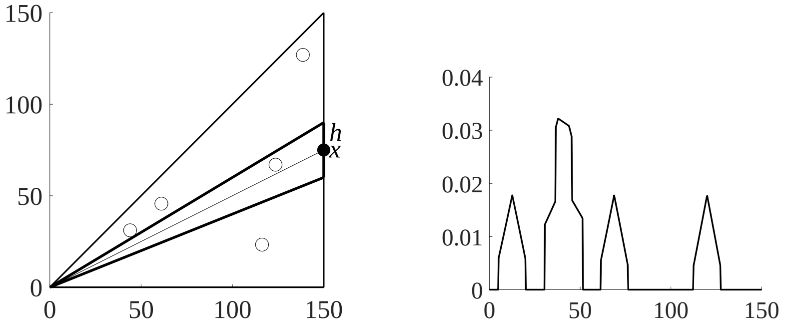

(a) Triangular kernel support (b) Constant kernel estimate

Figure 3: Kernel estimator based on constant 2D-kernel with triangular support

Next, we introduce the kernel estimates that requires only one motion direction. This involves using the kernel with a trapezoid-shaped support that moves away from the elastic diagonal so that its bases are always parallel to it (Fig. 4(a)). We take as the coordinate of this estimate the center of the trapezoid, which moves along the center of

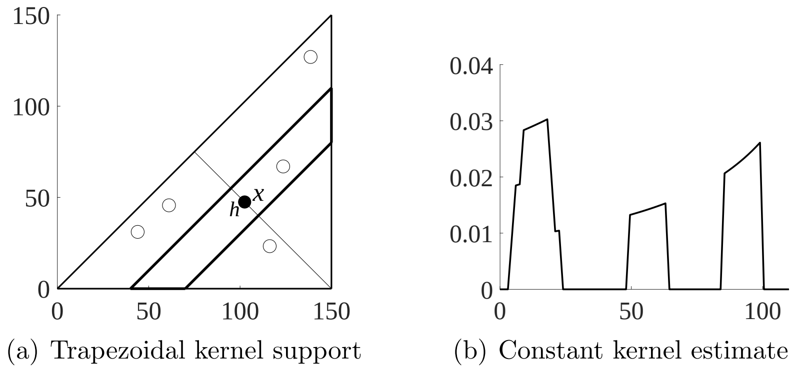

(a) Trapezoidal kernel support (b) Constant kernel estimate

Figure 4: Kernel estimator based on constant 2D-kernel with trapezoidal support

gravity of PM triangle and is therefore $\sqrt{2}/2$ times longer than previous estimates, where the coordinate moved along the legs of PM triangle.

The last proposed support is based on a quadrilateral kernel support whose two vertices are fixed at the origin and the upper right corner, and the other two are shifted along a media (axis of gravity) spaced apart by a smoothing parameter h. This wing-like support can be seen in Fig. 5(a).

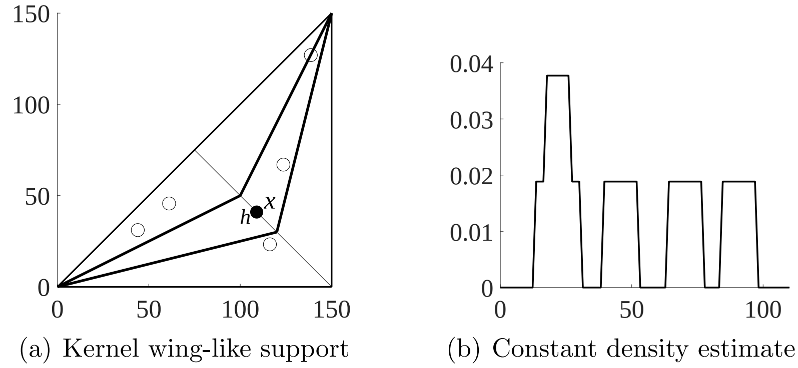

(a) Kernel wing-like support (b) Constant density estimate

Figure 5: Kernel estimator based on 2D-kernel with wing-like support

The previous kernel estimate consists, like the first proposed method, in projecting the points and then using the standard kernel estimator. This time, however, the points are projected onto the altitude that belongs to the hypotenuse of PM triangle. Thus, this altitude divides the triangle into two halves. Therfore, the points in the bottom half are projected via the lower left corner of PM triangle, and the points in the upper half are projected to the altitude via the upper right corner of PM triangle (Fig. 6(a)). We apply a standard Gaussian kernel to these newly distributed points (Fig. 6(b)), where the kernel estimation runs along the altitude again from the hypotenuse to the bottom right corner in order to capture the progression from perfectly elastic points to imperfectly elastic ones.

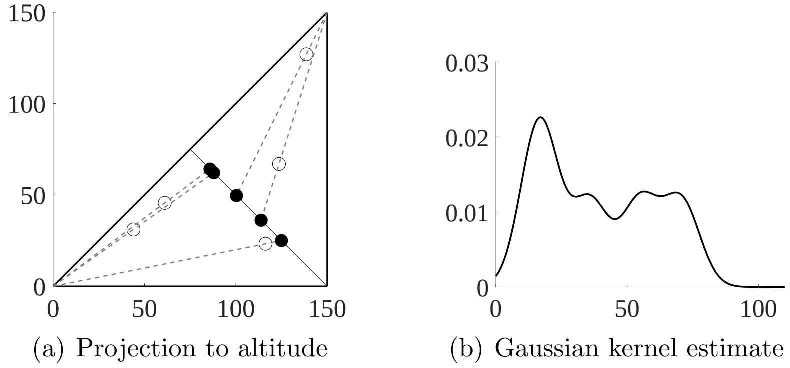

(a) Projection to altitude (b) Gaussian kernel estimate

Figure 6: Kernel estimator while projecting PM space to altitude

4 Design and evaluation of elasticity index

The individual kernel estimates presented in the previous section are used to design the elasticity index. To do this, we use the Le Cam distance of kernel estimate of the corresponding PM space under study and the kernel estimate of the perfectly elastic PM space that has all the hysterons on hypotenuse of the Preisach triangle. This value is re-normalized by the maximum value of the Le Cam divergence it takes for the perfectly inelastic space. We thus define elasticity index $IE_j = LC/LC_{max}$, where we use a projection onto both branches with the normal Gaussian kernel ($j = 1$), the kernel with triangular support, the kernel traversing both branches ($j = 2$), the constant kernel with trapezoidal support ($j = 3$), the constant kernel with wing-like support ($j = 4$), and finally, projecting onto the altitude of the triangle using normal Gaussian kernel ($j = 5$). These indexes were subjected to testing on generated data and also on cyclic stress tests of a metallic damper subjected to successive cycles. An example of a measured cycle can be seen in Fig. 7. The PM spaces from Fig. 8 correspond to these measured data.

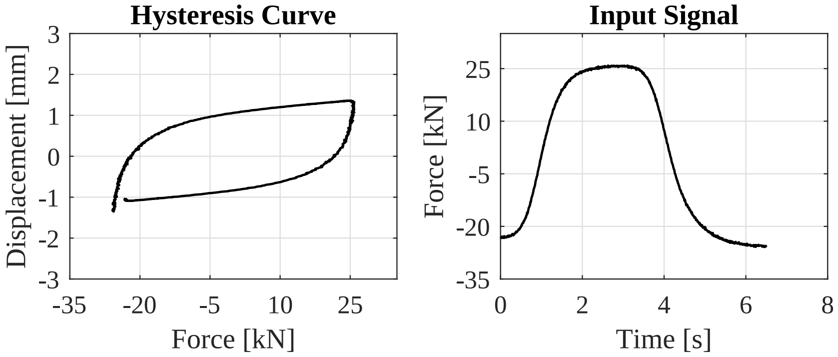

Figure 7: Hysteresis curve and input load for the third cycle on damper

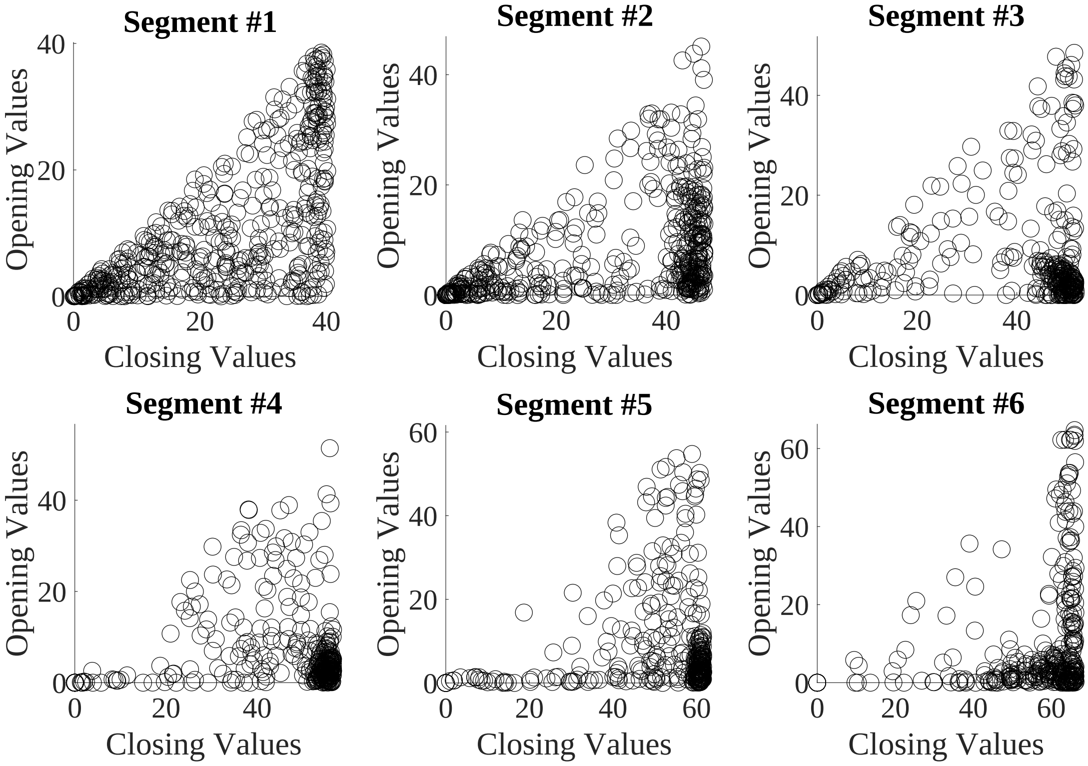

Figure 8: PM spaces identified on dissipative damper in all 6 cycles

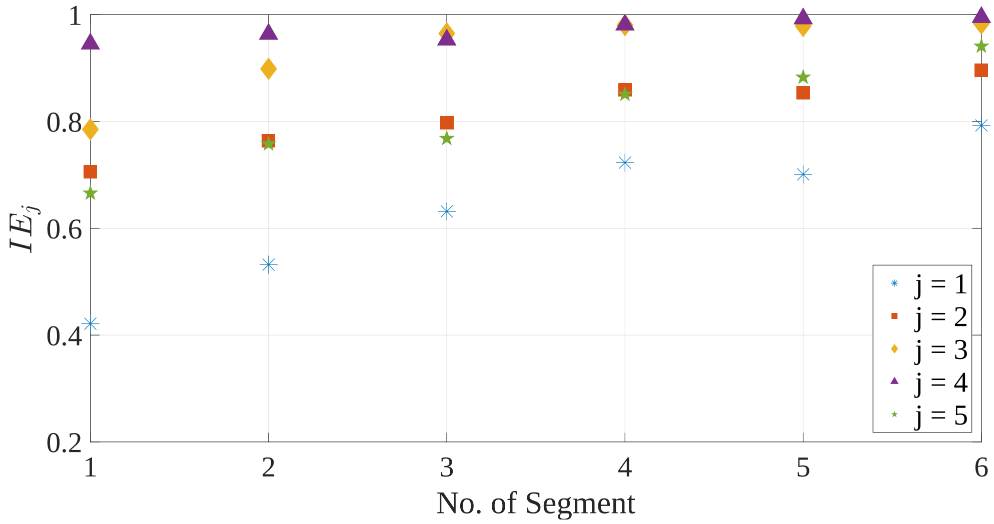

Figure 9: Final values of indexes IE_1 to IE_5 for earthquake damper test data

On these PM spaces we performed the kernel estimation introduced above and using the introduced methods we evaluated the individual indexes, which can be seen in Fig. 9. We can see that good results are achieved by IE_1, which grows almost monotonically for the measured damper data. Also IE_2 and IE_5 behave similarly, but its nominal values achieve rather narrow range. The IE_3 index increases only on the first three segments and then stagnates, which in practice reflects the potential significant damage of the damper from the 3rd segment onwards and the urgency of earlier replacement. The IE_4 behaves practically constant in all segments and is therefore unusable without any further re-normalization.

Acknowledgements

These results were supported by the research grant SGS21/165/OHK4/3T/14 (MEYS) and partly by LTT180001 (MEYS) in algorithmic approaches.

References

[1] I. D. Mayergoyz. *Mathematical models of hysteresis and their applications.* Academic Press - Elsevier, 2003.

[2] B. W. Silverman. *Density estimation for statistics and data analysis.* New York: Chapman & Hall, 1998.

[3] E. Dolejš. *Odhadování struktury hysterezních materiálů prostřednictvím Preisach-Mayergoyzova prostoru.* Bakalářská práce, FJFI, ČVUT, 2020.

[4] K. R. McCall, R. A. Guyer. Equation of state and wave propagation in hysteretic nonlinear elastic materials. *Journal of Geophysical Research*, **90**(B12), 1994.

[5] J. Anděl. *Základy matematické statistiky.* Matfyzpress, Praha, 2005.

[6] A. Benavent-Climent, A. Gallego, L. Romo-Melo, L. Morillas. Health monitoring of web plastifying dampers subjected to cyclic loading through vibration tests. *Structural Health Monitoring*, **13**(1), 33–49, 2014.

[7] M. Brokate, J. Sprekels. *Hysteresis nad Phase Transitions.* Berlin: Springer-Verlag, 1996.

[8] I. Vajda. *Information-Theoretic Methods in Statistics.* Výzkumná zpráva, ÚTIA AV ČR, 1995.

[9] C. Abarkane. *Monitoring through acoustics techniques of RC earthquake-resistant structures subjected to dynamic loads on shaking table.* Disertační práce, Technical School of Building Engineering, University of Granada, 2019.

Stochastic and Physical Monitoring Systems
SPMS 2021
June 24 - 28, 2021
Malá Skála, Czech Republic

Multisolution Approach to Classification Tasks in Biomedicine

Kateřina Henclová

Department of Mathematics, FNSPE, Czech Technical University in Prague, Czech Republic

Email: `katerina.henclova@fjfi.cvut.cz`

Abstract. Simultaneous search for multiple sparse solutions of a classification/regression problem differs fundamentally from common approaches to these classical machine learning problems. At the same time, it is strongly motivated by practical requirements, e.g. in applications in biomedicine. In such tasks, we face high dimensions, limited number of samples, errors in data and, most importantly, the necessity of providing a human-interpretable model. On the other hand, field-related expertise is usually available. This contribution shall convey the concept of multisolution feature selection within a classification problem. Using a real world example, we shall introduce the core ideas. We shall also outline the individual steps leading to the problem's formal definition and its potential solution.

Key words: machine learning; classification.

1 Introduction

Machine learning tools can be highly useful in many fields where big data is involved. With the arrival of ever more precise biochemical measurement techniques producing ever larger datasets, algorithms providing interpretable models can help to explain complex phenomena based solely on the information contained in the data.

This work is inspired by classification/regression problems in the context of biomedicine [7, 10, 9, 11]. However, their specifics are not limited to bioinformatics and can be easily found in other applications as well (e.g. malware detection [1]). We assume our data is produced by measurement techniques like mass spectroscopy or gel electrophoresis. The data is thus noisy and high-dimensional. There are a few dozen samples at best, possibly even having unreliable classification/regression labels. At this setting, we admit the inherent uncertainty and nonuniqueness of solutions. Instead, we aim to find the set of all candidate solutions that pass a given quality threshold. Since our primary goal is to find a humanly interpretable solution (i.e. a model – a classifier or a regressor), we focus primarily on feature selection (as opposed to prediction). Choosing the final appropriate model for a given application is then an object of further expert, non-mathematical examination.

2 The Problem

We shall use the l_0-norm to describe sparsity of a solution.

Definition 1 (l_0-norm) *Let the l_0-norm of a vector $\beta \in \mathbb{R}^p$ be defined as*

$$||\beta||_{l_0} = \sum_{i=1}^{p} \gamma_i, \quad \textit{where} \quad \gamma_i = \begin{cases} 0 & \textit{if } \beta_i = 0, \\ 1 & \textit{otherwise.} \end{cases}$$

Then the problem can be formulated as follows:

Problem 1 (The Multisolution Regression Problem) *Let $X \in \mathbb{R}^{n \times p}$, $p >> n$, be given data (samples) and $y \in \mathbb{R}^n$ their corresponding labels. For given $\varepsilon \in \mathbb{R}$, $\varepsilon > 0$ and $\delta \in \mathbb{N}$, find $\beta \in \mathbb{R}^p$ such that*

$$||X\beta - y||_{l_2} \leq \varepsilon \qquad \textit{and} \qquad ||\beta||_{l_0} \leq \delta.$$

Parameter δ provides a constraint on a solution's sparsity. Its value is easily provided by the application's context. Parameter ε describes the required optimality of a solution, directly influencing the number of possible solutions. Let us observe that each δ yields an independent problem, while tuning ε is an integral part of the problem.

3 Bayesian Approach to The Problem

Since we want to admit and work with uncertainty within our data, we choose Bayesian approach to Problem [2].

First, we assume Gaussian-distributed noise $e \sim \mathcal{N}(0, \sigma^2 I)$, where I is a unit matrix, in our linear model: $y = X\beta + e$. Therefore, it is

$$\pi(y|\beta) = \mathcal{N}(X\beta, \sigma^2 I).$$

Now let us endow β with an appropriate prior distribution $\pi(\beta) = \pi(\beta|\theta)$, where θ is a vector of the prior's parameters. Then we can compute the maximum a posteriori probability of β:

$$\beta_{MAP} = \mathrm{argmax}_\beta \log \pi(y|\beta) + \log \pi(\beta).$$

Finally, the Bayes theorem provides the formula for computing the posterior distribution of unobserved, latent variables and parameters $\mathcal{Z} = \{\beta, \theta, \sigma^2\}$ given our observed data $\mathcal{X} = \{X, y\}$:

$$\pi(\mathcal{Z}|\mathcal{X}) = \frac{\pi(\mathcal{X}|\mathcal{Z})\ \pi(\mathcal{Z})}{\pi(\mathcal{X})}. \tag{1}$$

Unfortunately, this posterior distribution is intractable in our case. Hence we shall take the following strategy:

1. select an appropriate prior $\pi(\mathcal{Z})$ – effectively the prior distribution on β – aiming for a set of sparse candidate solutions,
2. conveniently approximate the multimodal posterior $\pi(\mathcal{Z}|\mathcal{X})$ and
3. provide computational means to actually find (approximate) solutions of the original Problem 1.

4 The Building Blocks

4.1 Prior Distribution

The Bayesian approach does not only look for the optima, but it also models the shape of the posterior distribution. Since we expect our problem to have multiple solutions, the posterior distribution shall be multimodal. Therefore our choice of a prior must allow for multiple modes. Equally important is the requirement of sparsity upon βs.

As a result, there are three main prior choices that can be used: the Spike & Slab [6], the Student-t [2] and the Horseshoe prior [4].

4.2 Posterior Approximation

Next, we need to approximate the multimodal posterior $\pi(\mathcal{Z}|\mathcal{X})$ and the model evidence $\pi(\mathcal{X})$ with another distribution $q(\mathcal{Z})$ such that it can be used in computations.

Measuring the goodness of fit of such an approximation by the Kullback-Leibler divergence, we utilize the Evidence Lower Bound technique.

Definition 2 (Evidence Lower Bound) *Let π and q be probability distributions. Let the data $\mathcal{X}$ and the latent variables and parameters $\mathcal{Z}$ be as in equation (1). Then let us decompose the log marginal probability as*

$$\log \pi(\mathcal{X}) = \mathcal{L}\big(q(\mathcal{Z})\big) + \mathrm{KL}(q||\pi), \tag{2}$$

where

$$\mathcal{L}\big(q(\mathcal{Z})\big) = \int q(\mathcal{Z}) \log\left(\frac{\pi(\mathcal{X},\mathcal{Z})}{q(\mathcal{Z})}\right) d\mathcal{Z} \tag{3}$$

is the Evidence Lower Bound (ELBO) and

$$\mathrm{KL}\big(q(\mathcal{Z})||\pi(\mathcal{Z}|\mathcal{X})\big) = -\int q(\mathcal{Z}) \log\left(\frac{\pi(\mathcal{Z}|\mathcal{X})}{q(\mathcal{Z})}\right) d\mathcal{Z} \tag{4}$$

is the Kullback-Leibler divergence.

Because decomposition (2) holds, maximizing the lower bound (3) is equivalent to minimizing the KL-divergence (4).

Now it remains to find a surrogate function q such that the posterior's multimodality is preserved, the modes are approximated accurately and the surrogate is significantly easier to use.

The usual choice of q as a product of independent distributions does not comply with our needs. Instead, it is fitting to use a mixture of Gaussian distributions:

$$q(\mathcal{Z}) = \sum_{k=1}^{m} \alpha_k q_k(\mathcal{Z}_k), \tag{5}$$

where $\alpha_k > 0 \ \forall k \in \{1, \dots, m\}$ are the normalization weights. Each component of the mixture corresponds to one solution and/or one mode. Multimodal function $q(\mathcal{Z})$ is then defined as a superposition of these solutions.

To summarize: instead of the original problem, we shall solve the ELBO maximization problem 3, where q is a mixture described by 5.

Problem 2 (The Parametrized Maximization Problem)
Solve

$$\operatorname{argmax}_{\forall \mu^{(k)} \in \ \mathbb{R}^p; \ \forall \sigma_i^{(k)} > \ 0; \ \forall \alpha_k > \ 0} \iint \left(\sum_{k=1}^{m} \alpha_k q_k(\mathcal{Z}_k) \right) \log \left(\frac{\pi(\mathcal{Z}) \ \pi(\mathcal{X}|\mathcal{Z})}{\sum_{k=1}^{m} \alpha_k q_k(\mathcal{Z}_k)} \right) \, d\mu \, d\sigma, \tag{6}$$

where:

- $\pi(\mathcal{Z})$ *is the chosen sparse prior distribution, whose logarithm is not convex,*
- *the likelihood is*

  $$\pi(\mathcal{X}|\mathcal{Z}) = \sum_{k=1}^{m} \frac{1}{\left(\sqrt{2\pi}\sigma_e\right)^n} \ \exp\left\{ -\frac{1}{2\sigma_e^2} ||y - X\beta^{(k)}||_{l_2}^2 \right\},$$

  where the k-th candidate solution $\beta^{(k)}$ *is the mean value of the k-th normal distribution and* σ_e^2 *is the variance of observation error,*
- *components of the surrogate distribution are*

  $$q_k(\mathcal{Z}_k) = \frac{1}{\left(\sqrt{2\pi}\right)^p \prod_{i=1}^{p} \sigma_i^{(k)}} \ \exp\left\{ -\frac{1}{2} \sum_{i=1}^{p} \left(\frac{\beta_i - \mu_i^{(k)}}{\sigma_i^{(k)}} \right)^2 \right\}, \quad \forall k = 1, \dots, m,$$

- *and it is* $\sum_{k=1}^{m} \alpha_k = 1$.

4.3 Solving The Approximate Problem

In order to solve the maximization within Problem 2, we shall use a version of the Stochastic Gradient Descent (SGD) algorithm [3]. Due to the choice of q as a mixture, the maximization cannot be conveniently simplified (as it is in the case of the standard choice of q being a product). In order to compute the gradients within SGD, the implicit version of the reparametrization trick [5] must be used. Paper [8] derives the exact optimization algorithm we need. Within the actual computations, automatic differentiation shall be utilized.

Definition 3 (SGD algorithm for Reparametrized Mixtures) *Let us denote*

$$h(\mathcal{Z}) = \log\left\{\pi(\mathcal{Z})\ \pi(\mathcal{X}|\mathcal{Z})\right\} - \log\left\{\sum_{k=1}^{m} \alpha_k q_k(\mathcal{Z}_k)\right\}$$

and let η be the learning rate.
For a given number of iterations we repeat: for every $k \in \{1, \dots, m\}$ set:

$$\begin{aligned}
\left(\Sigma^{(k)}\right)^{-1} &= \left(\Sigma^{(k)}\right)^{-1} + \eta\delta_k\ \nabla^2\left[h(\mathcal{Z})\right], \\
\mu^{(k)} &= \mu^{(k)} - \eta\delta_k\Sigma^{(k)}\ \nabla\left[h(\mathcal{Z})\right], \\
\delta_k &= \frac{q_k(\mathcal{Z}_k)}{\sum_{k=1}^{m}\alpha_k q_k(\mathcal{Z}_k)}, \\
\alpha_m &= 1 - \sum_{k=1}^{m-1}\alpha_k, \\
\log\left(\frac{\alpha_k}{\alpha_m}\right) &= \log\left(\frac{\alpha_k}{\alpha_m}\right) - \eta\left(\delta_k - \delta_m\right) h(\mathcal{Z}).
\end{aligned}$$

5 Conclusion

We have formulated the multisolution classification/regression problem and outlined the strategy to tackle it. In spite of its similarities to its traditional single solution counterpart, it provides a very challenging setting.

The Bayesian approach is taken to admit all inherent uncertainty within the data as well as to incorporate our requirements of sparsity and multiple solutions. The posterior distribution is approximated by a Gaussian mixture while the goodness of fit is measured by the Kullback-Leibler divergence. The resulting new optimization problem is to be solved using a tailored version of the Stochastic Gradient Descent.

Future work on this problem shall focus on creating a robust and usable implementation of the described method.

6 Acknowledgements

This work was supported by grant SGS21/165/OHK4/3T/14.

References

[1] Daniel Arp, Michael Spreitzenbarth, Malte Hubner, Hugo Gascon, Konrad Rieck, and CERT Siemens. Drebin: Effective and explainable detection of android malware in your pocket. In *Ndss*, volume 14, pages 23–26, 2014.

[2] Christopher M. Bishop. *Pattern recognition and machine learning.* Springer, 2006.

[3] Léon Bottou. Large-scale machine learning with stochastic gradient descent. In *Proceedings of COMPSTAT'2010*, pages 177–186. Springer, 2010.

[4] Carlos M Carvalho, Nicholas G Polson, and James G Scott. Handling sparsity via the horseshoe. In *Artificial Intelligence and Statistics*, pages 73–80, 2009.

[5] Mikhail Figurnov, Shakir Mohamed, and Andriy Mnih. Implicit reparameterization gradients. In *Advances in Neural Information Processing Systems*, pages 441–452, 2018.

[6] Edward I George and Robert E McCulloch. Approaches for bayesian variable selection. *Statistica sinica*, pages 339–373, 1997.

[7] K. Henclová. Little data analysis of bone marrow transplant patients. In *SPMS 2018 Stochastic and Physical Monitoring Systems, Proceedings of the international conference.* ČVUT, Prague, 2018.

[8] Wu Lin, Mohammad Emtiyaz Khan, and Mark Schmidt. Fast and simple natural-gradient variational inference with mixture of exponential-family approximations. *arXiv preprint arXiv:1906.02914*, 2019.

[9] Amir Nikooienejad, Wenyi Wang, and Valen E Johnson. Bayesian variable selection for binary outcomes in high-dimensional genomic studies using non-local priors. *Bioinformatics*, 32(9):1338–1345, 2016.

[10] Cox Lwaka Tamba, Yuan-Li Ni, and Yuan-Ming Zhang. Iterative sure independence screening em-bayesian lasso algorithm for multi-locus genome-wide association studies. *PLoS computational biology*, 13(1):e1005357, 2017.

[11] Robert Tibshirani, Trevor Hastie, Balasubramanian Narasimhan, and Gilbert Chu. Class prediction by nearest shrunken centroids, with applications to dna microarrays. *Statistical Science*, pages 104–117, 2003.

Stochastic and Physical Monitoring Systems
SPMS 2021
June 24 - 28, 2021
Malá Skála, Czech Republic

Homogeneity Testing of Weighted Datasets in High Energy Physics

Kristina Jarůšková and Václav Kůs

Department of Mathematics, FNSPE, Czech Technical University in Prague, Czech Republic

Email: `jaruskri@fjfi.cvut.cz, kus@fjfi.cvut.cz`

Abstract. Simulations of elementary particles play a key role in the attempts to discover new laws of physics, which is why high precision is expected of them. The common approach to generating simulations is the use of Monte Carlo-based algorithms (MC). However, MC simulations are usually in the form of a weighted dataset that makes it impossible to use standard homogeneity tests to verify an agreement between simulations and real measurements. This work examines different approaches to homogeneity testing of weighted datasets and using numerical simulations.

Key words: high energy physics, homogeneity testing, kernel density estimates, re-arranging, weighted samples.

1 Introduction

New findings in High Energy Physics (HEP) often rely on the comparison of theoretical assumptions and experimental measurements. In this comparison, the theory is represented by artificially simulated particle interactions and decays acquired from complex simulation tools based on the Monte Carlo algorithms. One of the steps in the comparison process is verifying that selected physics quantities, e.g. particle energies, angles or momentum, follow the same probability distribution for both the simulated and the measured data without any prior knowledge of the parametric family. In general, this can be achieved using nonparametric tests of homogeneity with the null hypothesis of both datasets following the same distribution.

However, generating events with the Monte Carlo simulator is very time and computationally demanding [1]. For that reason, small changes in the initial simulation set-up often result in adjusting an already existing dataset by assigning weights to individual samples in that dataset rather than running the simulation algorithm again. Then the task changes to testing a weighted dataset against an unweighted one. Unfortunately, the standard homogeneity tests were not built to handle weighted data while neglecting the weights of the simulated data may lead to false conclusions.

First part of this article introduces three possible modifications that enable to account for the weights in the homogeneity testing using the two-sample Kolmogorov-Smirnov test as an example. The three approaches include modification of the test statistic [2] and transforming the weighted dataset to unweighted using a method of re-arranging [3] or the kernel density estimation. To verify the applicability of these approaches, numerical experiments were performed. The methodology and results are described in the second part of this article. Discussion over the results and a comparison of the presented modifications are included at the end.

2 Homogeneity tests

The aforementioned Kolmogorov-Smirnov test was used as an example to examine the different approaches to homogeneity testing of the weighted datasets. The Kolmogorov-Smirnov two-sample test is based on the Kolmogorov distance of distribution functions $F,\ G : \mathbb{R} \to [0,1]$ defined as

$$K(F,G) = \sup_{x\in\mathbb{R}} |F(x) - G(x)|. \tag{1}$$

Using the measured or simulated samples, the distribution functions in (1) are replaced by the empirical cumulative distribution function (ECDF)

$$F_n(x) = \frac{1}{n}\sum_{j=1}^{n} \mathbf{I}_{(-\infty,x]}(X_j), \quad \forall x \in \mathbb{R} \tag{2}$$

where $X_1, X_2, \dots, X_n$ are iid random variables and $\mathbf{I}_{(-\infty,x]}$ is an indicator function of the set $(-\infty, x]$. Let us assume that the simulated and measured datasets contain n and m samples respectively. Then we denote the Kolmogorov distance between ECDFs F_n and G_m as

$$K_{n,m} = \sup_{x\in\mathbb{R}} |F_n(x) - G_m(x)|. \tag{3}$$

Then under the assumptions of the two datasets being independent and the true distribution being continuous, the Kolmogorov-Smirnov test statistic satisfies

$$\sqrt{\frac{nm}{n+m}} K_{n,m} \xrightarrow[n,m\to+\infty]{\mathcal{D}} Z \tag{4}$$

if the data in both datasets were sampled from the same distribution. The random variable Z follows the distribution

$$H(\lambda) = \begin{cases} 1 - 2\sum_{k=1}^{+\infty}(-1)^{k-1}e^{-2k^2\lambda^2} & \text{pro } \lambda > 0, \\ 0 & \text{pro } y \leq 0. \end{cases} \tag{5}$$

The null hypothesis H_0 of the two datasets originating from the same distribution is rejected if

$$\sqrt{\frac{nm}{n+m}} K_{n,m} \geq h_{1-\alpha} \tag{6}$$

where $h_{1-\alpha}$ is the $(1-\alpha)$-quantile of the distribution H. The p-value can be calculated as

$$p - val = 1 - H\left(\sqrt{\frac{nm}{n+m}}K_{n,m}\right). \tag{7}$$

In general, there are two possible ways to testing the homogeneity of two weighted datasets. The first approach is based on a modification of the test statistic to account for the weights assigned to individual samples. The second approach takes the weighted dataset and transforms it into a unweighted data which means creating new samples all with unit weights that all together give similar ECDF.

2.1 Weighted test statistic

To modify the KS test statistic (3), we first replace the ECDF by a weighted empirical cumulative distribution function (WEDF) defined in [4]

$$F_n^W(x) = \frac{1}{W}\sum_{j=1}^{n} W_j\,\mathbf{I}_{(-\infty,x]}(X_j), \quad \forall x \in \mathbb{R} \tag{8}$$

where the $W_1, W_2, \ldots, W_n$ represent the weights assigned to the observations of random variables $X_1, X_2, \ldots, X_n$. Example of how the weights may change the empirical distribution is shown in image 1. Secondly, we replace the number of samples in a dataset that appears under the square root in (3) with an effective sample size

$$n_e = \frac{\left(\sum_{j=1}^{n} W_j\right)^2}{\sum_{j=1}^{n} W_j^2} \approx n\frac{(\mathrm{E}\,W)^2}{\mathrm{E}\,W^2}. \tag{9}$$

Hence, we get a modified KS test statistic

$$\frac{n_e m_e}{n_e + m_e}\sup_{x\in\mathbb{R}} |F_n^W(x) - G_m^V(x)|. \tag{10}$$

However, it was not proved yet that this modified statistic follows the distribution (5) like the standard KS statistic. The possibility to use the modified statistic with the (5) distribution was examined in [5] in the case of one weighted and one unweighted dataset.

This approach can be used for other non-parametric homogeneity tests that are based on the ECDF, e.g. the Anderson-Darling test or the Cramer-von Mises test. The results were satisfactory showing that the true distribution of the modified KS statistic under the null hypothesis is very close to the distribution (5).

2.2 Re-arranging

The approach of using the weighted dataset to generated a unweighted one was also tested. The re-arranging method replaces the weighted samples by a special set of weighted averages that form the new unweighted dataset [3]. Let us assume that we have an

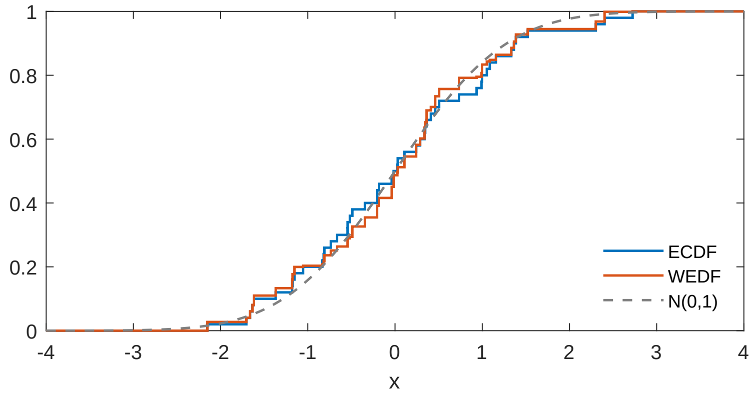

Figure 1: Illustration of the influence of weights to the empirical distribution. (blue) ECDF of 50 observations from N(0,1). (red) WEDF of the same observations with weights from U(0,1).

ordered set of observations $x_{(1)}, x_{(2)}, \ldots, x_{(n)}$ with weights $w_1, w_2, \ldots, w_n$ that satisfy $0 \leq w_i \leq 1\ \forall i$. Then k_1 is such a number that

$$1 \leq \sum_{i=1}^{k_1} w_i < 2. \tag{11}$$

The first observation of the new unweighted dataset is calculated as

$$y_{(1)} = \frac{\sum_{i=1}^{k_1} x_{(i)} w_i - x_{(k_1)} r_{k_1}}{\sum_{i=1}^{k_1} w_i - r_{k_1}} \tag{12}$$

where r_{k_1} denotes a weight residue $r_{k_1} = \sum_{i=1}^{k_1} w_i - 1$. This residual part of the weight w_{k_1} is used in the calculation of the next unweighted observation that is acquired in an analogous manner. An example of the WEDF of a weighted dataset and the ECDF of the re-arranged dataset is depicted in graph 2. Detailed explanation of the re-arranging method with more examples can be found in [4] or [6].

The distributions of the newly created re-arranged datasets can be compared using standard homogeneity test because all samples have unit weights. The obvious drawback is that we are no longer comparing the original data.

2.3 Kernel density estimation

In [6], we proposed using the weighted kernel density estimates to get an estimate of the probability density function and use that to generate a new set of unweighted samples from the estimated distribution. The weighted kernel density estimate (WKDE) in a point t is defined as

$$\hat{f}(t) = \frac{1}{h \sum_{j=1}^{n} W_j} \sum_{j=1}^{n} W_j \, K\left(\frac{t - X_j}{h}\right), \quad \forall t \in \mathbb{R} \tag{13}$$

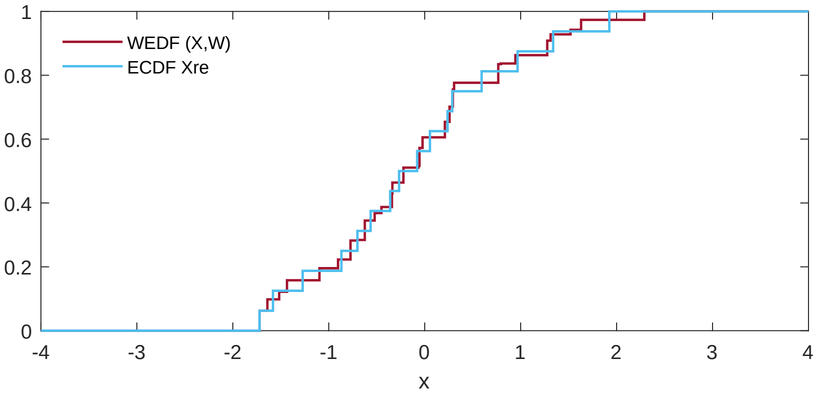

Figure 2: Example of re-arranged dataset. (red) WEDF of 30 samples from N(0,1) with weights from U(0,1). (blue) ECDF of the re-arranged dataset.

with h being the bandwidth parameter and a kernel $K : \mathbb{R} \to \mathbb{R}_0^+$, $\int_{\mathbb{R}} K(t)\,\mathrm{d}t = 1$. For our test, the Gaussian kernel function was used.

To generate new samples from the KDE, a procedure described in [7] was followed. First, a sample X_I is randomly selected taking into account the sample weights. Then a number ε is drawn from a probability distribution defined by the chosen kernel K. Then, the new unweighted observation is given by $X_I + h\varepsilon$. For the new observations, it is possible to use the standard KS test.

The use of adaptive weighted kernel density estimates (AKDE) was also examined. In this case, the bandwidth parameter h changes depending on the population density of the observed samples around the point t.

3 Numerical simulations

All approaches briefly described in the previous section were put to test by performing numerical simulations for observations and weights generated from different probability distributions. The observations were generated from the normal, logistic, lognormal, gamma, or Weibull distributions. It was anticipated that the weights lie in the interval $[0, 1]$. To test various distribution shapes of the weights, we used Beta distribution with different parameters to skew the distribution towards 0 or 1, U shaped variant of the beta distribution was also tested as well as a uniform distribution of the weights. Hence, it is assumed that the weights are independent of the observations.

3.1 Methodology

Firstly, two sets of equal size s were generated from the same distribution. Next, two sets of weights were generated and randomly assigned to the observations. Then we performed the chosen modification of the KS test at a significance level $\alpha = 0.05$ and recorded the p-value and whether the null hypothesis was rejected or not.

The steps described above were repeated $k = 10000$ times. With the certainty that both datasets do follow the same distribution, the proportion of the H_0 rejections on the number of repetitions k should be equal to the significance level α because of the definition of a critical region. This proportion was of our primary interest because it represents an estimate of the type I. error.

Two datasets generated from slightly different distribution were also tested against each other to evaluate the power of the test. To estimate the power, i.e. the ability to reject H_0 when it is not true, we used the proportion of H_0 rejections on the number of repetitions again but this time while knowing that H_0 is not true.

3.2 Results

The examined variants of the KS test were the test with modified statistic, the use of re-arranging technique, and the procedure that includes kernel estimates for both the classical and adaptive KDE. For demonstration purposes, we discuss results of simulations for samples generated from the normal distribution N(0,1) with weights following the Beta(2,4) distribution that is skewed towards 0. The results for different combinations of the sample and weight distributions were similar.

The first plot 3(a) shows the estimate of the type I error for homogeneity testing of two weighted samples generated from the same distribution. We observe that the test with modified statistic (denoted as 'Weighted') had the estimate of the type I error around the significance level $\alpha = 0.05$ for all examined sample sizes s depicted on the x-axis. In case of the tests with kernel estimates, the type I error estimates attained values around 0.1 and grew as we increased the dataset size s. On the other hand, the simulations for the test with re-arranging returned type I error estimates very close to 0 which itself is acceptable.

However, a very low type I error estimate may indicate a low power of a test. For that reason the image 3(b) depicts the stimates of a power of a test. In this case, the weights of both datasets were generated from the Beta(2,4) distribution and the observations in the first dataset followed N(0,1). Most of the samples in the second dataset were also generated from N(0,1) but a small portion of the data was generated from a so-called *error distribution*, in this case from N(0.5,1). The amount of error samples is represented on the x-axis. Both datasets contained $s = 1000$ samples.

Indeed the test with re-arranging has the lowest power. For a small portion of the error samples, the test procedures with kernel estimates show the highest power of test but as we increase the number of error samples, the power of the test with modified statistic increases more quickly than that of the KDE tests. Therefore, the test with modified statistic is the best option for homogeneity testing of two weighted datasets even though the limit distribution of the test statistic was not proved yet. It attains the desired type I error and has a good power of the test.

We tried to examine the reason behind the high value of type I error for the test with kernel estimates. Both a potential problem with PDF estimation in tails or with the choice of the bandwidth parameter h were disproved based on the plots shown in images 4. We also tested a different method to generate samples from the estimate to reject that it was caused by this part of the procedure.

It is most likely that too many inaccuracies are accumulated during the construction

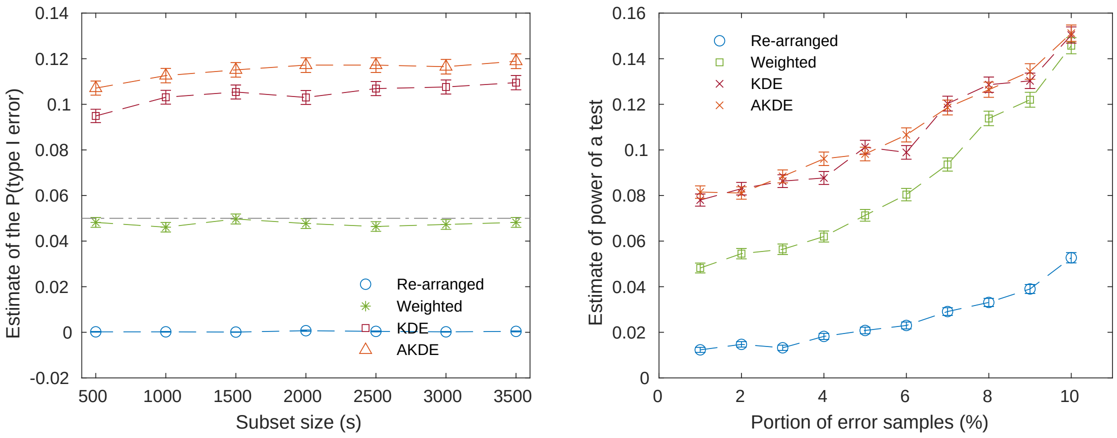

(a) Type I error (b) Power of test

Figure 3: Estimates of the type I error and the power of test for samples from N(0,1) and weights from Beta(2,4). Error samples generated from N(0.5, 1).

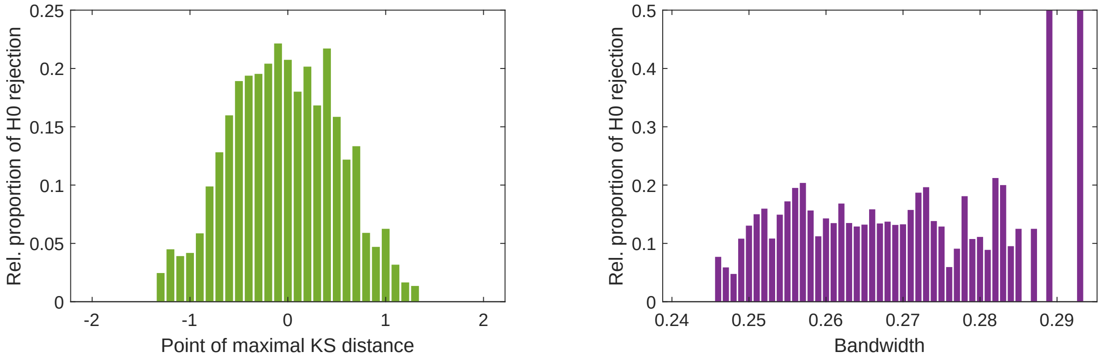

Figure 4: (left) Relative H_0 rejection rate for locations of the supremum in KS distance. (rights) Proportions of H_0 rejection for different bandwidths h.

of the kernel estimate and the random sampling procedure that the KS test is sensitive enough to capture it. As the dataset size increases, the KDE is wavier and more adapted to the given dataset because the bandwidth h gets smaller.

To correct this effect, we propose a solution based on the p-value. Since the results and type I error estimates were very similar for all examined distributions, we may choose a distribution similar to the data that we want to test and run the simulation procedure described earlier and record the p-values. Then the critical value for H_0 rejection can be determined as the α-quantile of the empirical cumulative distribution function of the recorded p-values. The homogeneity test with this critical value is approximately tuned to the significance level α and provides an alternative to the homogeneity tests with modified statistic.

An example of using this correction is shown in plot 5. The samples and weights followed the N(0,1) and Beta(4,2) distribution respectively. The critical value was set to

$p_{krit} = 0.0092$.

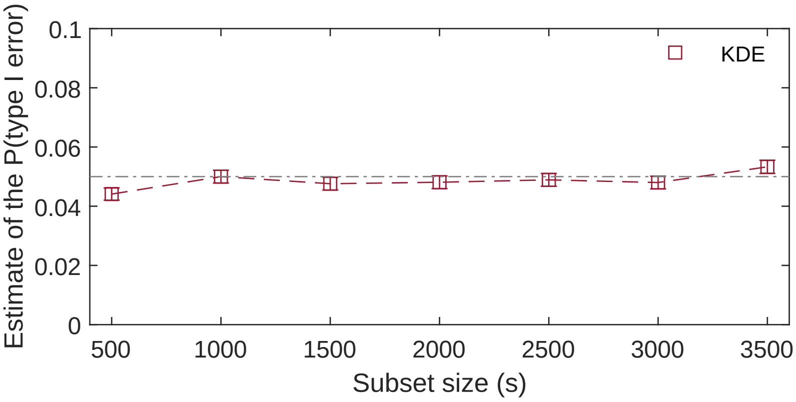

Figure 5: Estimate of type I error for the test with kernel density estimate after the critical value correction.

4 Summary

The homogeneity testing of weighted datasets is still an open problem that arises in many areas including HEP. We described three possible approaches to solving this task - modification of the test statistic and creation of unweighted dataset using re-arranging or kernel density estimates. We also performed numerical simulations to verify the applicability of the proposed procedures on the example of the Kolmogorov-Smirnov test for various sample and weight distributions.

The test with modified statistic attained the best results. The level of significance α was approximately kept together with a good power of the test. Even though the tests with kernel density estimates yielded a high estimate of the type I error, we proposed a correction method that can be applied to tune the test to the desired level of significance.

Acknowledgements

These results were supported by the research grants LTT180001 (MEYS), LM2015068, and SGS21/165/OHK4/3T/14 (MEYS).

References

[1] L. de Oliviera, M. Paganini, B. Nachman. Learning Particle Physics by Example: Location-Aware Generative Adversarial Networks for Physics Synthesis. *Computing and Software for Big Science* [online]. 2017, 1(1) [cit. 2021-4-16].

[2] J. Trusina, J. Franc, A. Novotný. Generalization of Homogeneity Tests for Weighted Samples and Their Implementation in ROOT. *Journal of Physics: Conference Series* [online]. 2020, 1525 [cit. 2021-3-2]. ISSN 1742-6588.

[3] P. Bouř, V. Kůs. Computer simulation on homogeneity testing for weighted data sets used in HEP. *Journal of Physics: Conference Series* [online]. 2018, 1085 [cit. 2021-3-2]. ISSN 1742-6588.

[4] P. Bouř. *Development of statistical nonparametric and divergence methods for data processing in D0 and NOvA experiments.* Mater's thesis. FNSPE CTU in Prague. Prague, 2016.

[5] J. Trusina. *Application of homogeneity testing and event classification in neutrino physics.* Master's thesis. FNSPE CTU in Prague. Prague, 2019.

[6] K. Jarůšková. *Statistical Data Processing of Simulations in High Energy Physics.* Master's thesis. FNSPE CTU in Prague. Prague, 2021.

[7] B. W. Silverman. *Density estimation for statistics and data analysis.* Boca Raton: Chapman & Hall/CRC, 1998. ISBN 0412246201.

Stochastic and Physical Monitoring Systems
SPMS 2021
June 24 - 28, 2021
Malá Skála, Czech Republic

Deep Learning Methods for Acoustic Emission Evaluation

Martin Kovanda[1]; Milan Chlada[2]

[1]Department of Mathematics, FNSPE, Czech Technical University in Prague
[2]NDT laboratory, Institute of Thermomechanics of the CAS, v.v.i.

Email: `kovanma2@fjfi.cvut.cz`

Abstract. The goal of this paper is to show the possibilities of state-of-the-art deep learning methods for ultrasound signals evaluation. Several neural network architectures are applied to acoustic emission signals measured during the tensile tests of metallic specimen to determine the beginning of plasticity in the material. Plastic deformation is accompanied by microscopic events such as a slip of atomic plane dislocations which is hardly detectable by other methods. The potential of machine learning is demonstrated on two tensile tests where the material is strained until it collapses. The examined networks proved well to reliably predict the risk of collapse together with changes in the ultrasound emission signals.

Key words: acoustic emission, deep learning, machine learning, plastic deformation, time series classification.

1 Introduction

The concept of neural networks began already in the 20th century. However, that time it was not popular since these networks have a high computational and memory demands. The learning of deep convolutional networks also require a lot of data which became easier recently, mostly because of the spread of internet and an extensive hardware development.

From the time of AlexNet in 2012 all the state-of-the-art architectures for image classification were based on Convolutional Neural Networks (ConvNets). In the next years a lot of research was made in this field. Soon ConvNets spread to many other recognition tasks. One of them is the Time Series Classification task (TSC) which involves various problems including the signal recognition, stock market analysis and other tasks including variables changing in time.

Contemporary rapid development of deep learning models enables also their application in various fields where traditional perceptron architectures generally fail, e.g. the evaluation of continuous ultrasound signals emitted by a plastic deformation of metals. Plasticity is the ability of materials to be permanently deformed using an external force.

This phenomena should be known very well for each type of material and considered properly to avoid fatal failures of designed structures.

A goal of this paper is to create a deep learning model capable of detecting the beginning of plasticity in metallic materials. For this purpose several experiments on this matter were made in the Institute of Thermomechanics of the Czech Academy of Sciences. In this paper we use results of two tensile tests of metallic specimen, while continuous acoustic emission (ultrasonic elastic waves) was recorded by USB oscilloscope using two sensors attached on the surface of material. These ultrasound signals were then used in order to train neural networks for the plastic deformation detection.

2 Experiments - tensile tests

Acoustic emission (AE) is a phenomenon of radiation of transient elastic waves occurring in solids due to dynamic changes inside the material [1]. This can be caused by many different processes such as mechanical twinning, dislocation slip, initiation and growth of cracks, phase transformation in metals, and corrosion.

A big advantage of the AE is that it offers a non-destructive way how to examine of all the material volume. For this reason this method can be used to analyze processes happening within the component, e.g. local microscopic changes in the material leading to a permanent deformation, i.e. plasticity [1].

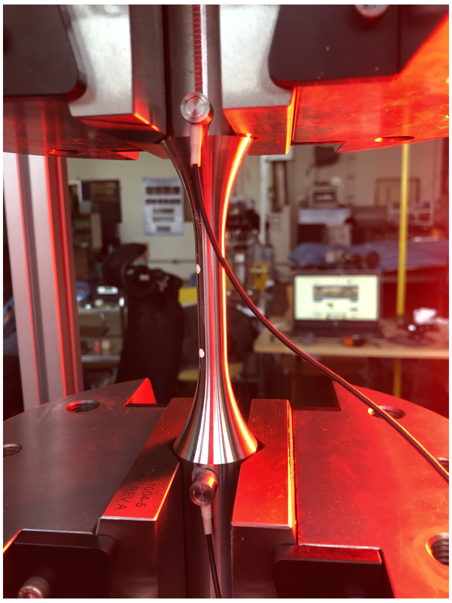

Figure 1: Metalic specimen with two attached sensors.

We will examine some neural network architectures created in recent years on real signals. Here tensile testing machine stretches a metallic component with a computer-controlled force or displacement, see figure 1. Two sensors (transducers) were measuring the AE arising from the material by converting the elastic waves into electrical signals. The sensing process also involves using a preamplifier in order to minimize inferences which would create a lot of noise in the signal [1].

In both experiments the signal was measured with a sampling frequency of around 1.6MHz saved in float32 data type. The first experiment (controlled by force) was almost 11.5 minutes long. Figure 2 shows the force and displacement in relation with time. Here the plasticity begins around 300s and further increases from about 520 second. The middle part (430s - 530s) is stable since the experiment was paused.

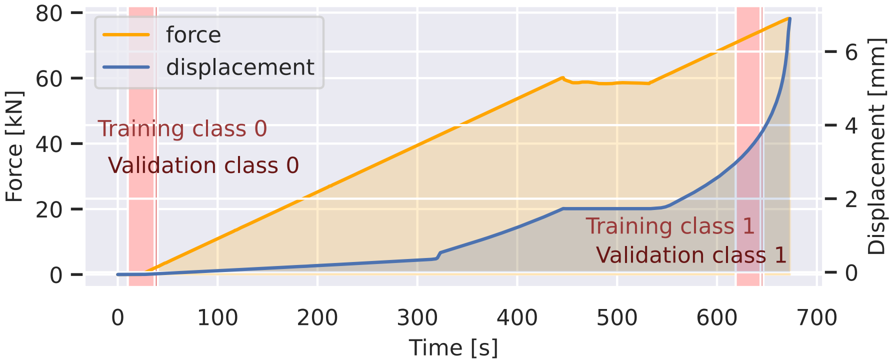

Figure 2: Loading force and displacement during the first experiment.

However, in this experiment one sensor failed due to an accidental weak acoustic coupling to the material surface. The training intervals were set to $[10, 37]$s for the elasticity part and $[618.7, 643.7]$s for the plasticity part. The validation intervals were $[37, 40]$s for the elasticity part and $[643.7, 646.5]$s for the plasticity part.

The second experiment is similar to the first one. The main difference is that this experiment was controlled by displacement and the noise from the tensile testing machine was damped by special polyamide plates in order to measure more relevant data, i.e. the signal arising exactly from the examined component. The time of the experiment also increased from 686.5s of the first experiment to 1404.0s of the second one, see Figure 3. The training intervals were set to $[60, 141]$s for the elasticity part and $[900, 981]$s for the plasticity part. The validation intervals were $[141, 150]$s for the elasticity part and $[981, 990]$s for the plasticity part.

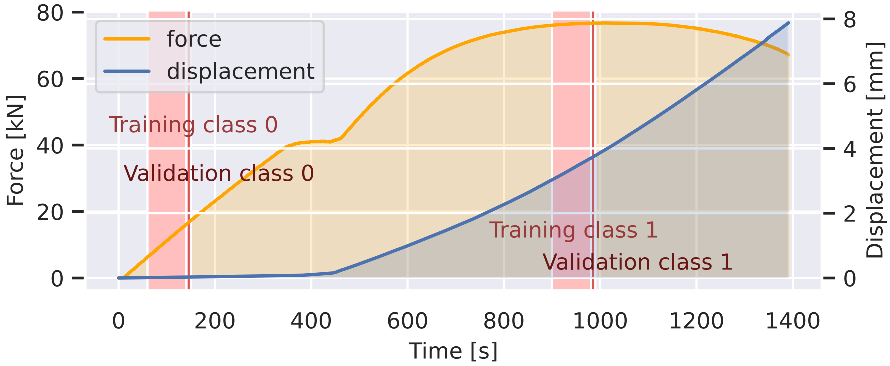

Figure 3: Loading force and displacement during the second experiment.

For simplicity, in the following results these graphs will be shown scaled to a range of $[0, 1]$ without any description.

3 Program backend

All the examined neural networks are created in the `keras` library with the `tensorflow` back-end since it is well implemented and optimized for training on GPU. Training on GPU instead of CPU is crucial in order to speed up all the process. For this reason the NVIDIA GEFORCE RTX 2070 with 8GB memory was used in both the training and evaluation process. After a successful training all the signal is evaluated in order to predict the beginning of plasticity. Since there is no reasonable way how to exactly determine what is happening between the training intervals, these results are then discussed with experts who can determine if this prediction is valid or not.

Since the signal is continuous, the input can be taken from any position in the training intervals. This allows creating an extensive set of input tensors (or arrays) which are all different. This approach can help reducing the overfitting.

Following experiments show that signal evaluation is in general very unstable so the results are always smoothed using a Gauss window with manually chosen deviation.

3.1 HFD Spectrogram

In order to use the 2D convolutional neural networks the signal has to be transformed into a matrix (tensor with one channel) using a carefully chosen time-frequency transformation. In this work we use a modified version of spectrogram called the High Frequency Density (HFD) spectrogram defined as

$$P(m, f_{rel} \cdot N_q) = \left| \sum_{n=0}^{N-1} x(n\Delta_s) \mathrm{e}^{-\pi i n f_{rel}} \omega(n - km) \right|^2, \tag{1}$$

where f_{rel} is a frequency relative to the Nyquist frequency, $\omega(t)$ represents a transformation window function, Δ_s denotes the sampling period, $x(t)$ stands for the signal, N for the transformed interval length, and k for a stride of the window application. Unlike the short-time Fourier transform, the HFD spectrogram does not have a problem with a dilemma between the frequency and time resolution and the time window length can be set arbitrarily.

4 Numerical experiments

For all the architectures several individual networks are always trained using different starting weights. This approach is important in order to determine the stability of the network with respect to the random initialization. Very different predictions could indicate wrongly chosen hyper-parameters of the network or inappropriate training parameters.

The first considered architecture is the multilayer Perceptron. The reason why we examine this architecture is that it is being mentioned in many scientific papers in the Time Series Classification (TSC). This model generally has a big memory demand and it is critically sensitive to the signal shift than the convolutional networks.

Since all the neurons from one layer are connected to all the neurons from the following layer, if the input size would be e.g. $2^{14} = 16384$ and the first layer would use 1024 neurons, there would be already around 16M parameters in that layer.

The 8 independently trained networks on 5582480 data with a shape of 1x16384 have a training accuracy of about 88% and validation accuracy varying between 48% and 83%. This extreme instability makes the prediction of Perceptron untrustworthy. In addition, this model has more than 200MB which makes Perceptron the worst efficient model we have examined.

The next considered architecture is a 2D convolutional neural network similar to AlexNet. It consists of 5 convolutional layers stacked to pooling layers, followed by flattening, a dropout with a value of 0.3 and two dense layers. There are many ways how to optimize this model better on the experimental data. However, these results are shown as a demonstration that these models are unstable and require a lot of manual hyper-parameter optimization.

As shown in Figure 4, the evaluation is more trustful than the Perceptron model. However, the training is still unstable. The same architectures trained on the same data with different initial weights are making various predictions. In addition, some of them completely failed to train properly since they predict the same class for most of the signal.

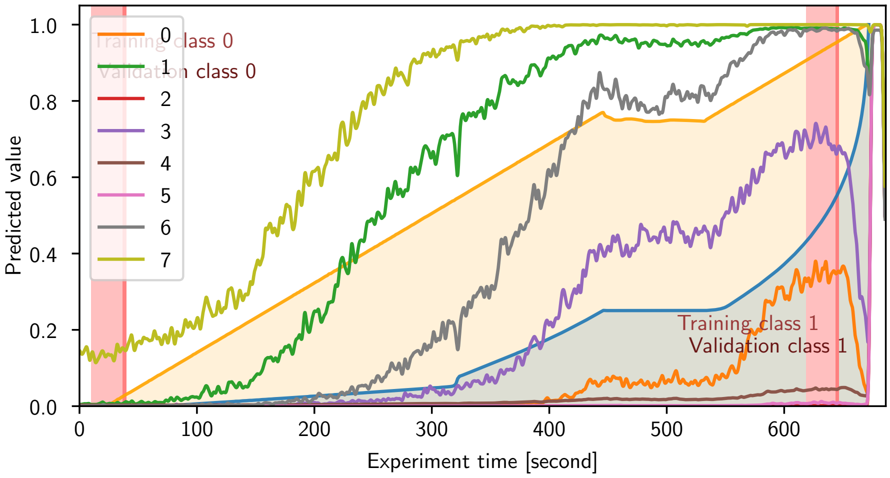

Figure 4: Simple ConvNets applied to all the signal from the first experiment.

Another architecture used to predict plasticity is based on the EfficientNet model [3]. Unlike the simple convolutional network, the EfficientNet uses residual learning together with multi-threaded modules. However, this whole family of models were created primarily to the ImageNet recognition task including 1000 classes. Since the ImageNet images are very different from the result of HFD spectrogram, we decided to train the model from randomly initialized weights and we chose the EfficientNet-B1 in order to make this model simple.

The result is shown in Figure 5. As the Alexnet model, some networks did not learn to detect plasticity at all, some of them with problems. There are many optimization options in training the EfficientNet model. However, these results already indicate that the training process is unstable or that the HFD spectrogram does not necessarily provide a proper feature extraction from the signal.

The last architecture we decided to test is based on the InceptionTime (see Figure 6) [2]. This architecture introduced by Fawaz et al. in 2020 has many advantages in

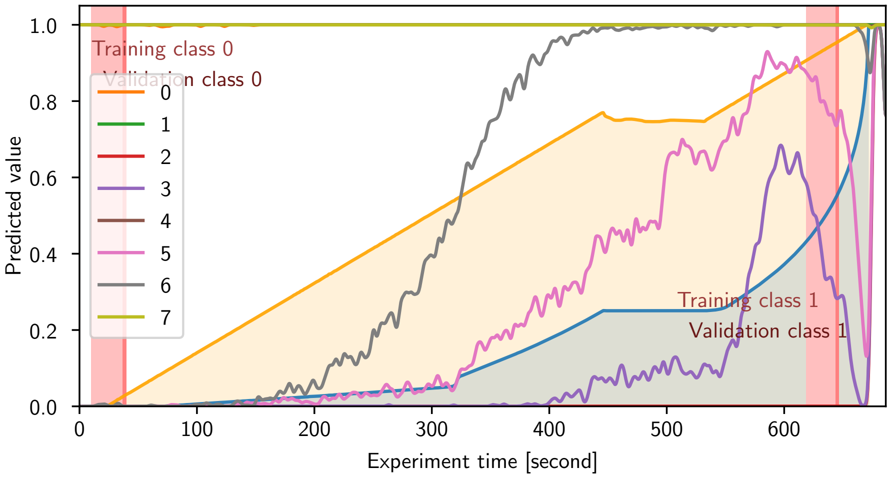

Figure 5: EfficientNet models applied to all the signal from the first experiment.

its usage. As the Perceptron model the InceptionTime does not need any additional transformation since it is being applied to a matrix (in this case vector) data.

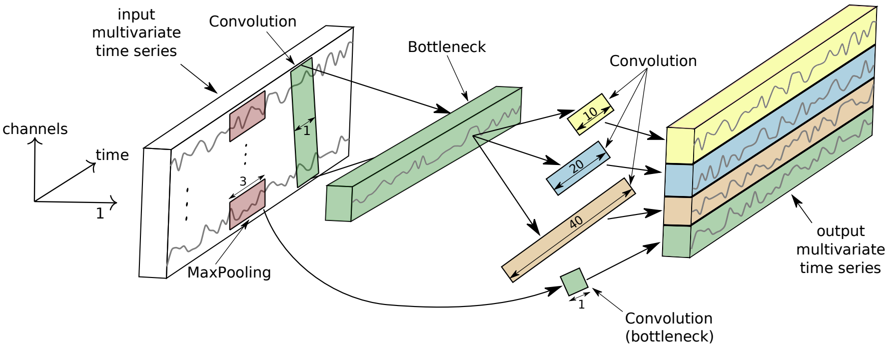

Figure 6: InceptionTime architecture.

However, unlike the Perceptron, the 1D convolution is used in order to extract the time features. This also makes the model less sensitive to a signal shift. Another advantage is that in the convolutional layers neurons are not connected densely. Instead, each neuron contains a convolution core with only a few parameters (in this case between 1 and 40). These cores are being applied along all the input signal in order to produce the output matrix.

The chosen InceptionTime architecture was build from 3 InceptionTime modules and a bottleneck with a size of 32. Since there are much less parameters, the network has less problems with overfitting while having a less memory demand. The tested models have only 2MB compared to more than 200MB of Perceptron while having much better prediction ability. The results are depicted in Figure 7. In all the 8 tested models the results look almost the same, only with a different scaling between the training intervals. Furthermore, in all of them the peak around the time of 320s is visible and all of them perfectly predict the training (and validation) intervals.

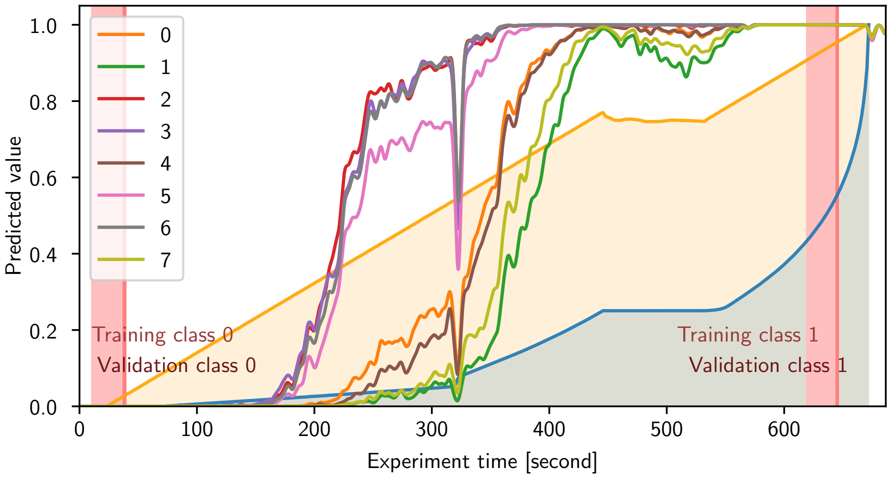

Figure 7: InceptionTime models applied to all the signal from the first experiment.

4.1 Cross-channel generalization

In the previous experiments all networks were validated on data from the same sensor which was used for their training. However, in order to create a model that could be used for detecting plasticity in unknown components, these networks have to be able to generalize their predictions also to sensors located on different places, preferably on different components.

In the second experiment there are data from two sensors available. In order to determine the level of generalization of each model, all the networks are trained on one channel and then evaluated on the second one. Perceptron and Alexnet networks were not good already on the same signal. EfficientNet appeared to work well on generalization between channels, however, only on the experiment which contained less noise. Compared to InceptionTime, the EfficientNet results were also less stable and require a computation demanding time-frequency transformation. For this reason we will only show the InceptionTime results.

Figure 8 shows that InceptionTime is still stable in prediction even though the elasticity part is scaled differently depending on the used network. It is also worth mentioning that none of InceptionTime networks that we trained would completely fail to learn to detect plasticity.

5 Conclusion

In this work four chosen architectures are tested throughout two experiments. From the examination we deduce following results.

The Perceptron model described in many papers appears to be inappropriate for the Time Series Classification task since it has a high memory demand together with very weak prediction abilities. A simple AlexNet-like model together with the EfficientNet-B1 models are performing better with less memory demand, however, they both overly rely on the used time-frequency transformation which requires a lot of manual work on choosing the hyper-parameters. In this paper we use solely a described HFD spectrogram.

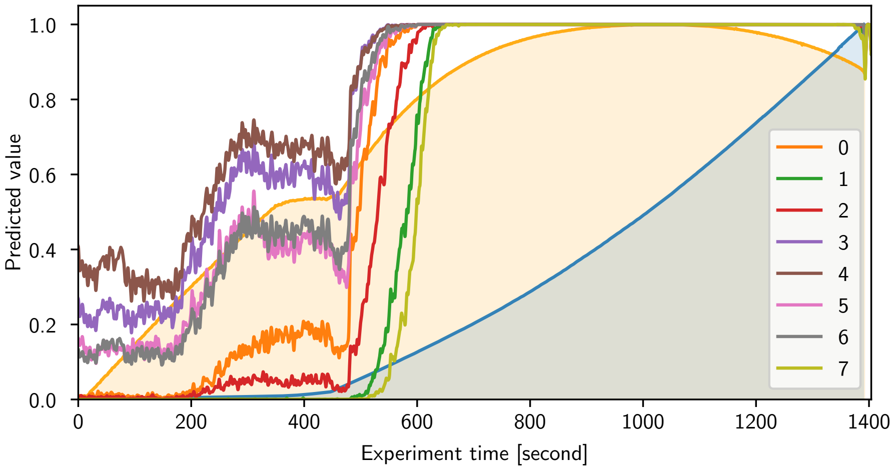

Figure 8: InceptionTime models applied to all the channel 1 signal from the second experiment.

Compared to the AlexNet-like model, the EfficientNet is better in generalization since it performs well even on signal which it was not trained on. However, as shown in the first experiment, it is still sensitive to noises presented in the signal.

Finally, the last model called the InceptionTime performs well on signals from both experiments regardless of the presented noise. Furthermore, this architecture predicts reliable values for a signal measured on other part of the material and even for a signal from another experiment. This makes InceptionTime the best examined model capable of detection the beginning of plastic deformation. This network also does not require any time-frequency transformation since it is being applied to the raw signal. However, it is worth mentioning that the measured signal contains noise coming from the tensile test machine and hence more research will be needed in order to confirm our results and to prove that the neural networks fit the coming information more likely from the material processes than the machine hydraulic system.

Acknowledgements

This work was funded by the institutional support RVO: 61388998.

References

[1] Patrik Dobroň. *An acoustic emission study of plasticity in crystalline materials.* 2016.

[2] Ismail Fawaz et al. InceptionTime: Finding AlexNet for time series classification *Data Mining and Knowledge Discovery*, **34**, 1936–1962, 2020.

[3] Mingxing Tan and Quoc V. Le *EfficientNet: Rethinking Model Scaling for Convolutional Neural Networks.* 2020.

Stochastic and Physical Monitoring Systems
SPMS 2021
June 24 - 28, 2021
Malá Skála, Czech Republic

Scaling of the Generalized Inverse Gaussian Distribution

Anežka Lhotáková and Milan Krbálek

Department of Mathematics, FNSPE, Czech Technical University in Prague, Czech Republic

Email: `lhotaane@fjfi.cvut.cz`

Abstract. The Generalized Inverse Gaussian distribution (GIG) is frequently used in the vehicular traffic modelling. Its properties for non-negative value of parameter α have been presented in previous research [7]. The objective of this paper is to follow up discovered relations and further explore properties of GIG with the negative value of parameter α, such as normalization constant and the approximation of scaling constant. Because of the symmetric properties of Macdonald's function, many procedures from previous research can be adjusted and re-applied for GIG with negative value of α. The main output of this article is analytical derivation of the scaling condition and asymptotical expression for the scaling constant.

Key words: GIG distribution; Scaling; Macdonald's function; Balanced density.

1 Introduction

The Generalized Inverse Gaussian distribution (GIG) became popular in the last decades, mainly in the field of vehicular headway modelling [1, 2, 3, 4, 6]. Since the calculations associated with the GIG distribution are mostly solved through numerical approach, many theoretical aspects remain unanswered. In this paper we will focus on one of this unresolved problem, namely the problem of scaling of the GIG distribution. Because of the application in the field of particle system modelling, we will focus on GIG parametrization, which is in consonance with the definition of balanced density.

Definition 1 (Balanced density) *Let* $f : \mathbb{R} \to \mathbb{R}$*. Then function* $f(x)$ *is called the balanced density (and denoted* $f(x) \in \mathscr{B}$*), if following axioms are fulfilled*

(1) $\mathrm{Ran}(f) \subset \mathbb{R}_0^+$ *and* $\mathrm{Dom}(f) = \mathbb{R}$*,*

(2) $f(x) \in \mathscr{PC}(\mathbb{R})$*, i.e.* $f(x)$ *is piecewise continuous;*

(3) $f(x) \in \mathscr{L}(\mathbb{R})$*, i.e.* $f(x)$ *is integrable;*

(4) $\mathrm{supp}(f) \subset (0, +\infty)$*, i.e.* $f(x)$ *has a positive support* $\mathrm{supp}(f) = \{x \in \mathbb{R} : \ f(x) > 0\}$*;*

(5) Balance axiom: $\exists\ \varkappa \in \mathbb{R}^+$ *such that*

$$\alpha > \varkappa \Rightarrow \lim_{x\to+\infty} f(x)\mathsf{e}^{\alpha x} = +\infty,$$
$$\alpha < \varkappa \Rightarrow \lim_{x\to+\infty} f(x)\mathsf{e}^{\alpha x} = 0.$$

According to the previous definition Generalized Inverse Gaussian distribution (see [5])

$$f(x) = A\Theta(x)x^{\alpha}\mathsf{e}^{-\frac{\beta}{x}}\mathsf{e}^{-\lambda x}, \tag{1}$$

where $\Theta(x)$ represents Heaviside unit-step function

$$\Theta(x) = \begin{cases} 1 \text{ for } x > 0, \\ 0 \text{ for } x \leq 0, \end{cases}$$

is the balanced density provided that $A > 0, \alpha \in \mathbb{R}, \beta > 0, \lambda > 0$. By solving the normalization equation given by $\int_{\mathbb{R}} f(x)\mathsf{d}x \overset{!}{=} 1$ for GIG distribution (1) we obtain a normalization constant in the form

$$A = \frac{\left(\sqrt{\frac{\lambda}{\beta}}\right)^{\alpha+1}}{2\mathscr{K}_{\alpha+1}(2\sqrt{\beta\lambda})},$$

where $\mathscr{K}_{\alpha}(x)$ represents Macdonald's function. Macdonald's function is also known as modified Bessel's function of the second kind, because it solves modified Bessel's differential equations known from [8] as

$$x^2\mathscr{K}_{\alpha}''(x) + x\mathscr{K}_{\alpha}'(x) - (x^2+\alpha^2)\mathscr{K}_{\alpha}(x) = 0.$$

Alternatively, Macdonald's function has a following integral representation

$$\mathscr{K}_{\alpha}(x) = \frac{2^{\alpha-1}}{x^{\alpha}}\int_0^{+\infty} y^{\alpha-1}\mathsf{e}^{-y}\mathsf{e}^{-\frac{x^2}{4y}}\mathsf{d}y. \tag{2}$$

2 Scaling equation

Finding normalization constant has been easily done in the previous section. However, finding scaling constant λ is more complex problem and requires more prudent approach. Scaling GIG distribution means to solve the following equations

$$\mu_0 = \int_{\mathbb{R}} f(x)\mathsf{d}x \overset{!}{=} 1 \text{ and } \mu_1 = \int_{\mathbb{R}} xf(x)\mathsf{d}x \overset{!}{=} 1. \tag{3}$$

First condition represents normalization equation, which is automatically fulfilled for GIG distribution in the form of

$$f(x) = \Theta(x)\frac{\left(\sqrt{\frac{\lambda}{\beta}}\right)^{\alpha+1}}{2\mathscr{K}_{\alpha+1}(2\sqrt{\beta\lambda})}x^{\alpha}\mathsf{e}^{-\frac{\beta}{x}}\mathsf{e}^{-\lambda x}. \tag{4}$$

The second condition (scaling equation) leads to the following expression

$$\int_0^{+\infty} \frac{\left(\sqrt{\frac{\lambda}{\beta}}\right)^{\alpha+1}}{2\mathscr{K}_{\alpha+1}(2\sqrt{\beta\lambda})} x^{\alpha+1}\mathtt{e}^{-\frac{\beta}{x}}\mathtt{e}^{-\lambda x}\mathtt{d}x = \sqrt{\frac{\beta}{\lambda}}\frac{\mathscr{K}_{\alpha+2}(2\sqrt{\beta\lambda})}{\mathscr{K}_{\alpha+1}(2\sqrt{\beta\lambda})} = 1. \tag{5}$$

Apparently, it is impossible to explicitly express the scaling constant λ from (5). Naturally, the question arises whether the solution of (5) exists for all possible parameter combinations? Let's make a small diversion and analyse the second moment $\mu_2 = \int_{\mathbb{R}} x^2 f(x)\mathtt{d}x$. Assume normalized and scaled GIG distribution, which means that conditions (3) are fulfilled. From (5) we know that

$$\sqrt{\frac{\beta}{\lambda}}\mathscr{K}_{\alpha+2}(2\sqrt{\beta\lambda}) = \mathscr{K}_{\alpha+1}(2\sqrt{\beta\lambda}). \tag{6}$$

The second moment is equal to

$$\mu_2 \overset{(2)}{=} \frac{\beta}{\lambda}\frac{\mathscr{K}_{\alpha+3}(2\sqrt{\beta\lambda})}{\mathscr{K}_{\alpha+1}(2\sqrt{\beta\lambda})} \overset{\star}{=} \frac{\beta}{\lambda}\frac{\mathscr{K}_{\alpha+1}(2\sqrt{\beta\lambda}) + \frac{2(\alpha+2)}{2\sqrt{\beta\lambda}}\mathscr{K}_{\alpha+2}(2\sqrt{\beta\lambda})}{\mathscr{K}_{\alpha+1}(2\sqrt{\beta\lambda})} \overset{(6)}{=} \frac{\alpha+\beta+2}{\lambda}, \tag{7}$$

where operation $\star$ represents application of the following recurrence property

$$\mathscr{K}_{\alpha-1}(x) - \mathscr{K}_{\alpha+1}(x) = -\frac{2\alpha}{x}\mathscr{K}_{\alpha}(x). \tag{8}$$

Since the second moment is defined by $\mu_2 = \int_{\mathbb{R}} x^2 f(x)\mathtt{d}x$, then

$$\mu_2 = \frac{\left(\sqrt{\frac{\lambda}{\beta}}\right)^{\alpha+1}}{2\mathscr{K}_{\alpha+1}(2\sqrt{\beta\lambda})}\int_0^{+\infty} x^{\alpha+2}\mathtt{e}^{-\frac{\beta}{x}}\mathtt{e}^{-\lambda x}\mathtt{d}x \geq 0,$$

which implies that

$$\mu_2 \overset{(7)}{=} \frac{\alpha+\beta+2}{\lambda} \geq 0.$$

Unfortunately, $\alpha \in \mathbb{R}$, which warn us that for some $\alpha, \beta \in \mathbb{R}$ it holds $\frac{\alpha+\beta+2}{\lambda} < 0$. This ascertainment encourages us to take further action in order to explain this anomaly.

3 Existence of the scaling equation's solution

Surprisingly, even the fact, that GIG is a density (and in its normalized form even probability density), does not guarantee a scalability. Described by words, scaling equation demands the expected value of a random variable X given by distribution g to be equal to 1. But what if for some parameter combinations the expected value of GIG distribution (4) cannot reach the value of 1? In the following text we will demonstrate, that such combinations of α and β do exist. That forces us to form a precise scaling condition for GIG distribution. In order to introduce the problem more closely, let's take a look at the function

$$f_\alpha(\beta,\lambda) = \sqrt{\frac{\beta}{\lambda}}\frac{\mathscr{K}_{\alpha+2}(2\sqrt{\beta\lambda})}{\mathscr{K}_{\alpha+1}(2\sqrt{\beta\lambda})}$$

occurring in the scaling equation (5). In the following Figure 1 it is illustratively shown that for combination of $\alpha = -5$ and small β, there is no value of function $f_{-5}(\beta, \lambda)$ exceeding the value of 1. In the following Figure 2 it is demonstrated how a density, which cannot be scaled, behaves. In this example it is shown, that even for extremely small values $\epsilon > 0$ the distribution's expected value cannot reach the unit value. Moreover, for this particular parameter combination, the function cannot even exceed the value of $\frac{1}{2}$.

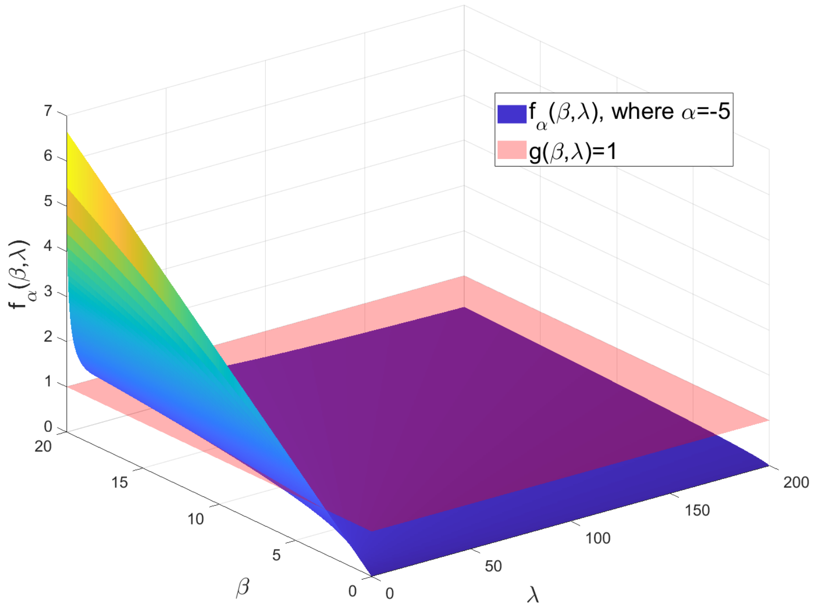

Figure 1: Demonstration that for some combinations of α, β it is impossible to find such λ, that the equality $f_\alpha(\beta, \lambda) = 1$ is fulfilled.

Theoretical explanation can be done via theory of implicit functions. For fixed α we define function $\Phi : \mathbb{R}^2 \to \mathbb{R}$ by

$$\Phi(\beta, \lambda) = \sqrt{\frac{\beta}{\lambda}} \frac{\mathscr{K}_{\alpha+2}(2\sqrt{\beta\lambda})}{\mathscr{K}_{\alpha+1}(2\sqrt{\beta\lambda})} - 1 = f_\alpha(\beta, \lambda) - 1. \tag{9}$$

We aim to find set M of all possible β, for which

$$\Phi(\beta, \lambda) = 0. \tag{10}$$

Under these circumstances $\Phi(\beta, \lambda)$ generates an unique implicit function $\lambda(\beta)$, i.e. the solution of the scaling equation exists. Let's consider this function as a function $\Phi(\lambda)$ with parameter $\beta > 0$ and for simplification let's substitute $z = 2\sqrt{\beta\lambda}$. We will analyse this function in the following form

$$\Phi(z) = \frac{2\beta}{z} \frac{\mathscr{K}_{\alpha+2}(z)}{\mathscr{K}_{\alpha+1}(z)} - 1. \tag{11}$$

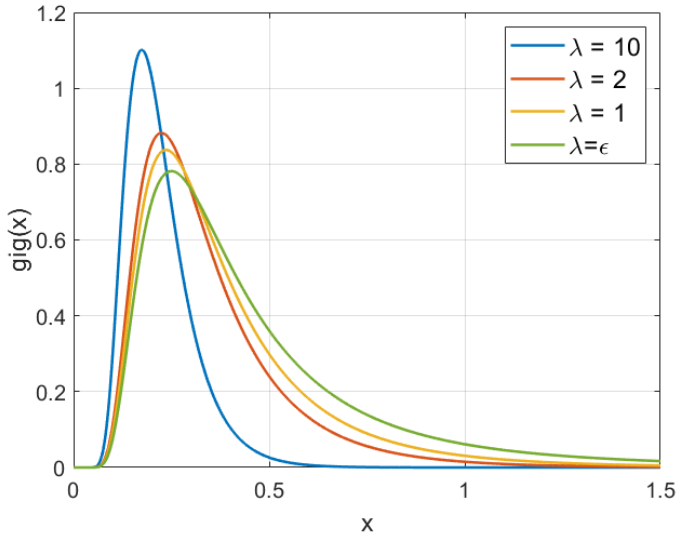

Figure 2: Normalized Generalized Inverse Gaussian distribution (4) with $\alpha = -5, \beta = 1$ and different $\lambda \in \{10, 2, 1, \epsilon\}$, where ϵ has a meaning of very small values.

Please note that $\mathrm{Dom}(\Phi) = (0, +\infty)$ and $\mathrm{Ran}(\Phi) \subset (-1, +\infty)$. As Figure 1 indicates, we try to explore if maximum/supremum of function (11) reaches or exceeds zero, because after relabelling the scaling equation transforms into the form $\Phi(z) = 0$. Let's concentrate our focus on the border point of $\mathrm{Dom}(\Phi)$, i.e. $z = 0$, and analyse the value of $\lim\limits_{z\to 0_+} \Phi(z)$. For the following calculation we consider – in addition to (8) – the second useful property of Macdonald's function

$$\mathscr{K}_\alpha(x) = \mathscr{K}_{-\alpha}(x) \tag{12}$$

and also the approximation of Macdonald's function for small x (known from [7]) as

$$x^\alpha \mathscr{K}_\alpha(x) \approx 2^{\alpha-1}\Gamma(\alpha)(2\alpha-1)^{\frac{1}{2}-\alpha}\,(2x+2\alpha-1)^{\alpha-\frac{1}{2}}\,\mathsf{e}^{-x} = \frac{1}{2}2^\alpha\Gamma(\alpha)\left[1 + \frac{2x}{2\alpha-1}\right]^{\alpha-\frac{1}{2}}\mathsf{e}^{-x}. \tag{13}$$

In order to inspect the following limit

$$\lim_{z\to 0_+} \frac{2\beta}{z}\frac{\mathscr{K}_{\alpha+2}(z)}{\mathscr{K}_{\alpha+1}(z)} - 1,$$

we will divide the calculation into five separate sections according to the value of parameter α

1) $\alpha > -1$:

$$\lim_{z\to 0_+} \frac{2\beta}{z}\frac{\mathscr{K}_{\alpha+2}(z)}{\mathscr{K}_{\alpha+1}(z)} - 1 = \lim_{z\to 0_+} \frac{2\beta}{z^2}\frac{z^{\alpha+2}\mathscr{K}_{\alpha+2}(z)}{z^{\alpha+1}\mathscr{K}_{\alpha+1}(z)} - 1 \overset{(13)}{=} \lim_{z\to 0_+} \frac{4\beta}{z^2}\frac{\Gamma(\alpha+2)\left[1+\frac{2z}{2\alpha+3}\right]^{\alpha+\frac{3}{2}}}{\Gamma(\alpha+1)\left[1+\frac{2z}{2\alpha+1}\right]^{\alpha+\frac{1}{2}}} - 1$$

$$\overset{\boxtimes}{=} 4\beta(\alpha+1)\lim_{z\to 0_+} \frac{1}{z^2}\frac{\left[1+\frac{2z}{2\alpha+3}\right]^{\alpha+\frac{3}{2}}}{\left[1+\frac{2z}{2\alpha+1}\right]^{\alpha+\frac{1}{2}}} - 1 \overset{\star}{=} +\infty,$$

2) $\alpha = -1$:

$$\lim_{z\to 0_+} \frac{2\beta}{z}\frac{\mathscr{K}_1(z)}{\mathscr{K}_0(z)} - 1 \overset{(8)}{=} \lim_{z\to 0_+} \frac{2\beta\mathscr{K}_1(z)}{z\mathscr{K}_2(z) - 2\mathscr{K}_1(z)} - 1 \overset{(13)}{=} \lim_{z\to 0_+} \frac{2\beta\left[1+2z\right]^{\frac{1}{2}}}{2\Gamma(2)\left[1+\frac{2z}{3}\right]^{\frac{3}{2}} - 2\left[1+2z\right]^{\frac{1}{2}}} - 1$$

$$= \beta \lim_{z\to 0_+} \frac{\left[1+2z\right]^{\frac{1}{2}}\left(\left[1+\frac{2z}{3}\right]^{\frac{3}{2}} + \left[1+2z\right]^{\frac{1}{2}}\right)}{\left[1+\frac{2z}{3}\right]^{3} - \left[1+2z\right]} - 1 = +\infty,$$

3) $\alpha \in (-1,-2)$:

$$\lim_{z\to 0_+} \frac{2\beta}{z}\frac{\mathscr{K}_{\alpha+2}(z)}{\mathscr{K}_{\alpha+1}(z)} - 1 \overset{(13)}{=} \lim_{z\to 0_+} \frac{\beta\, 2^{2(\alpha+2)}}{z^{2(\alpha+2)}} \frac{\Gamma(\alpha+2)\left[1+\frac{2z}{2\alpha+3}\right]^{\alpha+\frac{3}{2}}}{\Gamma(-\alpha-1)\left[1-\frac{2z}{2\alpha+3}\right]^{-\alpha-\frac{3}{2}}} - 1$$

$$= \beta \lim_{z\to 0_+} \underbrace{\frac{2^{2(\alpha+2)}\Gamma(\alpha+2)}{\Gamma(-\alpha-1)}}_{>0} \frac{\left(1-\frac{4z^2}{(2\alpha+3)^2}\right)^{\alpha+\frac{3}{2}}}{z^{2(\alpha+2)}} - 1 = +\infty,$$

4) $\alpha = -2$:

$$\lim_{z\to 0_+} \frac{2\beta}{z}\frac{\mathscr{K}_0(z)}{\underbrace{\mathscr{K}_{-1}(z)}_{\overset{(12)}{=}\mathscr{K}_1(z)}} - 1 \overset{(13)}{=} \lim_{z\to 0_+} \frac{2\beta\mathscr{K}_0(z)}{(1+2z)^{\frac{1}{2}}} - 1 = \frac{\lim\limits_{z\to 0_+} 2\beta\mathscr{K}_0(z)}{1} - 1 = +\infty,$$

5) $\alpha < -2$:

$$\lim_{z\to 0_+} \frac{2\beta}{z}\frac{\mathscr{K}_{\alpha+2}(z)}{\mathscr{K}_{\alpha+1}(z)} - 1 \overset{(12)}{=} 2\beta \lim_{z\to 0_+} \frac{z^{-\alpha-2}\mathscr{K}_{-\alpha-2}(z)}{z^{-\alpha-1}\mathscr{K}_{-\alpha-1}(z)} - 1$$

$$\overset{(13)}{=} \beta \lim_{z\to 0_+} \frac{\Gamma(-\alpha-2)\left[1+\frac{2z}{-2\alpha-5}\right]^{-\alpha-\frac{5}{2}}}{\Gamma(-\alpha-1)\left[1+\frac{2z}{-2\alpha-3}\right]^{-\alpha-\frac{3}{2}}} - 1$$

$$\overset{\boxtimes}{=} -\beta \lim_{z\to 0_+} \frac{\left[1+\frac{2z}{-2\alpha-5}\right]^{-\alpha-\frac{5}{2}}}{(\alpha+2)\left[1+\frac{2z}{-2\alpha-3}\right]^{-\alpha-\frac{3}{2}}} - 1 \overset{\star}{=} -\frac{\beta}{\alpha+2} - 1,$$

where symbol $\boxtimes$ represents the well-known relation $\Gamma(z+1) = z\Gamma(z)$ and symbol $\star$ indicates the limits

$$\lim_{x\to 0_+} \frac{1}{x^{\varkappa}} \frac{\left[1+\frac{2x}{2\alpha+3}\right]^{\alpha+\frac{3}{2}}}{\left[1+\frac{2x}{2\alpha+1}\right]^{\alpha+\frac{1}{2}}} = \begin{cases} 1 & \text{pro } \varkappa = 0, \\ +\infty & \text{pro } \varkappa \in \mathbb{N}, \end{cases}$$

$$\lim_{x\to 0_+} x^{\varkappa} \frac{\left[1-\frac{2x}{2\alpha+3}\right]^{\alpha+\frac{3}{2}}}{\left[1-\frac{2x}{2\alpha+1}\right]^{\alpha+\frac{5}{2}}} = \begin{cases} 1 & \text{pro } \varkappa = 0, \\ 0 & \text{pro } \varkappa \in \mathbb{N}. \end{cases}$$

Since for $\alpha \geq -2$ function $\Phi(z)$ goes to infinity, then $\Phi(z)$ has supremum in the right neighbourhood of zero. The result for $\alpha < -2$ implies, that this function in the right neighbourhood of zero reaches finite value. Let's examine if any other value of $\Phi(z)$ for $\alpha < -2$ can reach or exceed the limit value for $z \to 0_+$

$$\Phi(0_+) = -\frac{\beta}{\alpha+2} - 1 \gtreqqless \frac{2\beta}{z}\frac{\mathscr{K}_{\alpha+2}(z)}{\mathscr{K}_{\alpha+1}(z)} - 1 = \Phi(z),$$
$$-\frac{\beta}{\alpha+2} > -\frac{\beta}{\alpha+2} + \underbrace{\frac{\beta\mathscr{K}_{\alpha+3}(z)}{(\alpha+2)\mathscr{K}_{\alpha+1}(z)}}_{<0},$$

which means $\Phi(0_+) > \Phi(z)$. Therefore, we have just proved that

$$\sup(\Phi)_{\alpha\geq -2} = +\infty \quad \text{and} \quad \sup(\Phi)_{\alpha<-2} = -\frac{\beta}{\alpha+2} - 1.$$

From relabelling $z = 2\sqrt{\beta\lambda}$ it is clear that $\sup(\Phi(z)) = \sup(\Phi(\beta,\lambda))$. Now we will return to variables β and λ. We intend to find β fulfilling condition (10) and form the aforementioned set M. If the supremum is lower or equal to zero, then the condition (10) cannot be satisfied. In order to meet the condition we require $\sup(\Phi) > 0$. For $\alpha \geq -2$ the situation is simple:

$$\sup(\Phi)_{\alpha\geq -2} = +\infty > 0 \quad \forall \beta > 0.$$

For $\alpha < -2$ we obtain the following demand

$$\sup(\Phi)_{\alpha<-2} = -\frac{\beta}{\alpha+2} - 1 > 0 \quad \Leftrightarrow \quad \alpha+\beta+2 > 0. \tag{14}$$

In order to fulfill the condition (10), β must satisfied (14) in case of $\alpha < -2$. It leads to the assertion that

$$M = \Big\{\beta \in \mathbb{R}^+ : \ \alpha+\beta+2 > 0\Big\}.$$

To conclude, in this section it has been found the suitable set M of all β such that $\Phi(\beta,\lambda)$ meets the condition (10). Therefore, from the definition of implicit functions, $\Phi(\beta,\lambda)$ generates unique implicit function $\lambda(\beta)$, which guarantees the existence of the scaling equation's solution. Therefore, GIG distribution can be scaled if and only if the scaling condition

$$\alpha+\beta+2 > 0 \tag{15}$$

is met.

4 Approximation of the scaling constant

In the previous section we have checked the existence of scaling equation's solution. Since we cannot express λ from scaling equation (5) directly, we apply an approximative approach. The asymptotic approximation of the scaling constant for GIG distribution with non-negative value of parameter α was already proposed in research [7]. Because of the symmetric property of Macdonald's function (12), the procedure for non-negative α can be adjusted even for $\alpha < 0$. In this section, we will briefly introduce the process of finding asymptotic approximation for negative value of parameter α. For that purpose, let's relabel $\alpha \leftrightarrow -\alpha$, in order to highlight the negativity. Our goal is still to solve the scaling equation, but this time we choose a different procedure. Conditions (3) can also be understood as $\mu_0 = \mu_1 = 1$. Thus, if this problem requires the scaling equation to be satisfied, then we can write

$$A\int_0^{+\infty} x^{-\alpha}\mathtt{e}^{-\lambda x}\mathtt{e}^{-\frac{\beta}{x}}\mathtt{d}x = A\int_0^{+\infty} x^{-\alpha+1}\mathtt{e}^{-\lambda x}\mathtt{e}^{-\frac{\beta}{x}}\mathtt{d}x = 1, \tag{16}$$

where A is the explicit normalization constant $A = \frac{\left(\sqrt{\frac{\lambda}{\beta}}\right)^{\alpha+1}}{2\mathscr{K}_{\alpha+1}(2\sqrt{\beta\lambda})}$. For the following calculations, we denote $\beta = \left(\frac{y}{2}\right)^{\frac{2}{1-\alpha}}$, $\lambda = \varkappa^{\frac{2}{1-\alpha}}$, $\widetilde{A} = A(\beta(y), \lambda(\varkappa))$ and

$$\mathtt{I}(y,\varkappa) = \int_0^{+\infty} x^{-\alpha}\mathtt{e}^{-\frac{\left(\frac{y}{2}\right)^{\frac{2}{1-\alpha}}}{x}}\mathtt{e}^{-\varkappa^{\frac{2}{1-\alpha}}x}\mathtt{d}x \overset{(2)}{=} \frac{y}{\varkappa}\mathscr{K}_{-\alpha+1}\left(\left(2^{-\alpha}y\,\varkappa\right)^{\frac{1}{1-\alpha}}\right). \tag{17}$$

If we multiply the integral $\mathtt{I}(y,\varkappa)$ by the constant $\widetilde{A}$, obviously $\widetilde{A}\cdot\mathtt{I}(y,\varkappa) = 1$. Let's derive the integral $\mathtt{I}$ by the parameter $\varkappa$

$$\frac{\partial\mathtt{I}(y,\varkappa)}{\partial\varkappa} = -\frac{2\,\varkappa^{\frac{1+\alpha}{1-\alpha}}}{1-\alpha}\underbrace{\int_0^{+\infty} x^{-\alpha+1}\mathtt{e}^{-\frac{\left(\frac{y}{2}\right)^{\frac{2}{1-\alpha}}}{x}}\mathtt{e}^{-\varkappa^{\frac{2}{\alpha-1}}x}\mathtt{d}x,}_{\overset{(16)}{=}\ \widetilde{A}^{-1}}$$

when satisfying the assumptions of the theorem about the derivation of the integral by the parameter is discussed in the [9]. The derivation by parameter implies that

$$-\frac{1-\alpha}{2}\,\varkappa^{\frac{\alpha+1}{\alpha-1}}\frac{\partial\mathtt{I}(y,\varkappa)}{\partial\varkappa} = \widetilde{A}^{-1} = \mathtt{I}(y,\varkappa),$$

which leads us to differential equation

$$\mathtt{I}(y,\varkappa) + \frac{1-\alpha}{2}\,\varkappa^{\frac{\alpha+1}{\alpha-1}}\frac{\partial\mathtt{I}(y,\varkappa)}{\partial\varkappa} = 0. \tag{18}$$

Let's also derive the right-hand side of the integral $\mathtt{I}(y,\varkappa)$

$$\begin{aligned}\frac{\partial}{\partial\varkappa}\left[\frac{y}{\varkappa}\mathscr{K}_{-\alpha+1}\left(\left(2^{-\alpha}y\,\varkappa\right)^{\frac{1}{1-\alpha}}\right)\right] &= -\frac{y}{\varkappa^2}\mathscr{K}_{-\alpha+1}\left(\left(2^{-\alpha}y\,\varkappa\right)^{\frac{1}{1-\alpha}}\right)\\ &\quad+\frac{2^{\frac{-\alpha}{1-\alpha}}y^{\frac{2-\alpha}{1-\alpha}}}{\varkappa^{\frac{1-2\alpha}{1-\alpha}}}\frac{\mathscr{K}'_{-\alpha+1}\left(\left(2^{-\alpha}y\,\varkappa\right)^{\frac{1}{1-\alpha}}\right)}{1-\alpha}.\end{aligned}$$

If we add the appropriate right-hand sides of $\mathtt{I}$, resp. $\frac{\partial\mathtt{I}}{\partial\varkappa}$ to the differential equation (18) we obtain new differential equation

$$\left[\frac{2\varkappa^{\frac{2}{1-\alpha}}}{1-\alpha} - 1\right]\mathscr{K}_{-\alpha+1}\left(\left(2^{-\alpha}y\,\varkappa\right)^{\frac{1}{1-\alpha}}\right) + \frac{\left(2^{-\alpha}\,y\,\varkappa\right)^{\frac{1}{1-\alpha}}}{1-\alpha}\mathscr{K}'_{-\alpha+1}\left(\left(2^{-\alpha}y\,\varkappa\right)^{\frac{1}{1-\alpha}}\right) = 0. \tag{19}$$

From this point on, the procedure must be split for small and large values of y. In this article we show the procedure only for small y. As shown in [7] and [9], the procedure for large y is the same and also leads to the same results.

Let's remind the approximation of Macdonald's function $\mathscr{K}_{-\alpha}(x)$ for small x together with it's derivation $\mathscr{K}'_{-\alpha+1}(x)$ known from [9] as

$$\mathscr{K}_{-\alpha+1}(x) \approx 2^{-\alpha}\Gamma(-\alpha+1)(-2\alpha+1)^{\alpha-\frac{1}{2}}(2x-2\alpha+1)^{-\frac{2\alpha-1}{2}}x^{\alpha-1}\mathsf{e}^{-x},$$

$$\mathscr{K}'_{-\alpha+1}(x) \approx \frac{[-2x^2-2x(1-\alpha)+3\alpha-2\alpha^2]}{(2x-2\alpha+1)x}\mathscr{K}_{-\alpha+1}(x).$$

By adding the approximations $\mathscr{K}_{-\alpha+1}$ and $\mathscr{K}'_{-\alpha+1}$ to (19) and keeping the notation $(2^{-\alpha}y\ \varkappa)^{\frac{1}{1-\alpha}} = x$ we get

$$\left[\frac{2}{1-\alpha}\varkappa^{\frac{2}{1-\alpha}}-1\right](2x-2\alpha+1)+\frac{1}{1-\alpha}\left[-2x^2-2x(1-\alpha)+3\alpha-2\alpha^2\right]=0.$$

Then, by making a series of adjustments and substituting the argument of the Macdonald's function $(2^{-\alpha}y\ \varkappa)^{\frac{1}{1-\alpha}}$ instead of x, we come to a scaling equation for small values y

$$2^{\frac{2-3\alpha}{1-\alpha}}y^{\frac{1}{1-\alpha}}\varkappa^{\frac{3}{1-\alpha}}-2^{\frac{1-3\alpha}{1-\alpha}}y^{\frac{2}{1-\alpha}}\varkappa^{\frac{2}{1-\alpha}}-4\alpha\varkappa^{\frac{2}{1-\alpha}}+2\varkappa^{\frac{2}{1-\alpha}}+2^{\frac{2-3\alpha}{1-\alpha}}\alpha y^{\frac{1}{1-\alpha}}\varkappa^{\frac{1}{1-\alpha}}-2^{\frac{2-3\alpha}{1-\alpha}}y^{\frac{1}{1-\alpha}}\varkappa^{\frac{1}{1-\alpha}}-3\alpha-4\alpha^2=1, \quad (20)$$

where $\varkappa = \varkappa(y)$. Suppose that $\varkappa(y)$ is described by the asymptote $\varkappa(y) = ky$, where the real number k is the slope of the asymptote of this function. Let us put this relation into the equation (20), which gives

$$2^{\frac{2-3\alpha}{1-\alpha}}y^{\frac{4}{1-\alpha}}k^{\frac{3}{1-\alpha}}-2^{\frac{1-3\alpha}{1-\alpha}}y^{\frac{4}{1-\alpha}}k^{\frac{2}{1-\alpha}}-4\alpha y^{\frac{2}{1-\alpha}}k^{\frac{2}{1-\alpha}}+2y^{\frac{2}{1-\alpha}}k^{\frac{2}{1-\alpha}}+2^{\frac{2-3\alpha}{1-\alpha}}\alpha y^{\frac{2}{1-\alpha}}k^{\frac{1}{1-\alpha}}-2^{\frac{2-3\alpha}{1-\alpha}}y^{\frac{2}{1-\alpha}}k^{\frac{1}{1-\alpha}}-3\alpha-4\alpha^2=1.$$

Then, dividing this equation by the expression $y^{\frac{4}{1-\alpha}}$, we get

$$2^{\frac{2-3\alpha}{1-\alpha}}k^{\frac{3}{1-\alpha}}-2^{\frac{1-3\alpha}{1-\alpha}}k^{\frac{2}{1-\alpha}}-\frac{4\alpha k^{\frac{2}{1-\alpha}}}{y^{\frac{2}{1-\alpha}}}+\frac{2k^{\frac{2}{1-\alpha}}}{y^{\frac{2}{1-\alpha}}}+\frac{2^{\frac{2-3\alpha}{1-\alpha}}\alpha k^{\frac{1}{1-\alpha}}}{y^{\frac{2}{1-\alpha}}}-\frac{2^{\frac{2-3\alpha}{1-\alpha}}y^{\frac{1}{1-\alpha}}\varkappa^{\frac{1}{1-\alpha}}}{y^{\frac{2}{1-\alpha}}}-\frac{3\alpha-4\alpha^2-1}{y^{\frac{4}{1-\alpha}}}=0$$

whereby we will be interested in the situation where $y \to +\infty$, because as we have already mentioned, even for large values of y the procedure leads to the same results. After the suggested limit transition we have

$$2^{\frac{2-3\alpha}{1-\alpha}}k^{\frac{3}{1-\alpha}}-2^{\frac{1-3\alpha}{1-\alpha}}k^{\frac{2}{1-\alpha}}=0.$$

A simple adjustment leads to

$$k=\frac{1}{2}, \quad \text{i.e.} \quad \frac{\varkappa(y)}{y}=\frac{1}{2}. \tag{21}$$

Before plugging the found ratio (21) into the scaling equation (20), let's convert it to the form

$$2^{\frac{2-3\alpha}{1-\alpha}}\varkappa^{\frac{2}{1-\alpha}}-2^{\frac{1-3\alpha}{1-\alpha}}y^{\frac{1}{1-\alpha}}\varkappa^{\frac{1}{1-\alpha}}-4\alpha y^{-\frac{1}{1-\alpha}}\varkappa^{\frac{1}{1-\alpha}}+2y^{-\frac{1}{1-\alpha}}\varkappa^{\frac{1}{1-\alpha}}+2^{\frac{2-3\alpha}{1-\alpha}}\alpha-2^{\frac{2-3\alpha}{1-\alpha}}=0,$$

by multiplying with $(y\varkappa)^{-\frac{1}{1-\alpha}}$ and neglecting the fraction $\frac{-3\alpha-4\alpha^2-1}{(y\varkappa)^{\frac{1}{1-\alpha}}}$. Now let's add the relation (21) and modify the equation into the form

$$4\varkappa^{\frac{2}{1-\alpha}}-2^{\frac{1-2\alpha}{1-\alpha}}y^{\frac{1}{1-\alpha}}\varkappa^{\frac{1}{1-\alpha}}+2\alpha-3=0. \tag{22}$$

Substitute $\xi(y) = \varkappa^{\frac{1}{1-\alpha}}$ and transform equation (22) into quadratic equation

$$4\xi^2 - 2^{\frac{-2\alpha+1}{1-\alpha}} y^{\frac{1}{1-\alpha}} \xi - (-2\alpha + 3) = 0$$

with the roots

$$\xi(y)_\pm = 2^{\frac{\alpha-2}{1-\alpha}} y^{\frac{1}{1-\alpha}} \pm \sqrt{2^{\frac{2\alpha-4}{1-\alpha}} y^{\frac{2}{1-\alpha}} - \frac{\alpha}{2} + \frac{3}{4}}.$$

From the notation of $\xi(y)$, we will henceforward consider the positive root only. After applying the inverse substitution $\beta = \left(\frac{y}{2}\right)^{\frac{2}{1-\alpha}}$ we find

$$\xi(\beta) = \frac{\sqrt{\beta}}{2} + \sqrt{\frac{\beta}{4} - \frac{\alpha}{2} + \frac{3}{4}}$$

and then after the return to original variables $\xi(\beta) = \varkappa^{\frac{1}{1-\alpha}} \overset{(17)}{=} \sqrt{\lambda}$ we get

$$\lambda(\beta) = \frac{\beta}{2} - \frac{\alpha}{2} + \frac{3}{4} + \sqrt{\frac{\beta}{4}(\beta - 2\alpha + 3)}.$$

At the very end of the calculation, all that is left is to use the definition of the asymptote of the function $\lambda(\beta)$ at infinity given by the relation $\lambda = k\beta + q_0$, where k is the slope and q_0 is the intercept. Let us first calculate the slope

$$k = \lim_{\beta\to+\infty} \frac{\lambda(\beta)}{\beta} = 1.$$

Then the intercept q_0

$$q_0 = \lim_{\beta\to+\infty} (\lambda(\beta) - k\beta) = -\alpha + \frac{3}{2}.$$

If we add k and q_0 to the definition of asymptote, then for small y (small β) we get the asymptotic relation

$$\lambda(\alpha, \beta) \approx \beta - \alpha + \frac{3}{2}. \tag{23}$$

If we now reverse our relabelling $\alpha \leftrightarrow -\alpha$, we reach the final form of asymptotic approximation of scaling constant for GIG distribution

$$\lambda(\alpha, \beta) = \alpha + \beta + \frac{3}{2} + o(1); \quad \beta \to +\infty. \tag{24}$$

Note that in order to scale Generalized Inverse Gaussian distribution, the scaling condition (15) must be satisfied.

5 Conclusion

This paper analyzes mathematical properties of Generalized Inverse Gaussian distribution (GIG), which is frequently used in the areas of renewal processes, particle systems, and vehicular headway modelling. The presented theoretical study reveals unknown and surprising anomalies hidden in the scaling procedure. We show that searching the scaling constant λ in the probability density

$$f(x) = \Theta(x)\frac{\left(\sqrt{\frac{\lambda}{\beta}}\right)^{\alpha+1}}{2\mathscr{K}_{\alpha+1}(2\sqrt{\beta\lambda})}x^{\alpha}\mathtt{e}^{-\frac{\beta}{x}}\mathtt{e}^{-\lambda x},$$

whose value assures the unit expected value $\int_{\mathbb{R}} x f(x)\,\mathtt{d}x$, may not be successful. The basic condition for the probability density (with parameters $\alpha \in \mathbb{R}$ and $\beta > 0$) to be scalable has been derived in this article and has the form

$$\alpha + \beta + 2 > 0.$$

In addition, it has also been shown that the course of the scaling constant λ – understood as a function of β – is almost linear. The respective linear aproximation is of the shape

$$\forall\alpha \in \mathbb{R}: \quad \lambda(\beta) = \alpha + \beta + \frac{3}{2} + o(1); \quad \beta \to +\infty.$$

This generalizes the asymptotic behavior of the scaling constant λ derived in earlier works for non-negative values of the parameter α only.

Acknowledgements

Research presented in this paper has been supported by the Grant SGS21/165/OHK4/-3T/14 provided by the Ministry of Education, Youth, and Sports of the Czech Republic (MŠMT ČR).

References

[1] Krbálek, M., 2007. J. Phys. A: Math. Theor. 40, 5813.

[2] Krbálek, M., 2013. J. Phys. A: Math. Theor. 46, 445101.

[3] Li, L., Chen, X.M., 2017. Transportation Research Part C 76, 170.

[4] Krbálek, M., Apeltauer, J., Apeltauer, T., Szabová, Z., 2018. Physica A 491, 112.

[5] Jörgensen, B., 1982. Statistical Properties of the Generalized Inverse Gaussian Distribution, Lecture Notes in Statistics, 9, Springer, Heidelberg.

[6] Kollert, O., Krbálek, M., Hobza, T., Krbálková, M., 2019. Journal of Physics Communications 3, 035020.

[7] Vacková, J., 2016, *Multi-headway statistika systémů s kombinovanými potenciály,* Výzkumný úkol FJFI ČVUT, školitel doc. Mgr. Milan Krbálek, Ph.D.

[8] Krbálek, M., 2012. *Úlohy matematické fyziky, 1. vydání,* České vysoké učení technické, ISBN 9788001050002.

[9] Lhotáková, A., 2020. *Vlastnosti distribuční rodiny GIG s negativní hodnotou parametru,* Bakalářská práce, školitel doc. Mgr. Milan Krbálek, Ph.D.

Stochastic and Physical Monitoring Systems
SPMS 2021
June 24 - 28, 2021
Malá Skála, Czech Republic

Super-Poissonian States in Balanced Particle Systems

Vít Pánek and Milan Krbálek

Department of Mathematics, FNSPE, Czech Technical University in Prague, Czech Republic

Email: `panekvit@fjfi.cvut.cz`

Abstract. This article explains the causes of anomalous phenomena discovered during the analysis of vehicular traffic streams on multi-lane roads. Although this explanation is based primarily on a thorough mathematical analysis of the problem under study, it ultimately provides answers to questions about the specifics of the interaction dynamics that operate between individual vehicles of a multi-lane traffic flow. The article acquaints readers with the theory of balance particle systems and with a mathematical way leading to the classification of one-dimensional particle systems according to the level of statistical fluctuations. This classification then allows automatic detection of statistically anomalous states of all related systems.

Key words: Particle Systems; Super-Poisson States; Statistical Rigidity; Statistical Compressibility; Balanced Functions; Renewal Theory.

1 Introduction

The creation of this article (and the entire theory that represents a mathematical core of the issue) has been motivated by an open problem in the theory of vehicular traffic flow. While the microstructure of traffic streams on single-lane roads was relatively credibly described and justified at the beginning of this millennium, anomalies were detected for data measured on two-lane motorways. The origin of these anomalies has waited quite a long time for explanation. The basic building blocks of the respective solution is the unification of the procedure of empirical-traffic-data processing and the conversion of the problem into a mathematical formalism. This enabled the conversion of qualitatively-described anomalies into rigorously defined anomalous states (so-called super-Poisson states), which can be acquired only in some systems with mutually interacting particles.

The main pillars of the whole solution are:

1. Rigorous proof that in all one-dimensional particle systems, where the interaction acts on a small scale only (i.e. for interactions between several nearest neighbours),

the probability density describing the spacing (headway or clearance) between succeeding particles must be described by a function belonging to the class of the balanced densities (see [1]).

2. Anomalous states in empirical traffic data can be most easily detected through the so-called 3s-unification procedure [2].
3. The finding that a similar issue was investigated within the Random Matrix Theory [3], where the apparatus of statistical rigidity was advantageously applied for similar purposes.
4. Analytical derivation of the headway distribution for equilibrium states in a thermodynamic particle gas defined by a general interaction potential $\varphi(x)$ and by a general value of the statistical resistivity $\beta \propto 1/T$, where T is the thermodynamical temperature of the gas (see [4]).
5. Rigorous proof [2] that in one-dimensional particle systems with a zero or repulsive force between neighbours, the statistical compressibility is always less than one.

This article explains the background of the so-called super-Poisson states in particle systems similar to vehicular traffic streams. First, we recall the well-known fact that in the Poisson system of non-interacting agents, the statistical compressibility, which describes the rate of statistical fluctuations in the system, is equal to one. Furthermore, using a theoretical tool of the balanced particle systems (or renewal theory [5, 6, 7]) we explain what is the main cause of exceeding the limit value of statistical fluctuations in certain types of systems (or in certain states of one system). In this way, we de facto solve the above-mentioned open problem from the scientific field of Vehicular Headway Modelling.

2 Balanced particle systems

2.1 Concept of balanced particle systems

We consider an infinite one-dimensional particle system with a fixed origin. At the origin of this system lies a particle which is referred to as a reference particle. In the figure 1, the position of the reference particle is ξ_0. Then we denote the positions of the other particles by $\xi_1, \xi_2, \xi_3 \ldots$ Among the three basic random quantities that naturally describe any particle system, we count:

1. *Spacings,* i.e. distances of neighbouring particles, which we understand as absolutely continuous and non-negative random variables. These variables form the so-called sequence of spacing distributions $(\mathcal{R}_k)_{k=0}^{+\infty}$.
2. *Multi-spacings,* understood as distances of the selected particle from the reference particle (see figure 1). To be specific, multi-spacing $\mathcal{X}_k$ represents a distance between

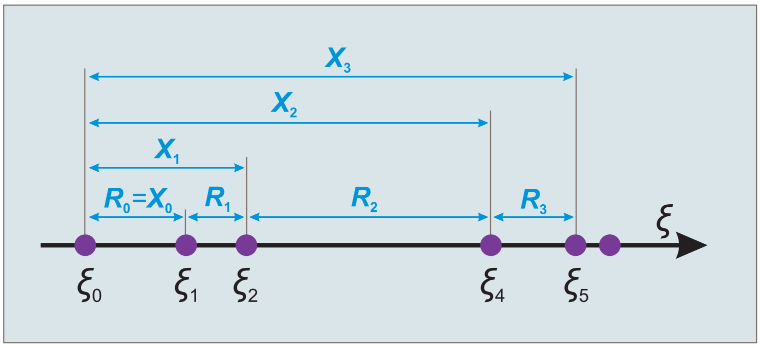

Figure 1: Basic descriptive quantities of a particle system.

the $(k+1)$th particle and the reference particle. It means that kth multi-spacing is possible to define by formula

$$\mathcal{X}_k = \sum_{i=0}^{k} \mathcal{R}_i.$$

3. *Interval frequency* N_L, which maps the number of particles occurring in the interval $(0, L)$ lying immediately next the reference particle. N_L is – contrary to spacings and multi-spacings – a discrete random variable, parameterized by the value of L. It is usually described by the probability of occurrence k particles inside the interval $(0, L)$. The corresponding probabilistic task can be logically formulated by means of the expression $\mathcal{P}[N_L = k] =?$

By the *balanced particle system* (BPS) we mean a sequence of multi-spacings $(\mathcal{X}_k)_{k=0}^{+\infty}$ established by expression $\mathcal{X}_k = \sum_{n=0}^{k} \mathcal{R}_n$ satisfying the following axioms:

1. *Axiom of the identical distribution (i.d.)*: Sequence $(\mathcal{R}_n)_{n=0}^{+\infty}$ is a sequence of non-negative, absolutely continuous and equally distributed random variables.

2. *Axiom of the balanced generator*: Probability density $h(x)$ for all random spacings $\mathcal{R}_0, \mathcal{R}_1, \mathcal{R}_2, \ldots$ (so-called *generator* of the balanced particle system) belongs to a class $\mathscr{B}$ of balanced densities, i.e. $h(x) \in \mathscr{B}$ (see definition below).

3. *Axiom of convolutional compatibility*: Sequence $(\mathcal{R}_n)_{n=0}^{+\infty}$ is sequence of convolutionally compatible random variables, i.e. for every pair of different random variables $\mathcal{R}_i$ and $\mathcal{R}_k$ $(i \neq k)$ it holds $\mathcal{R}_i + \mathcal{R}_k \sim (h \star h)(x)$.

The axiom of convolutional compatibility can, as understandable, be replaced by the more stringent requirement that the sequence $(\mathcal{R}_n)_{n=0}^{+\infty}$ is a sequence of i.i.d. random variables. Under this assumption it is easy to prove that

$$\mathcal{X}_k \sim \bigstar_{i=0}^{k} h(x).$$

2.2 The class of balanced functions

The class of balanced functions $\mathscr{B}$ is the space of piecewise continuous functions $f(x)$ on $\mathbb{R}$ with $\mathrm{Dom}(f) = \mathbb{R}$, $\mathrm{Ran}(f) \subset [0, +\infty)$, $\mathrm{supp}(f) \subset [0, +\infty)$, for which – above that – there exists positive number $\varkappa$ so that

$$(\forall \alpha > \varkappa): \lim_{x \to \infty} f(x)\mathrm{e}^{\alpha x} = +\infty \quad \wedge \quad (\forall \alpha < \varkappa): \lim_{x \to \infty} f(x)\mathrm{e}^{\alpha x} = 0 \quad \text{(balance axiom)}.$$

The number $\varkappa$ is referred to as *balancing index* and denoted by $\mathrm{inb}(f)$. In fact, belonging of headway distribution to the space $\mathscr{B}$ must be met for all one-dimensional particle systems, where inter-particle interactions are restricted to a few neighboring particles only [8, 2], which definitively corresponds with vehicular traffic systems.

2.3 Stochastic many-particle gas – physical realization of the balanced particle system

The physical realization of the above-discussed balanced particle system is represented by an ensemble of many identical particles located along a curve (typically a semi-line, line, or circle) subjected to stochastic noise of various intensities. The noise level in this system is controlled by the so-called *stochastic resistivity* coefficient β. The zero value of β implies an absolute noise-level in the ensemble, which therefore corresponds to the Poissonian system where purely random locations of particles generate the exponentially distributed inter-particle headways, whose steady-state headway distribution reads

$$g(x) = \Theta(x) a \mathrm{e}^{-ax}.$$

Conversely, if the resistivity β is increasing above all limits the system corresponds in fact to a deterministic system, whose inner dynamics is not burdened with any stochastic fluctuations. Under this condition it holds $g(x) = \delta(x - \nu)$, which means that particles are located equidistantly in locations $\xi_0, \xi_0 + \nu, \xi_0 + 2\nu, \xi_0 + 3\nu, \ldots$. Here $\delta(x)$ stands for the Dirac delta. The arrangement of particles in the two border variants does not depend in any way on interactions between individual particles. However, the situation will dramatically change for intermediate values $0 < \beta < +\infty$. Then the stationary state of the system will be strongly dependent not only on the value of resistivity but especially on interaction forces that determine mutual interactions between neighbouring particles in the system. In a homogeneous variant of the system, when all neighbouring particles are repulsed/attracted via the same force description (force $F(x)$ and interaction potential $\varphi(x)$), where $F(x) = -\varphi'(x)$, the associate steady-state of the system is described (see general derivation in [4]) by the following inter-particle headway distribution:

$$g(x) = A\Theta(x)\mathrm{e}^{-\beta\varphi(x)}\mathrm{e}^{-\lambda x}, \tag{1}$$

where constants $A = A(\beta)$ and $\lambda = \lambda(\beta)$ ensure the proper normalization and scaling, respectively.

In addition, under the conditions

$$\varphi'(x) \leq 0, \quad \lim_{x \to 0^+} \varphi'(x) = -\infty, \quad \lim_{x \to +\infty} \varphi'(x) = 0, \tag{2}$$

applied to p.d.f. (1) the following implication holds

$$\mu_1 = 1 \quad \Longrightarrow \quad \lambda \geq 1 \quad \wedge \quad \mu_2 \leq 2, \tag{3}$$

where $\mu_k = \int_{\mathbb{R}} x^k h(x)\,\mathrm{d}x$ is $k-$th statistical moment. Moreover, limiting values are $\lambda = 1$, $\mu_2 = 2$ are obtained for Poissonian system, which is either a system with absolutely non-interacting particles, i.e. $\varphi(x) = 0$, or stochastically irresistible system where $\beta = 0$. These variants are described by the same exponential headway distribution $h(x) = \Theta(x)\mathrm{e}^{-x}$, for which therefore the statistical variance $\mathrm{VAR}(\mathcal{X}) = \mu_2 - \mu_1^2$ is equal to one.

A note
As usual, we will assume without loss of generality that the balancing particle system is scaled, i.e. the mean value of the spacing is therefore $\int_{\mathbb{R}} xh(x)\,\mathrm{d}x = 1$.

3 Statistical rigidity and compressibility

One of the fundamental characteristics of the BPS is the so-called statistical rigidity $\Delta(L)$, mapping the variability of the interval frequency N_L. Application of this quantity in studies of particle systems can be found already in Random Matrix Theory [3], where statistical rigidity maps the variability of energy levels in spectra of heavy nuclei. It is defined by the relation

$$\Delta(L) = \mathrm{E}(N_L - L)^2. \tag{4}$$

The graph of statistical rigidity is relatively simple for classical systems. Immediately behind the origin of the coordinate system, statistical rigidity $\Delta(L)$ merges with its linear asymptote. Thus,

$$\Delta(L) \approx \chi L + \delta + o(L^2) \quad (L \to +\infty), \tag{5}$$

which means that the statistical rigidity can be approximated extremely accurately by the linear function $\chi L + \delta$. The constants χ, δ of this linear asymptote are called *compressibility* and *deflection,* respectively. It is a well-known observation of particle system theory that for expressing the compressibility and deflection of a given BPS it is sufficient to know the generator of the BPS. For compressibility and deflection the following relations hold:

$$\chi = \mu_2(h) - 1, \quad \delta = \frac{1}{6}(9\mu_2^2 - 9\mu_2 - 4\mu_3 + 6). \tag{6}$$

A detailed derivation of these two relationships can be found in the research project [9].

4 Classification of systems according to a rate of fluctuations of the interval frequency

Balanced particle systems may be – as expected – classified according to the compressibility χ. In Figure 3 we can see four color-coded regions, namely regions of *deterministic*

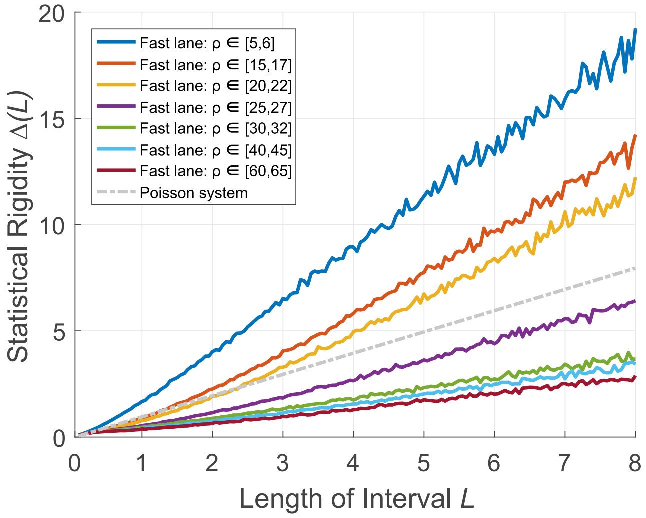

Figure 2: Statistical rigidity of freeway data in a fast-lane traffic flow. Vehicle-by-vehicle data have been collected during 90 days at freeway circuit R1 (located near Prague, Czech Republic) by technology of induction double-loop detection.

states (red), *sub-Poisson states* (blue), *Poisson states* (green), and *super-Poisson states* (turquoise). The Poisson states ($\chi = 1$) and deterministic states ($\chi = 0$) represent the boundary states for all particle system and are discussed in more details below. The blue region of sub-Poisson states includes the vast majority of real physical, biological, economic, or socio-dynamic systems, since in the physical theory of thermal-like systems this corresponds to systems with pure repulsive potentials $\varphi(x)$, where compressibility χ lies in the interval $(0, 1)$.

The most interesting type of particle system (and also the rarest and least researched) is the super-Poisson variant of the balanced particle system, for which the respective compressibility exceed the unit value. In such systems, the rate of fluctuations is – as obvious – greater than in Poisson systems, which are generally considered to be the systems with the highest fluctuation rates, since fluctuations are not reduced in any way.

These considerations force us to ask the following questions: Do super-Poisson systems exist at all? Can super-Poisson states be found in real-life (physical, biological, economic, or socio-dynamic) systems? The answers will be given in the following text.

4.1 Dirac particle systems

In a Dirac equilibrium particle system or deterministic system, the slope of the statistical rigidity, i.e. compressibility, is zero. It is the state of the system when the individual particles are equidistantly distributed and the stochastic resistance β grows beyond all limits. However, such a state is only a theoretical state. In real traffic streams, where vehicles are driven by somewhat imperfect humans, the Dirac arrangement of vehicles never can be reached.

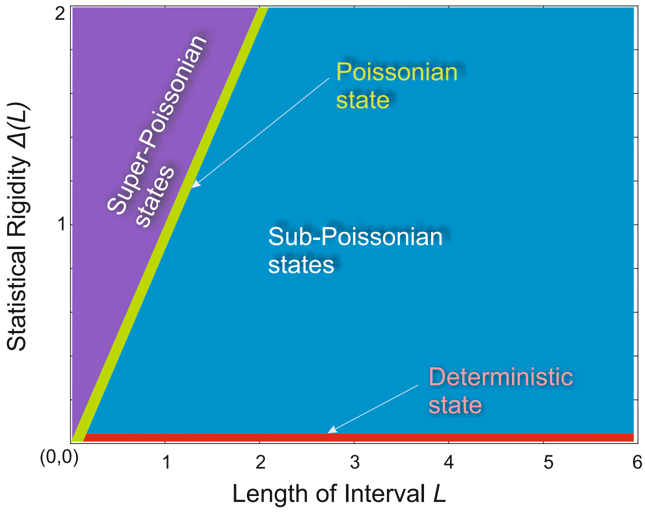

Figure 3: Classification of balancing particle system states.

4.2 Poisson particle systems

The opposite of Dirac's BPS is Poisson's BPS. In such a system, the stochastic resistivity is zero and the dispersion of the spacing is equal to one since the particles do not interact with each other and are therefore fully independent. This allows absolute freedom in decision making by individual particles and the spacing between them is therefore very spread out. In empirical traffic ensembles, this situation can be detected at very low traffic densities (up to 5 vehicles per kilometre of motorway). Since drivers in such sparse traffic are hardly influenced by neighbouring drivers at all, they have maximum freedom for traffic manoeuvring.

5 Super-Poisson particle systems

As already explained, a balanced particle system has a super-Poisson arrangement if the associate compressibility is greater than one. This means that in such a system, individual realizations of a selected random variable are even more dispersed around their mean value than in the Poisson system, where the particles are completely unaware of each other. Initially, measurements falling in super-Poisson region were considered to be measurement errors. With the passage of time, however, it became clear that measurements are not erroneous and that not only repulsive forces but also attractive forces act between the elements. As discussed above, if strictly repulsive forces are acting in a particle system, then the super-Poisson state cannot occur. If compressibility greater than one is detected in a particle system, then it can be logically assumed that there is also an attractive force acting between the elements in that system. This attractive force, similarly to a more common repulsive force, has a psycho-social origin. In vehicular traffic, the super-Poisson conditions occur, for example, at lower traffic densities in the fast lane of a motorway. Drivers located in the faster highway lane tend to catch up with the vehicle in front of

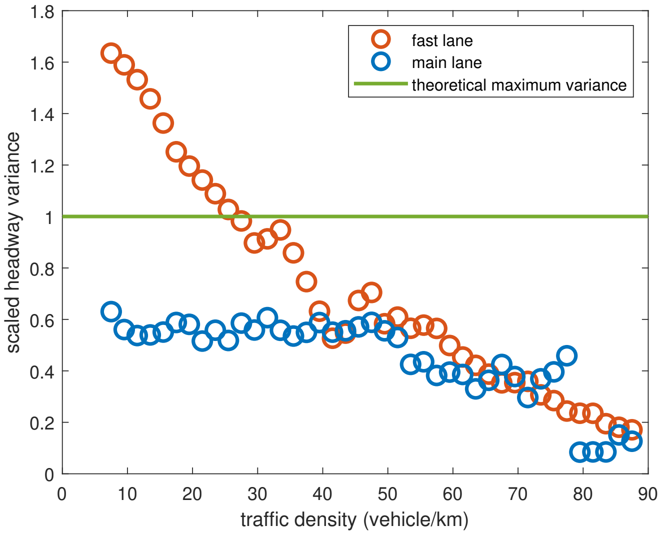

Figure 4: Data from the Dutch A9 highway.

them, and this tendency is the cause of an attractive force-impulse. Another reason for increasing compressibility above the theoretical limit is the fact, that in lower densities of traffic flow are overtaking manoeuvers possible and line changing causes super-Possion behaviour of traffic flow (see [2]).

In figure 4 we can see the result of the analysis of traffic data from a Dutch two-lane motorway. The measured spacings from the main lane are marked in blue, where the compressibility is inside the interval (0,1) all the time and thus falls into sub-Poisson states. The data from the fast lane are marked in red and as can be seen, the assumed upper bound on the value of the spacing variance (in green) is exceeded in the fast lane at lower traffic densities, namely at densities of $5 - 20$ vehicles per km. However, at these densities, the traffic flow is not so sparse that individual vehicles do not interact and repulsive forces are applied. What causes this deviation, however, is the action of the aforementioned attractive force. The existence of attractive forces in these traffic flow situations is due to the presence of more sporty drivers in the fast lane of traffic on highways. These drivers catch up with the vehicle in front of them and, with small gaps that are unusual at the given speed and density, try to push the vehicle in front of them out of the faster lane in order to continue driving fast.

The main cause of super-Poisson states is therefore the attractive force, which should be reflected in the force-description of respective particle gas. In order to be collision-free, the repulsive force must also be included, and hence the potential acting in respective ensembles is the so-called *combined potential.* Its physical shape is $\varphi(r) = \kappa \ln(r) + \frac{1}{r}$, where r is the distance between consecutive vehicles and κ represents a *power coefficient*, quantifying the ratio between the attractive component $\ln(r)$ and repulsive component $\frac{1}{r}$. By deriving the potential, we get the corresponding force

$$F(r) = -\frac{\mathrm{d}\varphi}{\mathrm{d}r} = -\frac{\kappa}{r} + \frac{1}{r^2}.$$

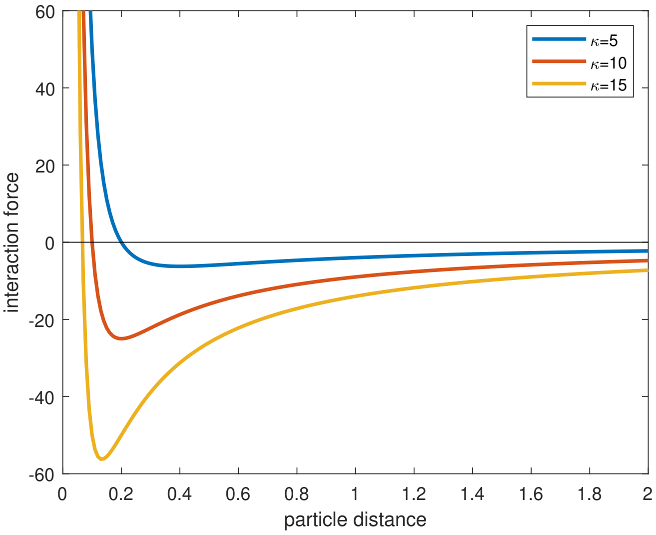

Figure 5: Force with different selection of κ.

As we can see, this force is preventing the collision, i.e.

$$\lim_{r \to 0^+} F(r) = \lim_{r \to 0^+} \left(-\frac{\kappa}{r} + \frac{1}{r^2} \right) = \lim_{r \to 0^+} \frac{-\kappa r + 1}{r^2} = +\infty,$$

and at the same time for large headways the interaction disappears, i.e.

$$\lim_{r \to +\infty} F(r) = \lim_{r \to +\infty} \left(-\frac{\kappa}{r} + \frac{1}{r^2} \right) = 0.$$

The attractive force-component is represented by the term $-\kappa/r$, whereas a repulsive force-component is represented by the term $1/r^2$. In figure 5 a few examples of combined forces are visualized. Near the origin, one can see a strong repulsion and then – below the horizontal axis – we detect the region where repulsion is dominated by attraction.

6 Conclusions

This article summarizes the latest findings on so-called super-Poisson states in the field of Vehicular Headway Modelling. This paper also provides a reader with an overview of balanced particle systems and their classification based on statistical rigidity resp. compressibility.

As we have seen, there is a significant difference in compressibility between the fast lane and the main lane on the motorway up to a certain traffic density (approx. 40 vehicles per kilometre). At higher densities, the behaviour of drivers on the main and fast lanes is quite the same. At lower traffic densities, the fast lane exhibits significantly higher compressibility than the main lane while the compressibility increases above the theoretical unit value of an interference-free Poisson system. In a BPS where purely repulsive forces are at work, this theoretical limit cannot truly be exceeded. Above-limit compressibility can be detected in a system only if there is an attractive component of the interaction force. The explanation for the existence of an attractive component is the presence of sporty drivers in a fast lane, the possibility of overtaking and switching lanes. That is consistent with the fact that super-Poisson states are detected in multi-lane traffic and do not occur in higher traffic densities where there is insufficient freedom for those factors.

Acknowledgements

Research presented in this paper has been supported by the Grant CK01000152 provided by Technology Agency of the Czech Republic (TAČR) and by the Grant SGS21/165/-OHK4/3T/14 provided by the Ministry of Education, Youth, and Sports of the Czech Republic (MŠMT ČR).

References

[1] Krbálek, M., Hrabák, P., Bukáček, M., 2018. Physica A 490, 38.

[2] Krbálek, M., Šeba, F., Krbálková, M., 2022. Physica A 585, 126418.

[3] Mehta, M.L., 2004. Random matrices (Third Edition). New York: Academic Press.

[4] Krbálek, M., 2007. J. Phys. A: Math. Theor. 40, 5813.

[5] Cox, D. R., 1962. Renewal Theory, Methuen & Co., London, New York.

[6] Cox, D. R., Lewis, P. A. W., 1978. The statistical Analysis of Series of Events, Chapman & Hall.

[7] Hannan, E. J., 1961. Time series analysis, Methuen & Co., London, New York.

[8] Krbálek, M., Šleis, J., 2015. J. Phys. A: Math. Theor. 48, 015101.

[9] Pánek, V., 2020. *Statistical compressibility for systems with middle-ranged potentials,* Research Project, FNSPE CTU in Prague, supervisor doc. Mgr. Milan Krbálek, Ph.D.

Stochastic and Physical Monitoring Systems
SPMS 2021
June 24 - 28, 2021
Malá Skála, Czech Republic

Conflict Solution in Cellular Evacuation Model

Matej Šutý

Faculty of Information Technology, Czech Technical University in Prague, Thakurova 9, 160 00 Prague 6, Czech Republic

Email: `sutymate@fit.cvut.cz`

Abstract. Agent-based cellular models can be used to simulate the process of evacuation of people from a room. The actions and interactions of heterogeneous agents create collective motion and capture complex phenomena of pedestrian dynamics. This article presents a multi-agent cellular model based on floor-field model extended by a new strategy for solving conflicts when two or more agents attempt to enter the same cell. The agents and the model have various parameters that influence the conflict solution. A sensitivity analysis on these parameters is performed that reveals the individual contribution of variance in the results.

Key words: multi-agent system, cellular model, aggressivity, conflict solution, evacuation simulation, sensitivity analysis.

1 Introduction

Increasing demands on safety procedures in buildings or during various events, such as evacuation, or demonstration, call for answers on pedestrian dynamics. Some available solutions provide precise simulations on how people move and interact, and others focus on real-time results and adaptation to a fast-changing environment.

The environment and setting are specific for each building, location, and various groups of people. It is essential to understand the influence of individual parameters on the process with so many possible settings. Simulating the process on a whole parametric space is very slow and could be sped up using only the significant parameters selected by sensitivity analysis.

The inspiration for the model used in this research is the floor field cellular model described by Katsuhiro Nishinari and Andreas Schadschneider in Article [1]. Main characteristic of this model is in the use of several floor fields — *static*, *dynamic*, *fire hazard*, … These can be explained as two-dimensional lattices made of discrete cells that hold some value and abide to certain rules. Pedestrians in the evacuation, who are agents with individual parameters, move in the rectangular two-dimensional lattice. Parameter of aggressivity was introduced in the work of Pavel Hrabák and Marek Bukáček in Article [2].

This article shows improved feature of conflict solution and provides a new approach to the movement of agents in the model. These improvements are linked to the sensitivity parameters of agents to the environment, because the conflict solution depends on them. The qualitative analysis focused on the relation between number of agents in the evacuation and the total evacuation time. The range of agent's sensitivity to static field was analyzed and a reason for limiting this range is explained. The final contribution of this research is the sensitivity analysis of input parameters to the variance in observable quantities, namely the total evacuation time.

2 Definition of the model

The evacuation model represents the people in evacuation as agents who move on a grid that acts as a room or other area. The grid is two-dimensional, rectangular, and consists of discreet cells. Cells can be occupied by agents who move from one cell to another in 8 directions or stay in the same cell. The movement in the model is strictly discrete due to the nature of the cellular model. Movements are executed simultaneously, which leads to conflicts when two or more agents attempt to enter the same cell. Only one agent can be present in a cell at a time.

The agents are somewhat autonomous and react to the environment. They generally move in the direction to the exit. In this paper, only grid with one exit is considered. Because the exit is a cell, only one agent can leave the room at every synchronous update of the simulation.

2.1 Strategies

The collective motion of agents is reproduced using two strategies (choosing destination cell and solving conflicts), and using heterogeneity in the parameters. The strategies are affected by parameters of aggressivity and sensitivity of each agent and by parameter of friction [2]. The parameter of aggressivity plays a role in situations when two or more agents attempt to enter the same cell.

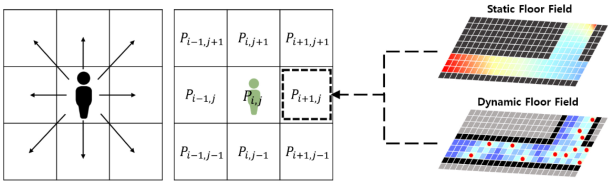

Figure 1: Example of cellular floor-field model utilizing *static* and *dynamic* field, where agent can move to cells in Moore neighbourhood. *Taken from [4].*

In each step of the simulation, all agents calculate the attractivity of individual cells in their neighborhood N. N is a set of adjacent cells to the cell occupied by agent, and the occupied cell as well. Attractiveness or attractivity is used to calculate probability $P \in [0, 1]$, which is the probability of agent selecting this cell as his preferred destination cell. The selection is executed in stochastic manner.

2.1.1 Cell selection strategies

Value of attractiveness depends on strategy for choosing destination cell. Former strategy was described by Pavel Hrabák and Marek Bukáček in Article [2].

The new strategy, proposed in the bachelor thesis *Conflict solution in cellular evacuation models* [5], is more affected by the sensitivity to the occupancy of cells k_O. Probability P of agent moving to cell y from cell x, is calculated from P_O and P_S.

In the equations below can be found following members: $S(y)$ is a function of static potential of cell y, where $S(y) \geq 0$. Associated parameter k_S is the sensitivity of agent to the static potential of a cell. $O(y)$ is the indicator of occupied cell y. When y is occupied by an agent, $O(y) = 1$, otherwise it is zero. Associated parameter k_O is the sensitivity of agent to the occupancy of cell. $D(y)$ is the indicator of diagonal motion from agent's origin cell x to destination cell y. When y can be entered from x by diagonal motion, $D(y) = 1$, otherwise it is zero. Associated parameter k_D is the sensitivity of agent to diagonal motion.

$$P(y \leftarrow x \mid N) = k_O P_O(y) + (1 - k_O) P_S(y) \tag{1}$$

The term P_O focuses on occupancy of cell. Notice the missing parameter k_O in $(1 - O(y))$ which is different from former strategy [2]. Term P_O is normalized across P_O of neighbor cells from N,

$$P_O(y) = \frac{\exp(-k_S S(y))(1 - O(y))(1 - k_D D(y))}{\sum_{z \in N} \exp(-k_S S(z))(1 - O(z)(1 - k_D D(z))}. \tag{2}$$

The term P_S takes into account the static potential $S(y)$ and makes the agent move in the correct direction to the exit, and the indicator of diagonal motion $D(y)$. Term P_S is also normalized across neighbor cells from N,

$$P_S(y) = \frac{\exp(-k_S S(y))(1 - k_D D(y))}{\sum_{z \in N} \exp(-k_S S(z))(1 - k_D D(z))}. \tag{3}$$

2.1.2 Conflict solution strategy

Above was described the first part of conflict solution - the selection of target cell by agents. Evaluation of each cell depends on the sensitivity parameters. When two or more agents attempt to enter the same cell, conflict occurs and consequent action is the selection of the winning agent. Main factor in the process is the aggressivity parameter γ of individual agents and the friction parameter μ.

From agents $\{x_1, \ldots, x_k\}$ attempting to enter target cell, an agent x_j is chosen with $j = \mathrm{argmax}_{\mathrm{i=1,\ldots,k}} \gamma_i$. If no other agent has same the aggressivity, agent x_j wins the conflict immediately. If there are two or more agents with same highest aggressivity a parameter of friction μ affects the conflict. With probability $B = \mu(1 - \gamma_j)$ none of the agents will enter the cell and they will all remain in their positions. This event is called blocking event. With $\bar{B} = 1 - B$ agent x_j will enter the cell. This strategy is explained in detail in Article [2].

2.2 Implementation

My research of available agent-based modeling frameworks revealed Mesa [6] as an up-to-date Python framework which is currently used in many projects [7, 8]. This framework allows broad customization: from discrete to continuous movement, synchronous or asynchronous update and various types of data collection. Mesa framework allows progressing in the simulation with different speed or by single steps, which is very helpful for examination of the course of the simulation. Overview of the situation can also be demonstrated with real-time graphs of data-collectors for various observed values. Implementation details can be found in the original thesis [5].

3 Sensitivity analysis

This section presents research based on quantitative and qualitative analysis of the input parameters. On one hand, the quantitative analysis measures the influence of the individual input parameters on the simulation using sensitivity analysis in OptiSLang software. On the other hand, qualitative analysis of the model shows how the parameters are linked together. The qualities of the model were researched by observing running simulations and by statistical methods of analysis.

To start with the analysis a number of simulations were executed, all using the Mesa framework with data collection of the agents in each step - their position, number of wins in conflicts etc. The most important observable is the total evacuation time - number of steps in the simulation needed for evacuation of *all agents*.

3.1 Sensitivity analysis using MOP

To measure the contribution of individual input parameters on the variance in T_{TET}, OptiSLang uses Metamodel of Optimal Prognosis (MOP). The metamodel includes Polynomial, MLS or Krigins model. At first, OptiSLang calculates the prognosis quality of each available model, (Polynomial, MLS, Kriging) using Coefficient of Prognosis (COP) and then chooses the one with the highest quality.

As a result of the MOP, we obtain an approximation model, which includes the important variables. Based on this meta-model, the total effect sensitivity indices, ..., are used to quantify the variable importance. The variance contribution of a single input variable is quantified by the product of the CoP and the total effect sensitivity index estimated from the approximation model [9]. $\mathrm{COP}(X_i)$ is variance contribution of single input variable X_i, that shows how much X_i contributed to the approximated variance using MOP. When MOP has COP 60%, it means that it was able to capture 60% of the variance in observed quantity. Some parameters can be related to each other and the sum of individual parameters $\mathrm{COP}(X_i)$ can exceed total COP or even 100%. For example, in MOP with COP 60%, parameters X_1 and X_2 with $\mathrm{COP}(X_2) = 50\%$ and $\mathrm{COP}(X_2) = 20\%$ individually contributed with 50%, respectively with 20%, to variance in observed quantity.

All simulations had the same model configuration of grid 15×15, exit placed at border $(0, 8)$. Simulations in this article always assign aggressivity γ to agents uniformly from the interval $[0, 1]$ with granularity $m = 10$, thus for all agents $\gamma_i \in \{0.0, 0.1, \ldots, 0.9, 1.0\}$. These values are generated by PRNG G_1, initialized by seed I, which also generates the positions of the agents on the grid. All simulations share the same seed.

The sensitivity parameters ($k_S,\ k_D,\ k_O$) are uniformly assigned to all agents (if not stated otherwise). The friction parameter μ is a global parameter of the model that affects the stochastic occurrence of blocking occasions from conflicts.

		Simulation name		
Parameters	**Step**	S_2	S_3	S_4
iterations	-	3	2	2
k_S	0.1	[0.3, 5.0]	[1.5, 4.5]	{1.5, 3.0, 4.5}
k_O	0.1	[0.0, 1.0]	[0.0, 1.0]	[0.0, 1.0]
k_D	0.2	[0.0, 0.1]	[0.0, 1.0]	[0.0, 0.9]
μ	0.2	[0.0, 0.1]	[0.0, 1.0]	[0.0, 0.9]

Table 1: Settings for simulations in SA.

4 Results

The results of SA in this chapter are explained by graphs from OptiSLang: the 3D plot of total evacuation time (T_{TET}) and COP of individual parameters. The discoveries of qualitative analysis, such as linear dependency of T_{TET} on number of agents n, are depicted by other graphs, for example histograms or boxplots.

4.1 Number of agents n

It was expected, that the increase of total evacuation time T_{TET} is linear and depends on the number of agents n. Figure 4 demonstrates the linear dependency of T_{TET} on n.

The sensitivity parameters for blue boxplots are $k_O = 0.9,\ k_D = 0.5,\ \mu = 0.9$ and for red boxplots $k_O = 0.9,\ k_D = 0.5,\ \mu = 0.1$. Horizontal axis x is the number of agents n in tens and vertical axis y is total evacuation time T_{TET}. The boxplots show the variance in T_{TET} for each n. There are two graphs with different $k_S \in \{1.5, 3.5\}$.

In both figures, the simulations with higher friction $\mu = 0.9$ show increasing variance of T_{TET}, because with more agents the conflicts occur more frequently and this results in more blocking occasions. Contrary to this, the boxplots in red, where μ is low, are rather consistent. These figures also demonstrate linear dependency of T_{TET} on number of agents. The slope of linear dependency is influenced by other parameters, just as the variance in T_{TET}.

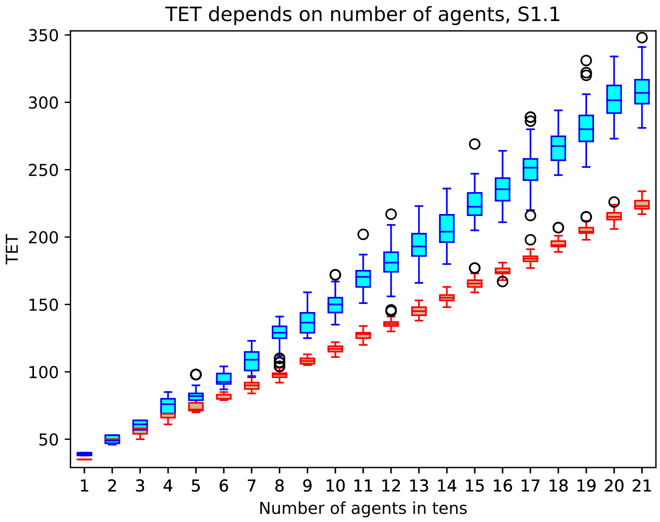

Figure 2: $k_S = 1.5$

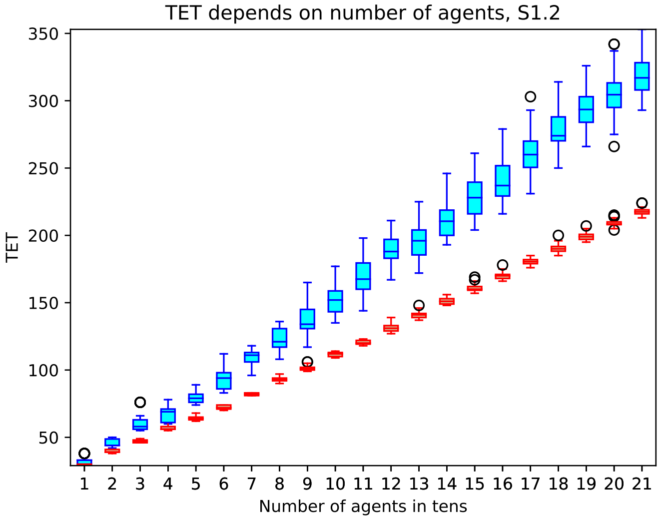

Figure 3: $k_S = 3.5$

Figure 4: Linear dependency of TET on number of agents. Higher friction, blue boxplots, increases variance of T_{TET}. Two graphs with different k_S show linear dependency of total evacuation time on n, regardless of k_S.

5 Sensitivity to static field k_S

The probability of choosing destination cell y is calculated from members P_O and P_S in the new strategy for choosing destination cell. Notice P_S member in equation below:

$$P_S(y) = \frac{\exp(-k_S S(y))(1 - k_D D(y))}{\sum_{z \in N} \exp(-k_S S(z))(1 - k_D D(z))}.$$

For better demonstration, the member $(1 - k_D D(y))$ is left out from the edited equation $\bar{P_S}$, where y is destination cell from neighborhood N for agent A in cell x,

$$\begin{aligned}\bar{P_S}(y) &= \frac{\exp\left(-k_S S(y)\right) \cdot \exp\left(k_S S(x)\right)}{\sum_{z \in N} \exp\left(-k_S S(z)\right) \cdot \exp\left(k_S S(x)\right)} \\ &= \frac{\exp\left(-k_S (S(y) - S(x))\right)}{\sum_{z \in N} \exp\left(-k_S (S(z) - S(x))\right)}.\end{aligned} \tag{4}$$

The equation above leads to discovery of member $\bar{P_S}$ being proportional to exponential difference in static potential:

$$\bar{P_S}(y) \propto \exp\left(-k_S (S(y) - S(x))\right). \tag{5}$$

For cell y, which is closest to exit — lowest $S(y)$ from adjacent cells — the relative attractivity (the right hand side of Equation (5)) grows exponentially with increasing k_S.

The influence of k_S can be very strong for high numbers, and marginal for values lower than 1. It was noticed during the testing phases of the model implementation, when the simulations with very low k_S values lasted very long. Visual examination of simulation exposed the erratic movement of agents that did not progress to the exit.

Figure 5 shows the 3D plot of approximated T_{TET}, from simulation S_2 in Table 1, exported from OptiSLang. The black dots are the values of T_{TET} from the simulations. *MLS* model was selectedy by MOP. Vertical axis T is the T_{TET}, on horizontal axis F are values of friction μ and horizontal axis S holds the values of sensitivity to static field k_S. This graph shows very high T_{TET} for $k_S < 1.5$.

In the same figure, on the right, is a graph with COP of individual parameters. The COP(k_S) is prevalent and other parameters have marginal values of COP. This is because of undesired erratic movement of agents, that increases T_{TET} and it's variance, when k_S is lower than 1.5. In Figure 7 can be spotted how T_{TET} does not change much for values higher than 4.5. Because of these reasons, the interval of k_S was limited to $[1.5, 4.5]$ in further simulations.

In Figure 5, the influence of μ on axis F might seem marginal, but, as will be presented later, the friction parameter μ plays an important role in the course of the evacuation.

In simulations with $k_S \in [1.5, 4.5]$, other parameters influence the simulation more significantly, as can be seen in Figure 6 in COP graph on the right. According to COP, the most significant parameter is friction μ, that contributed with 48% to variance in observed quantity T_{TET}. Formerly, the most significant parameter was k_S, with COP(k_S) higher than 86%. Now, COP(k_S) dropped to 6%, on par with COP(k_D). COP of MOP on the top of the graph, is lower as well: was 88% and now is 67%. This can be explained with very high variance in T_{TET} for $k_S < 1.5$, which was attributed to k_S. In simulations with limited k_S, the variance in T_{TET} is lower.

6 Sensitivity to occupancy k_O

Lower values of k_O allow the agent to choose an occupied cell as his target cell. At the start of the simulation, the agents are densely packed. The same applies to the congestion, when more agents are approaching the exit (or bottleneck in general), than

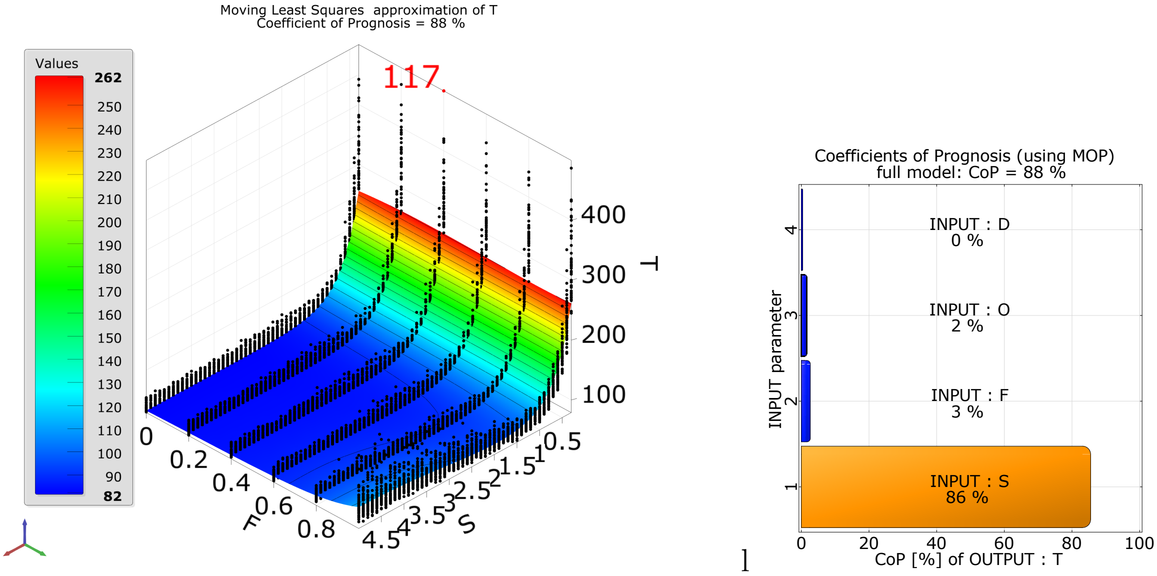

Figure 5: Left: 3D graph of total evacuation time, exported from OptiSLang. Right: COP of input parameters, exported from OptiSLang. Data from simulation S_2. For $k_S < 1.5$ the total evacuation time is erratic and meaningless, which lead to limit of the range of k_S to $[1.5, 4.5]$.

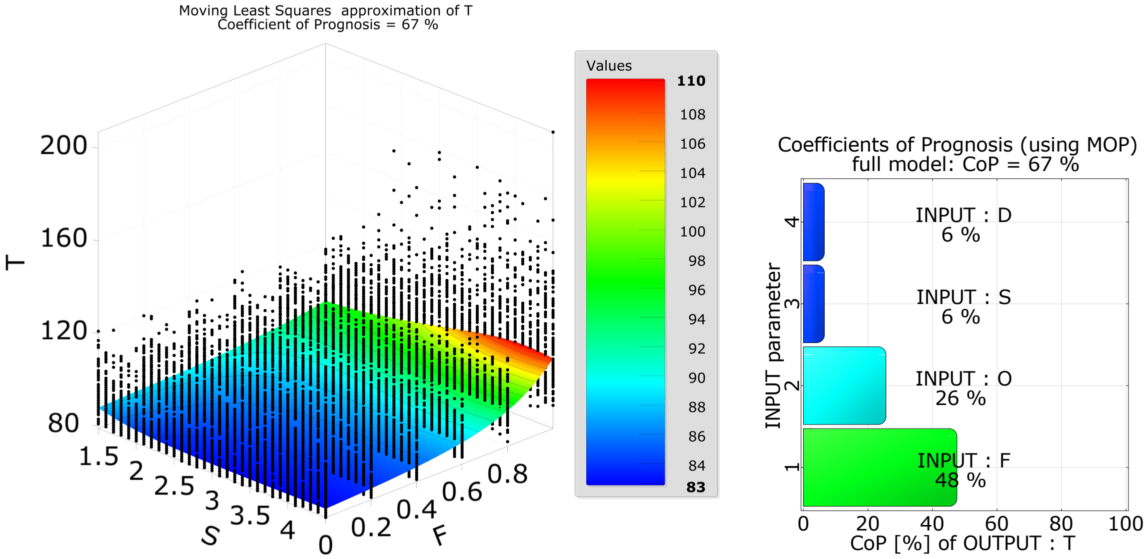

Figure 6: Left: 3D graph of T_{TET} from OptiSLang. Right: COP of input parameters, exported from OptiSLang. Data from simulation S_3. With limited range of k_S, the COP of individual parameters, on the right, is well distributed. *Note: The angle of view is different compared to Figure 5, axes F and S are switched.*

are being egressed. In both situations, k_O plays a role, as agents near the exit, and agents on the border of the congestion cluster, can choose empty or occupied cells.

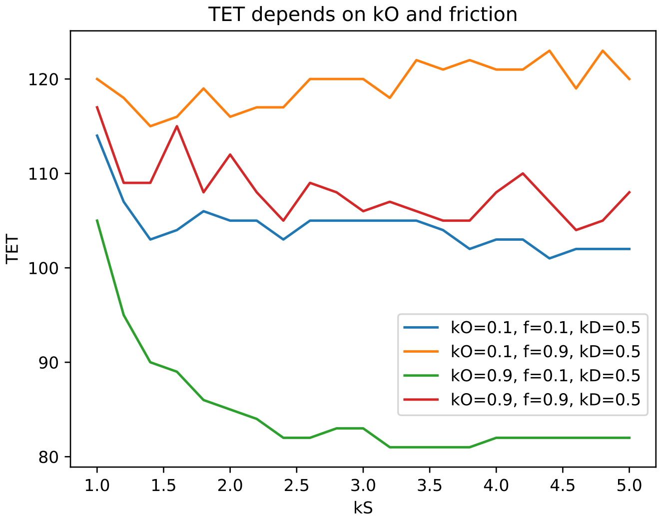

Figure 7: Different sets of parameters k_O, μ and how they affect T_{TET}. Vertical axis is averaged T_{TET} from three simulations and horizontal axis is variable k_S. Lower k_O and higher μ increase evacuation time.

Figure 7 shows the characteristics of four constant parameters sets with variable $k_S \in [1.0, 5.0]$ on *x axis*. Each set of parameters was simulated 100 times and the vertical y axis is the averaged T_{TET} from these simulations. Even though the lines are not very smooth, it needs to be said that the resolution of T_{TET} is high — T_{TET} is in range from 80 to 125. All sets have the same $k_D = 0.5$.

The green line shows how parameters $k_O = 0.9, \mu = 0.9$ are affected by k_S. The relative position of the green line, compared to others, shows that by allowing agents to overtake queue (high k_O) and with low number of conflicts (low μ), the evacuation times are the shortest (81 to 105 epochs). Contrary to this, with same k_O and higher $\mu = 0.9$, the evacuations take longer (105 to 117 epochs) and the results for various k_S vary a lot due to more frequent conflicts. The remaining two sets have low $k_0 = 0.1$, which minimizes overtaking, and forces the agents to stay in *queues*.This results in longer evacuations. The higher $\mu = 0.9$ in the orange line is rough. It should be noticed, that with increasing k_S, the evacuations take longer than in the beginning (115 epochs for low k_S and 125 epochs for higher k_S). In the end the total evacuation time is increased with lower k_O and it also increases with higher μ.

7 Other discovery: heterogeneity in parameters

The evacuation model can assign different parameters to individual agents from a uniform distribution, or assign different parameters to groups of agents. Values generated by PRNG are subject to stochastic selection. To see how the model responds to homogeneous and heterogeneous parameters, simulations $S_{6.1}$ and $S_{6.2}$ were performed. In both simulations grid 15×15 was used, with *exit* placed at $(0, 8)$ and populated with 70 agents.

Simulations were repeated 1000 times,

First simulation $S_{6.1}$ with set of input parameters $k_S = 2.0$, $k_D = 0.5$ and low $\mu = 0.1$. This simulation was, at first, run with *homogeneous* $k_O = 0.5$ for all agents. The blue histogram in Figure 7 shows distribution of T_{TET} from 1000 iterations of this simulation. Most iterations, more than 300, resulted in $T_{\text{TET}} \approx 85$ and all iterations had $T_{\text{TET}} \in [80, 96]$.

This simulation was then rerun, also repeated 1000 times, with *heterogeneous* distribution of k_O. The 70 agents were split to two groups of 35. First groups was assigned $k_O = 0.1$ and second group $k_0 = 0.9$, so the average k_O of all agents was 0.5, identical to the previous run. The orange histogram in Figure 7 shows that this simulation resulted in shorter evacuations — all iteration had $T_{\text{TET}} \in [80, 91]$.

Another simulation $S_{6.2}$ was performed, this time with increased friction $\mu = 0.9$, other parameters remained unchanged $k_S = 2.0, k_D = 0.5$. Identical to $S_{6.1}$, simulation was repeated 1000 times — once for *homogeneous* and then for *heterogeneous* k_O of agents. Figure 7 shows that distribution of T_{TET} for *homogeneous* k_O, blue histogram, is similar to *heterogenenous* k_O for two groups of agents, orange histogram.

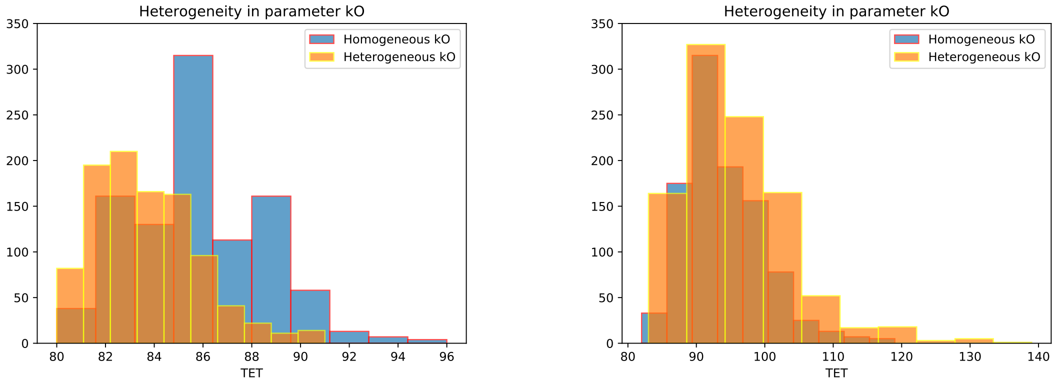

Figure 8: Simulations $S_{6.1}$ (left) and $S_{6.2}$ (right) with heterogeneous and homogeneous distribution of parameter k_O, repeated 1000 times. Blue histograms show T_{TET} for homogeneous $k_O = 0.5$. Simulations with two groups of agents with with different $k_O = 0.1$ and $k_O = 0.9$ are captured in orange histograms.

8 Conclusions

In this article research on cellular models, that simulate the evacuation of people from a room, was described. The process of conflict solution, when two or more agents attempt to enter the same cell, was analyzed. The *floor-field* model, which was an inspiration for this model, uses two cellular fields: *dynamic* and *static* field. Also present is a set of input parameters that influence the behavior of agents in the model and the microscopic processes within (conflict solution, choosing destination cell, formation of structures). The agents in the simulation, who represent pedestrians in evacuation, can have homogeneous or heterogeneous parameters, for example the parameter of aggressivity, specific for each agent, that plays a role in solving conflicts.

To perform said research, an agent based cellular evacuation model was implemented using Mesa ABM framework for Python. Using agents, the model is able to capture the collective motion of pedestrians during an evacuation. It also demonstrates various phenomena of the evacuation, for example, the congestion at the exit. Individual agents are autonomous and interact with each other. These interactions, mainly the *conflicts*, are analyzed. The model consists of various components, that can be further extended or customized.

During the implementation of the model, after observing the evacuation process, a new strategy for choosing destination cell was proposed and implemented. It affects the movement of agents and thus significantly impacts the conflicts that emerge from these movements. Also, this strategy puts more attention to the input parameter of sensitivity to occupation k_O, which produces more evenly distributed probabilities of moving to adjacent cells. Compared to the old strategy, the probabilities of adjacents cells are more intuitive and the impact of k_O can be thus explained better.

The model uses a stochastic selection for several processes in the simulation. It is a desirable feature as it replicates the randomness in human behavior. Due to variance in observed quantities (total evacuation time) with the same input parameters, it was necessary to analyze the contribution of individual input parameters to the variance in T_{TET}. This was achieved by means of sensitivity analysis in OptiSLang software and by other auxiliary methods.

The results of SA show the influence of individual input parameters on the course of the evacuation. One concrete contribution of this article is connected to sensitivity to *static* potential k_S. SA of k_S revealed, that low values of $k_S < 1$ produce erratic movement of agents, that degrades the course of the simulation. On the other end, with increasing k_S, for example $k_S > 3.0$, the influence of individual sensitivity parameters $k_O,\ k_D$ is marginalized.

Contrary to sensitivity parameters, friction parameter μ showed consistent influence on the variance in T_{TET}, regardless of other parameters. This parameter directly affects the number of blocking occasions, which increase the total evacuation time.

The sensitivity to occupancy k_O allows agent to choose an occupied cell as his destination cell. Qualitative analysis of k_O revealed that parameters k_O and sensitivity to diagonal motion k_D affect each other, as k_D allows agents to overtake queues, which are formed due to k_O.

Other notable discoveries consist in analysis of number of agents n, and of heterogeneity in parameters. Numerous simulations with variable n showed that with increasing n, increase in T_{TET} is linear regardless of other parameters. Other simulations examined the course of the evacuation with different distribution of k_O of agents. In simulations where all agents are uniformly assigned one value of $k_O = a$, total evacuation times are different than in simulations, where two values of k_O are assigned to equally sized groups — the average k_O of agents in both groups is a. This discovery needs to be further researched.

Acknowledgements

Research covered in this article was executed on my university Czech technical university in Prague under keen supervision of Ing. Pavel Hrabák, PhD. whom I want to thank for his help and guidance. I am also grateful for being given the opportunity to attend the SPMS 2021 conference in Malá Skála, where great topics were presented and where I met wonderful people.

References

[1] Nishinari, K.; Kirchner, A.; et al. Extended Floor Field CA Model for Evacuation Dynamics. IEICE Transactions on Information and Systems, 2003.

[2] Hrabák, P.; Bukáček, M. Conflict Solution According to "Aggressiveness" of Agents in Floor-Field-Based Model. Springer International Publishing, 2006.

[3] Kretz, T.; Schreckenberg, M. F.A.S.T. - Floor field- and Agent-based Simulation Tool Universität Duisburg-Essen, 2009.

[4] Minhyuck L.; et al. An extended floor field model considering the spread of fire and detour behavior. Physica A: Statistical Mechanics and its Applications, 2021.

[5] Šutý M. Conflict solution in cellular evacuation model. Czech Technical university in Prague, 2021. https://dspace.cvut.cz/handle/10467/95146.

[6] Masad, D.; Kazil, J. Mesa: An Agent-Based Modeling Framework 14th PYTHON in Science Conference, 2015.

[7] Tashakor, G. Agent-based model for tumour-analysis using Python+Mesa. HPCS Dublin, 2019.

[8] Namany S.; et al. Sustainable food security decision-making: An agent-based modelling approach. Journal of Cleaner Production, 2020.

[9] Most, T.; Will, J. Sensitivity analysis using the Metamodel of Optimal Prognosis. Proceedings of 8th Weimar Optimization and Stochastic Days 2011.

Stochastic and Physical Monitoring Systems
SPMS 2021
June 24 - 28, 2021
Malá Skála, Czech Republic

State of the Art of Pedestrian Density Estimates

Jana Vacková and Marek Bukáček

Department of Mathematics, FNSPE, Czech Technical University in Prague

Email: `janca.vackova@fjfi.cvut.cz`

Abstract. Density is one of the fundamental quantities for a description of pedestrian dynamics. In the last decade, there is an increasing need to define density better than 'the count of pedestrians divided by the size of the detector'. Hence this contribution deals with the very promising approach defining pedestrian density using the assumption that every pedestrian is a source of the density distribution. This kind of (kernel) density estimate opens up a lot of new possibilities in real applications.

Key words: Density Distribution, Pedestrian Dynamics, Kernel Functions.

1 Introduction

Flow, velocity and density are considered fundamental quantities in the both traffic flow [30] and pedestrian dynamics [4, 23]. Primal models discovered relationship between these essentials in a plain macroscopic way, for instance [31]. Although they describe the current phase of the system, they make it without any specific information about the dynamics inside the whole. It is possible to obtain two systems under very different internal conditions, however they both achieve the same value of flow or density [14].

Lots of ways to compute their values come from their physical definitions

$$J = \frac{N}{\Delta T} \quad [\mathrm{ped} \cdot \mathrm{s}^{-1}], \qquad \rho = \frac{N}{|A|} \quad [\mathrm{ped} \cdot \mathrm{m}^{-2}], \tag{1}$$

where N represents the number of agents that left an observed area in time interval T or were found in an observed area A of the size $|A|$. Hydrodynamic approximate equality [23]

$$J = \rho \cdot v \tag{2}$$

brings the (mean) velocity relation. Many authors dealt with different definitions during evaluation these quantities in data analysis. e.g. [6, 25, 27, 29], in details see Section 3.

Let us, firstly, present the used concept in this study which was introduced in [27], and applied in [2, 33] from macroscopic and also microscopic point of view. After that we will present the contemporary state of the art in Section 3.

2 Concept and Definition

We bet on the following approach to estimate the density. We assume every single pedestrian to be a source of *individual density distribution.* Let us rewrite the definition of *density* in an area A as an estimate using kernel distribution theory [1, 3, 35]

$$\rho = \frac{N}{|A|} = \frac{\int_A p(\boldsymbol{x})\,\mathrm{d}\boldsymbol{x}}{|A|} = \frac{\int_A \sum_{\alpha=1}^{N} p_\alpha(\boldsymbol{x})\,\mathrm{d}\boldsymbol{x}}{|A|} = \sum_{\alpha=1}^{N} \frac{\int_A p_\alpha(\boldsymbol{x})\,\mathrm{d}\boldsymbol{x}}{|A|}, \tag{3}$$

where N represents the number of pedestrians, $|A|$ the size of considered area A, $p_\alpha(\boldsymbol{x})$ the individual density distribution generated by each pedestrian $\alpha \in \{1, 2, \ldots, N\}$ and $p(\boldsymbol{x}) = \sum_{\alpha=1}^{N} p_\alpha(\boldsymbol{x})$ the *density distribution* in the area A.

The area A does not have to be static (a detector approach) like in [27] – if it represents the surroundings of pedestrian α, which can be variable in time (a dynamic approach), we call the density *individual* [2, 32]. For clarity in further text, let denote ω_α as the surroundings of pedestrian α, then we note $\rho_{\omega_\alpha}(\boldsymbol{x})$ as the individual density for pedestrian α, in contrast to the static detector density $\rho_A(\boldsymbol{x})$.

In a case that area A fills the whole examined area, the individual density distribution holds normalization condition

$$\int_A p_\alpha(\boldsymbol{x})\,\mathrm{d}\boldsymbol{x} = 1, \tag{4}$$

therefore the relation $\int_A p(\boldsymbol{x})\,\mathrm{d}\boldsymbol{x} = N$ is fulfilled and the density ρ_A is called *global.* When an area $B \subset A$ covers only the part of the possible area A, the pedestrian can contribute to the density ρ_B only partially and the normalization condition is not fulfilled.

If the kernels intersect the walls, they have reduced bases not to expand from the room, i.e. we trim the bases just for the part lying inside the room without damaging the normalization condition (4) - therefore the peak of the individual density distribution will be higher than usually.

To emphasize the generality of relation (3), we can write the definition of the density including kernel parameters

$$\rho_A = \frac{\int_A \sum_{\alpha=1}^{N} p_\alpha(\boldsymbol{x}, R)\,\mathrm{d}\boldsymbol{x}}{|A|}, \tag{5}$$

moreover the individual density including surroundings of pedestrians

$$\rho_{\omega_\alpha(\boldsymbol{r})} = \frac{\int_{\omega_\alpha(\boldsymbol{r})} \sum_{\beta=1,\beta\neq\alpha}^{N} p_\beta(\boldsymbol{x}, R)\,\mathrm{d}\boldsymbol{x}}{|\omega_\alpha(\boldsymbol{r})|}, \tag{6}$$

where we exclude the individual density distribution of the pedestrian α, i.e. pedestrian α does not contribute to the density in their surroundings. It has better meaning now because if there is not any other pedestrian near pedestrian α, the individual density is equal to zero. For instance: if we do not exclude the pedestrian α, the individual density will be equal to the mass of pedestrian α in the circular surroundings $\omega_\alpha(r)$, i.e. $\rho_{\omega_\alpha(r)} = 1$ ped/m^2 for $R <= r$ and any other pedestrian represented by cone at least $r + R$ m far away.

In accordance with characteristics mentioned above, we refer to parameter R as *blur* (it represents the size of area affected by one pedestrian) and $\boldsymbol{r}$ as *range* (it expresses the size of pedestrian surroundings defining the area taken into account for evaluating the density).

It is clear now that we can set two factors before evaluating the density - the shape of the detector or pedestrian surroundings (i.e. the area where the density is evaluated) and the shape of the individual density distribution (i.e. the way how the pedestrian contributes to the total density distribution). It is worth to note that these two factors are completely independent and should be established with respect to the following application.

2.1 Type of Kernels

If the surroundings is set to the whole considered area and Dirac function is used as the individual density distribution, the standard approach (1) is obtained. However there is more different choices of kernels as the individual density distribution. Denoting $\boldsymbol{x}_\alpha := \boldsymbol{x}_\alpha(t)$ as the (head) position of pedestrian α at fixed time $t \in \mathbf{R}_0^+$, let us mention a few of them which will be used in further analysis.

- **Point approximation**

  $$p_\alpha(\boldsymbol{x}) = \delta_{\boldsymbol{x},\boldsymbol{x}_\alpha}$$

  as already mentioned Dirac delta function.

- **Stepwise function**

  $$p_\alpha(\boldsymbol{x}, R) = \mathbb{1}_{A_\alpha(R)}(\boldsymbol{x})\,\frac{1}{|A_\alpha(R)|},$$

  where $\mathbb{1}_X$ represents the indicator function of set X.

  1. **Cylindrical kernel**

     $$A_\alpha(R) = \left\{\boldsymbol{x} \in \mathbf{R}^2 : \|\boldsymbol{x} - \boldsymbol{x}_\alpha\| \leq R\right\}$$

     and

     $$\mathbb{1}_{A_\alpha(R)}(\boldsymbol{x}) = \Theta\left(R - \|\boldsymbol{x} - \boldsymbol{x}_\alpha\|\right).$$

  2. **Voronoi kernel** is a specific kernel influenced by kernels around.
     - Each spatial point $\boldsymbol{x} \in \mathbf{R}^2$ is assigned to the nearest pedestrian α at position $\boldsymbol{x}_\alpha$. The set of these points is called Voronoi cell and it is denoted as A_α for pedestrian α [27].
     - A_α does not depend on any blur parameter R. It is possible to use a parameter as an upper boundary of the size of Voronoi cell [27]. Nevertheless we do not implement this kind of parameter in our study - it would have a different meaning (maximum blur) than a simple blur of pedestrian used in other kernels, thus it would not have been comparable. Beside that the maximum blur would influence only the low occupied room, i.e. only a beginning of density time series under conditions of our experiment. However it is necessary to think about usage the maximum blur in general situations.

- We have to remark that the authors of [27] summed in relation (3) Voronoi cells of pedestrians that lie inside the detector at least by a part of their Voronoi cells (the sum is greater than real contained mass), or Voronoi cells of pedestrians that lie inside the detector (the sum is lower than real contained mass). We use here the accurate sum of the part of Voronoi cells lying inside the detector - not less, not more. The situation is depicted in Figure 1.

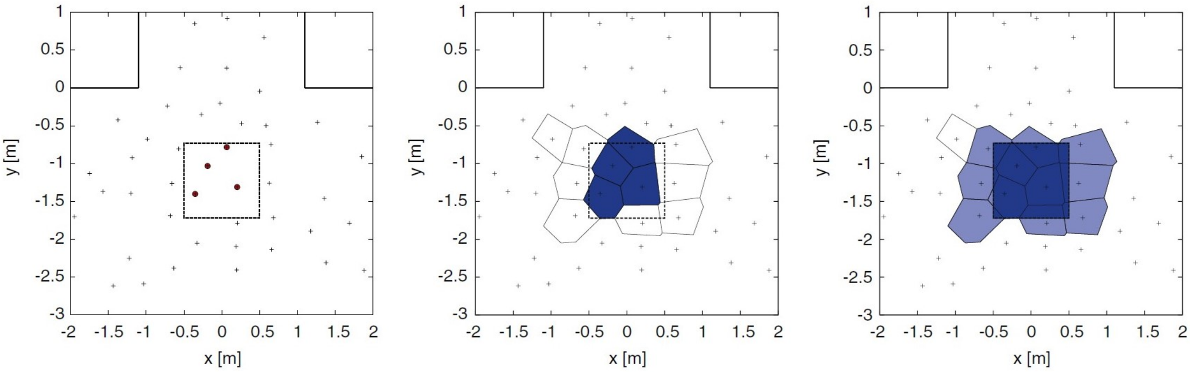

Figure 1: Using Voronoi diagram according to [27] from [27].

- **Conic kernel**
$$p_\alpha(\boldsymbol{x}, R) = \frac{3}{\pi R^3} \mathbb{1}_{A_\alpha(R)}(\boldsymbol{x}) \left(R - \|\boldsymbol{x} - \boldsymbol{x}_\alpha\|\right),$$
where
$$\mathbb{1}_{A_\alpha(R)}(\boldsymbol{x}) = \Theta\left(R - \|\boldsymbol{x} - \boldsymbol{x}_\alpha\|\right).$$
It has several desired features for representing pedestrians compared to the stepwise kernels, e.g. decreasing trend with increasing distance, limited support and the independence of one pedestrian to the others.

- **Borsalino kernel** from [15], where it is defined for one dimension. Generalization used in this paper for two dimensions can be defined as follows
$$p(\boldsymbol{x}, R) = \frac{1}{Z}\frac{1}{R} \mathbb{1}_{A_\alpha(R)}(\boldsymbol{x}) \exp\left\{\frac{R^2}{\|\boldsymbol{x} - \boldsymbol{x}_\alpha\|^2 - R^2}\right\}$$
where
$$\mathbb{1}_{A_\alpha(R)}(\boldsymbol{x}) = \Theta\left(R - \|\boldsymbol{x} - \boldsymbol{x}_\alpha\|\right)$$
and Z is numerically calculated normalization constant.

  This kernel has similar properties as the conic kernel. However they differ in theoretical features - Borsalino kernel is differentiable and this fact can be helpful in analytical calculations. On the contrary, the conic kernel does not have to be normalized using numerical computation. More about their differences with respect to the evaluating of densities will be found in further text.

- **Gaussian kernel** in a symmetric version, i.e. with diagonal covariance matrix,

$$p_\alpha(\boldsymbol{x}, R) = \frac{1}{2\pi R^2} \exp\left\{-\frac{\|\boldsymbol{x} - \boldsymbol{x}_\alpha\|^2}{2\,R^2}\right\}.$$

  This is the only representative with a limitless area of influence (i.e. with unbounded support) in this study.

Blur parameter R represents the kernel bandwidth in our study, thus it is comparable through all used kernel shapes. The example of density distribution with blur equal to 0.5 m for different kernels can be seen in Figure 2.

We work with all mentioned kernels in their symmetric version here. It does not have to be this way in general, though. Furthermore the kernel size can be definitely enhanced by varying in time in accordance with the conditions in pedestrian surroundings. We will not cover that in this study, it is the main point of the following research.

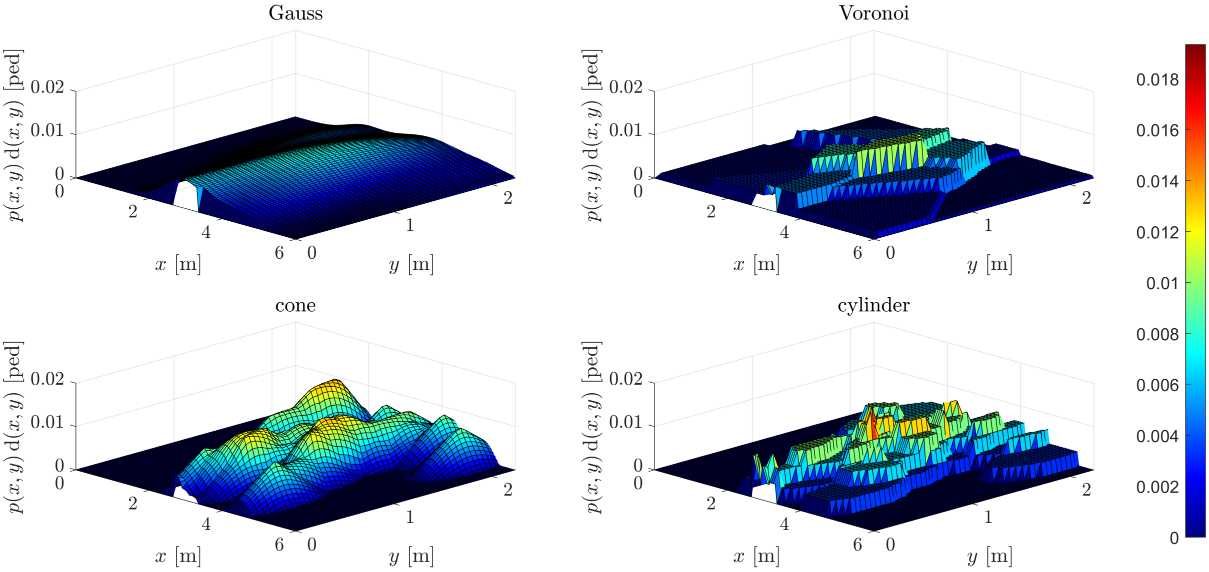

Figure 2: Density distribution with $R = 0.5$ m.

2.2 Type of Surroundings

Having introduced the individual density of pedestrian α (6), we need to specify the shape of the pedestrian surroundings in the meaning of the dynamic detector. The choice of the specific shape is very promising in bending of the definition (6) for a specific purpose in the microscopic point of view. This individual approach is a crucial point of the ongoing research - we will be investigating sector, circle and ellipse in the sense of surroundings.

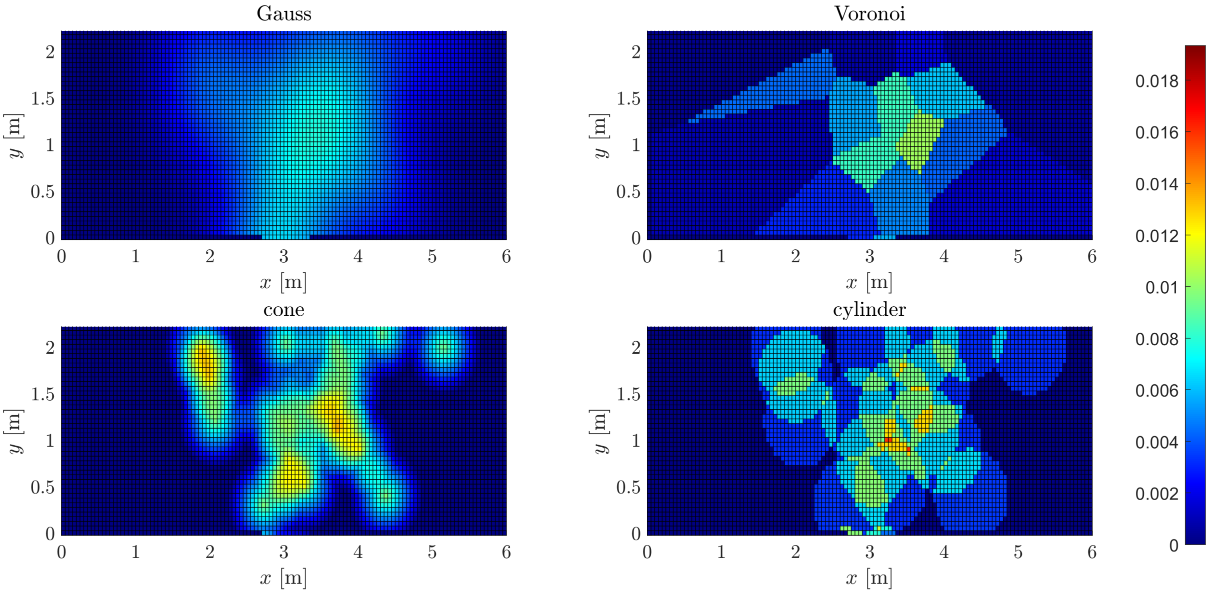

Figure 3: Density distribution with $R = 0.5$ m.

3 History and Relation to other Works

Having defined all important terms, it is necessary to set the used concept into the context of work by other research groups. Definition of pedestrian density estimate is still the contemporary topic in question, which is clearly seen from Table 1, where we summarized the estimate evolution (not only for the kernel concept). The standard definition (and its upgrades) were studied a lot, after that researchers started to use approaches based on statistics methods, including kernel estimates. Subsequently, the kernel smoothing parameter begun to be the centre of attention. Since we came with the application of the kernel approach bended into the individual density, we are not interested only in the bandwidth of the kernel. This extended approach brings more parameters to explore.

We have to note that it is not possible to choose a specific approach as the only correct one. Nevertheless, the chosen method affects the evaluation of quantities significantly, therefore it may have an impact on results, e.g. an examined phenomenon, like researchers already discussed [24, 11, 29, 27]. Then our motivation for this parametric study is absolutely clear.

3.1 Density Estimate Evolution

As we have already mentioned, the standard density definition is the ground (1). However, this density estimate has lots of negative properties, e.g. discontinuousness, large scatter and it gives only an averaged information about current system state [27]. Thus alternative definition of density was required. The smooth number of pedestrian in space and time was used in [10]. Finally, the smooth contribution of pedestrian into the density in space and time was introduced in [9], and applied in [13, 12]. This definition is also an initial step to the individual density concept with dynamic detector. This weighting of pedestrians is mentioned in [22, 23], including the density estimate defined as the body projection into the observed area [21] or by an inverse headway.

Very important paper [27] about measuring fundamental quantities introduced the concept that we use in this work. Authors discus in detail the properties of the standard definition (1) and come with the kernel approach, they note few kernels that can be used (Gaussian, conic, cylindrical) and pick Voronoi diagram to estimate the density distribution in the observed area with additional parameter (maximum blur is fixed as 2 m^2). We mentioned differences between their and our Voronoi density in Section 2. To stabilize the Voronoi method, an averaging over time is applied in [17].

Comparison of lots of different method was brought in [6]. Another comparison of different methods (which are similar as the methods marked above) can be found also in [11] with the aim of the measuring of pedestrians safety.

Authors across all the mentioned papers definitely agree in one important fact - the disadvantage of using Gaussian kernel is the scaling parameter which has to be calibrated (this is also the reason why Voronoi kernel was preferred up to the present). Let us note that huge advantage is the possibility of interpretation, i.e. weighting of the pedestrian into the space in accordance with the distance to a specific point. It is noticed in [6] that different estimate can be appropriate (the best) for different situation. For this reason, it is more than important to study the parameters in the kernel concept to realise how the specific setting can influence the result.

At this stage of research, we became with our first paper about this topic [2], where we brought the kernel approach with respect to the individual density (6). If we put together the idea about weighting of the pedestrians [9], range-based method [6] and our idea about the dynamic detector in every time step, we obtain our definition of individual density (6) which brings another set of parameters into the density estimate. We performed very preliminary parametric study of the size of the conic kernel and the circular surroundings using velocity response [2]. However, it was showed that the velocity-density relationship cannot be quantified so easily (by Pearson correlation) in the crowd. We summarized this paper with outlook to the future work. Thus we extended the research in [33] using follower-leader concept for the crowd behaviour where the classic velocity-density relationship does not work.

3.2 Kernel Bandwidth (Smoothing Parameter)

Silverman solved this issue in statistics [26]. However, this kind of solution is not appropriate for pedestrian dynamics - it should be recomputed every single time step, because the pedestrian density is dynamic in time. It would result in the variable kernel size. It is definitely possible, although this dynamic change would not come from the pedestrian dynamics, but from statistics - it takes into account only variance and interquartile range. And this property does not make a good sense to us. For these reasons, it has to be found something different. Few researchers dealt with it [16], [20, 19], [18], [8, 7].

We have to notice that there is not one correct method to use for finding the bandwidth of the kernel - for the same reasons as in the case of the kernel shape. Authors might to work with any smoothing parameter that is appropriate for their density application. Due to this fact, it is very important to understand the blur parameter in detail, before more complex usage, to make sure that the author's choice is justifiable.

Ref.	Year	First Author	Dim	Kernel	Details
[5, 4]	2005	Daamen	2	-	density defined using travel times
[10]	2006	Helbing	1	-	smooth particle count
[9]	2007	Helbing	2	exponential	weighted pedestrian contribution
[13, 12]	2008	Johansson	2	exponential	local density as in [9] using weights
[16]	2009	Krisp	2	Gauss	tool for visual choice of bandwidth
[27]	2010	Steffen	2	Voronoi	the concept used here
[22, 23]	2010	Schadschneider	2	exponential	concept from [9] mentioned
[24]	2011	Schadschneider	2	-	no consensus for the estimates
[17]	2011	Liddle	2	Voronoi	stabilization of the result
[28]	2011	Tipakornkiat	1	-	density at sidewalks (crossing lines)
[36]	2011	Zhang	2	Voronoi	comparing of few methods
[20, 19]	2012	Plaue	2	Gauss	bandwidth depends on time
[7, 8]	2013	Fan	2	Gauss	density of vehicular streams
[29]	2015	Tordeux	1	Voronoi, Gauss	comparing of few methods
[6]	2015	Duives	2	Voronoi, exp.	comparing of few methods
[15]	2018	Krbálek	1	Borsalino	smooth particle count
[18]	2019	Mollier	2	Gauss	opt. bandwidth for vehicles [7]
[2]	2019	Bukáček	2	Cone	individual density study
[11]	2020	Hillebrand	2	Voronoi, Gauss	comparing of few methods
[33]	2020	Vacková	2	Cone	application of individual density

Table 1: State of the Art: Estimates of Densities in Pedestrian Dynamics.

4 Conclusions

Having done the brief excursion through the history of pedestrian density estimates, we see that the whole thing has to be studied much deeper than it was already done. The density is undoubtedly affected by the parametric setting. Motivation of our research [34] is then evident.

Acknowledgements

This work was supported by the grant SGS21/165/OHK4/3T/14.

References

[1] Aleksandra Baszczyńska et al. Kernel estimation of cumulative distribution function of a random variable with bounded support. *Statistics in Transition. New Series*, 17(3):541–556, 2016.

[2] Marek Bukáček and Jana Vacková. Evaluation of pedestrian density distribution with respect to the velocity response. In *Traffic and Granular Flow'17*. Springer, 2019.

[3] José E Chacón and Tarn Duong. *Multivariate kernel smoothing and its applications.* Chapman and Hall/CRC, 2018.

[4] Winnie Daamen and Serge P Hoogendoorn. Flow-density relations for pedestrian traffic. In *Traffic and granular flow'05*, pages 315–322. Springer, 2007.

[5] Winnie Daamen, Serge P Hoogendoorn, and Piet HL Bovy. First-order pedestrian traffic flow theory. *Transportation research record*, 1934(1):43–52, 2005.

[6] Dorine C Duives, Winnie Daamen, and Serge P Hoogendoorn. Quantification of the level of crowdedness for pedestrian movements. *Physica A: Statistical Mechanics and its Applications*, 427:162–180, 2015.

[7] Shimao Fan. *Data-fitted generic second order macroscopic traffic flow models.* PhD thesis, Temple University. Libraries, 2013.

[8] Shimao Fan, Michael Herty, and Benjamin Seibold. Comparative model accuracy of a data-fitted generalized aw-rascle-zhang model. *arXiv preprint arXiv:1310.8219*, 2013.

[9] Dirk Helbing, Anders Johansson, and Habib Zein Al-Abideen. Dynamics of crowd disasters: An empirical study. *Physical review E*, 75(4):046109, 2007.

[10] Dirk Helbing, Anders Johansson, Joachim Mathiesen, Mogens H Jensen, and Alex Hansen. Analytical approach to continuous and intermittent bottleneck flows. *Physical review letters*, 97(16):168001, 2006.

[11] Arne Hillebrand, Han Hoogeveen, and Roland Geraerts. Comparing different metrics quantifying pedestrian safety. *Collective Dynamics*, 5:158–166, 2020.

[12] Anders Johansson. Data-driven modeling of pedestrian crowds. 2009.

[13] Anders Johansson, Dirk Helbing, Habib Z Al-Abideen, and Salim Al-Bosta. From crowd dynamics to crowd safety: a video-based analysis. *Advances in Complex Systems*, 11(04):497–527, 2008.

[14] Boris S Kerner. Three-phase traffic theory and highway capacity. *Physica A: Statistical Mechanics and its Applications*, 333:379–440, 2004.

[15] Milan Krbalek and Michaela Krbalkova. 3s-unification for vehicular headway modeling. *arXiv preprint arXiv:1811.05325*, 2018.

[16] Jukka M Krisp, Stefan Peters, Christian E Murphy, and Hongchao Fan. Visual bandwidth selection for kernel density maps. *PFG-Photogrammetrie Fernerkundung Geoinformation*, 5:441–450, 2009.

[17] Jack Liddle, Armin Seyfried, Bernhard Steffen, Wolfram Klingsch, Tobias Rupprecht, Andreas Winkens, and Maik Boltes. Microscopic insights into pedestrian motion through a bottleneck, resolving spatial and temporal variations. *arXiv preprint arXiv:1105.1532*, 2011.

[18] Stéphane Mollier, Maria Laura Delle Monache, Carlos Canudas-de Wit, and Benjamin Seibold. Two-dimensional macroscopic model for large scale traffic networks. *Transportation Research Part B: Methodological*, 122:309–326, 2019.

[19] Matthias Plaue, Günter Bärwolff, and Hartmut Schwandt. On measuring pedestrian density and flow fields in dense as well as sparse crowds. In *Pedestrian and Evacuation Dynamics 2012*, pages 411–424. Springer, 2014.

[20] Matthias Plaue, Minjie Chen, Günter Bärwolff, and Hartmut Schwandt. Multi-view extraction of dynamic pedestrian density fields. *PFG Photogrammetrie, Fernerkundung, Geoinformation*, pages 547–555, 2012.

[21] WM Predtetschenski and AI Milinski. Personenströme in gebäudenberechnungsmethoden für die projektierung rudolf müller, 1971.

[22] Andreas Schadschneider, Debashish Chowdhury, and Katsuhiro Nishinari. *Stochastic transport in complex systems: from molecules to vehicles.* Elsevier, 2010.

[23] Andreas Schadschneider, Mohcine Chraibi, Armin Seyfried, Antoine Tordeux, and Jun Zhang. Pedestrian dynamics: From empirical results to modeling. In *Crowd Dynamics, Volume 1*, pages 63–102. Springer, 2018.

[24] Andreas Schadschneider and Armin Seyfried. Empirical results for pedestrian dynamics and their implications for modeling. *Networks & heterogeneous media*, 6(3):545, 2011.

[25] Armin Seyfried, Bernhard Steffen, Andreas Winkens, Tobias Rupprecht, Maik Boltes, and Wolfram Klingsch. Empirical data for pedestrian flow through bottlenecks. In *Traffic and Granular Flow'07*, pages 189–199. Springer, 2009.

[26] BW Silverman. Density estimation for statistics and data analysis, publisher chapman and hall. *London, UK*, 1986.

[27] Bernhard Steffen and Armin Seyfried. Methods for measuring pedestrian density, flow, speed and direction with minimal scatter. *Physica A: Statistical mechanics and its applications*, 389(9):1902–1910, 2010.

[28] Chalat Tipakornkiat, Hyunyung Kim, and Thirayoot Limanond. Method to estimate the speed and density of the pedestrian sidewalk. In *Proceedings of the Eastern Asia Society for Transportation Studies Vol. 8 (The 9th International Conference of Eastern Asia Society for Transportation Studies, 2011)*, pages 205–205. Eastern Asia Society for Transportation Studies, 2011.

[29] Antoine Tordeux, Jun Zhang, Bernhard Steffen, and Armin Seyfried. Quantitative comparison of estimations for the density within pedestrian streams. *Journal of statistical mechanics: theory and experiment*, 2015(6):P06030, 2015.

[30] Martin Treiber and Arne Kesting. Traffic flow dynamics. *Traffic Flow Dynamics: Data, Models and Simulation, Springer-Verlag Berlin Heidelberg*, 2013.

[31] Robin T Underwood. Speed, volume, and density relationships. 1960.

[32] Jana Vacková and Marek Bukáček. The microscopic analysis of velocity-density paradigm. In *International Conference on Applied Mathematics 2019*. APLIMAT, 2019.

[33] Jana Vacková and Marek Bukáček. Follower-leader concept in microscopic analysis of pedestrian movement in a crowd. In *Pedestrian and Evacuation Dynamics 2018*. Collective Dynamics, 2020.

[34] Jana Vacková and Marek Bukáček. Pedestrian density estimates and their real applications. In *Stochastic and Physical Monitoring Systems 2021*. SPMS, 2021.

[35] Matt P Wand and M Chris Jones. *Kernel smoothing*. Chapman and Hall/CRC, 1994.

[36] Jun Zhang, Wolfram Klingsch, Andreas Schadschneider, and Armin Seyfried. Transitions in pedestrian fundamental diagrams of straight corridors and t-junctions. *Journal of Statistical Mechanics: Theory and Experiment*, 2011(06):P06004, 2011.

Stochastic and Physical Monitoring Systems
SPMS 2021
June 24 - 28, 2021
Malá Skála, Czech Republic

Pedestrian Density Estimates and Their Real Applications

Jana Vacková and Marek Bukáček

Department of Mathematics, FNSPE, Czech Technical University in Prague

Email: `janca.vackova@fjfi.cvut.cz`

Abstract. Having done the brief excursion through the history of pedestrian density estimates [7], we see that the whole thing has to be studied much deeper than it was already done. The pedestrian density is undoubtedly affected by the parametric setting used in a method. We choose the concept using kernel functions described in [7] which opens up a lot of new possibilities in real applications.

Key words: Density Distribution, Pedestrian Dynamics, Kernel Functions, Static Detector.

1 Introduction

We need to note that this paper is a direct follow-up to [7]. To preserve the reading experience, we recommend the reader to read the predecessor first. Briefly, we need to remind that we have defined and explained a kernel approach used for density estimates in [7]. Every kernel representing individual density distribution (i.e. the way how the pedestrian contributes to the total density distribution) has its size denoted by parameter R called blur (it represents the size of area affected by one pedestrian). Besides, there is one more factor which has to be set before evaluating the density - the shape of the detector (i.e. the area where the density is evaluated).

Motivation for this contribution is that the density estimate depends on the parametric settings and it cannot be said which parametric settings is the best. Thus the parametric study is needed because it may bring new insights into the understanding of this topic.

The following parametric study is based on the egress experiment organized in the study hall of FNSPE, CTU in Prague in 2014, see [1, 2, 3] for details. Pedestrians (undergraduate students wearing recognition caps) randomly entered the room by one of three entrances, walked to the opposite wall and left the room by one exit. By controlling input flow, different conditions from free flow to congestion in the exit area were achieved. In total, our sample is made up of 2000 paths through 10 experimental runs captured using 48 frames per seconds.

Cone, cylinder, Gauss and Borsalino kernels are evaluated for $R \in \{0.1, 0.2, \ldots, 3\}$.

Voronoi distribution and point approximation are evaluated only once (there is no parameter).

2 Study of the Static Detector

Let start our parametric study with a simple static detector in order to examine the kernel shape and size without any need to take into account the shape and size of pedestrian surroundings. We choose to start with one experimental round from E4 and the static detector defined as the red rectangle area A in Figure 1

$$A := \left\{ \boldsymbol{x} = (x_1, x_2) \in \mathbf{R}^2 : x_1 \in \langle 2, 4 \rangle \wedge x_2 \in \langle 0, 1 \rangle \right\}$$

and denote $\rho(t) := \rho_A(t)$ for simplicity in this section.

We will examine what the change in the kernel settings causes in the density values and even in the fundamental diagram itself. We will use the variable called *count* $C(t) := C_A(t)$ instead of the density very often - the reason is that we have the static detector here, thus the value of the density would be divided by a same constant in all cases. Finally, we will use a normalized time t_{norm} in the meaning that the start is represented by $t_{norm} = 0$ and the end by $t_{norm} = 1$. Due to this normalization it is possible to compare more experimental runs in the future in the same figure without any ambiguousness.

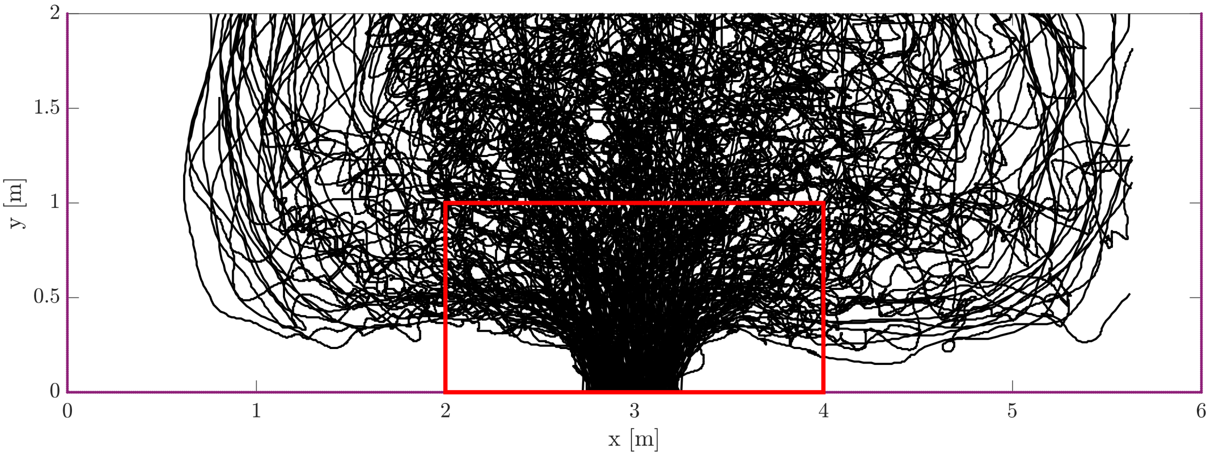

Figure 1: Trajectories in the round 6 of the experiment and chosen static detector (red rectangle).

2.1 Roughness and Featureless

We plotted the pedestrian count $C(t)$ in Figure 2 for all examined kernels (explanation why the Borsalino kernel is missing here will be found in the further text in Section 2.5) and $R \in \langle 0.1, 2 \rangle$ m. We can see an essential difference between Guassian kernel and the conic or the cylindrical kernels, which behave similarly. The kernel of Gauss smooths the pedestrian count from $R = 1.5$ m significantly - it is caused by the limitless support, however this reason can be subsequent to different scaling of Gauss and other kernels, for detail explanation see Section 2.3.

Voronoi cannot be discussed in this way because it has no parameter to change. The similarity of the count generated by Voronoi diagram and other kernels will be researched in Section 2.4 separately.

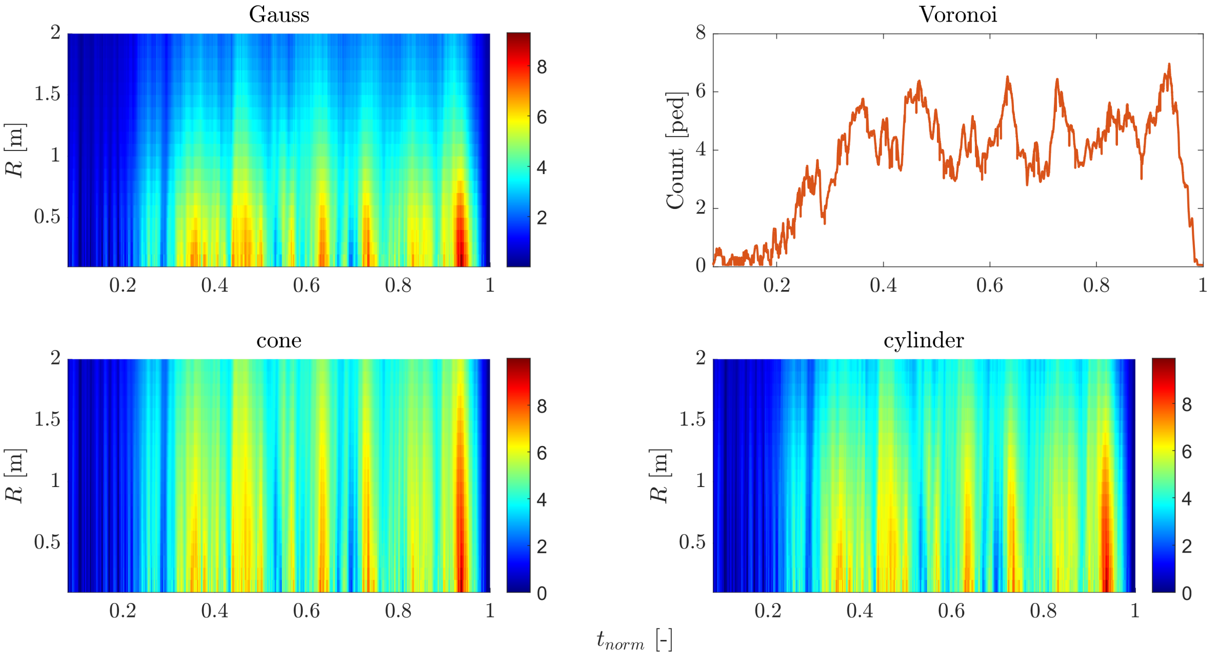

Figure 2: Pedestrian count with respect to time and kernel size.

To quantify this observation, we define mean absolute derivative (depicted in Figure 3) understood as the *roughness* of the curve

$$\langle \dot{C} \rangle := \frac{1}{N_{\sharp time}} \sum_{i=2}^{N_{\sharp time}} \frac{|C(t_i) - C(t_{i-1})|}{t_i - t_{i-1}} \qquad [\text{ped/s}],$$

where $\sharp time$ denotes the total number of times (frames) that we have available from the experiment. Let us mention that $(t_i - t_{i-1})^{-1}$ = frame rate = 48 s^{-1}.

Already mentioned properties can be clearly seen in Figure 3. Moreover, the point approximation (Dirac distribution) generates (as the most scattered curve with lots of jumps) an upper boundary for the others and Voronoi count can be interpreted as the median value for conic or cylindrical curves. Gaussian curve confirms that the Gaussian kernel is the most smoothed kernel shape. Besides, the conic kernel converges to the Gaussian one for increasing R. Cylindrical kernel converges too, if we exclude the trend from $R > 2.5$ m, which can be caused by a (very smoothed) pedestrian leaving the detector (and the rest of their kernel still being in the detector at the same time) - this situation can make a significant change in the count. It is, of course, influenced by the size of the detector - the larger the detector, the smaller the jump. Cylindrical kernel is almost the same as the curve of the conic kernel, for low values of R is cylinder greater than cone - it is produced by the fact that cylinder is similar to Dirac distribution, especially for R small.

We are not interested only in the trend, but also in the range of the curve. This property is described by the maximum of pedestrian count $\max_t C(t)$ [ped] which is understood as the level of the *featureless*. Gaussian kernel is the most smoothed kernel, thus its maximum of the pedestrian count has the lowest value from the all compared kernels for every blur R. Due to the definition of the kernels, it is obvious that cone has greater values of maximums than cylinder for all values of blur. Dirac has the greatest value again and Voronoi values has the same interpretation as above. We can say that

$$\max_t C_{\text{Dirac}}(t) \geq \max_t C_{\text{Cone}}(t) \geq \max_t C_{\text{Cylinder}}(t) > \max_t C_{\text{Gauss}}(t).$$

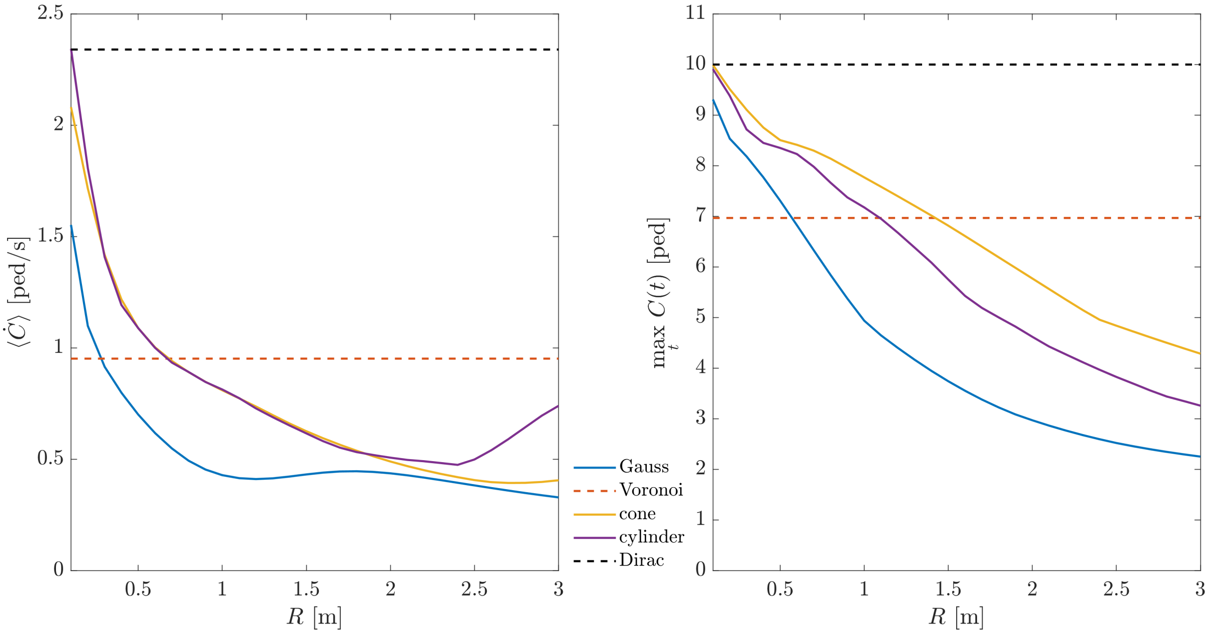

Figure 3: Left: the mean absolute derivative of the pedestrian count. Right: the maximum of the pedestrian count.

2.2 Fundamental Diagram

Having discussed the time development of the pedestrian count, it is important to investigate the impact of the parametric choice (kernel and its size) on fundamental diagram, especially the fundamental relationship between velocity and density (the flow can be computed using hydrodynamic approximation).

We define the corresponding speed as the mean (current) speed of all pedestrians occurring in the detector at the same time, because we assume the speed as the speed of the pedestrian mass in the detector - every speed has the same weight.

There is more options to define the mass speed for fundamental diagram. For instance, we could define the speed as the size of the velocity which is the resultant of the velocities of all pedestrians in the detector. It is definitely possible to define the speed using kernels too. However, it is the point of the possible future work to study the difference between these definitions.

It is not feasible to plot fundamental diagrams for all parametric settings, therefore we fit the curves and compare two parameters of these fits. We use fit defined by Pipes [6] from vehicular stream

$$v(\rho) = v_0 \left(1 - \frac{\rho}{\rho_J}\right)^3, \tag{1}$$

where two banal equalities are fulfilled $v(0) = v_0$, $v(\rho_J) = 0$. Parameters $v_0, \rho_J \in \mathbf{R}^+$ with respect to R are drawn in Figure 4.

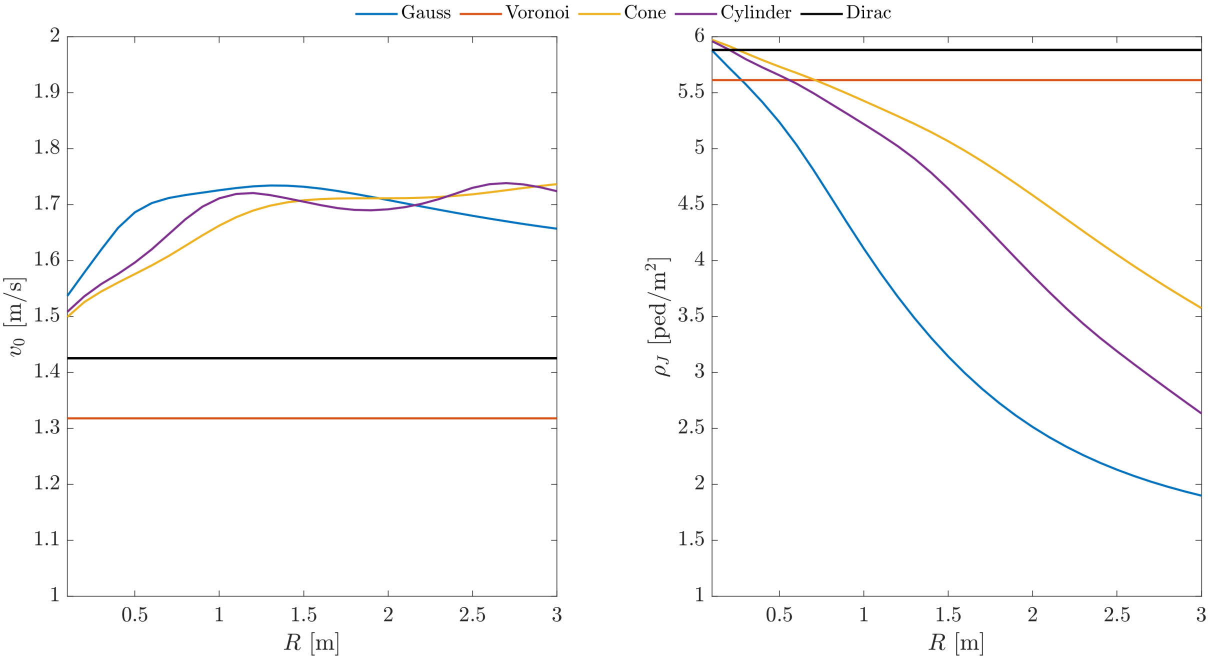

Figure 4: Parameters of the fit of Pipes with respect to blur R for 6th experimental round.

We can see that the range of values is much smaller for parameter v_0 than for parameter ρ_J - v_0 is very similar for all kernels. The most different kernel is the Voronoi diagram because the other kernels generate more mass already during the entering into the detector - the Voronoi creates the most blurred pedestrians if the occupancy in the room is low. Parameter ρ_J is distinguishable between kernels and show us the main difference in the fundamental diagrams - the 'width' of the data cloud.

2.3 Mass Recomputation of Gaussian Kernel

We have noticed from previous discussions that Gaussian kernel has very similar result in trends as conic kernel, however the results are shifted due to the fact that Gaussian kernel has limitless support as opposite to cone. We would like to examine now if any formula exists between Gaussian and conic kernel that it would erase the shift between them.

To reach our aim, it is necessary to get 'almost all' mass of Gaussian kernel into the base of the cone $A_R = \{\boldsymbol{x} \in \mathbf{R}^2 : \|\boldsymbol{x}\| \leq R\}$. Let us denote Gaussian kernel at zero with variance σ^2

$$p(\boldsymbol{x}, \sigma) = \frac{1}{2\pi\sigma^2}\, \mathsf{e}^{-\frac{\|\boldsymbol{x}\|^2}{2\sigma^2}}.$$

Thus we solved the following integral

$$\int_{A_R} p(\boldsymbol{x}, \sigma)\, \mathsf{d}\boldsymbol{x} = \int_0^{\frac{R^2}{2\sigma^2}} \mathsf{e}^{-t} \mathsf{d}t.$$

The result is lower incomplete Gamma function which has numerically known values. As we want to find relation between R and *sigma*, let assume that $R = k\,\sigma$. Then

$$\int_{A_{k\,\sigma}} p(\boldsymbol{x}, \sigma)\, \mathsf{d}\boldsymbol{x} = \int_0^{\frac{k^2}{2}} \mathsf{e}^{-t} \mathsf{d}t.$$

Values of this integral are computed in Table 1 for $k \in \{1, 2, 3, 4\}$. We can see, for instance, that for choice $\sigma = \frac{R}{3}$ the Gaussian mass is inside the base of the cone with radius R by almost 99%. This is the reason why their densities are comparable - see Figure 5.

k [-]	1	2	3	4
mass [%]	39.35	86.47	98.89	99.97

Table 1: Gaussian mass inside the base of cone for different values of k.

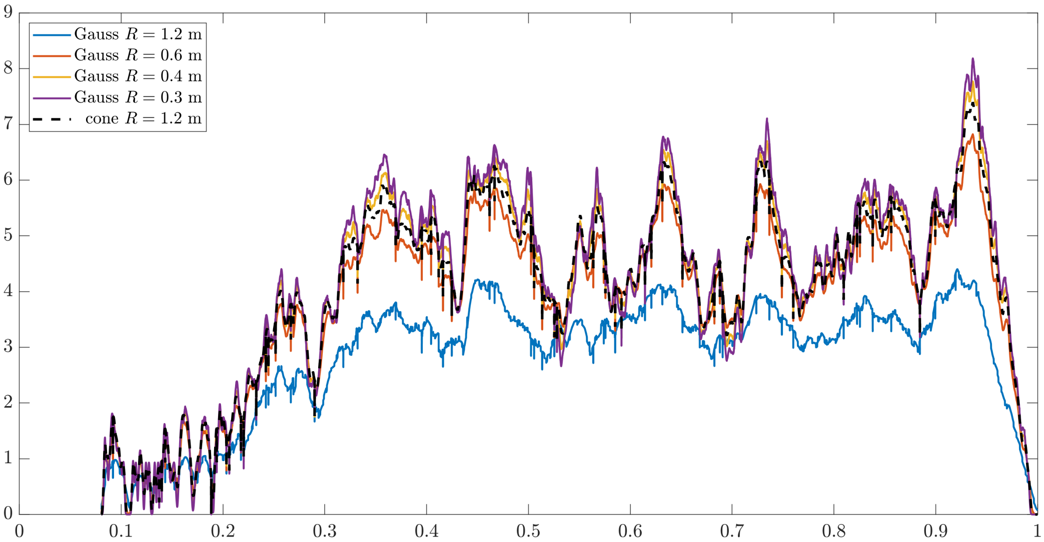

Figure 5: Gaussian and conic densities in time for experimental round number 6.

2.4 Alternatives of Voronoi Diagram

Having researched impact of kernels on density and fundamental diagram, it could be interesting and useful to realize if there is any parametric settings of kernels which is very close to pedestrian count computed with Voronoi distribution. To measure this (dis)similarity, we choose total absolute deviation.

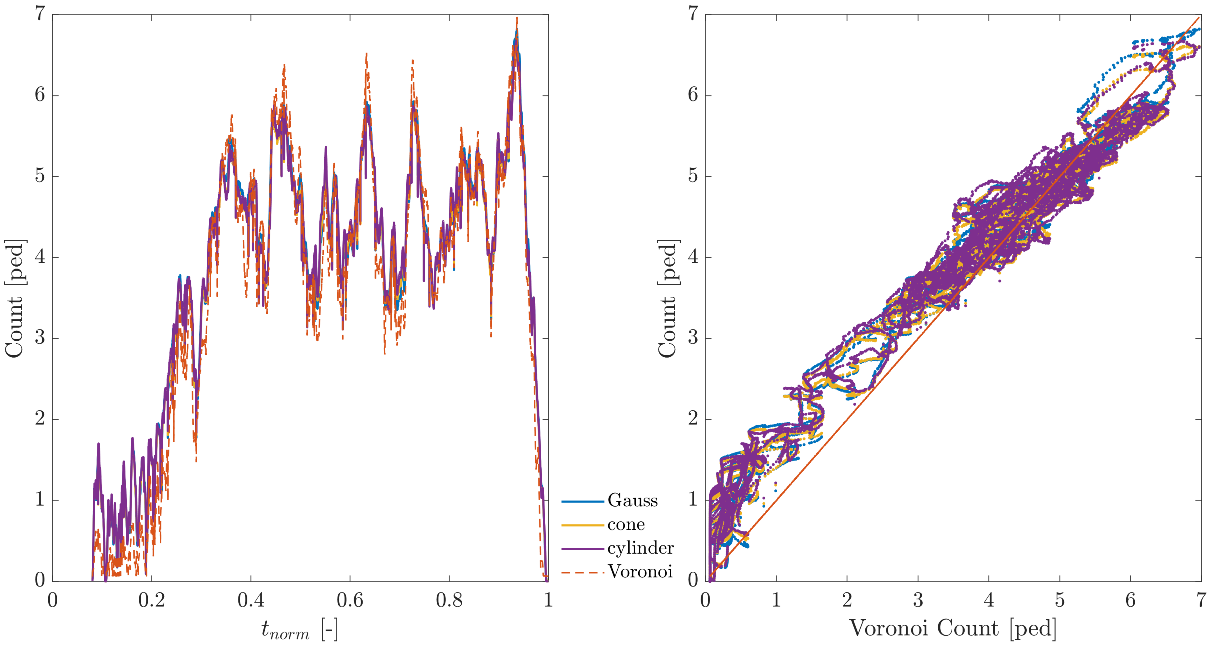

Figure 6: Alternatives of Voronoi diagram for round number 6: time development (left), pedestrian count distribution (right).

Time development of pedestrian count (left) and pedestrian count distribution for different kernels versus Voronoi distribution (right) are denoted in Figure 6. We can say that Voronoi diagram has its alternatives among other kernels, specifically for $R \in (0.7, 1.5)$ m. However there is greater range for Voronoi than for other kernels and also slight differences for low densities in Figure 6 (left). This undervaluation of Voronoi pedestrian count is evident in Figure 6 (right). The greater range could be caused due to the property that Voronoi can resemble Dirac distribution under specific condition (dense crowd).

2.5 Conic versus Borsalino Kernel

Finally we want to compare two very similar kernels - conic kernel and Borsalino kernel [5] which were properly defined earlier and their density distributions are depicted in Figure 7. Considering properties of these two functions (limited support, decreasing trend), we expect the same behaviour.

Mean absolute derivative and maximum of pedestrian count for conic and Borsalino kernel are in Figure 8. We can see that the results are almost identical.

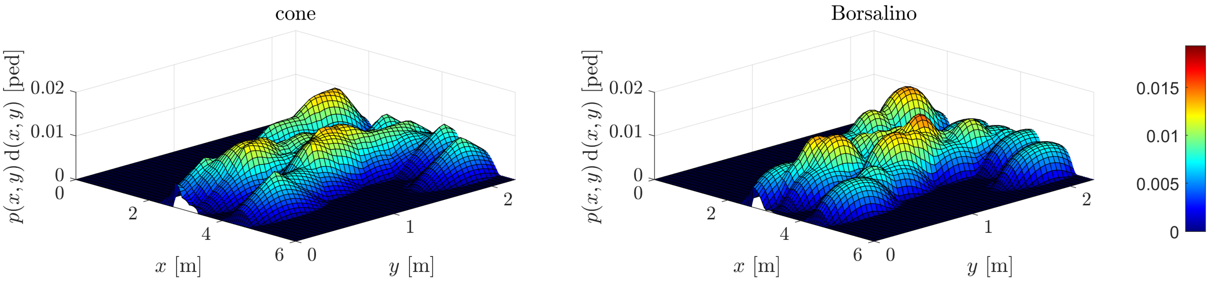

Figure 7: Density distribution of conic and Borsalino kernel.

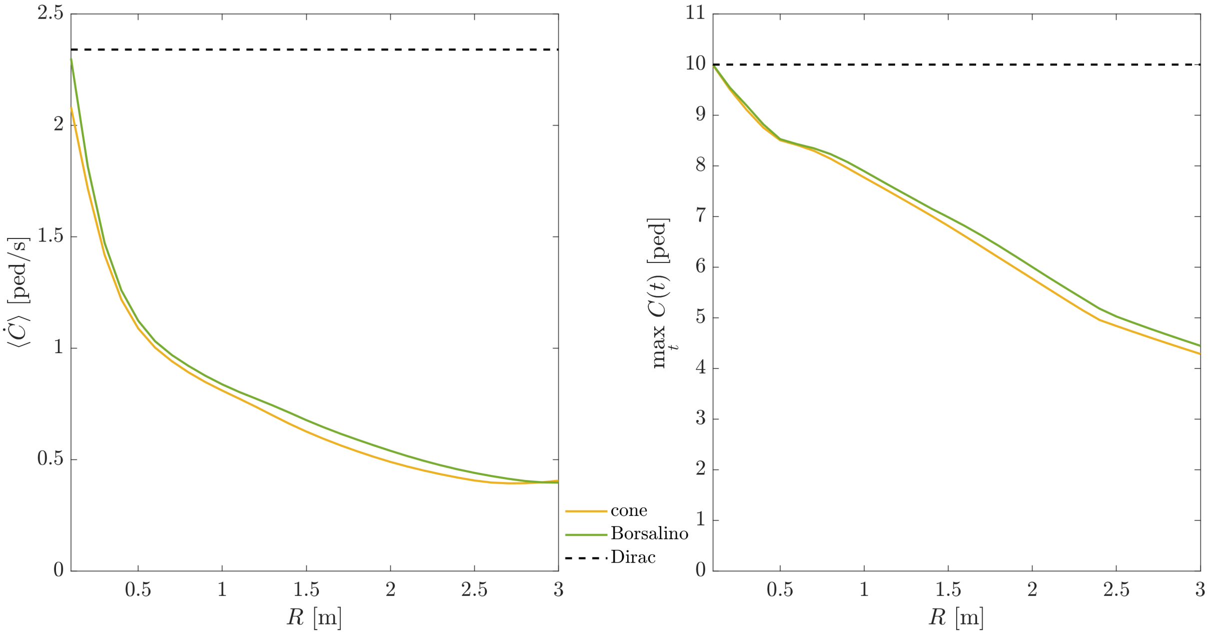

Figure 8: Mean absolute derivative and maximum of pedestrian count for cone and Borsalino for round number 6.

3 Real Applications

Density distributions can be very useful - very important quantity for civil engineering is pedestrian *comfort*. First author is currently part of the research team at Faculty of Civil Engineering, Brno University of Technology, which want to properly define and appropriately use this quantity. Firstly, during work under project *TAČR ZETA Effective spatiotemporal predictions using machine learning methods*, well working definition of comfort was created which led to use density by density distributions in the way of median value (over time), i.e. $\rho_{0.5}(\boldsymbol{x}, R)$. To find appropriate kernel size, proxemic zones were assumed [4] and 80 percent of the mass of the Gaussian kernel was chosen to fit into personal space (which was delimited by Hall). The rest of the kernel covers other proxemic zones. This definition give us reasonable findings according to preliminary results. More information can be found in the project report.

Nowadays, new definition arises and the further results will be published in the future.

4 Conclusions

To conclude, the density evaluated inside the detector significantly depends on the blur parameter hidden inside the individual density kernel. As shown by this study, desired behaviour of detector density from perspective of 'roughness', 'pedestrian blending' and 'stability in time' may be achieved by a specific setting of this parameter. Presented (symmetric) kernels may differ by scaling (e.g. conic versus Gaussian kernel), however all of them converge to similar value of density. Even the shape itself can be used for fine-tuning, the final choice may be driven rather by an implementation preference than data requirements.

Analysed non-parametric density evaluation methods (point approximation, Voronoi diagram) bring similar values as the kernel methods with the appropriate value of blur parameter - to be more specific, the blur going to zero mimic the point approximation and the blur in interval $(0.7, 1.5)$ m fits the Voronoi method.

Further research would extend presented work by pedestrian surrounding analysis, i.e. studying the area that impacts pedestrian behaviour. However, the results have promising impacts to the real application (by 'comfort' metrics) and theory (possible analytical solutions of density development).

Acknowledgements

This work was supported by the grant SGS21/165/OHK4/3T/14.

References

[1] Marek Bukáček, Pavel Hrabák, and Milan Krbálek. Experimental analysis of two-dimensional pedestrian flow in front of the bottleneck. In *Traffic and Granular Flow'13*, pages 93–101. Springer, 2015.

[2] Marek Bukáček, Pavel Hrabák, and Milan Krbálek. Individual microscopic results of bottleneck experiments. In *Traffic and Granular Flow'15*, pages 105–112. Springer, 2016.

[3] Marek Bukáček, Pavel Hrabák, and Milan Krbálek. Microscopic travel-time analysis of bottleneck experiments. *Transportmetrica A: transport science*, 14(5-6):375–391, 2018.

[4] E.T. Hall. The silent language. 1959.

[5] Milan Krbalek and Michaela Krbalkova. 3s-unification for vehicular headway modeling. *arXiv preprint arXiv:1811.05325*, 2018.

[6] Louis Albert Pipes. Car following models and the fundamental diagram of road traffic. *Transportation Research/UK/*, 1966.

[7] Jana Vacková and Marek Bukáček. State of the art of pedestrian density estimates. In *Stochastic and Physical Monitoring Systems 2021*. SPMS, 2021.

Stochastic and Physical Monitoring Systems
SPMS 2021
June 24 - 28, 2021
Malá Skála, Czech Republic

Classification of AE Signals Based on Statistics and Machine Learning

Jan Zavadil, Václav Kůs

Department of Mathematics, FNSPE, Czech Technical University in Prague, Czech Republic

Email: `zavadja4@fjfi.cvut.cz`

Abstract. Reliable classification of acoustic emission signals is crucial for practical use of this nondestructive testing technique. During the classification, signals are represented by a convenient, low-dimensional set of attributes. This contribution adresses the problem of selecting appropriate atributes and consequently describes and compares several classification methods, specifically Division methods, Model Based clustering, KDE method and classification using Supervised Divergence Decision Tree. The paper proposes new attribute and classification method. The methods were tested and compared on a set of laboratory measured data. The most reliable method seems to be the supervised KDE classification method.

Key words: Acoustic emission, clustering, KDE clustering, ϕ-divergence, MBC, signal attributes.

1 Introduction

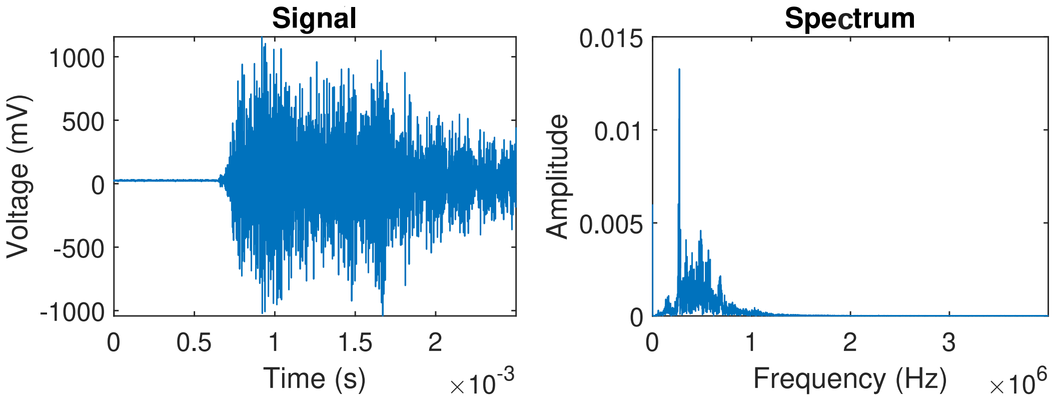

Figure 1: Typical example of acoustic emission signal with its spectrum.

Acoustic emission (AE) is the phenomenon of releasing accumulated deformation energy in the form of elastic waves in solid materials. AE naturally occurs as a result of permanent changes in material internal structure e.g. formation of a crack, plastic deformation, or mechanical loading. Therefore, screening of AE has huge potential in the field of non destructive testing, where it allows detecting, locating, and, with some prior knowlege, even characterising damage. AE waves are detected on the surface of given object using piezoelectric sensors. An example of typical AE signal, along with its spectrum computed using FFT, is given in Figure 1. This paper shortly describes the attributes extracted from such signals as well as classification methods used to classify the signals based on their physical origin. The results of classification methods and their comparison are presented.

To test and compare implemented methods we used a dataset from an experiment [2], in which AE was initiated on a thin metal plate by various artificial sources (pen-test, fall of ping pong ball, etc.). Available data are presented in Table 1.

Source type	src. 1	src. 2	src. 3	src. 4	src. 5
N. of observations	65	173	103	126	135

Table 1: Available AE data

2 Signal Attributes

Usage of the whole measured signal for classification purposes appears to be inefficient [4], it is therefore necessary to represent the measured signal by a low dimensional set of attributes that are extracted from the signal. These attributes assign each signal to a point in the factor space so the task of classifying signals is transformed into finding clusters of these points in the factor space. During classification we usually use 2 or 3 dimensional factor space. Further, we describe implemented attributes, x_t denotes the measured signal and S_f is its normalized spectrum.

1. Attribute Z_c:

$$Z_c = \sum_{t=\tilde{t}}^{T-1} \delta(x_t),$$

$$\text{where } \tilde{t} = \min J, J = \left\{ j \in [0, T-1] : x_j \geq c \max_{t \in [0,T-1]} |x_t| \right\}, \quad c \in (0,1),$$

$$\delta(x_t) = \begin{cases} 1 & \text{if } \operatorname{sgn}(x_t x_{t+1}) = -1, \\ 0 & \text{otherwise.} \end{cases}$$

2. Attribute M:

$$M = \operatorname{argmax}_{t \in [0,T-1]} |x_t|.$$

3. Attribute W_α:

$$W_\alpha = \mathrm{argmin}_{l\in[0,T-1]} \sum_{f=0}^{T-1} |l-f| \left| |S_f| - |\,\overline{S_T}\,| \right|^\alpha,$$

$$\text{where} \quad |\,\overline{S_T}\,| = \frac{1}{T}\sum_{f=0}^{T-1} |S_f| \quad \text{and} \quad \alpha \in [1,\infty).$$

4. Attribute Q_β:

$$Q_\beta = \min\Big\{F \in [0,T-1] : \sum_{f=0}^{F} |X_f| \geq \beta\Big\} \quad \text{for a fixed } \beta \in (0,1).$$

5. Attribute S_γ:

$$S_\gamma = \max J - \min J,$$

$$\text{where } J = \Big\{j \in [0,T-1] : |X_j| \geq \gamma \max_{f\in[0,T-1]} |X_f|\Big\}, \quad \gamma \in (0,1).$$

6. Attribute P:

$$P = \frac{1}{T}\sum_{f=0}^{T-1} f S_f.$$

3 Classification Methods

Let us suppose that we measured n signals of AE coming from M different physical sources. Each signal is represented using d attributes as a point in d-dimensional factor space. The set of n measured signals represented in factor space is denoted as $\boldsymbol{x} = (x_1,\dots,x_n) \subset \mathbb{R}^d$. All implemented classification methods except MBC are supervised, therefore it is necessary to provide them with a training dataset $\boldsymbol{T} = (T_1,\dots,T_M) \subset \mathbb{R}^d$, where $x_{ik} \in T_i$ if and only if x_{ik} comes from i-th source.

Model Based Clustering

Model Based Clustering (MBC) method treats data as a realization of a random variable with probability density in the form of distribution mixture [7] composed of M normal components p_j of corresponding dimensions. We can write this mixture as

$$p(x|\Theta) = \sum_{j=1}^{M} \alpha_j p_j(x|\theta_j), \qquad \sum_{j=1}^{M} \alpha_j = 1.$$

To estimate the parameters $\Theta = (\alpha_1,\dots,\alpha_M,\theta_1,\dots,\theta_M)$, fully describing the distribution, we use an EM (expectation minimization) algorithm [1], because it is not possible to maximize the likelihood function of the mixture directly since we do not know the affiliation of samples to components. EM is an iterative algorithm which maximizes the conditioned expectation of likelihood

$$E_z(l(\Theta|\boldsymbol{z},\boldsymbol{x})|\boldsymbol{x},\Theta), \tag{1}$$

where $\boldsymbol{z}$ is an affiliation matrix. We then assign i-th sample to j-th cluster if

$$j = \text{argmax}_{j\in\hat{M}}\Big(\alpha_j p_j(x_i|\theta_j)\Big).$$

Supervised Model Based Clustering

Supervised Model Based Clustering (SMBC) method is an improvement of MBC method using provided training data $\boldsymbol{T}$. In MBC the initial values of parameters $\Theta = (\alpha_1,\ldots,\alpha_M,\theta_1,\ldots,\theta_M)$ in EM algorithm are chosen randomly, SMBC uses training data to initialize these parameters closer to their actual values, making EM algorithm more likely to converge to a global maximum of expectation in (1).

Since we suppose that the components of distribution mixture are normal distributions, the paramethers θ_i are of the form $\theta_i = (\mu_i, \mathbb{C}_i)$. We use the MLE to estimate these parameters from each dataset T_i through

$$\widehat{\mu_i} = \frac{1}{n_i}\sum_{k=1}^{n_i} x_{ik}, \tag{2}$$

$$\widehat{\mathbb{C}_i} = \frac{1}{n_i}\sum_{k=1}^{n_i}(x_{ik}-\widehat{\mu_i})(x_{ik}-\widehat{\mu_i})^T, \tag{3}$$

where n_i is number of observations in T_i. Parameters α_i are initialized as

$$\widehat{\alpha}_i = \frac{n_i}{\sum_{j=1}^{M} n_j}, \tag{4}$$

in order to take into account different sizes of sets T_i. After the EM algorithm estimates the final values of parameters, data $\boldsymbol{x}$ are assigned to the clusters the same way as in MBC.

Gaussian Mixture Model Clustering

Gaussian Mixture Model Clustering (GMMC) method is derived from MBC method as a naive, more simple classificator, which does not use the EM algorithm and is therefore extremely light and fast. We suppose again that the data come from a mixture of normal distributions

$$p(x|\Theta) = \sum_{j=1}^{M}\alpha_j p_j(x|\theta_j).$$

However, this time we estimate the parameters Θ only based on the training dataset $\boldsymbol{T}$, while we use (2),(3),(4), so the final form of the mixture distribution is

$$p(x|\widehat{\Theta}) = \sum_{j=1}^{M}\widehat{\alpha}_j p_j(x|\widehat{\theta}_j), \qquad \widehat{\theta}_j = (\widehat{\mu}_j, \widehat{\mathbb{C}}_j).$$

Data $\boldsymbol{x}$ are then divided the same way as in MBC and SMBC.

Supervised Kernel Density Estimation Clustering

Supervised Kernel Density Estimation Clustering (SKDEC) method still keeps the notion of mixture distribution, in this case, however, instead of working with parameterized normal distributions, we use the nonparametric kernel density estimator described in [3]. We are using Epanechnikov kernel and Silverman bandwidth parameter minimalizing the MISE, see [1].

Mixture distribution is now in the form of

$$\hat{f}(x) = \sum_{i=1}^{M} \alpha_i \hat{f}_i(x),$$

where each component $\hat{f}_i$ is the kernel density estimate of the training data from T_i, i.e.

$$\hat{f}_i(x) = \frac{1}{n_i h_i} \sum_{k=1}^{n_i} K\left(\frac{x - x_{ik}}{h_i}\right),$$

and the coefficients α_i are defined as

$$\alpha_i = \frac{n_i}{\sum_{j=1}^{M} n_j}.$$

Observation x_k from $\boldsymbol{x}$ is then classified into the j-th cluster if

$$j = \operatorname{argmax}_{i \in \widehat{M}} \left(\alpha_i \hat{f}_i(x_k)\right).$$

Supervised Divergence Decision Tree

Supervised Divergence Decision Tree (SDDT) is a binary classification tree developped in [5], [6]. It was primarily used to classify data from high energy physics experiments. Unlike other methods implemented, the SDDT always works with all the attributes available. The tree is built and initialized with training data $(T_{signal}, T_{bckground})$. Since it is a binary classifier, it is necessary to run it M times if we want to classify into M clusters, always chosing a different set T_i as T_{signal} and the rest of training data as $T_{bckground}$. The tree is initialized recursively, further we describe the stages carried out in every node beggining with the root.

1. We check if the set of observations we receive is clean enough, if so the growth of the tree is terminated.

2. For a given $k < d$ and for all combinations of k attributes, we estimate densities of data from $T_{signal} \sim \hat{f}_s$ and $T_{bckground} \sim \hat{f}_b$ using quantile histograms. We have $\binom{d}{k}$ pairs of densities.

3. For all the pairs of densities we compute their Rényi divergence $R_{\frac{1}{2}}^{(j)} = R_{\frac{1}{2}}(\hat{f}_s^{(j)}, \hat{f}_b^{(j)})$ [8].

4. We choose the j^*-th combination maximizing the Rényi divergence

$$j^* = \operatorname{argmax}_{j \in \widehat{\binom{d}{k}}} \left(R^{(j)}_{\frac{1}{2}} \right).$$

5. We use the j^*-th combination of k attributes to classify observations in this node using kernel estimation based clustering. Data classified as signal are passed into the right son and the rest to the left son of the current node.

After finishing the training process, the data, we want to classify, are inserted into the root and based on their trajectory through the tree an affiliation score is assigned for each cluster. Data are then classified based on this score.

4 Classification Results

For the attributes dependent on their inner parameters, the following setting was chosen

$$Z = Z_{\frac{1}{20}},\ \ W = W_2,\ \ Q = Q_{0{,}33},\ \ S = S_{\frac{1}{3}}.$$

During the comparison and testing of methods a vast number of combinations of attributes were inspected and parameters Z, Q, P proved themselves to be the most efficient.

In Table 2, the results of classification of signals coming from 3 and 5 sources are listed. Only the most successfull combinations of attributes are presented. These classifications are depicted for chosen methods in Figures 2, 3.

Attributes	MBC	SMBC	GMMC	SKDEC	SDDT
3 sources (Q-Z)	96,5	96,5	96,2	96,5	**97,3**
5 sources (Z-P)	86,7	88,7	**92,0**	91,1	89,9

Table 2: Classification results in % of correctly classified

It has proven that the choice of attributes is crucial for a successfull classification. For well separated clusters, the diferences in succes rate between methods were insignificant. On the other hand, for clusters which were overlapping, the supervised methods making use of the training data, were often far more successfull. Overall, the most successfull method appears to be SKDEC, especially because it is not limited to eliptically shaped clusters like all the other methods expecting normal components included in the data. The method SDDT is not very appropriate for this application, mostly because of lack of training data.

Acknowledgements

These results were supported by the research grants LTT180001 (MEYS), LM2015068, and SGS21/165/OHK4/3T/14 (MEYS).

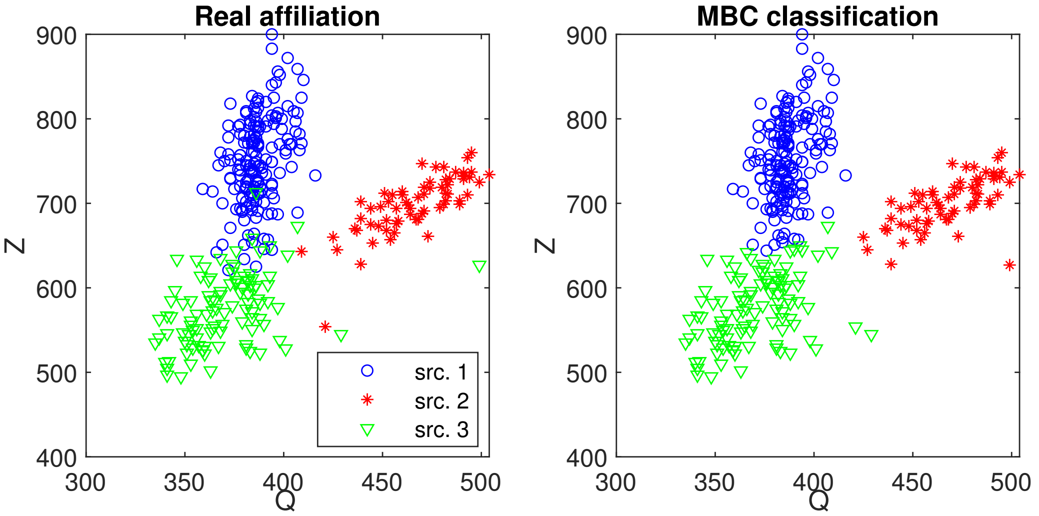

Figure 2: Classification of 3 sources of signals using MBC method

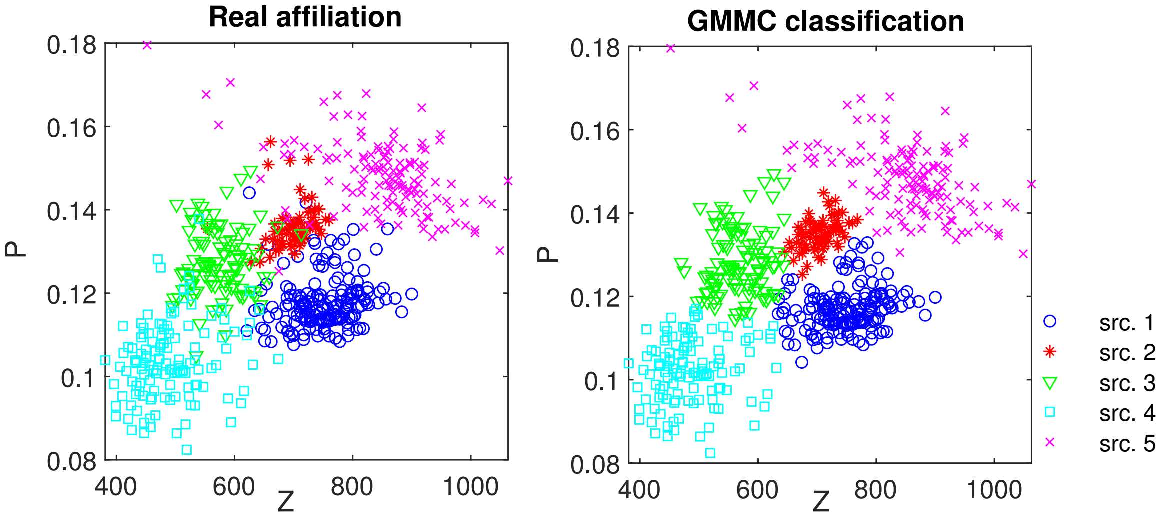

Figure 3: Classification of 5 sources of signals using GMMC method

References

[1] J. Zavadil. *Statistická a strojová klasifikace signálů akustické emise pro detekci defektů v materiálech.* Bakalářská práce, KM FJFI ČVUT, 2021.

[2] Z. Farová. *Statistické metody odhadu hustot a klasifikace signálů.* Výzkumný úkol, KM FJFI ČVUT, 2010.

[3] B.W. Silverman. *Density estimation for statistics and data analysis.* Boca Raton: Chapman & Hall/CRC, 1998.

[4] S. Aghabozorgi, A. Shirkhorsidi, T. Wah. Time-series clustering – A decade review *Information Systems*, **53**, 16–38, 2015.

[5] K. Jarůšková. *Identifikace energetických prongů při oscilaci neutrin v experimentu NOvA*. Výzkumný úkol, KM FJFI ČVUT, 2019.

[6] P. Bouř. *Divergenční metody ve statistických separacích.* Diplomová práce, KM FJFI ČVUT, 2014.

[7] G. J. McLachlan, D. Peel. *Finite Mixture Models.* John Wiley & Sons, 22. 3. 2004.

[8] L. Pardo. *Statistical Inference Based on Divergence Measures.* Chapman and Hall/CRC, 2020.